"Synthesis, structure and properties of Al-based borohydrides for hydrogen storage"

Dovgaliuk, Iurii

Abstract

This thesis is dedicated to chemistry and hydrogen storage properties of novel complex hydrides. The main efforts were focused on synthesis and characterization of new Al-based borohydrides and amidoboranes. Somewhat different investigation on the hydrolysis of KBH4 in the atmosphere of CO2 was also performed. The series of mixed-cation M[Al(BH4)4] (M = Li+, Na+, K+, NH4+, Rb+, Cs+) were successfully obtained by a reaction of the corresponding MBH4 with Al(BH4)3. This method provides a high theoretical hydrogen capacity and enables to store highly reactive and unstable Al(BH4)3 in a solid-state form. A good quality of the obtained samples allowed to solve their crystal structures using variable temperature synchrotron X-ray powder diffraction (XRPD). The thermal decomposition of M[Al(BH4)4] shows various pathways: Al(BH4)3 is released below 100 °C for M = Li+ and Na+, while heavier derivatives evolve hydrogen and diborane at about 150 °C. Li[Al(BH4)4] firstly decomposes into Li4Al3...

Document type : *Thèse (Dissertation)*

Faculty of Sciences

Institute of Condensed Mater and Nanosciences

(IMCN)

The division of Molecules, Solids and Reactivity

(MOST)

Synthesis, Structure and Properties of Al-based Borohydrides for Hydrogen Storage

Doctoral dissertation submitted for the PhD degree in Sciences

Iurii Dovgaliuk

Louvain-la-Neuve

December 2015

Jury Members:

Professor Radovan Černý
Université de Genève

Professor Luc Van Meervelt
Katholieke Universiteit Leuven

Professor Joris Proost
Université catholique de Louvain

Professor Eric Gaigneaux
Université catholique de Louvain (President)

Professor Michel Devillers (Supervisor)
Université catholique de Louvain

Professor Yaroslav Filinchuk (Supervisor)
Université catholique de Louvain

Table of Contents

Acknowledgements

First of all, I would like to thank my supervisors, Professors Yaroslav Filinchuk and Michel Devillers. Without your help this work would have been impossible. I'm grateful for your trust in me and for all the support.

I thank Prof. Radovan Černý for help in data interpretation as well as teaching me solving crystal structures from X-ray powder diffraction. It is a big pleasure to thank Prof. Torben Jensen from Aarhus University for the collaboration. I would like to thank also Lars Jepsen and Kasper Trans Møller, his PhD-students, who helped me in several projects.

The high quality of the diffraction data would not be possible without help of people, who kindly supported my experiments at Material Science beam line (PSI, Villigen, Switzerland) and at Swiss-Norvegian Beam Lines (ESRF, Grenoble, France). I thank to all beamline scientists, who provided the best ever experimental conditions and support during long days and nights at the synchrotrons. Especially I would like to mention Prof. Vladimir Dmitriev, Dr. Dmitry Chernyshov and Dr. Vadim Dyadkin from SNBL.

I thank Prof. Zbigniew Łodziana from Department of Structural Research INP Polish Academy of Sciences for his contribution with valuable DFT calculations. We thank Prof. Olivier Riant for providing the Plexiglas glovebox for our experiments on aluminium borohydride.

I'm very grateful to my colleagues from IMCN, very friendly and helpful people. In particular, I want to thank Drs. Koen Robeyns and Cécile Le Duff as well as Prof. Tom Leyssens. I will always

remember your help and support, not only in scientific questions, but also with my live and study in Belgium.

I would like to thank to all the members of the group of Prof. Yaroslav Filinchuk. Firstly, to the people who helped me to develop together with my supervisor: Drs. Damir Safin, Mariya Babashkina, Nikolay Tumanov and Voraksmy Ban. I am also grateful to my colleagues in the group, PhD-students: Caroline Picasso (for her infinite enthusiasm) and Fabrice Morelle (for a nice collaboration and love to the music).

I wish to mention some people, who made my leisure in Belgium definitely more interesting. Thank you gays, who played football with me (unfortunately I cannot list all of you): Ricky Payen, Boris Nshi, Thomas Xhurdebise and others. Also my thanks to the best co-drinkers of Belgian beer and my friends: Mariuzh Wolff, Bram Harmsen and Kasper Trans Møller.

Special thanks to the most helpful person in the world – to my friend Antoine Railliet. Without joking, you've saved my life and my thesis' preparation… I will never forget you, your positive humor and your kindness.

Finally, it was a great pleasure to spend these 4 years in IMCN. My work would not be finished without help of technicians, secretaries and other stuff of the university. I thank them very much for help and always positive mood.

My great thanks for the financial support from the Academie Universitaire Louvain (AUL), Belgium, under Grants ADi/DB/1058.2011 and FNRS (CC 1.5169.12, PDR T.0169.13, EQP U.N038.13).

Abstract

This thesis is dedicated to chemistry and hydrogen storage properties of novel complex hydrides. The main efforts were focused on synthesis and characterization of new Al-based borohydrides and amidoboranes. Somewhat different investigation on the hydrolysis of KBH_4 in the atmosphere of CO_2 was also performed.

The series of mixed-cation $M[Al(BH_4)_4]$ ($M = Li^+$, Na^+, K^+, NH_4^+, Rb^+, Cs^+) were successfully obtained by a reaction of the corresponding MBH_4 with $Al(BH_4)_3$. This method provides a high theoretical hydrogen capacity and enables to store highly reactive and unstable $Al(BH_4)_3$ in a solid-state form. A good quality of the obtained samples allowed to solve their crystal structures using variable temperature synchrotron X-ray powder diffraction (XRPD).

The thermal decomposition of $M[Al(BH_4)_4]$ shows various pathways: $Al(BH_4)_3$ is released below 100 °C for $M = Li^+$ and Na^+, while heavier derivatives evolve hydrogen and diborane at about 150 °C. $Li[Al(BH_4)_4]$ firstly decomposes into $Li_4Al_3(BH_4)_{13}$ at ~60 °C, desorbing $Al(BH_4)_3$, and the latter decomposes at ~90 °C releasing the rest of the starting borohydrides. $NH_4[Al(BH_4)_4]$ occupies a special position, as it contains protic and hydridic hydrogens, recombining into hydrogen already at 35 °C. In general, the experimental decomposition temperatures of metal borohydrides linearly correlate with the square root of the ionic potential of metal atoms calculated from dynamical charges on cations.

$Al(BH_4)_3$ reacts with ammonia borane, NH_3BH_3, producing mononuclear $Al(BH_4)_3 \cdot NH_3BH_3$ complex. It releases at ~70 °C

two equivalents of hydrogen, showing considerably lower decomposition temperature, compared to pure NH_3BH_3. The striking property of this system is an endothermic dehydrogenation on the first decomposition step, compared to the exothermic one for ammonia borane and its other known complexes. This opens a possibility for its direct rehydrogenation. The main drawback of this system is the low stability of the dehydrogenation intermediate, $Al(BH_4)_3 \cdot NHBH$, decomposition above 100 °C. In order to suppress its decomposition, we investigated N-substituted derivatives of ammonia borane, obtaining a more promising complex, $Al(BH_4)_3 \cdot CH_3NH_2BH_3$.

$Al(BH_4)_3$ serves as a template in the potentially reversible ammonia borane dehydrogenation, with Al atom coordinating both the starting and the final products. Aiming to substitute highly reactive $Al(BH_4)_3$ by a halide salt, and using N-substituted NH_3BH_3, we obtained an ionic form of $AlCl_3 \cdot CH_3NH_2BH_3$, namely $[Al(CH_3NH_2BH_3)_2Cl_2][AlCl_4]$. The further analysis of these compounds will help to define a system for the reversible storage of hydrogen in ammonia borane.

A different way to obtain hydrogen using new Al-based reactive hydride composite (RHC) was also explored in this work. In particular, $NaAlH_4$–$4NH_3BH_3$ system showed fascinating properties of releasing high purity H_2 and low hydrogen release temperature of 70 °C and formation of $Na[Al(NH_2BH_3)_4]$. The properties of the first Al-based amidoborane look promising. This compound decomposes in two steps with the formation of $NaBH_4$, 8 equivalents of pure hydrogen and an amorphous product $AlN_4B_3H_{(0\div1.8)}$. The latter reversibly reabsorb about 27% of released hydrogen. The example of $Na[Al(NH_2BH_3)_4]$

decomposition to $AlN_4B_3H_{(0\div1.8)}$ requires further in-depth studies, *viz.* its chemical structure and an optimization of the rehydrogenation process.

The interest in Al-based complex hydrides has been growing during the last years. Any knowledge about new Al-containing complex hydrides is very important for the future solid-state hydrogen storage. Data obtained in this work might be important in the further predictions of potential RHC systems, applying the computational methods. On the practical side, the combination of any of the described compounds with other hydrides may open avenues to new RHCs with enhanced hydrogen storage properties.

Abbreviations

AB	**A**mmonia **B**orane, NH_3BH_3
AFC	**A**lkaline **F**uel **C**ell
AMB	**A**mmine **M**etal **B**orohydride, $M(BH_4)_x \cdot nNH_3$
DAC	**D**iamond **A**nvil **C**ell
DADB	**Di****a**mmoniate of **D**i**b**orane, $[(NH_3)_2BH_2][BH_4]$
DFT	**D**ensity **F**unctional **T**heory)
DOE	US **D**epartment **o**f **E**nergy
DSC	**D**ifferential **S**canning **C**alorimetry
EDBB	**E**thylene**d**iamine-**b**is**b**orane, $(CH_2NH_2BH_3)_2$
ESRF	**E**uropean **S**ynchrotron **R**adiation **F**acility
FTIR	**F**ourier **T**ransformed **In****f**rared
GGA	**G**eneralized **G**radient **A**pproximation
HyFLEET	**Hy**drogen **Fleet**
IR	**I**nfra**r**ed
MAB	**M**etal **A**mmonia **B**orane, $M(BH_4)_x \cdot nNH_3BH_3$
MCFC	**M**olten **C**arbonate **F**uel **C**ell
MeAB	**Me**thyl**a**mine **B**orane, $CH_3NH_2BH_3$
MOF	**M**etal-**O**rganic **F**ramework
MS	**M**ass **S**pectrometry
NMR	**N**uclear **M**agnetic **R**esonance
PAB	**P**oly**a**mino**b**orane, $(NHBH)_x$
PAFC	**P**hosphoric **a**cid **f**uel **c**ell
PEMFC	**P**roton **E**xchange **M**embrane **F**uel **C**ell
PIMs	**P**olymers having **I**ntrinsic **M**icroporosity
PSDB	**P**oly(**s**tyrene-*co*-**d**ivinyl**b**enzene)
PSI	**P**oul **S**cherrer **I**nstitute
RHC	**R**eactive **H**ydride **C**omposite

RT	**R**oom **T**emperature
SG	**S**pace **G**roup
SNBL	**S**wiss-**N**orwegian **B**eam **L**ines
SOFC	**S**olid **O**xide **F**uel **C**ells
SRXRPD	**S**ynchrotron **R**adiation **X**-**r**ay **P**owder **D**iffraction
T_{dec}	**D**ecomposition **T**emperature
TGA	**T**hermal **G**ravimetric **A**nalysis
TPPA	**T**emperature **P**rogrammed **P**hotographic **A**nalysis
TMS	**T**etra**m**ethyl**s**ilane, $Si(CH_3)_4$
UCL	**U**niversité **c**atholique de **L**ouvain
XRPD	**X**-**r**ay **P**owder **D**iffraction

Chapter I – State of the Art

1. Why Do We Need Hydrogen Economy?

It is estimated that energy consumption will double over the next half-century,[1] due to the increasing population and the reasonable assumption that inhabitants of less developed countries would wish to increase their living standards which goes hand in hand with an increase of their energy demand. So the question is not if but when the world will run out of non renewable fossil fuels. In addition, the latter have an adverse effect on the environment by increasing the CO_2 content in the Earth's atmosphere, aggravating the greenhouse effect and its global negative consequences. These reasons clarify that for sustainable development of a new energy transition is needed. Among possible alternatives to substitute hydrocarbon fuels, mechanical energy storage is able to support only short-timed demands of electricity supply. Moreover, an energy storage in batteries also looks quite complicated for the whole economy scale, due to high demands of energy storage densities. Thus, possible storage in the form of energy rich compounds is currently the most desired method. Ideally, such compounds have to be abundant, environmentally benign, renewable, safe, and cost-effective. In this case hydrogen is considered being an alternative energy carrier and hydrogen-based energy infrastructure must be built to address our global concerns of fossil fuel depletion and global climate changes in a meaningful way.[2-6]

Although stationary applications could also be envisaged, the main drive to use hydrogen as an energy carrier comes from its potential

to replace petrol derived fuels in cars and other vehicles. The chemical energy per mass of hydrogen (142 MJ kg^{-1}) is at least three times larger than that of other chemical fuels (for example, the equivalent value for liquid hydrocarbons is 47 MJ kg^{-1}).[7] Once produced, hydrogen is a clean synthetic fuel: when burnt with oxygen, the only exhaust gas is water vapor, but when burnt with air, lean (with an excess of air) mixtures have to be used to avoid the formation of nitrogen oxides. Whether hydrogen can be considered as a clean form of energy on a global scale depends on the primary energy that is used to split water.

This work is devoted to the synthesis and characterization of new compounds and composites based on hydrogen-rich chemical and complex hydrides. The highest attention will be given to the new aluminum-based hydrides, herein characterized as potential materials for hydrogen storage.

2. The Advantages and Types of Proton Fuel Cells

There are essentially two ways to run a road vehicle on hydrogen. In the first, hydrogen in an internal combustion engine is burnt rapidly with oxygen from air. The efficiency of the transformation from chemical to mechanical through thermal energy is limited by the Carnot efficiency and is slightly higher for hydrogen–air mixtures (around 25%) than for petrol–air mixtures. When a lean mixture is used, the exhaust gas contains nothing but water vapor; richer mixtures also produce NO_x.[2]

In the second method, hydrogen is "burnt" electrochemically with oxygen from air in a fuel cell, which produces electricity (and heat) and drives an electric engine, according to half-reactions:[8]

$$2H_2(g) \rightarrow 4H^+ + 4\ e^- \text{ (anode)} \qquad (1.1)$$

$$O_2(g) + 4H^+ \rightarrow 2H_2O - 4e^- \text{ (cathode)} \qquad (1.2)$$

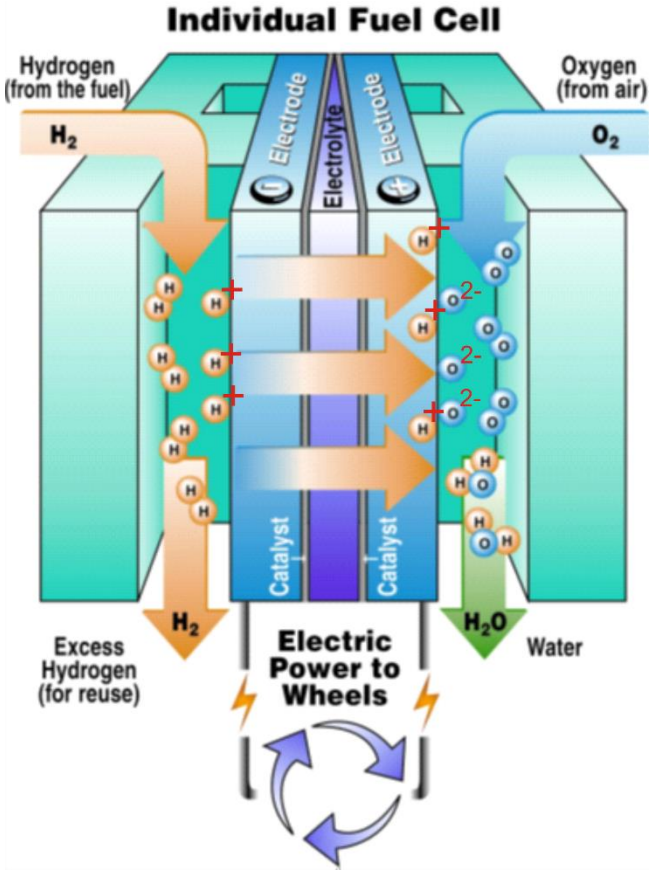

Figure 1.1 – The scheme of proton exchange membrane fuel cell (PEMFC).[9]

The ions of H^+ and O^{2-} are forming at separate electrode sites, where H^+ or O^{2-} diffuse through on ion-conducting membrane, see Figure 1.1. The physical separation is a major point which allows the thermodynamic tendency for both half-reactions to express itself as a

half-cell voltage. Usually the surfaces where hydrogen dissociation and the reaction with oxygen occur are made from catalysts to accelerate the kinetics of half-reactions. These surfaces are separated by ion-exchanging (H^+, O^{2-}, OH^- or CO_3^{2-}) membranes allowing a voltage and external current to be developed.

The efficiency of the direct process of electron transfer from oxygen to hydrogen is not limited by the Carnot efficiency; it can reach 50–60%, twice as much as the thermal process.[2,7] This advantage makes fuel cells good alternative for the currently used internal combustion engines.

According to the temperature, the fuel cell types can be described as low-temperature fuel cells within 50-220 °C (PEMFC) and high-temperature fuel cells that operate around 650 °C (molten carbonate (MCFC) and solid oxide fuel cells (SOFC)), see characteristics in Table 1.1.

Table 1.1 – Types of Fuel Cells. [2]

Fuel Cell type	Mobile ion	Operating temperature (°C)
Proton-exchange membrane fuel cell (PEMFC)	H^+	50-100
Alkaline fuel cell (AFC)	OH^-	50-200
Phosphoric acid fuel cell (PAFC)	H^+	~220
Molten carbonate fuel cell (MCFC)	CO_3^{2-}	~650
Solid oxide fuel cell (SOFC)	O^{2-}	500–1000

The low-temperature proton-exchange membrane fuel cells, which are based on H^+ mobility, have several advantages for practical applications compared to the other types of fuel cells. PEMFCs do not require highly corrosive solutions (KOH) like AFCs, and their operational temperatures are considerably lower than for SOFCs. The MCFCs and PAFCs limit their applicability due to the common use of fossil-fuel-derived natural gas as the hydrogen feedstock and release of

CO_2. However, the most important requirement for PEMFCs is the high purity of hydrogen needed, as some impurities (e. g. NH_3 on B_2H_6) are poisoning sensitive catalysts (typically Pt) and dramatically reduces their life-time and efficiency.

3. Requirements for Hydrogen Storage

For on-board energy storage, vehicles need a compact, light, safe and affordable containment. The systems used so far are based on compressed or liquefied hydrogen. The mentioned systems have limited application due to the technical difficulties.

Gas cylinders able to support gaseous hydrogen, compressed at an initial pressure of 350–700 bar (350 bar cylinders are used in HyFLEET buses) are too heavy to be used in private cars.[4,6]

The liquefied hydrogen has to be stored in a cryogenic tank at 20.3 K, so the liquefaction consumes about 20 % of the recoverable energy and daily evaporation (to keep the hydrogen tank cool) takes away an additional 2 %, that is why most of the large car manufactures concentrate their efforts in the field on conventional hydrogen storage, in particular on 700 bar pressure containers.[4]

The previously (2007) published[10] and recently (2009) revised[11] targets of the US Department of Energy (DOE) for on-board H_2 storage systems (for 2010) are shown in Table 1.2. They required higher gravimetric and volumetric capacities than can be achieved by compression or liqufication of hydrogen. Better capacity of hydrogen can be achieved by a solid-state hydrogen-storage where the host material is used as hydrogen carrier (Figure 1.2).

Table 1.2 – A subset of original and revised DOE targets for on-board hydrogen storage systems for light-duty vehicles. The most current DOE targets are contained in the "revised 2010", 2017 and ultimate categories.[10,11]

Storage system parameter	Original 2010 target (accepted in 2007)	Revised 2010 target (accepted in 2009)	2017 target	Ultimate target
Gravimetric capacity, kgH_2/kg system	6 %	4.5 %	5.5 %	7.5 %
Volumetric capacity, g H_2/L system	45	28	40	70
Operational cycle life	1000	1000	1500	1500
Fill time (min, for 5 kg)	3	4.2	3.3	2.5
Minimum full flow rate ($gH_2/s/kW$)	0.02	0.02	0.02	0.02
Min. delivery pressure at 85 ° C PEMFC (atm.)	8	5	4	3
Fuel purity	99.99 %	99.97 %	99.97 %	99.97 %

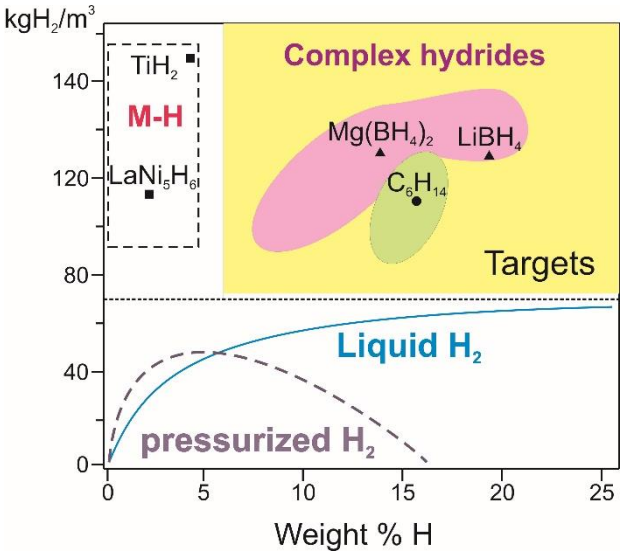

Figure 1.2 – A compilation of volumetric and gravimetric hydrogen densities of elemental H_2, complex and metal hydrides along with hexane (The targets shown correspond to those accepted in 2007 for 2010). The picture is simplified from Refs. [7] and [12].

4. Materials for Solid-State Hydrogen Storage

In general terms, solid materials most actively investigated for hydrogen storage can be separated into two distinct groups – the adsorbents of molecular hydrogen (physical adsorbents) and those which form hydrogen-containing compounds by chemisorption, metal hydrides. The latter can be additionally divided into a few groups: metal (interstitial), complex and chemical hydrides.

The physical sorbents of hydrogen are represented by highly porous solids, comprising mainly active carbons (including carbon nanostructures) and solids formed by open metal-organic frameworks (MOFs), as well as zeolites and (organic) polymers having intrinsic microporosity (PIMs). There is also a research on potential hydrogen storage materials such as hydrogen clathrates and nanostructures not based on carbon. The compilation of investigations from many different groups suggested that carbon materials will not reach technically relevant adsorption capacities for hydrogen storage.[13,4] For zeolitic material, such as ITQ-33 [14] with predicted silica structure and high micropore volume of 0.37 cm^3g^{-1}, the hydrogen capacity would be about 2.5 wt%.[4] Thus, it can be expected that zeolite-based storage materials will not be suitable for hydrogen storage in technical applications. Some MOFs show encouraging hydrogen uptake values at 77 K (e. g. MOF-177),[15] however their maximal uptake at ambient temperature is not yet good enough and other problems are low volumetric storage capacities, only slightly higher than 30 kg/m^3 (40 kg/m^3 are required by DOE in 2017).[2] PIMs were also investigated as potential hydrogen storage materials.[16] They can achieve hydrogen

uptake near 3 wt% at 77 K and 15 bar,[17] which is slightly far from the desired values. All the mentioned materials appeared quite recently and are being intensively developed.

Hydrogen directly reacts with many metallic elements and alloys providing various possibilities for hydrogen storage.[18,19] Several classical intermetallic (interstitial) metal hydrides belong to AB_2, A_2B, AB and AB_5 types have been used for hydrogen storage.[12] The most commonly used are AB_5 hydrides, where "A" is usually a lanthanide element, Ca or mischmetal (rare earth metal mixture), and "B" is Ni, substituted by Co, Al, Mn, Fe, Sn, Cu, Ti etc. The hydrogen is stored interstitially in the lattice of heavy atoms. Despite the fact that these hydrides are reversible and have an excellent kinetics, for on-board applications they suffer from the disadvantage of having a low gravimetric density of 1-2 wt% of H_2 (depicted by the white area in the left upper corner of Figure. 1.2), resulting in a large weight penalty. The second problem is a low abundance of rare earth metals that makes these materials more expensive and less available for large scale applications.

5. Complex Hydrides

In contrast to classical metal hydrides, in which interstitial sites are occupied with hydrogen atoms, in light metal hydrides, such as complex hydrides, hydrogen is covalently bound to a complex-forming element, metal or nonmetal.[20,21] In general, to these compounds belong alanates, borohydrides and amides with $[AlH_4]^-$, $[BH_4]^-$ and $[NH_2]^-$ complex anions, respectively. They have the highest hydrogen content compared to all the above mentioned ways of storage. The properties of

some alanates and imides are shown on Table 1.3, the information about borohydrides and their derivatives will be discussed in details in the next section.

Table 1.3 – Material properties of complex hydrides.[21]

Complex hydride	Density (g/mol)	Density (g/cm^{-3})	Hydrogen (wt. %)	Hydrogen (kg/m^3)	T_m (°C)	$\Delta H_f°$ (kJ/mol)
$LiAlH_4$	37.95	0.917	10.54		190	−119
$NaAlH_4$	54.10	1.28	7.41		178	−113
$KAlH_4$	70.11		5.71	53.2		
$Ca(AlH_4)_2$	86.33		9.27	72.3		
$Mg(AlH_4)_2$	102.10		7.84	70.4	>230	
$LiNH_2$	22.96	1.18	8.78	103.6	372-400	−179.6
$NaNH_2$	39.01	1.39	5.15	71.9	210	−123.8
KNH_2	55.12	1.62	3.66	59.3	338	−128.9
$Mg(NH_2)_2$	56.37	1.39	7.15	99.4	360	
$Ca(NH_2)_2$	72.13	1.74	5.59	97.3		−383.4

The crystal structures of alkali, alkali-earth and binary metal alanates, except $Ca(AlH_4)_2$, were determined recently both by X-ray and neutron diffraction, the details are shown in Table 1.4. For single cation $M(AlH_4)_n$ alanates ($M = Na^+$, Li^+, K^+; $n = 1$ and $M = Mg^{2+}$; $n = 2$), the crystal structures consist of isolated $[AlH_4]^-$ tetrahedra with A···H interatomic distances in the range of 1.55−1.67 Å.[22–25] The crystal structure of $Ca(AlH_4)_2$ was predicted from DFT calculations.[26] The variations in the crystal structures of $MAlH_4$ compounds ($M = Na^+$, Li^+, K^+) arise from the difference in size of corresponding alkali cations, hence the coordination numbers of 5, 8 and 10 respectively. For Mg^{2+} cations in $Mg(AlH_4)_2$ octahedral coordination takes place, which was also predicted for $Ca(AlH_4)_2$.

$NaAlH_4$ is the most intensively studied complex hydride due to its reversibility and high hydrogen content (5.6 wt%). The hydrogen content of the first decomposition step (3.7 wt%) exceeds by a factor of two the classical low-temperature metal hydrides. It was shown that $NaAlH_4$ can be used as a solid reversible hydrogen storage material by

doping it with titanium compounds, in particular by $Ti(OBut)_4$.[27] The following studies demonstrate the reversible hydrogen cycling over 100 cycles with a measured capacity of about 4 wt% at 160 °C.[28]

Table 1.4 – Crystal structure data (at RT) and decomposition pathways for alkali and alkali-earth alanates.

Alanate	Space group	Cell parameters, Å	Refs.	Dehydrogenation reaction	Refs.
$LiAlH_4$	$P2_1/c$	a = 4.8254(1) b = 7.8040(1) c = 7.8968(1) β = 112.268(1)°	[23]	For M = Li, T = 187-218 °C; M = Na, T = 210-220 °C; M = K, T =300 °C $3MAlH_4 \rightarrow M_3AlH_6 + 2Al + 3H_2$ For M = Li, T =228-282 °C; M = Na, T = 250 °C; M = K, T = 340 °C $2M_3AlH_6 \rightarrow 6MH + 2Al + 3H_2$	[29]
Li_3AlH_6	R-3	a = 8.07117(10) c = 9.5130(2)	[30]		
$NaAlH_4$	$I4_1/a$	a = 5.0119(1) c = 11.3147(4)	[22]		[31]
Na_3AlH_6	$P2_1/n$	a = 5.390(2) b = 5.514(2) c = 7.725(3) β = 89.86(3)°	[32]		
$KAlH_4$	$Pnma$	a = 5.8515(14) b = 5.8119(8) c = 7.3457(11)	[24]		[33]
$Ca(AlH_4)_2$				T = 180 °C $Ca(AlH_4)_2 \rightarrow CaAlH_5 + Al + H_2$ T = 230 °C $CaAlH_5 \rightarrow CaH_2 + Al + H_2$	[34]
$Mg(AlH_4)_2$	P-3m	a = 5.1949(2) c = 5.8537(2)	[25]	$Mg(AlH_4)_2 \rightarrow MgH_2 + 2Al + 3H_2$	[35]

6. Borohydrides

Borohydrides (tetrahydroboranes) are complex hydrides which contain the $[BH_4]^-$ anion. They and their nitrogen-containing derivatives were intensively investigated over the last decade as potential hydrogen storage materials.[36,37] The physical properties of light borohydrides are shown in Table. 1.5. All the mentioned compounds are solid at ambient conditions except $Al(BH_4)_3$ which is liquid (m.p. −65 °C). Most of them are sensitive to air and moisture, and in particular $Al(BH_4)_3$ along with $Be(BH_4)_2$ reacts vigorously with

air moisture. That is why the manipulation with $Al(BH_4)_3$ should be performed under inert atmosphere.

Table 1.5 – Physical properties of selected metal tetrahydroboranes.[38,39]

Complex hydride	Density (g/mol)	Density (g/cm^{-3})	Hydrogen (wt. %)	Hydrogen (kg/m^3)	T_m (°C)	$\Delta H_f°$ (kJ/mol)
$LiBH_4$	21.78	0.66	18.36	122.5	268	−194
$NaBH_4$	37.83	1.07	10.57	113.1	505	−191
KBH_4	53.94	1.17	7.42	87.1	585	−229
$RbBH_4$	100.28	192	3.99	77.2		
$CsBH_4$	147.72	2.405	2.71	65.66		
$Be(BH_4)_2$	38.69	0.702	20.67	145.1	123[d]	
$Ca(BH_4)_2$	69.76	1.072	11.47	124.07	260[d]	
$Mg(BH_4)_2$	53.99	0.989	14.82	146.5	320[d]	
$Al(BH_4)_3$	71.51	0.7866	16.78	132	44.5[d]	

[d] – Decomposition before melting.

The crystal structures of the main borohydrides were recently investigated by conventional, synchrotron and neutron powder diffraction methods and briefly described in Ref. [40]. The investigations of the crystal structures of alkali-metal and alkali-earth metal borohydrides concluded that the borohydride $[BH_4]^-$ anion has a nearly ideal tetrahedral geometry, with the B–H bond length of ~1.22 Å. These compounds have mixed bonding nature – ionic with metal and covalent regarding the $[BH_4]^-$ group. Higher decomposition temperatures for borohydrides compared with alanates can be explained by the stronger covalent interaction of the B–H bond compared with the Al–H. Alkali-metal borohydrides show more ionic character and consist of M^+ cations and $[BH_4]^-$ anions which are usually coordinated via edges to the central atoms. The crystal structures of alkali-earth metal borohydrides are more complex, thus $Be(BH_4)_2$ forms helical polymeric chains with two bridging and one terminal $[BH_4]^-$ group, $Ca(BH_4)_2$ and $Mg(BH_4)_2$ form complex frameworks, herein borohydride groups can be described as inorganic linkers. $Al(BH_4)_3$ is a covalent borohydride and has a molecular structure.

A lot of investigations are being devoted to the determination of decomposition pathways and products of thermolysis, as well as their influence on reversibility of borohydrides, see Table 1.6. In contrast to the alanate systems which usually decompose into crystalline products, which can be determined with *in-situ* X-ray diffraction, the systems with borohydrides often yield amorphous phases which are more difficult to interpret. Some attempts to describe possible decomposition products were made by theoretical calculations.[e.g. 41] The experimental investigations of decomposition products often require the use of non-conventional methods such as solid-state MAS-NMR, in particular the evidence for $Li_2B_{12}H_{12}$, $CaB_{12}H_{12}$ and $MgB_{12}H_{12}$ intermediates was presented by this method.[42]

Further research was made in order to observe the relationships between intermediates of $M(B_{12}H_{12})_n$ and the reversibility of hydrogen desorption of borohydrides. It was suggested that rehydrogenation of $Mg(BH_4)_2$ undergoes with formation of intermediate of $MgB_{12}H_{12}$ from decomposition products.[57] The end product of the dehydrogenation from $Mg(BH_4)_2$, MgB_2, was subjected to hydrogenation at high pressures (1200 bar) and high temperatures (500 °C) using a high pressure hydrogenation cell. The results showed that $Mg(BH_4)_2$ can be regenerated by hydrogen exposure, with following pyrolysis releasing ~12 wt% of hydrogen, the highest reversible value published so far.[11,43]

Table 1.6 – Crystal structure data (at RT) and decomposition pathways *via* thermolysis of light borohydrides.

Compound	Space group	Cell parameters, Å	Refs.	Dehydrogenation reaction	Refs.
$LiBH_4$	*Pnma* (20 °C)	*a* = 7.17858(4) *b* = 4.43686(2) *c* = 6.80321(4)	[44]	For Li, T_{d1} = 200 °C $12LiBH_4 \rightarrow Li_2B_{12}H_{12} + 10LiH + 12H_2$ $T_{d2} \approx 454$ °C $Li_2B_{12}H_{12} \rightarrow 2LiH + 12B + 10H_2$ For Na and K, T_d = 565 and 585 °C $2MBH_4 \rightarrow 2MH + 2B + 3H_2$ The second decomposition pathway is also possible: $MBH_4 \rightarrow M + B + 2H_2$	[45,46,47]
	*P*6$_3$*mc* (135 °C)	*a* = 4.27631(5) *c* = 6.94844(8)			
$NaBH_4$	*Fm*-3*m* (20 °C)	*a* = 6.148(1)	[48]		[49,50]
	Fm-3*m* (200 K)	*a* = 6.13080(10)	[51]		
	P-42$_1$*c* (10 K)	*a* = 4.332(1) *b* = 5.869(1)	[48]		
KBH_4	*Fm*-3*m*	*a* = 6.728(1)	[52]		[53]
	P-4$_2$/*nmc*	*a* = 4.7004(2) *b* = 5979(3)	[54]		
$Be(BH_4)_2$	*I*-42$_1$*cd* (20 °C)	*a* = 13.62(1) *b* = 9.10(1)	[55]	Unknown	
$Mg(BH_4)_2$	*P*6$_1$ (20 °C)	*a* = 10.3182(1) *b* = 36.9983(5)	[56]	$T_{d1,2}$ = 290-350 °C $6Mg(BH_4)_2 \rightarrow MgB_{12}H_{12} + 5MgH_2 +$ $+ 13H_2 \rightarrow 6MgB_2 + 4H_2$	[46,57]
	*P*6$_1$22 (20 °C)	*a* = 10.33555(4) *b* = 37.0891(2)	[58]		
	Fddd (20 °C)	*a* = 37.072(1) *b* = 18.6476(6) *c* = 10.9123(3)	[59]		
	Id-3*a* (20 °C)	a = 15.758(2)	[60]		
$Ca(BH_4)_2$	*Fddd* [1] (20 °C)	*a* = 8.791(1) *b* = 13.137(1) *c* = 7.500(1)	[61]	$T_{d1,2}$ = 330-370 °C $Ca(BH_4)_2 \rightarrow CaB_2H_x + (4\text{-}x/2)H_2 \rightarrow$ $\rightarrow 2/3CaH_2 + 1/3CaB_6 + 1/10H_2$ Or $6Ca(BH_4)_2 \rightarrow CaB_{12}H_{12} + 5CaH_2 +$ $+ 13H_2$	[62,63]
	F2dd [1] (91 K)	*a* = 8.7759(3) *b* = 13.0234(4) *c* = 7.4132(2)	[64]		
	*P*4$_2$/*m* [2] (107 °C)	*a* = 6.9468(1) *b* = 4.3661(1)	[65]		
	P-4 [2] (132 °C)	*a* = 6.9189(1), *b* = 4.3471(1),	[64]		
	I-42*d* (222 °C)	*a* = 5.8446(3) *b* = 13.228(1)	[64]		
$Al(BH_4)_3$	*Pna*2$_1$ (195 K)	*a* = 18.021(3) *b* = 6.138(2) *c* = 6.199(1)	[66]	Decomposes and reacts with products of decomposition at 25 °C $2Al(BH_4)_3 \leftrightarrow [AlH(BH_4)_2]_2 + B_2H_6$ $2Al(BH_4)_3 + B_2H_6 \rightarrow 2AlB_4H_{11} + 4H_2$	[67,68]
	*C*2/*c* (150 K)	*a* = 21.917(4) *b* = 5.986(1) *c* = 21.787(4) *β* = 111.90(3)°			

[1,2] Two different models were purposed for the same phases.

For $Ca(BH_4)_2$ the reformation from $CaB_{12}H_{12}$ and CaH_2 under 10 MPa of H_2 was reported with possible reactions:[63,69]

$$CaB_{12}H_{12} + CaH_2 \rightarrow 2CaB_6 + 7H_2 \quad \text{(step 1)} \quad (1.3)$$

$$CaB_6 + 2CaH_2 + 10H_2 \rightarrow 3Ca(BH_4)_2 \quad \text{(step 2)} \quad (1.4)$$

As one can notice, the decomposition reactions of borohydrides take place at temperatures >200 °C, which are at the high end or significantly higher than the requirements of 50−220 °C, suitable for low-temperature PEMFC applications. Several approaches were proposed to destabilize borohydrides for the improvement of hydrogen storage properties. Among them, the most widespread are the addition of other metals into the structure, forming mixed-metal borohydrides (thermodynamic tuning), as well as combinations with other hydrides (formation of reactive hydride composites, RHC).

7. Thermodynamic Tuning of Metal and Complex Hydrides

One of the simplest approaches to change the properties of complex hydrides is based on cation/anion substitution in the structure. The first trials to improve the thermodynamic properties of complex hydrides were performed in hexahydroaluminates, where numerous mixed-metal complexes are possible. The formation of numerous $A_{3-x}B_xAlH_6$ where A and B are Li^+, Na^+ or K^+, was previously predicted from DFT calculations in 2004.[70] The experimental data showed that the decomposition temperature and enthalpy depend upon the size of alkali metals of A and B. Usually they increase with the size of the alkali metal. The stability of the complexes was found to decrease within the row: $K_3AlH_6 > K_2NaAlH_6 > K_2LiAlH_6$.[71]

Mixed-metal borohydrides with compositions $A_x[B_y(BH_4)_n]$ (A = alkali metal, B = Na^+, K^+, Rb^+, Ca^{2+}, Mn^{2+}, Zn^{2+}, Cd^{2+}, Al^{3+}, Sc^{3+}, Y^{3+}, Zr^{4+}, ext.) can be obtained by metathesis reactions between different borohydrides and/or halide salts of *s*-, *p*- and some *d*-metals:

$$xA(BH_4)_{n1} + yB(BH_4)_{n2} \rightarrow A_x[B_y(BH_4)_n] \quad (1.5)$$

$$aA(BH_4)_{n1} + bBCl_{n2} \rightarrow cA_x[B_y(BH_4)_n] + dACl_x \quad (1.6)$$

In particular, $LiK(BH_4)_2$ is the first reported mixed-metal borohydride.[72] The decomposition temperature for the bialkali metal borohydride $LiK(BH_4)_2$ was found to be approximately the average of the decomposition temperature for the simple alkali borohydrides, $LiBH_4$ and KBH_4. This observation boosted the investigation into other combinations of mixed-metal borohydrides, in order to improve the decomposition temperatures of light borohydrides, see Table 1.7.

Table 1.7 – The table of mixed-metal borohydrides from alkali-metals and other *s*-, *p*- and *d*- elements.

Metal	Li^+	Na^+	Mg^{2+}	Al^{3+}	K^+	Ca^{2+}	Sc^{3+}	V^{2+}	Mn^{2+}	Zn^{2+}	Sr^{2+}	Y^{3+}	Zr^{4+}	Cd^{2+}	Pb^{2+}
Li^+		–	–	$+^*$	+	+–	+	+–	–	+	–	–	+–	–	–
Na^+	–		–	$+^*$	+	–	+	+–	–	+	–	$+^*$	?	–	–
K^+	+	+	+	+		+	+	+–	+	$++^*$	–	+	?	+	–
Rb^+	?	?	–	?	?	+	?	?	+	?	+	+	?	?	–
Cs^+	?	?	+	?	?	+	?	?	+	?	+	+	?	?	+
Refs.	[73,72]	[73,74]	[73,75]	[76–78]	[72,74]	[73,75]	[79–81]	[82,83]	[73,84,75]	[85,86]	[75]	[87–89]	[90]	[91]	[75]

\+ Compounds with determined crystal structure
$+^*$ Chloride –substituted compounds with determined crystal structure.
– Compounds were not observed
+– Unknown crystal structures, which can belong to mixed-cation borohydrides or other byproducts.
? No literature data

As one can notice, only *d*-block metal borohydrides based on metals with d^0, d^5 and d^{10} electron configurations have been successfully obtained so far. Thus not only the electronegativity but also the electron configurations of the metal may play a significant role in the stability of the borohydrides.[92]

A nearly linear relationship exists between the experimentally observed decomposition temperature and the electronegativity of the metal, which coordinates most strongly to the $[BH_4]^-$ groups (complex forming metal), Figure 1.3.[92] In particular, in the structure of $Na[Y(BH_4)_2Cl_2]$, the decomposition is observed 75 °C higher than that of $Y(BH_4)_3$.[87] This "stabilizing" effect is due to the presence of the alkali metal and also the smaller chloride ion in the structure. Hence, the decomposition temperature T_{dec} comes closer to the average between those of $NaBH_4$ and $Y(BH_4)_3$, like in $LiK(BH_4)_2$.

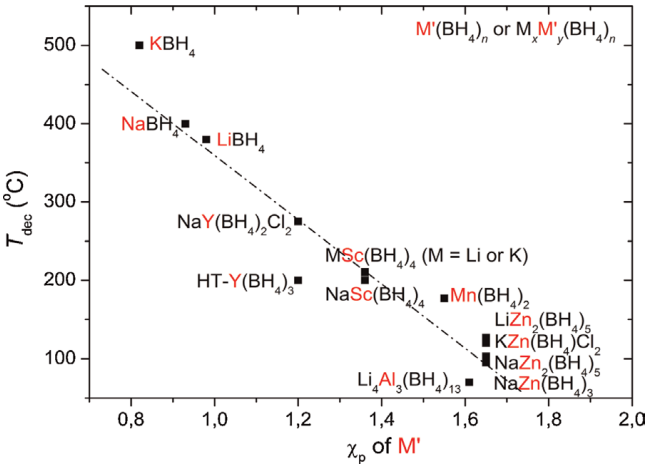

Figure 1.3 – The plot of decomposition temperatures *vs* Pauling electronegativity of complex-forming metal M', taken from Ref. [92]

In contrast, borohydride structures containing complex anions, such as $[Sc(BH_4)_4]^-$ or $[Zn_2(BH_4)_5]^-$ in $M[Sc(BH_4)_4]$ and $M[Zn_2(BH_4)_5]$ ($M = Li^+$, Na^+, K^+), show only minor variations in the decomposition temperature with various alkali metals.[92] The strong correlation between the decomposition temperature and the electronegativity of the complex-forming metal indicates the key role of the complex anions in the structural stability of bimetallic borohydrides.

The formation of several ternary mixed-metal borohydrides was also published recently by Černý and coworkers, with the first representative of $Li_3MZn_5(BH_4)_{15}$ ($M = Mg^{2+}$ and Mn^{2+}).[93] The latter compounds are rather interesting from the structural point of view due to the formation of frameworks, and as potential lithium conductors. The hydrogen storage properties are limited in trimetallic compounds, as they usually decompose to the starting metal borohydrides.

Thus, the crystal structure determination of *mono-*, *bi-* and trimetallic borohydrides is highly desirable in the understanding of the potential hydrogen storage and other properties of novel complex hydrides.

8. Destabilization of Complex Hydrides and Reactive Hydride Composites (RHC)

The other way of tailoring hydrogen storage materials is based on the chemical reaction between two or more hydrides, altering the decomposition reaction pathway and the reaction enthalpies. Remarkably, the gravimetric hydrogen storage capacity remains as high as the weighted hydrogen storage capacity of the individual hydrides. This concept is illustrated in Figure 1.4.

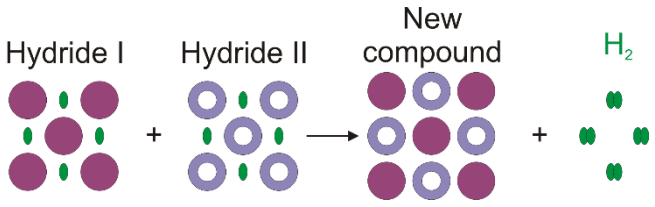

Figure 1.4 – The simplified scheme of the RHC system.

Several systems were found to release reversibly hydrogen under mild conditions in this way. In particular, the systems with $[NH_2]^-$ and $[BH_4]^-$ complex anions which react with protic H^+ from metal hydrides are among the most promising. An example of sequential dehydrogenation and rehydrogenation reaction of $LiNH_2$ and LiH is shown below:[94,95]

$$LiNH_2 + LiH \rightleftharpoons Li_2NH + H_2 \text{ (1 step)} \quad (1.7)$$

$$Li_2NH + LiH \rightleftharpoons Li_3N + H_2 \text{ (2 step)} \quad (1.8)$$

This reaction requires high temperatures (>400 °C) for complete desorption and are therefore not practical for many applications. An alternative approach, recently proposed by Luo et al.,[96] employs lithium hydride and magnesium amide ($Mg(NH_2)_2$):

$$Mg(NH_2)_2 + 2LiH \rightleftharpoons Li_2Mg(NH)_2 + 2H_2 \quad (1.9)$$

This reaction theoretically evolves 5.6 wt% of hydrogen at much lower temperatures than lithium amide reaction. However, the decomposition temperature remains too high (about 190–220 °C) for low temperature fuel cell application. The second disadvantage of the amides systems is the production of ammonia as decomposition byproduct. The loss of nitrogen degrades the material capacity and the reversibility, moreover ammonia poisons the fuel cell catalysts. The nitrogen-based systems are being intensively investigated today with the aim to avoid ammonia evolution and to improve desorption/absorption kinetics.

Metal borohydrides and metal amides can also form RHCs, such as $LiBH_4$–$2LiNH_2$:[97,98]

$$LiBH_4 + 3LiNH_2 \rightarrow Li_4BN_3H_{10} \rightarrow Li_3BN_2 + 4H_2 \quad (1.10)$$

$Li_4BN_3H_{10}$ is an intermediate compound which forms upon mechanochemical treatment prior to the formation of stable Li_3BN_2. The onset temperature for hydrogen release decreases from ~380 to 250 °C for $LiBH_4$ in the composite $LiBH_4$–$3LiNH_2$ and thermal decomposition releases more than 10 wt% H_2 in the temperature range of 250–350 °C. Unfortunately, this system is irreversible.

There are a lot of other possible combinations of complex hydrides, which showed good hydrogen storage properties. One of the most successful examples of reversible hydrogen storage in form of complex hydrides is based on addition of MgH_2 to lithium borohydride. In this system formation of the MgB_2 as a product provides destabilization of $LiBH_4$. The result is a reduction of the decomposition enthalpy for the system of about 25 kJ/mol of H_2 relative to pure $LiBH_4$:[99]

$$2LiBH_4 + MgH_2 \rightleftharpoons 2LiBH_4 + Mg + H_2 \rightleftharpoons 2LiH + MgB_2 + 4H_2 \quad (1.11)$$

Remarkably, the theoretical hydrogen storage capacity of this system is 11.4 wt%. Hydrogen absorption from the MgB_2–LiH composite is facilitated from the composite by 50 bar of hydrogen at $T < 300$ °C. The full reversibility of $2LiBH_4$–MgH_2 is only obtained when decomposition was performed under hydrogen back pressure of $p(H_2) \approx 1$–5 bar, possibly due to suppression of self-decomposition of $LiBH_4$ to non-reversible products.[100]

9. Complexes of Borohydrides with Ammonia, Ammonia Borane and Ammonium Borohydride

The other groups of materials with competitive hydrogen storage properties are borohydride complexes with ammonia NH_3 and ammonia borane NH_3BH_3. The presence of $N–H^{\delta+}…H^{\delta-}–B$ dihydrogen bonds in these compounds facilitates hydrogen splitting and considerably decreases the dehydrogenation temperatures to the range of 60–250 °C, as compared to alkali and alkali-earth metal borohydrides. The recent overview of M–B–N–H systems is given by Ref. [101].

Ammonia, which is catalytically split to H_2 and N_2, is a candidate for potential on-board hydrogen storage due to its high hydrogen content of 17.3 wt%. However, there are substantial safety issues that hamper wide utilization of this toxic compound. The latter reacts with metal borohydrides by coordination to the metals and by formation of dihydrogen bonds to $[BH_4]^-$ groups. The ammine metal borohydrides $M(BH_4)_n{\cdot}mNH_3$ (AMBs) were discovered in the 1950s and have recently attracted significant attention as potential hydrogen storage materials.

Several AMBs should be mentioned as potential hydrogen storage materials: $LiBH_4{\cdot}NH_3$,[102,103] $M(BH_4)_2{\cdot}2NH_3$ ($M = Mg^{2+}$, Ca^{2+}, Zn^{2+}),[104,105,106] $Ti(BH_4)_3{\cdot}3NH_3$,[107] $Al(BH_4)_3{\cdot}nNH_3$,[108,109] $LiMg(BH_4)_3{\cdot}2NH_3$,[110,111] $Li_2Ti(BH_4)_5{\cdot}5NH_3$ and $Li_2Al(BH_4)_5{\cdot}6NH_3$.[107,112] The hydrogen decomposition properties of these AMBs are affected both by the metal cation's nature and by the number of ammonia per cation and $[BH_4]^-$ groups. The borohydrides of

metals with low electronegativity are destabilized *via* complexation with ammonia, see Figure 1.5.

In contrast, the unstable borohydrides of highly electronegative metals, like $Al(BH_4)_3$ and $Zn(BH_4)_2$, become stabilized. The molecules of ammonia always coordinate directly to the metal atoms and prevent formation of neutral volatile molecular borohydrides, like $Al(BH_4)_3$, or avoids their reduction, like in $Zn(BH_4)_2$.

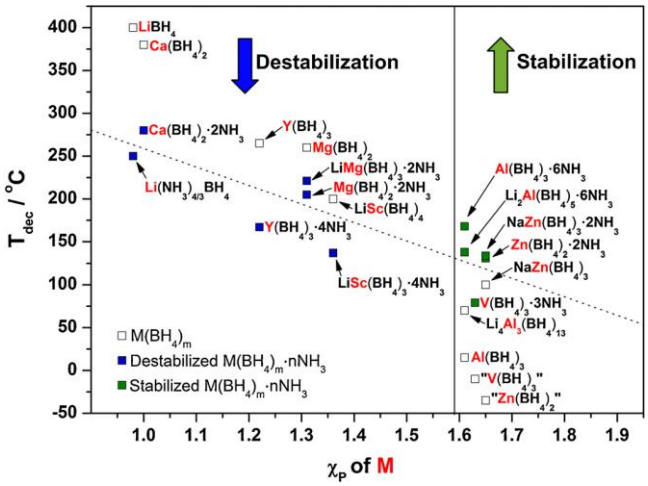

Figure 1.5 – The influence of NH_3 to stability of metal and mixed-metal borohydrides, taken from Ref. [113]

The influence of the cation on the dehydrogenation properties can be illustrated by the different $M(BH_4)_2{\cdot}2NH_3$ ($M = Mg^{2+}$, Ca^{2+}, Zn^{2+}) complexes, which contains equal $[BH_4]^-/(NH_3)$ (8/6 of H^-/H^+) ratio. Upon thermal decomposition $Ca(BH_4)_2{\cdot}2NH_3$ releases a significant amount of ammonia, $Mg(BH_4)_2{\cdot}2NH_3$ release only traces and $Zn(BH_4)_2{\cdot}2NH_3$ evolving highly pure hydrogen within this row.[104–106] The detailed electronic structure of $M(BH_4)_2{\cdot}2NH_3$ ($M = Mg^{2+}$, Ca^{2+}, Zn^{2+}) reveals a highly ionic character of Ca^{2+} in $Ca(BH_4)_2{\cdot}2NH_3$ and partial covalence of $Mg{-}NH_3$ and $Zn{-}NH_3$ which

prevents the release of NH_3 from the latter complexes.[114] Other representatives of AMBs, such as $Al(BH_4)_3 \cdot 6NH_3$ produce only traces of ammonia, while $Ti(BH_4)_3 \cdot 3NH_3$ as well as $Al(BH_4)_3 \cdot 4NH_3$–$LiBH_4$ composite, mixed-metal $LiMg(BH_4)_3 \cdot 2NH_3$, $Li_2Ti(BH_4)_5 \cdot 5NH_3$ and $Li_2Al(BH_4)_5 \cdot 6NH_3$ release high purity hydrogen.

The H^-/H^+ ratio of hydridic and protic hydrogens in MABs and the presence of catalysts also have an influence onto the decomposition properties of the complexes. It was reported that $LiBH_4 \cdot NH_3$ mainly releases ammonia rather than hydrogen under the dynamic inert gas flow,[115] however Co-catalyzed $LiBH_4(NH_3)_{4/3}$ evolves 17.8 wt% of practically pure H_2.[116]

The other representatives of nitrogen-containing borohydrides are complexes with ammonia borane (AB), NH_3BH_3. Despite the high hydrogen content in AB (about 19.6 wt%) and acceptable stability upon transportation and storage, NH_3BH_3 undergoes a stepwise thermal decomposition produsing a number of non-reversible products:

$$n NH_3BH_3 \rightarrow (NH_2BH_2)_x + n H_2 \rightarrow (NHBH)_x + n H_2 \rightarrow BN + n H_2 \quad (1.12)$$

Upon thermolysis of NH_3BH_3, 6.5 wt% hydrogen is released below 112 °C (first decomposition step) and 14.5 wt% near 200 °C (second step) giving polymeric products $(NH_2BH_2)_x$ and $(NHBH)_x$, as well as undesirable borazine $(NHBH)_3$ and aminoborane NH_2BH_2.[117,118] The final (third) decomposition step occurs at relatively high temperature > 500 °C and leads to the formation of stable BN and a third equivalent of hydrogen.[119]

A considerable suppression of toxic decomposition products of borazine and aminoborane was achieved by forming metal salts of

ammonia borane. This improves the decomposition temperature to ~90 °C for (Li, Na)NH_2BH_3,[120] giving way to a large family of materials. Ammonia borane metal-containing derivatives (MABs) $M(NH_2BH_3)_n$ (n = 1, M = Li^+, Na^+; n = 2, M = Ca^{2+}, Mg^{2+}),[120-123] including bimetallic $NaLi(NH_2BH_3)_2$, $Na_2Mg(NH_2BH_3)_4$ and mixed-anion $Li_2(NH_2BH_3)(BH_4)$/$LiNH_2BH_3$, were obtained in recent years.[124,125,126] However, all the listed MABs release hydrogen as well as toxic ammonia and NH_2BH_2 traces. For the mixed MAB−AB complex $LiNH_2BH_3{\cdot}NH_3BH_3$, the hydrogen release was reported up to 14.0 wt% in stepwise manner at 80 and 140 °C and neither borazine nor aminoborane were detected.[127]

The other derivatives of ammonia borane complexes are metal borohydride ammonia boranes $M(BH_4)_n(NH_3BH_3)_m$ (n = 1, m = 1, 2 for M = Li^+; n = m = 2 for M = Ca^{2+}, Mg^{2+}).[128–131] They showed easier hydrogen desorption with less ammonia evolution compared to pure ammonia borane and MABs. Further improvements in the properties of these complexes were achieved by combining some AMBs with ammonia borane, such as $Li_2Al(BH_4)_5(NH_3BH_3)_3{\cdot}6NH_3$ and $Mg(BH_4)_2{\cdot}2NH_3$–NH_3BH_3, where high purity hydrogen was detected.[132,130]

Great efforts have been made during the last years in the investigations of regeneration of ammonia borane and its derivatives.[133] Remarkably, partially decomposed ammonia borane $(NHBH)_x$ might be completely regenerated from the spent fuel by chemical treatment with hydrazine in liquid ammonia within a single step.[134] This discovery is among the most important breakthroughs for

possible utilization of ammonia borane and its derivatives for hydrogen storage.

Another derivative of NH_3BH_3 is ammonium borohydride, NH_4BH_4, which is the richest (24.5 wt% of hydrogen) solid state hydrogen-containing compound reported so far. It decomposes in three exothermic steps according to the following reactions:[135]

$$n NH_4BH_4 \rightarrow n/2[(NH_3)_2BH_2][BH_4] + nH_2 \quad (1.13)$$

$$n/2[(NH_3)_2BH_2][BH_4] \leftrightarrow nNH_3BH_3 \rightarrow (NH_2BH_2)_n + nH_2 \quad (1.14)$$

$$(NH_2BH_2)_n \rightarrow (NHBH)_n + nH_2 \quad (1.15)$$

The reaction steps are taking place at about 50, 85 and 130 °C, respectively. The fact that NH_4BH_4 releases 12 wt% of hydrogen below 100 °C makes it an extremely attractive hydrogen storage material. However, short half-life (~6 h) at room temperature due to the decomposition to diammoniate of diborane (DADB), $[(NH_3)_2BH_2][BH_4]$, makes it less suitable for practical applications. For long-term storage, NH_4BH_4 should be kept at $T < -40$ °C, therefore stabilization of NH_4BH_4 still remains a challenge. The first example of chemical stabilization of NH_4BH_4 was achieved in 2015 *via* formation of the perovskite-like structure of $NH_4[Ca(BH_4)_3]$.[75,136]

10. Hydrolysis of Borohydrides

The second method of obtaining hydrogen from borohydrides derives from their hydrolysis. The general reaction of borohydrides with water can be described as following:[137]

$$MBH_4 + (2+n)H_2O \rightarrow MBO_2 \cdot nH_2O + 4H_2 \quad (1.16)$$

Depending on hydrolysis conditions, such as temperature, $LiBH_4$ gives different products:[138,139] $LiBO_2$, $LiBO_2 \cdot H_2O$, $LiBO_2 \cdot 2H_2O$, the latter also known as $Li[B(OH)_4]$.[140] $NaBH_4$ attracted the biggest attention due to its higher stability and ease to handle as compared with $LiBH_4$ (the latter reacts vigorously with water at room temperature), and high hydrogen content of 10.6 wt%, contrary to 7.4 wt% in KBH_4.[141] Aqueous solutions of $NaBH_4$ are usually chemically stabilized by rendering solutions basic and do not generate significant amounts of H_2 under ambient conditions.[142] However, the $NaBH_4$ hydrolysis rate can be dramatically accelerated upon the addition of certain heterogeneous catalysts.[143,144] Among the conventional catalysts studied for the reaction, ruthenium-based catalysts were proposed to be most effective for promoting H_2 generation.[145,146] The hydrolysis of KBH_4 was also reported,[147] showing the lowest hydrolysis rate without the use of catalysts.

The recovery and regeneration technology is an important issue for MBH_4. It is attractive to find a procedure for reversing the spent MBH_4 in the form of MBO_2 (e. g. $NaBH_4$ and $NaBO_2$) back to MBH_4. For promotion of this research, a target of 60 % of regeneration efficiency has been set up.[148] In particular, many different methods have been developed to convert dried $NaBO_2$ to $NaBH_4$.[149] Further investigations are in process to improve the efficiency and cost of the recycling process. In this work, we tried to determine the influence of CO_2 in the water solution of KBH_4 to accelerate the hydrolysis, despite the main topic of the thesis is devoted to the hydrogen-rich compounds of aluminum.

11. Other Potential Applications for Complex Hydrides

The systems of complex hydrides listed above can be also interesting for several other applications such as a stationary hydrogen storage. These systems do not require as high hydrogen capasities as on-board hydrogen storage, but the reversibility plays a major role. Such application is interesting due to potential convertion of electricity to hydrogen in order to store energy, which can not be used imidiately by the customers. In this cycle hydrogen can be reconverted back to electricity in fuel cells, when it will be demanded. There is a significant recent interest in solar-driven photoelectrochemical water splitting, which produce hydrogen.[150] Stationary hydrogen storage systems will be complementary for these renewable energy technologies.

Borohydrides are also well known as reducing agents in organic synthesis. They can be used as powerful fuels in combination with oxidizing agents (like H_2O_2). Recent research on $[Al(BH_4)_4]^-$-based ionic bipropellants suggests them as alternative green rocket fuels.[151]

The most recent application of complex hydrides arises from thir capability to conduct cations in solid state. The developmet of novel solid electrolites is very important for battaries applications. In particular, recently found mixed-anion $Na_3(BH_4)(B_{12}H_{12})$ provides superionic conduction of Na^+, corresponding to highly disordered cations and continuous migration paths in the structure.[152] The alternative to substitute less abondant Li^+ in the battaries by Na^+ opens a possibility to make desent amount of cheap energy accumulators in the future.

12. Al-Based Hydrides: Hydrogen-Rich and Unstable

Remarkably, $Al(BH_4)_3$ is among the least studied borohydrides to date, the compound with a high potential, contains 16.9 wt% of hydrogen. This is a highly pyrophoric liquid at ambient conditions, explosive in contact with air. This feature is used in jet engines as an ignition source and has also been examined for possible use as a rocket fuel.[153,154] Thus, the stabilization of $Al(BH_4)_3$ in form of more stable complexes is a challenge for hydrogen and energy storage.

It should be mentioned, that one of the first trials to stabilize $Al(BH_4)_3$-based complexes with another alkali-metal borohydride was performed in 1972.[155] The authors obtained $K[Al(BH_4)_4]$ which showed higher thermal stability than the starting $Al(BH_4)_3$. This compound attracted again a great attention and was recently reinvestigated for hydrogen storage properties by our group (see Chapter III) and by other researchers.[78] Other authors also claimed the formation of $[Ca(BH_4)][Al(BH_4)_4]$ complex.[156] However, no further structural evidence of formation of any alkali-earth aluminum borohydrides was reported in the literature. Instead, further efforts were focused on other possible alkali-metal aluminum borohydrides, with high hydrogen content. In particular, the compounds with the lowest decomposition temperatures of 70 and 90 °C in $Li_4Al_3(BH_4)_{13}$ and $Na[Al(BH_4)_{4-x}Cl_x]$ were reported recently.[76,77] At the beginning of this project, the decomposition behavior of the Li-Al and Na-Al borohydrides was unclear, and the method of their synthesis revealed Cl-stabilization of $Li_4Al_3(BH_4)_{13}$ as well as the presence of LiCl and NaCl as “dead mass” products after the mechanochemical synthesis.

Numerous complexes of $Al(BH_4)_3 \cdot nNH_3$ ($1 \leq n \leq 6$) and their composites with $LiBH_4$, $Mg(BH_4)_2$ and NH_3BH_3 were established recently, during the period of this work (2011–2013), showing excellent hydrogen storage properties, see Table 1.8. Despite the low dehydrogenation temperatures (starting from 108 °C) and high hydrogen purity (> 99 wt%), these compounds/composites are capable of partial chemical rehydrogenation. Both $Al(BH_4)_3 \cdot 6NH_3$–4AB and $Li_2Al(BH_4)_5(NH_3BH_3)_3 \cdot 6NH_3$ were partially recycled (~4 wt%) by direct reaction with hydrazine in liquid ammonia at 40 °C for 3 days.[132] Furthermore, the improvement of $Al(BH_4)_3 \cdot 6NH_3$ decomposition kinetics and purity (>99 mol%) can be achieved by its immobilization in nanoporous polymer stabilizers, like poly(styrene-*co*-divinylbenzene), PSDB.[157] The partial chemical regeneration of $Al(BH_4)_3 \cdot 6NH_3$ with PSDB was also achieved.[157]

Despite the recent explosive interest in the development of numerous MABs, there is a lack of the information about Al-based complexes. The attention to these systems was also recently drawn by other researches, which published several works in 2013 and 2014, in parallel to our investigations.[158–160]

Table 1.8 – Some hydrogen storage properties of $Al(BH_4)_3$-based ammoniates and its composites with AB.

Compound/Composite	H_2 capacity (wt%)	H_2 purity (%)	Peak *T*/°C	Main impurity	Refs.
$Al(BH_4)_3 \cdot 6NH_3$	11.8	67.4	168	NH_3	[108,109]
$Al(BH_4)_3 \cdot 5NH_3$	16.8	90.6	159	NH_3	[109]
$Al(BH_4)_3 \cdot 4NH_3$	15.5	>99	128	—	[109]
$Al(BH_4)_3 \cdot 3NH_3$	13.7	>99	113	—	[109]
$Al(BH_4)_3 \cdot 2NH_3$	13.7	66.7	108	B_2H_6	[109]
$Al(BH_4)_3 \cdot 6NH_3$–$2LiBH_4$	15.5	79.0	138	NH_3	[109,112]
$Al(BH_4)_3 \cdot 5NH_3$–$LiBH_4$	15.4	81.0	145	NH_3	[109]

Compound/Composite	H_2 capacity (wt%)	H_2 purity (%)	Peak *T*/°C	Main impurity	Refs.
$Al(BH_4)_3{\cdot}5NH_3$–$2LiBH_4$	15.8	92.4	142	NH_3	[109]
$Al(BH_4)_3{\cdot}4NH_3$–$LiBH_4$	16.1	>99	109,128	—	[109]
$Al(BH_4)_3{\cdot}4NH_3$–$2LiBH_4$	14.2	96.6	121	B_2H_6	[109]
$Al(BH_4)_3{\cdot}6NH_3$–$0.5Mg(BH_4)_2$	11.2	100[1]	130[2]	—	[161]
$Al(BH_4)_3{\cdot}6NH_3$–$0.5Ca(BH_4)_2$	10.9	99.2[1]	130[2]	NH_3	[161]
$Li_2Al(BH_4)_5{\cdot}6NH_3$–$0.5Mg(BH_4)_2$	12.4	99.0[1]	130[2]	NH_3	[161]
$Al(BH_4)_3{\cdot}6NH_3$–NH_3BH_3	13.8	96.4	?	?	[132]
$Al(BH_4)_3{\cdot}6NH_3$–$2NH_3BH_3$	14.2	97.3	?	?	[132]
$Al(BH_4)_3{\cdot}6NH_3$–$3NH_3BH_3$	14.4	98.1	?	?	[132]
$Al(BH_4)_3{\cdot}6NH_3$–$4NH_3BH_3$	14.5	98.3	119, 154	NH_3	[132]
$Al(BH_4)_3{\cdot}6NH_3$–$5NH_3BH_3$	14.7	98	?	?	[132]
$Al(BH_4)_3{\cdot}6NH_3$–$6NH_3BH_3$	14.8	97.8	?	?	[132]
$Li_2Al(BH_4)_5{\cdot}6NH_3$	15.1	94.3	125, 190–300	NH_3	[132]
$Li_2Al(BH_4)_5{\cdot}6NH_3$–$NH_3BH_3$	16.5	97.6	?	?	[132]
$Li_2Al(BH_4)_5{\cdot}6NH_3$–$2NH_3BH_3$	16.6	98	?	?	[132]
$Li_2Al(BH_4)_5(NH_3BH_3)_3{\cdot}6NH_3$	16.9	98.6	105, 125	NH_3	[132]
$Li_2Al(BH_4)_5{\cdot}6NH_3$–$4NH_3BH_3$	16.8	97.1	?	?	[132]
$Li_2Al(BH_4)_5{\cdot}6NH_3$–$5NH_3BH_3$	16.6	96.9	?	?	[132]
$Li_2Al(BH_4)_5{\cdot}6NH_3$–$6NH_3BH_3$	16.4	95	?	?	[132]

[1]Isothermal treatment of the samples.

[2]The capacity and purity of the H_2 emission gas were determined using gravimetric and volumetric results, with the assumption that the impurity was only NH_3, to facilitate the calculation.

[?]Not mentioned in the publications.

13. The Main Objectives and the Working Strategy

The main objectives of this work are synthesis, crystal structure determination and characterization of hydrogen storage properties of novel Al-based complex hydrides (borohydrides and amidoboranes). According to the processed literature data, several strategies to obtain and characterize new hydrogen-storage materials could be performed.

The first strategy turned our attention to the synthesis of the series of mixed-cation $M[Al(BH_4)_4]$ (M = alkali metal or NH_4^+). They

can be directly obtained from the starting borohydrides, solving the "dead mass" problem. These systems have also not been characterized before in terms of crystal structures and hydrogen storage/decomposition properties.

The second possibility to stabilize $Al(BH_4)_3$ is the complexation with chemical hydrides, in particular with AB and its derivatives. It is based on the analogy of the alkali and alkali-earth metal complexes with AB. On the other hand, the stabilization of the H-richest solid of NH_4BH_4 is also a challenging problem nowadays. Combination of $Al(BH_4)_3$ and other metal borohydrides with this compound is very interesting for the hydrogen storage community. Moreover, the synthesis of NH_4-containing borohydrides without "dead mass" was not known so far.

In the final stage, we tried an RHC approach to obtain hydrogen from the composite $MAlH_4$–$4NH_3BH_3$. This is the first proof of Al amidoborane formation from a RHC based on alanates and ammonia borane. These complexes are interesting both from the point of view of their hydrogen storage properties and crystal structures/compositions. Previous investigations in this direction gave vague description of the obtained results and our work sheds a light on this perspective class of compounds.

The implementation of the objectives required several steps for characterization of the crystal structures and hydrogen storage properties of new compounds. Firstly, the crystal structures and compositions of the samples were determined from the X-ray single crystal and the *in situ* synchrotron X-ray powder diffraction, vibrational spectroscopy measurements and DFT calculations. Further

characterization of hydrogen storage properties were performed using the TGA (thermal gravimetric analysis), DSC (differential scanning calorimetry) and MS (mass spectrometry) together with volumetric studies. NMR spectroscopy was used in order to investigate the decomposition products of $Al(BH_4)_3$ complexed with AB. The mentioned results are given in each chapter in accordance with the mentioned strategy of the characterization.

Chapter II – Experimental Methods

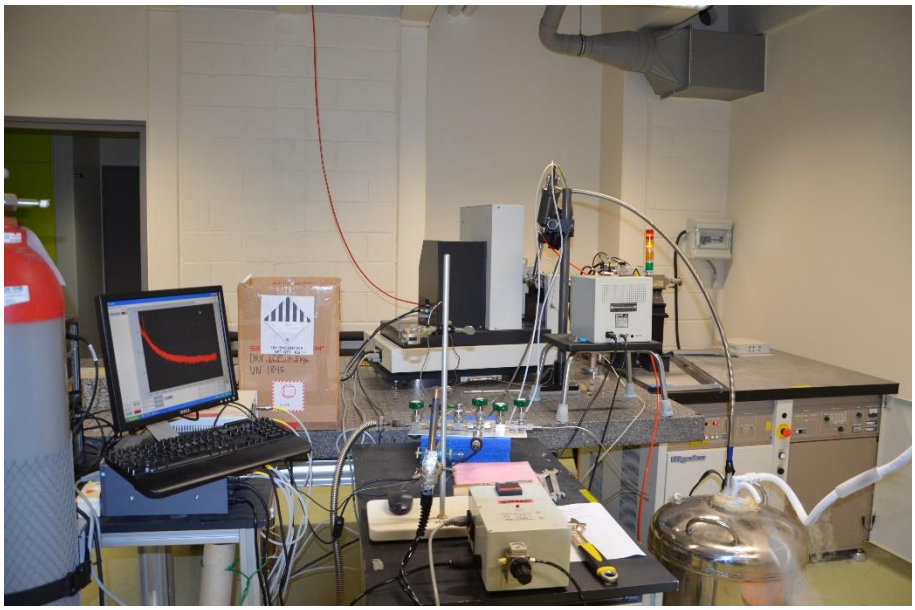

1. Single Crystal X-ray Diffraction

Diffraction is the coherent scattering of a wave by the atoms in a crystal. The origin of this scattering comes from the fact, that the electromagnetic X-ray wave is elastically scattered by the electrons which behave as an oscillating electric field.

Atoms consist of multiple electrons distributed around a nucleus, thus the scattering power of atoms is proportional to the total number of electrons, *Z*. Every element also has an intrinsic angular dependence of the X-ray amplitude on scattering angle θ, which is called the atomic scattering function (or form factor), $f(\theta)$. Thus, the diffraction pattern of stationary, periodically arranged atoms is the result of a superposition of interference and the corresponding squared scattering function.[162]

The periodic lattice produces diffraction maxima at specific angles, which are defined by both the lattice repeat distances (*a*, *b*, *c*) and the X-ray wavelength (λ). One of the ways to describe this relation is based on Braggs' law:

$$2d_{hkl}\sin\theta_{hkl} = n\lambda \qquad (2.1)$$

where d_{hkl} is the distance between crystallographic planes, θ_{hkl} is the angle of the diffracted beam, *n* is integer (order of reflection, which is taken as 1 for calculations) and λ is the X-ray wavelength.

The structure factor (amplitude), *F*, accounts all for the scattering (form) factors in the unit cell, together with other relevant atomic parameters. As a result, a diffraction pattern produced by a crystal is also a function of the triplet of Miller indices (*hkl*). Hence, in general the intensities of discrete points (*hkl*) in the reciprocal space are given as:

$$I(hkl) \propto |F_{hkl}|^2 \quad (2.2)$$

The structure factor, F_{hkl}, contains the main information about the atomic positions. In the non-centrosymmetric systems, this factor is a complex number:

$$F_{hkl} = |F_{hkl}|\exp(i\alpha_{hkl}) \quad (2.3)$$

From the known coordinates for the j atom of x_j, y_j and z_j, the structure factor can be presented as:

$$F_{hkl} = \sum_j f_j \exp(2\pi i(hx_j + ky_j + lz_j)) \quad (2.4)$$

The main problem in crystallography is the "phase problem" of the unknown α_{hkl}. There is no mathematical solution for it, but a lot of methods can be applied for its solution. The most widely used for structure determination of small molecules is "direct methods".[163] We applied direct methods in our work using SHELXS2014.[164] This method is based on the probability approach between the phases of different reflections, from which it is possible to gather phase information from the experimentally obtained structure amplitudes. Initial model of the structure is then obtained after a Fourier transformation with the calculated phase information:

$$\rho(x,y,z) = \frac{1}{V}\sum_h \sum_k \sum_l F_{hkl} \left[exp[-2\pi i(hx + ky + lz)]\right] \quad (2.5)$$

The maximum on this electron density map shows the positions of the atoms, from which the crystal structure might be solved.

Once the model of the structure was correctly found, the final refinement of the crystal structure can be performed. It is based on the updating of the initial model during subsequent refinement cycles. This is an iterative process, where the corrected model provides better phase information, which in turn (after Fourier transformation) will generate an improved structural model. The model is improved by changing

atomic parameters (coordinates and thermal displacement parameters) and is finalized by minimizing the difference between the square of observed (obs) and calculated (cal) weighted F^2:

$$\omega R_2 = \sqrt{\frac{\sum \omega(|F_o|^2 - |F_c|^2)^2}{\sum \omega |F_o|^2}} \quad (2.6)$$

2. Crystal Structure Solution from X-ray Powder Diffraction

In general, X-ray powder diffraction (XRPD) is used less often for crystal structure solution than a single crystal method, due to the fact that structure determination from XRPD is much more difficult.[165] This is associated almost entirely with the collapse of the three dimensions of the crystallographic information onto the single dimension of a powder diffraction pattern.

However, during the last two decades new diffractometers and solution methods made it possible to solve quite complicated structures from XRPD. In particular, the variable temperature synchrotron X-ray powder diffraction setups available at the European Synchrotron Radiation Facility (ESRF in Grenoble, France) and Paul Scherrer Institute (PSI in Villigen, Switzerland) were used in this work. Together with a modern microstrip solid-state detector, Mythen II, and a large area detector PILATUS 2M with fast reading time and high spatial resolution, they provide the possibility for *in situ* observation of decomposition reactions and structure determination of decomposing/forming light hydrides. For these compounds, XRPD is quite helpful due to the presence of small crystallites of several different phases, which cannot be separated from the synthesis or which they are forming during the temperature-induced processes.

Moreover, additional setups for the measurements of the powders can be installed. In particular, powder diffraction under high gas and dynamic pressure (using glass capillaries or sapphire cells, connected with the gas source, as well as determination of phase transitions under high dynamic pressure in diamond anvil cells, respectively), which will be discussed separately in this chapter.

Regarding the crystal structure solution form XRPD, there are several steps, which can be pointed out: phase analysis, peak indexing, choice of space group, profile fitting, crystal structure determination and refinement.

Phase analysis was performed using the structure models from the starting and other possible reaction products taken from the structural databases or literature data. The remaining peaks were indexed, using DICVOL and FOX.[166,167] The obtained unit cells were also analyzed by CHEKCELL[168] in order to check for possible derived lattices accounting for superstructure peaks or for space group symmetry.

Once the possible unit cell was found, profile fitting was performed to the known compounds in the powder pattern. This is done by the Le Bail modeling for the intensities and peak profiles of the indexed phases. These preliminary fittings were firstly performed for primitive lattices. After their refinement the generated *.hkl* files were analyzed by CHEKCELL, in order to determine the possible systematic absences and space groups. Profile fits were repeated for different suggested space groups, until the best fit (and not many predicted but unobserved peaks) was obtained. All these procedures were applied within the Fullprof Suite software package.[169]

The obtained parameters of the refinement with Le Bail modeling were transferred to FOX for crystal structure solution.[167] The crystal structure determination was based on global optimization methods or so-called direct space methods. The latter deals with the task of finding the absolutely best set of parameters to optimize a user-defined function, called the cost function. This is accomplished by scanning the crystal structure parameter space in the search of the global minimum, as shown schematically in Figure 2.1. Direct space methods rely on a maximum of user input. This means that prior knowledge of the structure is extremely useful, since it can be actively used in direct space modelling, but not in the reciprocal space. For condensed solids such as borohydrides, this refers to information on expected coordination polyhedra and inter-atomic distances. The structural model is then parametrized in real space to minimize the degrees of freedom in the system during the global optimization. The criteria to evaluate trial structures are defining the cost function.

In order to simplify and ease the optimization process, we used a rigid-body model for BH_4^- groups, based on the tetrahedral symmetry of the anion with the interatomic B···H distance of 1.13 Å (as "visible" to X-rays). For the most complicated situations, the bulky anions, like $[Al(BH_4)_4]^-$ anion, were also modeled as rigid bodies for structure determination.

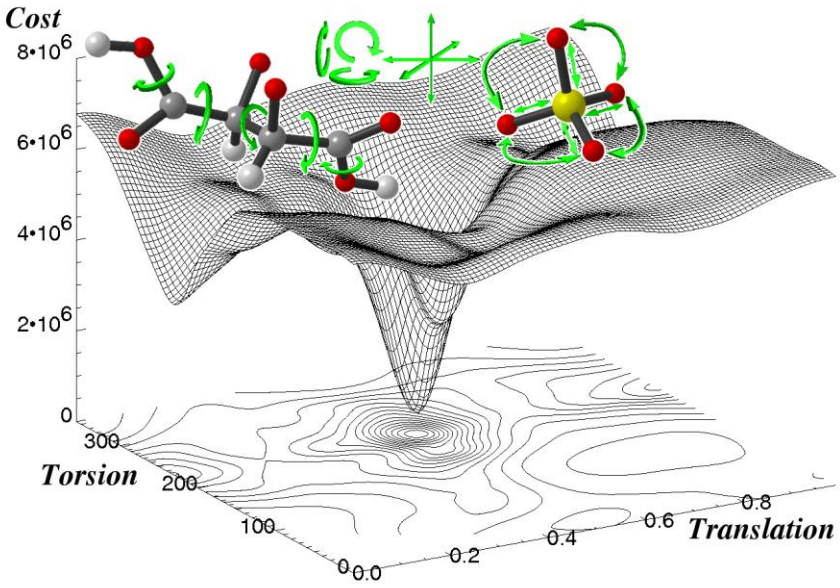

Figure 2.1 – Global optimization in crystal structure parameter space as implemented in direct space methods. Trial structures are evaluated by means of cost functions, shown on the *z* -axis, taken from Ref. [170]

3. Rietveld Refinement in X-ray Powder Diffraction

The refinements of the obtained structures were performed in Fullprof Suite[6] using the Rietveld method.[171] This method works as least-squares refinement, which minimizes the difference between the observed and calculated profiles from the whole recorded pattern (every point), but not from the individual reflections. Besides the conventional parameters in the least-square procedure (i.e. scale factor, atomic coordinates and temperature factors), additional parameters for the powder pattern simulation are required: the lattice parameters, a zero-point error for the detector, and four parameters which describe the half-

width with scattering angle and the peak shape. In contrast to neutron powder diffraction data, where the peak shapes can be modelled as ideal Gaussian distributions shape, X-ray powder diffraction refinement usually implies combination of Gaussian/Lorentzian peak shape (profile) functions, in particular the pseudo-Voigt function was used in this work.

Typically, many Bragg reflections contribute to the intensity, y_i, observed at any arbitrary chosen point, *i*, in the pattern. The calculated intensities y_{ci} are determined form the corresponding to the structural model $|F_{hkl}|^2$ by summing the calculated contributions from neighbouring Bragg reflections plus the background y_{bi} (manually chosen in our work):

$$y_{ci} = s \sum_{hkl} L_{hkl} |F_{hkl}|^2 \phi(2\theta_i - 2\theta_{hkl}) P_{hkl} A + y_{bi} \qquad (2.7)$$

where *s* is the scale factor, L_{hkl} contains the Lorentz polarization and multiplicity factors, ϕ is the reflection profile function, P_{hkl} is the preferred orientation function, *A* is an absorption factor.

Similarly to single crystal method, the criteria of structure fit and convergence can be taken from integrated intensities (structure factors taken as square roots of the intensities), like in the equation (2.6), or from all the calculated and observed points, in the form of the "weighted profile *R*-factor":

$$R_{\omega p} = \frac{\sum \omega |y_i(obs) - y_i(calc)|}{\sum \omega y_i(obs)} \qquad (2.8)$$

4. Vibrational Spectroscopy

Infrared and Raman spectra were collected in order to confirm the structural models of the complexes determined by XRPD.

The Raman spectra were recorded at room temperature with Bruker RFS 100/s FT-Raman spectrometer in the 100–4000 cm^{-1} range and (I = 200 mW) in the 100–4000 cm^{-1} using a diode-pumped, air-cooled Nd:YAG laser for 1064 nm excitation and Raman Thermo Scientific with a 532 nm DXR laser between 200 and 3500 cm^{-1} (the experiment with KBH_4 hydrolysis products).

Variable-temperature Raman spectroscopy was also performed using a Bruker RFS 100/s Raman spectrometer equipped with temperature control chamber under an argon flow. The spectra were collected in stepwise manner from 30 °C to the required temperature (see the experimental details for every particular compound).

The infrared (IR) spectra were measured with a FTIR-8400S SHIMADZU spectrophotometer at UCL and with a NICOLET 380 FTIR (Fourier Transformed Infrared) spectrometer from Thermo Electron Corporation in collaboration with Aarhus University. Prior to the IR measurements, the samples were mixed with KBr matrix in inert atmosphere. Pure KBr was used for background subtraction.

Time-resolved online ATR-FTIR spectra were recorded on a ReactIR 15 spectrometer (Mettler-Toledo) equipped with a diamond probe with a resolution of 4 cm^{-1}.

5. NMR Spectroscopy

Multinuclei NMR spectra were acquired in toluene-d_8 on a Bruker Avance DRX500 spectrometer operating at 500.1, for ^{1}H (160.5 MHz for ^{11}B and 130.3 MHz, for ^{27}Al). Chemical shifts are

reported with reference to $SiMe_4$ (TMS) for ^{1}H, $BF_3{\cdot}OEt_2$ for ^{11}B and 1.1M of $Al(NO_3)_3$ in D_2O for ^{27}Al. The other necessary details for measurements of $Al(BH_4)_3{\cdot}NH_3BH_3$ and $NH_4[Al(BH_4)_4]$ will be described in the corresponding chapters.

6. Thermal Analysis

Variable-temperature X-ray powder diffraction was performed in order to resolve the diffraction peaks from several crystalline phases upon thermal decomposition and to determine their thermal stability before further investigation by other methods (refer to the corresponding chapters for detailed experimental information). In general, the data sets were collected using either laboratory MAR345 diffractometer with rotating anode Mo Kα radiation and XENOCS focusing mirror or with synchrotron radiation from the ESRF or PSI facilities. Temperature was increased linearly in time using laboratory heat blower (calibrated with thermocouple) and Oxford Cryostreams 700/700+ at the corresponding temperature heating rates (see the details for every compound, respectively).

Thermal gravimetric analysis (TGA) and differential scanning calorimetry (DSC) methods were performed on powder samples after preliminary X-ray powder diffraction analysis. The data were collected independently with TGA/SDTA 851 Mettler and DSC 821 Mettler instruments with heating rates of 1−5°C/min from room temperature (25 °C) to a set point given for each compound individually (see the next chapters). Some data collection was also performed in collaboration with Aarhus University, using a

PerkinElmer STA 6000 instrument. The samples for the TGA and DSC analysis were loaded in an argon glove box into crucibles with caps or sealed into aluminum pans, respectively. The experiments were performed under 10-100 ml/min nitrogen flow to prevent oxidizing reactions. The reaction entalpies were obtained by integration of the DSC peaks subtracting an interpolated background.

TGA coupled with mass spectrometry (MS) of the residual gas was performed using several devices. Most of the measurements for $M[Al(BH_4)_4]$ (M = alkali metal) samples were performed using a ThermoStar^{TM} GSD 301T spectrometer coupled with simultaneous TGA/DTA 851 Mettler. The characterization of $K[Al(BH_4)_4]$ was performed in collaboration with Institut Jean Lamour, where an Omnistar GSD 301C - Pfeiffer Vacuum spectrometer coupled with SETARAM Setsys Ev 1750 TGA was used. The Hiden Analytical HPR-20 QMS sampling system from Aarhus University was used for the highly sensitive sample of $Al(BH_4)_3{\cdot}NH_3BH_3$. All measurements were done under 10−100 ml/min argon flow with a heating rates of 1−5 °C/min, see the details for each experiment in the next chapters.

Temperature programmed photographic analysis (TPPA) was performed in collaboration with Aarhus University. The method is applied to observe the mechanical behavior of the samples upon thermal decomposition. Approximately 10 mg of sample (see the details for $NaAlH_4$–$4NH_3BH_3$ composite description) were sealed under argon in a glass tube placed in a home-built aluminium heating block as described in Ref. [172]. Photos of the samples were collected every fifth second.

7. Volumetric Analysis and Reversibility Tests

Volumetric analysis was performed using a Hiden Isochema IMI-SHP analyzer. 40–50 mg of sample were heated from 30 °C to a preset temperature at 1−5 °C/min rate under back pressure of $p(H_2)$ = 5 bar. Subsequently, re-hydrogenation of the decomposed samples was performed at $p(H_2)$ = 150 bar by first heating back to the same preset temperature and then cooling slowly (0.1 °C/min) to 30 °C. Gas release was calculated from the calibrated volumes of the system, excluding the volume of the sample and of the protecting glass wool (2.06 g/cm^3). The final uptake was calculated as the difference between the average start uptake at 30 °C (equal to the temperature of the manifold) and the decomposition uptake after cooling to the same temperature, in order to decrease uncertainties of calibrations. It was found that the uptake calculated by the manifold's IMI software at 250 °C is usually about 3% lower (~0.2 mol) than at 30 °C.

8. *In situ* X-ray Powder Diffraction Using Sapphire Cells

The *in situ* monitoring of the potential hydrogen reabsorption is critical to the further development of materials and additives to improve thermodynamics, kinetics, gas separation and the hydrogen storage capacity. It is very important for understanding the hydrogen absorption processes of different materials. For that purpose, during the first year of the study, we designed and built the system for such experiments (see Figure 2.2). The idea of the system was partially taken from the Ref.

[173], and was discussed with the group of Prof. Hauback at the Institute of Energy Technology in Kjeller, Norway.

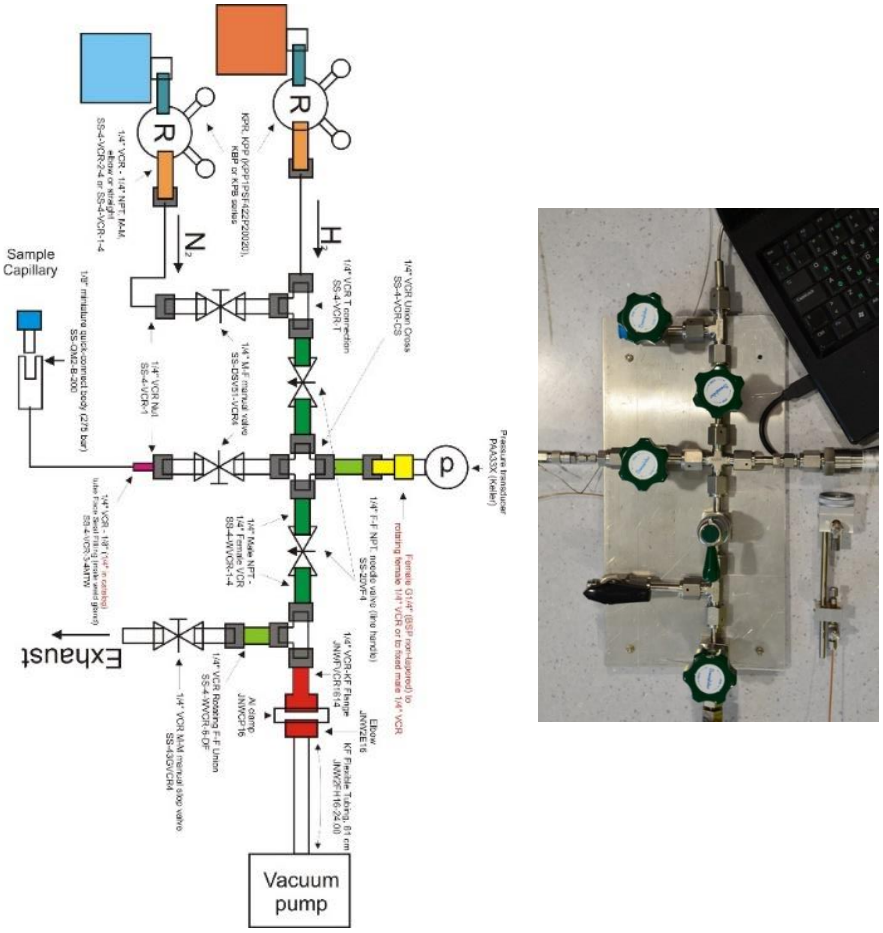

Figure 2.2 – The scheme (left) and the view (right) of the high pressure (up 250 bar) gas system for *in situ* X-ray powder diffraction. The sapphire sample cell shown in the lower right corner can be mounted on a goniometer. The pressure is monitored with high precision via a pressure gauge connected to a PC, the gas is taken from a 200 bar cylinder.

In particular, the rehydrogenation of $K[Al(BH_4)_4]$ was attempted using a sapphire-based cell in the *in situ* synchrotron X-ray powder diffraction experiment at the Materials Science Beamline at PSI

(Villigen, Switzerland), λ = 0.775045 Å. The starting powder was held in a single-crystal sapphire (Al_2O_3) capillary of 1.09 mm outer diameter. The decomposition of the $K[Al(BH_4)_4]$ under 1 bar of H_2 was performed by heating the capillary from room temperature to 210 °C at 5 °C/min heating rate. The decomposed sample was cooled to 50 °C and 100 bar of H_2 was applied and powder diffraction data were collected during 70 min. When no changes were observed, an additional heating step to 320 °C of the same decomposed sample at 100 bar of H_2 was made, followed by cooling at 10 °C/min rate.

Figure 2.3 – Sapphire capillary filled with the sample and connected to the gas dosing system in the *in situ* synchrotron X-ray powder diffraction experiment (mounted at the Material Science beam line, PSI).

9. Synchrotron Radiation X-ray Powder Diffraction in Diamond Anvil Cells (DACs)

The experiments described below require special skills and were carried out by Dr. N. Tumanov. Hydrostatic pressure during the X-ray powder diffraction experiments was created in an ETH-type[174]

diamond anvil cells, DACs (flat culets with diameter of 0.5 mm, a stainless steel gasket, a starting thickness of 0.200 mm, pre-indented to 0.060 mm, a hole diameter of 0.25 mm). The pressure was estimated from the shift in the R_1-band of a ruby calibrant (±0.05 GPa).[175,176] Since $Al(BH_4)_3$–derived samples are sensitive to oxygen and moisture, the fine powders of $M[Al(BH_4)_4]$ ($M = K^+, Rb^+, NH_4^+$) were loaded into the DACs in a glovebox equipped with a microscope, under high-purity argon atmosphere. No pressure-transmitting medium was used, but quasi-hydrostatic conditions were achieved, as we found from the small broadening of ruby fluorescence lines[176,177] and the splitting of R_1-R_2 lines.[178]

XRPD experiments were carried out using the synchrotron radiation source at the BM1A station of the Swiss-Norwegian Beamlines at the ESRF. A PILATUS 2M hybrid pixel detector was used for the data collection. The beam was slit-collimated down to 100-150 μm. Nominal sample-to-detector distances (200 and 193 mm, respectively), coordinates of beam center and detector tilts were calibrated using LaB_6 (NIST standard 660b) loaded in a DAC of the same type without applying pressure.

Raw powder diffraction data were processed (calibration, masking of the reflections from diamond and ruby, integration) using the Fit2D program.[179]

Chapter III – Crystal Structures and Decomposition Properties of the Series of Mixed-Cation $M[Al(BH_4)_4]$[1]

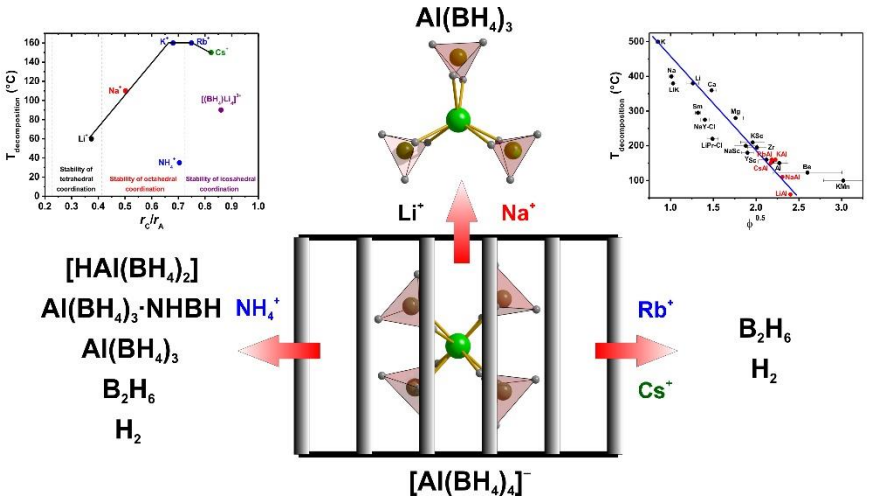

[1] This chapter is based on the following publications:

a) Dovgaliuk, I.; Ban, V.; Sadikin, Y.; Černý, R.; Aranda, L.; Casati, N.; Devillers, M.; Filinchuk, Y. The first halide-free bimetallic aluminum borohydride: synthesis, structure, stability, and decomposition pathway, *J. Phys. Chem. C* **2014**, *118*, 145–153.

b) Dovgaliuk, I.; Safin, D. A.; Tumanov, N. A.; Morelle, F.; Łodziana, Z.; Černý, R.; Devillers, M.; Filinchuk, Y. Stabilizing explosive aluminum borohydride in a $M[Al(BH_4)_4]$ series with versatile properties beneficial for hydrogen storage, *Adv. Func. Mater.* **2015**, submitted.

1. Introduction

Metal borohydride complexes and their derivatives are of great interest as materials for potential hydrogen storage due to their high hydrogen content.[21] Most alkali and alkali-earth metal borohydrides are matching the recently revised by the U. S. Department of Energy, hydrogen ultimate gravimetric and volumetric system targets of 7.5 wt% and 70 g/L, respectively.[11] However, metal borohydrides showed high stability towards hydrogen release by pyrolysis as they decompose at high temperatures (e.g. ~470 °C for $LiBH_4$, and 290-500 °C for $Mg(BH_4)_2$).[180,181] The latter can be significantly lowered for the mixed-metal borohydride complexes, where the decomposition temperature decreases with increasing of Pauling electronegativity for the complex forming cations.[182,183] The B–H bond weakens with the increase of covalence of the M–H bond. This improves thermal decomposition properties of mixed-metal complexes and some of them are favorable for the fuel cells temperature range of 60–120 °C:[184] $Li_4Al_3(BH_4)_{12.74}Cl_{0.26}$, containing some chloride anions on the borohydride sites,[76] $Na[Al(BH_4)_{4-x}Cl_x]$,[77] $NaZn_2(BH_4)_5$ and $NaZn(BH_4)_3$,[85] $KCd(BH_4)_3$ and $K_2Cd(BH_4)_4$.[91] All the listed mixed-metal borohydrides evolve diborane, B_2H_6, as a hydrogen desorption byproduct, which prevents full reversibility and is undesirable for fuel cell applications. Moreover, the Al-containing $Li_4Al_3(BH_4)_{12.74}Cl_{0.26}$ has recently been found to be the source of $Al(BH_4)_3$ upon the decomposition.[185] The latter compound suffers from being unstable on storage and explosive on the contact with air.[186]

Combination of borohydrides of different metals in a single molecule, leading to the formation of mixed-metal borohydrides, make it possible to stabilize $Al(BH_4)_3$. The use of pure borohydride precursors instead of the borohydride-chloride mixture studied previously allow to avoid the formation of metal halides as the so-called "dead mass" phases. Furthermore, halides can also efficiently substitute borohydride sites in the final product, that is commonly observed in mechanochemical reactions.[187,188] Chlorides can also change the reaction pathway of borohydrides, as was found for the mechanochemical reaction of $AlCl_3$ with $LiBH_4$. This reaction does not lead to $Li[Al(BH_4)_4]$, previously suggested from the NMR data,[189] but results in $Li_4Al_3(BH_4)_{12.74}Cl_{0.26}$.[76] A new synthetic approach involving the use of bulky anions in wet synthesis was proposed to overcome the stability limitations imposed by mechano-chemical processes.[190] However, the synthesis of $Al(BH_4)_3$-based mixed-cation borohydrides still remained a great challenge.

In this work, we report for the first time on the synthesis, crystal structures, thermal analysis, Raman spectroscopy studies along with a theoretical investigation of a series of $Al(BH_4)_3$-based mixed-cation borohydrides, $M[Al(BH_4)_4]$ ($M = Li^+$, Na^+, K^+, NH_4^+, Rb^+, Cs^+). It was found, that $Li[Al(BH_4)_4]$ and $Na[Al(BH_4)_4]$ each decompose with the formation of the starting borohydrides, MBH_4 ($M = Li^+$, Na^+) and $Al(BH_4)_3$. Furthermore, $Li_4Al_3(BH_4)_{13}$ was found to be an intermediate in the decomposition pathway of $Li[Al(BH_4)_4]$. The decomposition of $NH_4[Al(BH_4)_4]$ starts at ~40 °C, which is the lowest reported temperature for the mixed-cation complex hydrides. Heavier mixed-cation borohydrides, $M[Al(BH_4)_4]$ ($M = Rb^+$, Cs^+), decompose with the

formation of starting the MBH_4 as well as elimination of hydrogen and some B_2H_6.

2. Synthesis of Mixed-Cation $M[Al(BH_4)_4]$ ($M = Li^+, Na^+, K^+, NH_4^+, Rb^+, Cs^+$) and Their Stability

The synthesis of $M[Al(BH_4)_4]$ ($M = Li^+, Na^+, K^+, NH_4^+ Rb^+, Cs^+$) consists of two steps: synthesis of $Al(BH_4)_3$ and its reaction with the corresponding MBH_4. Due to the fact that our first successful trial of $M[Al(BH_4)_4]$ synthesis was made for $K[Al(BH_4)_4]$, the detailed synthesis approach will be mostly given for this compound. The other $M[Al(BH_4)_4]$ ($M = Li^+, Na^+, Rb^+, Cs^+$) were obtained by similar procedures with some small changes, which will also be mentioned. The synthesis of $NH_4[Al(BH_4)_4]$ will be described separately, as its also requires the preparation of highly unstable NH_4BH_4.

Caution! $Al(BH_4)_3$ is highly pyrophoric and explosive in contact with moisture and air. In order to prevent explosive reaction of $Al(BH_4)_3$ with air, all manipulations were carried out in a nitrogen-filled Plexiglas glove box (courtesy of Prof. O. Riant). All reactions were performed using commercially available reagents: $AlCl_3$, $LiBH_4$, $NaBH_4$ (all from Sigma Aldrich with >95 % purity), KBH_4 (Sigma Aldrich, 99 %) and $LiBH_4$ (Boss chemical industry Co., China with 96 % purity), $RbBH_4$, $CsBH_4$ (both from Katchem), NH_4F (from Sigma Aldrich, 98.8 % purity) and anhydrous NH_3 (from Praxair).

The first stage of the synthesis is the preparation of $Al(BH_4)_3$ from $AlCl_3$ and $LiBH_4$ according to the reaction:

$$AlCl_3 + 3LiBH_4 \rightarrow Al(BH_4)_3 + 3LiCl \qquad (3.4)$$

We have modified the procedure described in Refs. [186,191]. The grinded mixture with 5% excess of $LiBH_4$ (Boss chemical industry Co.) relative to the stoichiometry of the reaction was steadily heated in the glass flask, connected to a tandem of two liquid nitrogen traps. $Al(BH_4)_3$ starts to evolve as the mixture melts at about 100 °C. At this moment the system was pumped down to 10^{-2} mbar and the product with some $AlCl_3$ impurity was condensed in the traps. The pumping was ended when the mixture stopped boiling. The content of the first trap was unfrozen and purified by distillation at ambient pressure, all in the nitrogen-filled glove box, see Figure 3.1.

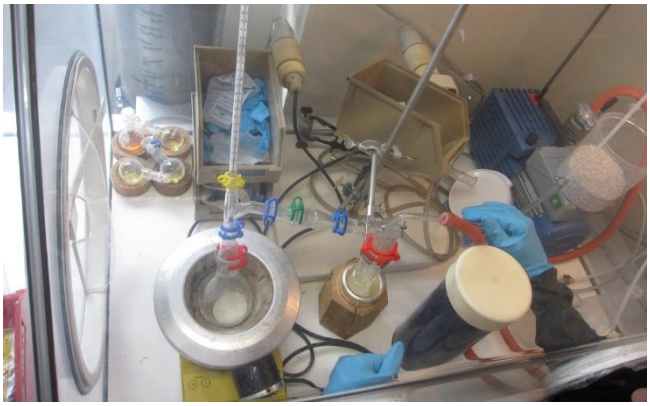

Figure 3.1 – The photo of the nitrogen-filled Plexiglas glove box, specially equipped for $Al(BH_4)_3$ synthesis.

It should be noted, that $Al(BH_4)_3$ is extremely reactive, reacting even with polydimethylsiloxane vacuum grease.[192] That is why the distillation was carried out with Teflon-coated greaseless ground glass joints using water-cooled condenser. Only the fraction boiling at 44.5°C or slightly below was collected, in order to separate $Al(BH_4)_3$ from undesired chloride-containing derivatives. It is also worth noting, that the used glassware should be washed by isopropanol

before exposing to air, as the traces of $Al(BH_4)_3$ may explode during washing outside the inert box.

In the second stage of synthesis, 1-2 ml of the fresh $Al(BH_4)_3$ was transferred via a syringe to a bottle with 200 mg of grinded KBH_4 powder, with continuous stirring. The reaction (3.5) took place over four to six days, similar to the reaction made by Semenenko et al.:[155]

$$Al(BH_4)_3 + KBH_4 \rightarrow K[Al(BH_4)_4] \quad (3.5)$$

The excess of volatile $Al(BH_4)_3$ was removed by pumping with an oil pump for a few minutes. The final products of the reaction were identified by XRPD. After the first soaking of KBH_4 in $Al(BH_4)_3$ the resulting $K[Al(BH_4)_4]$: KBH_4 weight ratio was found to be about 1:1. It increases successively after the following soakings, i.e. grinding and stirring with $Al(BH_4)_3$ liquid, see Figure 3.2, as observed by Semenenko et al.[155] We reached yields up to 95% in a few cycles, especially for heavier borohydrides. Ball milling of the mixture containing liquid aluminium borohydride would likely yield pure products in one step, but we did not attempt this procedure because of the safety issues.

Similar to the reaction of KBH_4 with $Al(BH_4)_3$, the other MBH_4 ($M = Na^+, Rb^+, Cs^+$) form mixtures containing about 1:1 weight ratio of $M[Al(BH_4)_4]$ to MBH_4 after the first synthetic cycle:

$$Al(BH_4)_3 + MBH_4 \rightarrow M[Al(BH_4)_4] \ (M = Li^+, Na^+, NH_4^+, Rb^+, Cs^+) \quad (3.6)$$

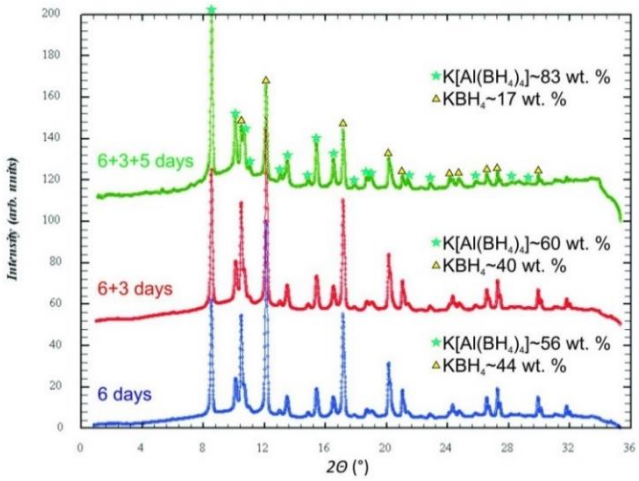

Figure 3.2 – Evolution of $K[Al(BH_4)_4]$ formation yield in the reaction between KBH_4 and $Al(BH_4)_3$, with the progress of the soaking-grinding cycles. The duration of soakings is indicated in days. Data were collected with MAR345 diffractometer using MoKα radiation.

The yield of the desired product was significantly increased, up to ~90 wt%, after the reaction of the well-grinded mixture of $M[Al(BH_4)_4]$ and MBH_4 with $Al(BH_4)_3$. The formation of $Li[Al(BH_4)_4]$ is accompanied by the chloride-free $Li_4Al_3(BH_4)_{13}$ and required four cycles to reach ~85 wt% yield. The fact that several synthetic cycles are required can be explained by the formation of $M[Al(BH_4)_4]$ on the surface of MBH_4.

It is worth noting that the yield of $M[Al(BH_4)_4]$ considerably depends on the purity of $Al(BH_4)_3$: the monoclinic $KAlCl_4$[193] forms as a side product if $Al(BH_4)_3$ is not purified by distillation, see Figure 3.3. This problem was also observed for the synthesis of $M[Al(BH_4)_4]$ ($M = Li^+, Rb^+$), resulting in LiCl and $RbAlCl_4$ as byproducts. Moreover, the crystal structure of the latter was not determine so far, but in this work

it was found to be isostructural to the $CsAlCl_4$ analogue, see Figure 3.4.[194]

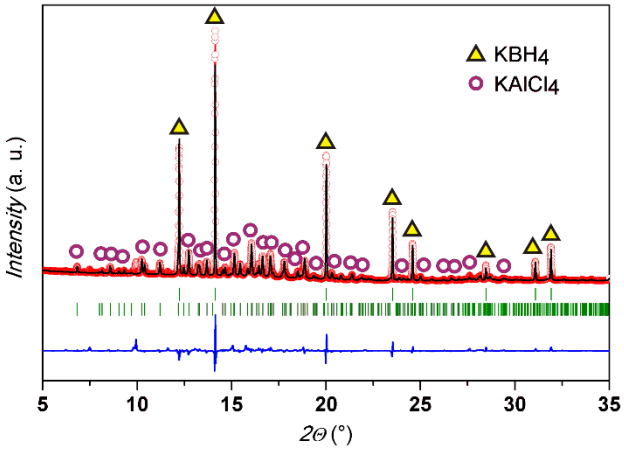

Figure 3.3 – Formation of $KAlCl_4$[193] from non-distilled $Al(BH_4)_3$ and KBH_4. The powder pattern (R_{wp} = 26.3 %) measured with synchrotron radiation (λ = 0.826887 Å) at SLS reveals $KAlCl_4$, R_F = 11.4 % (Space group (SG.) $P2_1/n$, a = 7.1866, b = 10.4822, c = 9.2713 Å, β = 93.07 °) and KBH_4 R_F = 2.15 % (SG. Fm-3m, a = 6.7241 Å).

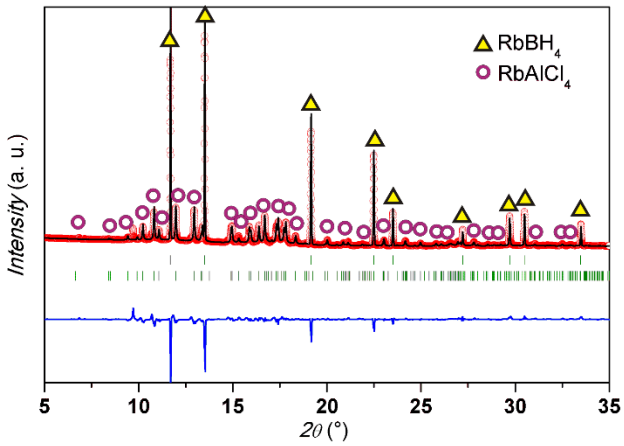

Figure 3.4 – The powder pattern of $RbAlCl_4$ from non-distilled $Al(BH_4)_3$ and KBH_4. The powder pattern (R_{wp} = 36.6 %) measured with synchrotron radiation (λ = 0.826887 Å) at SLS contains $RbAlCl_4$, R_F = 12.8 % (SG. *Pnma*, a = 11.1530(4), b = 7.0940(3), c = 9.2737(4) Å) and $RbBH_4$ R_F = 13.4 % (SG. Fm-3m, a = 7.0286(1) Å).

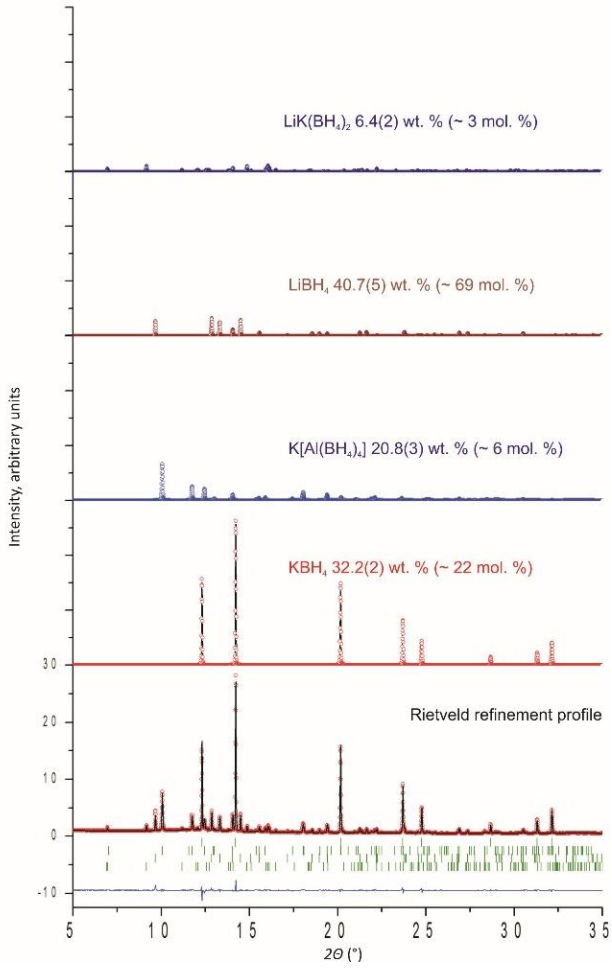

Figure 3.5 – Formation of $LiK(BH_4)_2$[72] and $K[Al(BH_4)_4]$ from $2LiBH_4 + KBH_4 + Al(BH_4)_3$ mixture. The pattern shows four phases (R_{wp} = 9.20 %): $LiK(BH_4)_2$, $K[Al(BH_4)_4]$, $LiBH_4$ and KBH_4. Data were collected at SNBL, λ = 0.827270 Å.

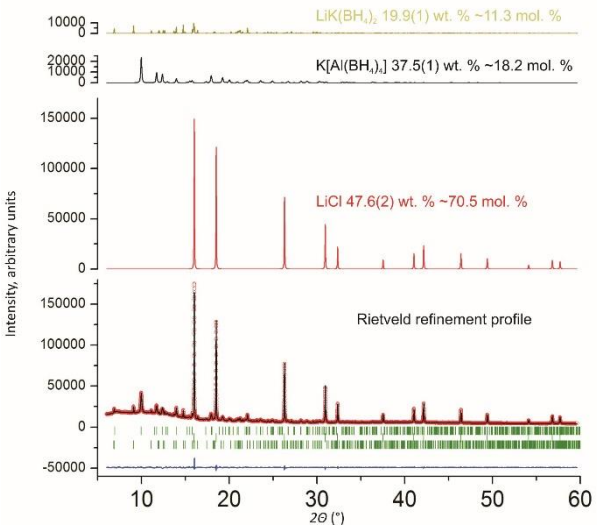

Figure 3.6 - Formation of $LiK(BH_4)_2$ [72] and $K[Al(BH_4)_4]$ from $9LiBH_4 + 3KBH_4 + 2AlCl_3$ ball-milled mixture. The pattern shows three phases (R_{wp} = 10.1 %): $K[Al(BH_4)_4]$, LiCl and $LiK(BH_4)_2$ (from top to bottom). Data were collected at PSI, λ = 0.82712 Å. The refined cell parameters of $K[Al(BH_4)_4]$ indicate negligible chlorine substitution: unit cell volume at room temperature is 1783.1(1) $Å^3$ against 1782.36(9) $Å^3$ for chlorine-free sample.

The attempts to obtain trimetallic Al-based borohydrides was also performed in this work, which was made by soaking $2LiBH_4$:KBH_4 mixture in $Al(BH_4)_3$ and removing its excess in vacuum, yielding $LiK(BH_4)_2$ and $K[Al(BH_4)_4]$, see Figure 3.5. No trimetallic borohydride has crystallized.

Ball-milling of $9LiBH_4 + 3KBH_4 + 2AlCl_3$ mixture also leads to a formation of $K[Al(BH_4)_4]$, in a mixture with LiCl and $LiK(BH_4)_2$, suggested from the Rietveld refinement, see Figure 3.6:

$$9LiBH_4 + 3KBH_4 + 2AlCl_3 \rightarrow 2K[Al(BH_4)_4] + 6LiCl + LiK(BH_4)_2 \quad (3.7)$$

This presence of LiCl "dead mass" as well as the absence of new ternary borohydrides suggested to stop further trials on that synthetic direction. Thus, neither the further mechanochemical reactions with other MBH_4 and $AlCl_3$ nor characterization of the hydrogen storage properties of $K[Al(BH_4)_4]$, LiCl and $LiK(BH_4)_2$ mixture were performed.

Synthesis of ammonium borohydride (NH_4BH_4) and $NH_4[Al(BH_4)_4]$. Ammonium borohydride was synthesized with the help of Fabrice Morelle by a slightly modified procedure[195] *via* a metathesis reaction between ammonium fluoride and sodium borohydride in liquid ammonia:

$$NaBH_4 + NH_4F \rightarrow NH_4BH_4 + NaF \quad (3.8)$$

Stoichiometric amounts of ammonium fluoride and sodium borohydride were weighted in an argon-filled glove box and loaded together with a magnetic stirrer into a round bottom flask №1 equipped with a glass filter. The latter was connected to a Schlenk line and kept under slight argon overpressure to avoid moisture contamination. Ammonia gas was first condensed at –78 °C, using a cold finger condenser filled with dry ice and acetone, in a Schlenk flask №2, containing a small amount of sodium metal, to ensure complete dryness. When the desired amount of liquefied ammonia (100 mL) was obtained, the ammonia bottle was disconnected and the condenser was replaced on flask №1, thus dry ammonia evaporated from the flask №2 and was recondensed into the flask №1. Once the ammonia transfer was complete, the reaction was left stirring at reflux for 1 h. Then the solution was filtered to remove precipitated sodium fluoride and the solvent was removed in vacuum. The resulting product was transferred

to an argon-filled glove box and kept in the freezer at –35 °C. Due to high instability of ammonium borohydride one of the main challenges of this synthetic procedure is to keep the product at low temperature during synthesis and transfer from the Schlenk line to a storage freezer. The low stability of NH_4BH_4 also requires low temperature for the reaction with $Al(BH_4)_3$. That is why $NH_4[Al(BH_4)_4]$ can be obtained from 4ml of fresh $Al(BH_4)_3$, which was added to the cooled powder of NH_4BH_4 and kept at –35 °C in the glove box freezer for 7 days.

Relative stability of $M[Al(BH_4)_4]$ ($M = Li^+, Na^+, K^+, NH_4^+, Rb^+, Cs^+$). $M[Al(BH_4)_4]$ ($M = Li^+, Na^+, NH_4^+$) are unstable at room temperature and should be stored in the fridge (at –35 °C). In particular, storing of $Na[Al(BH_4)_4]$ at room temperature shows the formation of $NaBH_4$ upon decomposition of $Na[Al(BH_4)_4]$. It is also worth noting, that the formed $NaBH_4$ has smaller particle size, compared with the starting unreacted powder with $Al(BH_4)_3$. The latter can be seen from the larger peak width for $NaBH_4$ in powder diffraction patterns, compared with the starting sample (Figure 3.7a) and the one decomposed after 2 month of storing (Figure 3.7b). In this particular case, the modeling of $NaBH_4$ powder pattern from the decomposed sample requires the separate fitting for the “starting” (narrow peaks) and the “forming” (wide peaks) $NaBH_4$. This change can be seen from two rows of green bars in the bottom of the Figure 3.7b, indicating peak positions for the two different $NaBH_4$ phases, where the “forming” phase has larger peak width than the “starting” one, see Figure 3.7c.

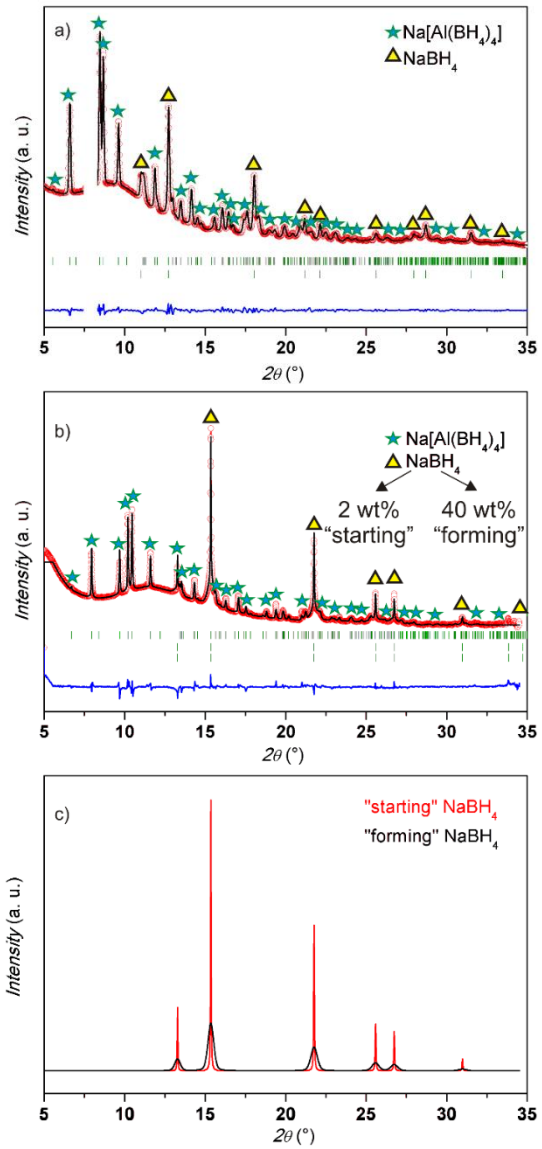

Figure 3.7 – a) Powder pattern (R_{wp} = 8.65 %) obtained with the synchrotron radiation (λ = 0.682525 Å, SNBL) on the "starting" $Na[Al(BH_4)_4]/NaBH_4$ mixture, b) powder pattern (R_{wp} = 15.1 %) after 2 months of storage at room temperature (λ = 0.823065 Å, SNBL) and c) the comparison of profiles from "starting" (present from synthesis) and "forming" $NaBH_4$ (forms after decomposition of $Na[Al(BH_4)_4]$).

3. Experimental Details

Raman spectroscopy. Spectra were recorded at room temperature with a Bruker RFS 100/s FT-Raman spectrometer (I = 200 mW) in the 100–4000 cm^{-1} range, using a diode-pumped, air-cooled Nd:YAG laser with 1064 nm excitation.

NMR spectroscopy. NMR spectra in toluene-d_8 were collected on a Bruker Avance DRX500 spectrometer operating at 500.1 for ^{1}H, 160.5 MHz for ^{11}B and 130.3 MHz for ^{27}Al nuclei, respectively. Chemical shifts are reported with reference to $SiMe_4$ (TMS) for ^{1}H, $BF_3{\cdot}OEt_2$ for ^{11}B and 1.1 M of $Al(NO_3)_3$ in D_2O for ^{27}Al.

Thermal analysis. Thermal gravimetric analysis (TGA) and differential scanning calorimetry (DSC) were performed on powder samples. TGA of $M[Al(BH_4)_4]$ ($M = Li^+$, Na^+, Rb^+, Cs^+) were performed using a PerkinElmer STA 6000 apparatus. The samples (~2 mg) were loaded into an Al_2O_3 crucible and heated from room temperature to 400 °C (5 °C/min heating rate) in a dynamic argon flow of 20 mL/min. $NH_4[Al(BH_4)_4]$ and $K[Al(BH_4)_4]$ were measured on a TGA/DTA 851 Mettler instrument (1 and 5 °C/min heating rate, respectively) from 25 to 150 °C and from 25 to 500 °C with a dynamic nitrogen flow of 100 and 10 mL/min, respectively. $K[Al(BH_4)_4]$ was measured on a DSC 821 Mettler instrument with a heating rate of 5°C/min from 25 to 500 °C. All the samples for thermal analysis were loaded in an argon inert glove box.

Volumetric analysis and reversibility tests. Volumetric analysis was performed using a Hiden Isochema IMI-SHP analyzer. $NH_4[Al(BH_4)_4]$ (~40 mg) was heated from 30 to 40 °C (1 °C/min,

p(He) = 1 bar) and kept at this temperature for ~2 weeks. $M[Al(BH_4)_4]$ ($M = Rb^+$, Cs^+) were heated from 30 to 160 °C (5 °C/min, p(He) = 1 bar). Subsequently, the gas release for all experiments was calculated from the calibrated volumes of the system, excluding the volume of the glass wool (2.06 g/cm^3) and samples skeletal volumes, taken from their crystal structures. The rehydrogenation of the remaining solid residues was performed, applying $p(H_2)$ = 100 bar at 40 °C for $NH_4[Al(BH_4)_4]$ and 160 °C for $M[Al(BH_4)_4]$ ($M = Rb^+$, Cs^+), respectively.

Crystal structure determination. Powders of samples were filled into 0.5 and 0.7 mm thin-walled glass capillaries and filled under high purity argon atmosphere in the glove box. Laboratory diffraction data were obtained with a MAR345 diffractometer equipped with a rotating anode (MoKα radiation) and a XENOCS Fox3D focusing mirror.

The crystal structure of $Li[Al(BH_4)_4]$ was solved from the variable temperature *in-situ* XRPD on the Materials Science Beamline at PSI (Villigen, Switzerland), using a Mythen II detector and λ = 0.775045 Å. The temperature was increased linearly in time with a 5 °C/min heating rate. The unit cell was indexed using FOX, [170] and the obtained space group $P2_1/c$ was checked by CHEKCELL.[168] In order to simplify the structure solution for the structure with 4 independent formula units in the asymmetric unit, the anion $[Al(BH_4)_4]^-$ was modeled as a rigid body using the structure of $K[Al(BH_4)_4]$. The K^+ atom was removed from the structure of $K[Al(BH_4)_4]$, and the remaining positions of $[Al(BH_4)_4]^-$ in the original *Fddd* space group were transformed to the reduced triclinic *P*1 subgroup using

POWDERCELL.[196] The obtained coordinates were transformed into the *z*-matrix format, using the program Open Babel.[197] Finally, the model of $[Al(BH_4)_4]^-$ was transferred into FOX and optimized as four independent molecules with four Li^+ cations. The resulting structure was refined in Fullprof (Figure 3.8), relaxing only the atomic temperature displacement parameters.[169]

The crystal structure of $Li_4Al_3(BH_4)_{13}$ was refined according to the model of the isostructural $Li_4Al_3(BH_4)_{12.74}Cl_{0.26}$, which contained some chloride atoms on the borohydride sites.[76] In our work we refined atomic positions of BH_4^- without Cl^- substitution (Figure 3.9).

The crystal structure of $Na[Al(BH_4)_4]$ was solved from *in situ* synchrotron XRPD data collected at the SNBL/ESRF (Grenoble, France) with a PILATUS 2M pixel detector and λ = 0.823065 Å. The temperature was increased linearly in time with a 5 °C/min heating rate. The unit cell was indexed and the preliminary space group *Cc* was established using FOX.[170] The final refinement was performed from the synchrotron XRPD data, collected on the Materials Science Beamline at PSI (Villigen, Switzerland), using a Mythen II detector and λ = 0.775045 Å. ADDSYM routine in the program PLATON[198] was applied in order to find higher symmetry. It suggested the *C*2/*c* space group. The resulting Rietveld refinement profile was obtained from the DFT (Density functional theory) optimized structure, where boron and hydrogen atomic positions as well as atomic displacement parameters were refined together in Fullprof (Figure 3.10).[169]

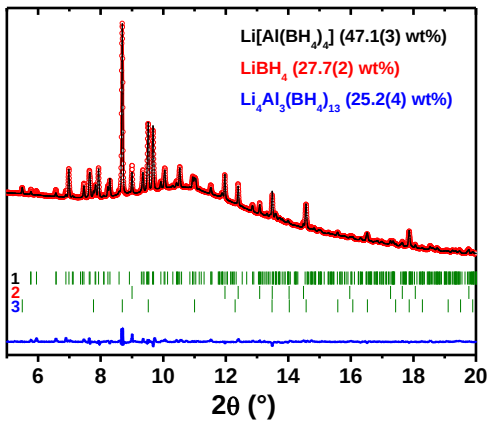

Figure 3.8 – Rietveld refinement profile from synchrotron XRPD (Materials Science Beamline at PSI in Villigen, Switzerland; Mythen II detector, λ = 0.775045 Å, R_{wp} = 15.7 %). Li[Al(BH$_4$)$_4$]: SG. $P2_1/c$, a = 19.6259(4), b = 13.5317(3), c = 13.5206(3) Å; β = 107.457(2)°; R_F = 16.2 %. Li$_4$Al$_3$(BH$_4$)$_{13}$: SG. P–43n, a = 11.4371, R_F = 5.8 %. LiBH$_4$: SG. *Pnma*, a = 7.1781, b = 4.4363, c = 6.8025 Å, R_F = 8.0 %.

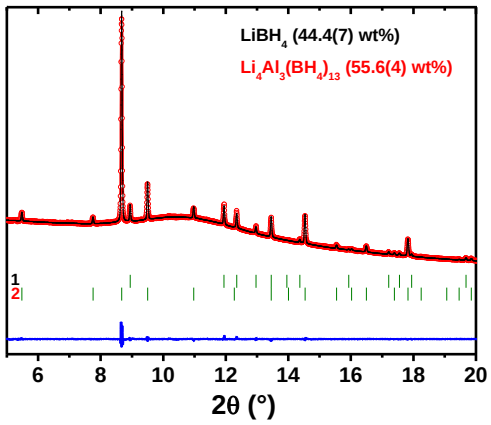

Figure 3.9 – Rietveld refinement profile from synchrotron XRPD (Materials Science Beamline at PSI in Villigen, Switzerland; Mythen II detector, λ = 0.775045 Å, R_{wp} = 12.9 %). Li$_4$Al$_3$(BH$_4$)$_{13}$: cubic SG. P–43n, a = 11.4622(1), R_F = 6.9 %. LiBH$_4$: orthorhombic SG. *Pnma*, a = 7.2063(2), b = 4.4334(1), c = 6.8650(2), R_F = 7.6 %.

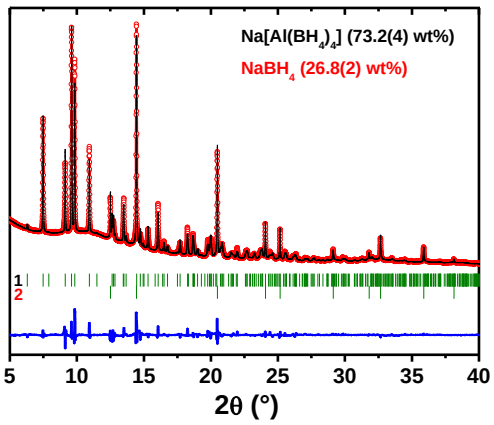

Figure 3.10 – Rietveld refinement profile from synchrotron XRPD (Materials Science Beamline at PSI in Villigen, Switzerland; Mythen II detector, λ = 0.775045 Å, R_{wp} = 18.1 %). $Na[Al(BH_4)_4]$: SG. *C*2/*c*, *a* = 9.3375(3), *b* = 11.2499(4), *c* = 8.4112(3) Å; β = 104.706(2)°, R_F = 7.3 %. $NaBH_4$: SG. *Fm*-3*m*, *a* = 6.16396(9), R_F = 2.8 %.

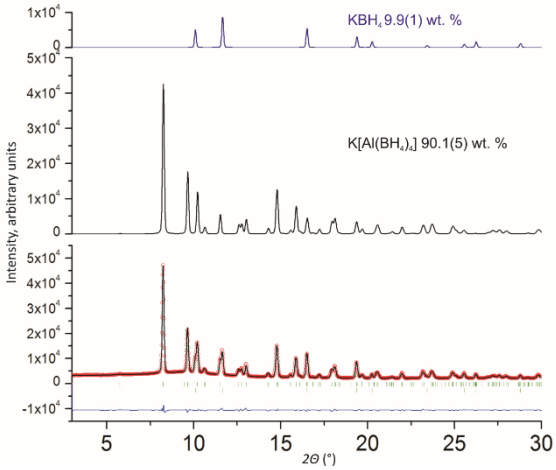

Figure 3.11 – Rietveld refinement profile for ESRF synchrotron data, λ = 0.682525 Å, R_{wp} = 7.55 %. $K[Al(BH_4)_4]$: SG. *Fddd*, *a* = 9.7405(3), *b* = 12.4500(4), *c* = 14.6975(4) Å, R_F = 3.8 %; KBH_4: SG. *Fm*-3*m*, *a* = 6.72556(1) Å, R_F = 3.2 %.

The orthorhombic crystal lattice of $K[Al(BH_4)_4]$ was indexed and the structure was solved in the *Fddd* space group with the program

FOX[170] and refined with the Rietveld method using Fullprof.[169] The symmetry was confirmed with the ADDSYM routine in the program PLATON.[198] The structure was solved and refined with BH_4^- groups as semi-rigid ideal tetrahedra with one common refined B−H distance of 1.13 Å. No other restraints were used. Rietveld refinement, see Figure 3.11, suggested a negligibly small chloride substitution of 0.03(1) on the borohydride site, confirming the Cl-free composition.

The crystal structures of $NH_4[Al(BH_4)_4]$ and $Rb[Al(BH_4)_4]$ were both solved from *in situ* synchrotron XRPD data, collected at the SNBL/ESRF (Grenoble, France) on a PILATUS 2M pixel detector and λ = 0.68884 and 0.682525 Å, respectively. Temperature was increased linearly in time using Oxford Cryostream 700+ at a 5 °C/min heating rate. The 2D images were azimuthally integrated using Fit2D program and data on the LaB_6 standard.[179] The unit cells were indexed in the *Fddd* space group by DICVOL[166] and the structures were refined with the Rietveld method using Fullprof (Figures 3.12 and 3.13).[169] The structures were found to be identical to $K[Al(BH_4)_4]$ and refined with the NH_4^+ and BH_4^- groups as semi-rigid ideal tetrahedra with common refined B–H and N–H distances of 1.20 and 1.04 Å, respectively. No other restraints were used.

The crystal structure of $Cs[Al(BH_4)_4]$ was solved from variable temperature *in situ* XRPD data collected at the Materials Science Beamline at PSI (Villigen, Switzerland), on a Mythen II detector and λ = 0.775045 Å. The temperature was increased linearly in time with a 5 °C/min heating rate. The unit cell was indexed in the $I4_1/amd$ space group by DICVOL[166] and the structure was solved in

FOX,[170] finally refined with the Rietveld method using Fullprof (Figure 3.14).[169]

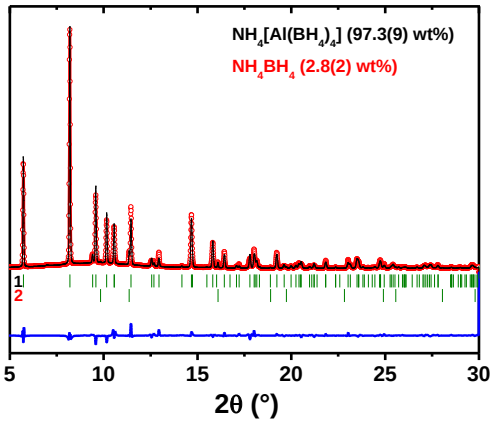

Figure 3.12 – Rietveld refinement profile from synchrotron XRPD (SNBL/ESRF in Grenoble, France; PILATUS 2M pixel detector, λ = 0.68884 Å, R_{wp} = 17.6 %). $NH_4[Al(BH_4)_4]$: SG. *Fddd*, a = 9.8873(4), b = 12.6005(5), c = 14.9656(5) Å; R_F = 5.27 %. NH_4BH_4: SG. *Fm*-3*m*, a = 6.9609(5), R_F = 5.11 %.

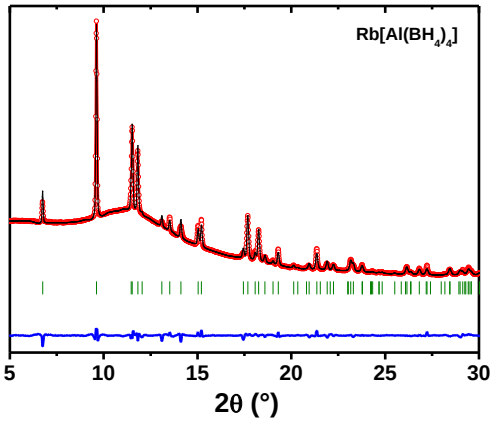

Figure 3.13 – Rietveld refinement profile from synchrotron XRPD (SNBL/ESRF in Grenoble, France; PILATUS 2M pixel detector, λ = 0.81712 Å, R_{wp} = 14.9 %). $Rb[Al(BH_4)_4]$: SG. *Fddd*, a = 9.8889(4), b = 13.3009(7), c = 14.3252(8) Å; R_F = 5.77 %.

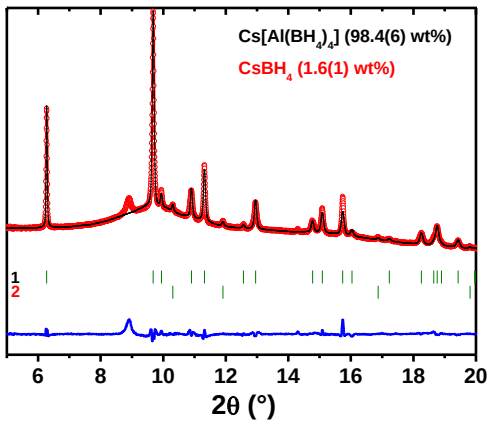

Figure 3.14. – Rietveld refinement profile from synchrotron XRPD (Materials Science Beamline at PSI in Villigen, Switzerland; Mythen II detector, λ = 0.775045 Å, R_{wp} = 17.8 %). Cs[Al(BH$_4$)$_4$]: SG. $I4_1/amd$, a = 7.8594(3), c = 16.3173(8); R_F = 10.3 %. CsBH$_4$: SG. Fm-3m, a = 7.4714(8), R_F = 12.9 %.

DFT calculations. The theoretical calculations were performed in collaboration with Prof. Zbigniew Łodziana (INP Polish Academy of Sciences). The structure analysis was performed for all compounds in order to check and confirm the thermodynamic stability and to reliably determine positions of the hydrogen atoms. The calculations were performed within periodic plane wave expansion of the electronic wave functions and DFT formalism as implemented in Vasp package.[199] The electronic configuration of elements was represented by projected augmented wave[200] potentials with the following valence states: $1s^1$ for H, $1s^2 2s^1$ for Li, $2s^2 2p^1$ for B, $2s^2 2p^3$ for N, $2p^6 3s^1$ for Na, $3p^6 4s^1$ for K, $4s^2 4p^6 5s^1$ for Rb and $5s^2 5p^6 6s^1$ for Cs. The gradient corrected (GGA) exchange correlation functional was used.[201]

Static structural optimization was performed with a conjugate gradient method; for each structure the internal atomic positions as well

as the lattice parameters were optimized until forces excerpted on atoms were smaller than 0.01 eV/Å. The experimentally determined configurations were used as starting ones, and the crystalline symmetry was constrained during initial structure optimization. Afterwards a simulated annealing search for the possible more stable configuration was performed. This was done by heating the structure to 350 K at the rate of 100 K/ps and cooling it down to 0 K at the rate of 50 K/ps. No constraints were imposed on the internal atomic positions and the unit cell parameters were kept fixed during the annealing process. Nosé-Hoover thermostat[202] was applied for this procedure, and the time step for integration of equations of motion was 0.6 fs. The symmetry of each system was analyzed.[203] after the simulated annealing procedure. Any new symmetry was re-optimized with methods used for the static calculations. For all structures the normal modes were analyzed. The normal mode frequencies were calculated at the Γ point by displacing the symmetry non-equivalent atoms in each crystallographic direction by ±0.01 Å.

In order to compare the thermodynamic stability at the ground state of the mixed-cation compounds with respect to the decomposition into $Al(BH_4)_3$ and corresponding MBH_4 ($M = Li^+, Na^+, K^+, NH_4^+, Rb^+, Cs^+$), the structural optimization and normal mode analysis was performed for all relevant phases. The energy cutoff was increased to 600 eV for the calculations of the ground state energy. The enthalpies of reactions (3.5 and 3.6) were calculated as $\Delta H = E(M[Al(BH_4)_4]) - E(Al(BH_4)_3) - E(MBH_4) + E_0(M[Al(BH_4)_4]) - E_0(Al(BH_4)_3) - E_0(MBH_4)$, where E is the ground state energy and E_0 is the contribution from zero point vibrations ($E_0 = \sum h\omega_i/2$).

The Born effective charges Z* Ref. [204] were calculated for $M[Al(BH_4)_4]$ ($M = Li^+, Na^+, K^+, Rb^+, Cs^+$). The isotropic component of Z* is equal to one-third of the trace. The ionic radii for cations are based on the recently established criteria.[205]

High pressure experiments in Diamond Anvil Cells (DACs) were performed on the samples of $M[Al(BH_4)_4]$ ($M = K^+, NH_4^+, Rb^+$). High-resolution X-ray powder diffraction for $K[Al(BH_4)_4]$ was carried out using a synchrotron radiation source (λ = 0.682525 Å, PILATUS 2M pixel detector) at the BM1A station at the SNBL (ESRF, Grenoble). The samples of $M[Al(BH_4)_4]$ ($M = NH_4^+, Rb^+$) were also measured at the same facility using λ = 0.714420 Å. LaB_6 powder was used for the calibration of the sample-to-detector distance. The frames of $K[Al(BH_4)_4]$ were measured at 29 pressure points during the compression up to 15.24 GPa and at 3 points during the decompression back to the ambient pressure with an exposure time of 15 minutes. The frames for $Rb[Al(BH_4)_4]$ were recorded at 13 pressure points during the compression up to 10.01 GPa. The powder patterns of $NH_4[Al(BH_4)_4]$ were recorded at 8 pressure points during the compression up to 7.74 GPa and 6 points during the decompression to the ambient pressure.

4. Results and Discussion

4.1. Variable Temperature *in situ* XRPD of MBH_4:$Al(BH_4)_3$ ($M = Li^+, Na^+, K^+, NH_4^+, Rb^+, Cs^+$) Systems

$LiBH_4$:$Al(BH_4)_3$ System. The variable temperature *in situ* plot of powder patterns, collected from the sample, obtained after the reaction of $Al(BH_4)_3$ with $LiBH_4$, exhibits the presence of three

different compounds, namely $Li[Al(BH_4)_4]$, $Li_4Al_3(BH_4)_{13}$ and $LiBH_4$ (Figure 3.15). The yield of the former one can be significantly increased by applying several synthetic cycles. The peaks for $Li[Al(BH_4)_4]$ gradually decrease with temperature and vanish at about 60 °C, while the amount of $Li_4Al_3(BH_4)_{13}$ abruptly increases at the same temperature. Thus, $Li[Al(BH_4)_4]$ transforms into $Li_4Al_3(BH_4)_{13}$ upon heating according to the following reaction (note, that the boiling point of $Al(BH_4)_3$ is 44 °C and, thus, it cannot be observed in XRPD patterns):

$$4Li[Al(BH_4)_4] \rightarrow Li_4Al_3(BH_4)_{13} + Al(BH_4)_3 \quad (3.9)$$

The complex $Li_4Al_3(BH_4)_{13}$ is the major phase at 60–80 °C and completely disappears at about 90 °C releasing $Al(BH_4)_3$ and $LiBH_4$ according to the known reaction:[185]

$$Li_4Al_3(BH_4)_{13} \rightarrow 4LiBH_4 + 3Al(BH_4)_3 \quad (3.10)$$

It should be noted that the crystal structure of $Li[Al(BH_4)_4]$ was unknown so far and $Li_4Al_3(BH_4)_{12.74}Cl_{0.26}$ was published recently.[76]

$NaBH_4$:$Al(BH_4)_3$ System. The variable temperature *in situ* plot of powder patterns, after the reaction of $Al(BH_4)_3$ with $NaBH_4$, exhibits two compounds, namely $Na[Al(BH_4)_4]$ and $NaBH_4$ (Figure 3.16).

Remarkably, the monoclinic crystal structure of $Na[Al(BH_4)_4]$ is different to the previously described orthorhombic $Na[Al(BH_4)_{4-x}Cl_x]$.[77] We found that $Na[Al(BH_4)_4]$ decomposes at about 90 °C releasing the starting reagents, according to the reaction:

$$Na[Al(BH_4)_4] \rightarrow NaBH_4 + Al(BH_4)_3 \quad (3.11)$$

$LiBH_4$:KBH_4:$Al(BH_4)_3$ and KBH_4:$Al(BH_4)_3$ systems. The X-ray powder diffraction analysis was performed for ternary Li–K–Al and binary K–Al borohydride systems, the details are given in the synthesis section, see Figure 3.5. The trimetallic Li–K–Al–BH_4 system

contains $LiBH_4$ as LT and HT polymorphs (within their stability ranges),[46] KBH_4,[40] $LiK(BH_4)_2$[72] and a new bimetallic phase, $K[Al(BH_4)_4]$. The formation of $K[Al(BH_4)_4]$ is more favorable than those of $Li_4Al_3(BH_4)_{13}$ or $Li[Al(BH_4)_4]$ because the Li cation is more polarizing than the K cation. In other words, K^+ stabilizes the $[Al(BH_4)_4]^-$ anion better.

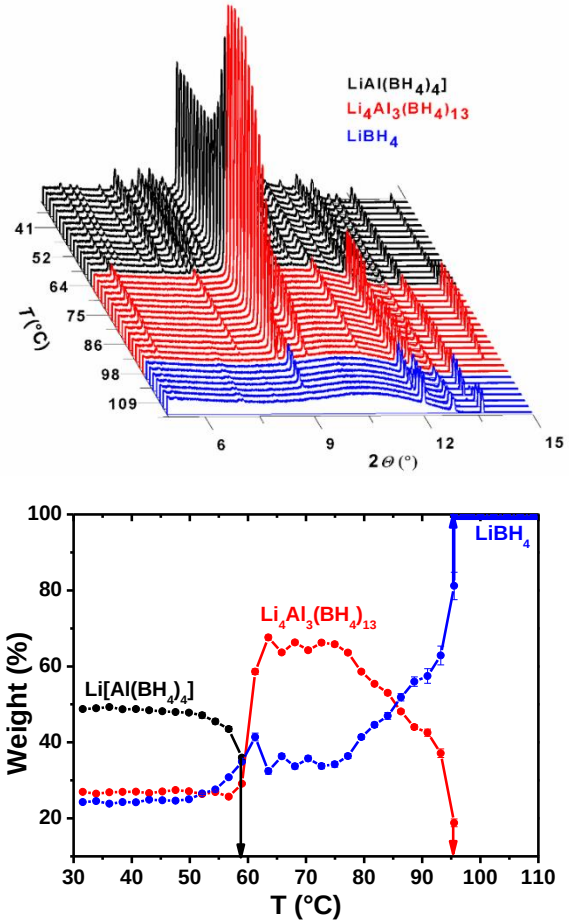

Figure 3.15 – The variable temperature *in situ* plot of XRPD patterns for the product, obtained after the reaction of $Al(BH_4)_3$ with $LiBH_4$ (Materials Science Beamline at the PSI synchrotron in Villigen, Switzerland; Mythen II detector, λ = 0.775045 Å) (top), and fractional content of compounds extracted from the Rietveld refinement of the powder patterns (bottom).

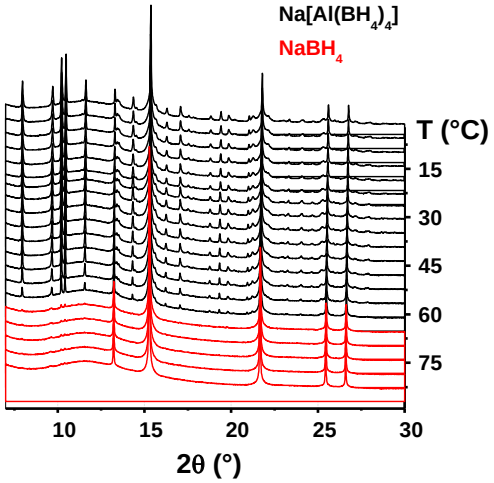

Figure 3.16 – The variable temperature *in situ* plot of XRPD patterns for the product, obtained after the reaction of $Al(BH_4)_3$ with $NaBH_4$ (Materials Science Beamline at the PSI synchrotron in Villigen, Switzerland; Mythen II detector, λ = 0.775045 Å).

In the condition of our experiment the known bimetallic $LiK(BH_4)_2$ forms readily at room temperature, while an annealing at 120 °C was required for the $LiBH_4$:KBH_4 sample.[72] Formation of $LiK(BH_4)_2$ in mild conditions is thus mediated by $Al(BH_4)_3$. It can be explained by the partial solubility of solid $LiBH_4$ and KBH_4 borohydrides in liquid $Al(BH_4)_3$, facilitating the addition reaction. Notably, $LiK(BH_4)_2$ in our sample decomposes into a $LiBH_4$+KBH_4 mixture at much lower temperatures than reported previously, namely at 95 °C against 240 °C attributed to melting and 380 °C for the decomposition of this phase.[72] The disappearance of diffraction peaks from $LiK(BH_4)_2$ correlates nicely with the increasing intensities from $LiBH_4$ and KBH_4. This observation confirms the hypothesis, made on the basis of theoretical calculations, that $LiK(BH_4)_2$ is unstable with respect to the decomposition into $LiBH_4$ and KBH_4.[206] The

decomposition temperatures, however, do not fully reflect the equilibrium state but also the kinetic barriers intrinsic to a particular multi-component system. The lower stability of $LiK(BH_4)_2$ than originally declared has been also stated in another work published in 2014.[207] Interestingly, the $LiBH_4$:KBH_4 system showed the lowest eutectic temperature of 95 °C among all borohydride systems characterized so far. It may be used for crystal growth from borohydride melts.

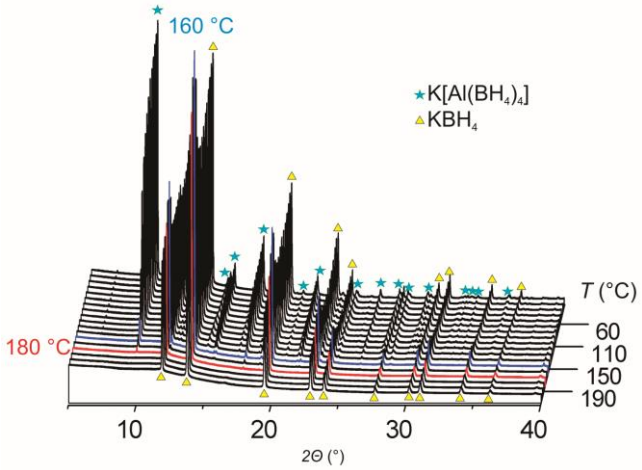

Figure 3.17a – Temperature evolution of powder diffraction patterns for $K[Al(BH_4)_4]$/KBH_4 mixture from 30 to 210 °C (Materials Science Beamline at the PSI synchrotron in Villigen, Switzerland; Mythen II detector, λ = 0.81560 Å). Red line highlights the pattern collected right after the decomposition of $K[Al(BH_4)_4]$ at 180 °C, showing Bragg peaks of KBH_4 alone. The blue line shows the highest intensity of KBH_4 at 160 °C.

We focused our attention on the new K-Al bimetallic compound, which we firstly observed by diffraction in this ternary system. Our further attempts were to obtain and characterize this complex from the binary KBH_4 + $Al(BH_4)_3$ mixture. Two cycles of soaking in excess of $Al(BH_4)_3$ and its removal in vacuum resulted in

samples containing ~70 weight % of $K[Al(BH_4)_4]$ with 30 % of the remaining KBH_4. The yield was increased to 90% by three soaking - vacuum pumping cycles. As mentioned before, the important intermediate step in the synthesis is grinding the sample before adding a new portion of $Al(BH_4)_3$.

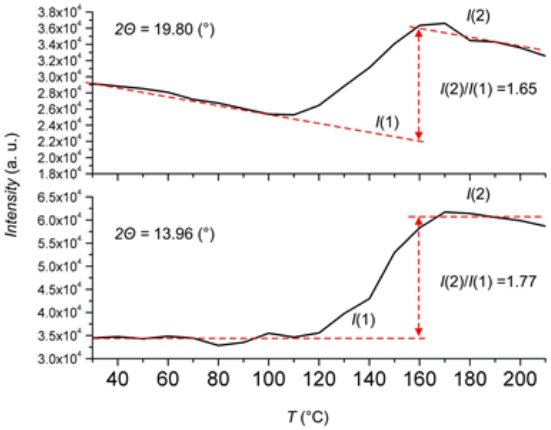

Figure 3.17b – The evolution of the integrated intensities (bottom) of the strongest peaks of KBH_4 with temperature. The average intensity's ratio between the peak and starting KBH_4 content is about 1.7.

In situ synchrotron XRD in the 30–210 °C temperature range reveals decomposition of $K[Al(BH_4)_4]$ at ~180 °C, with an onset at 110–120 °C, into amorphous products and KBH_4. Remarkably, the diffraction intensities of the crystalline KBH_4 are increasing during the decomposition of $K[Al(BH_4)_4]$ (Figure 3.17a and b), showing a maximum of the integrated intensity at 170 °C. This observation complements nicely the thermal analysis and mass spectrometric data, helping to suggest a decomposition reaction pathway (see in the next chapters).

NH_4BH_4:$Al(BH_4)_3$ system. The variable temperature *in situ* plot of powder patterns, collected from the sample, obtained after the

reaction of $Al(BH_4)_3$ with NH_4BH_4 revealed almost exclusively a single phase assigned to $NH_4[Al(BH_4)_4]$ (Figure 3.18). This compound was found to be the least stable within the series of the herein studied mixed-cation borohydrides, and it decomposes at 35 °C. Lack of the peaks of NH_4BH_4 upon decomposition of $NH_4[Al(BH_4)_4]$ makes this system different from the previously described $M[Al(BH_4)_4]$ ($M = Li^+$, Na^+, K^+) and required additional methods to describe its decomposition pathway (see the description below). Unique thermal decomposition of $NH_4[Al(BH_4)_4]$ may be explained by the presence and the recombination of the protic H^+ and hydridic H^- hydrogens within the same compound.

$RbBH_4$:$Al(BH_4)_3$ system. The variable temperature *in situ* plot of powder patterns, collected on the sample obtained after the reaction of $Al(BH_4)_3$ with $RbBH_4$, exhibits peaks for $Rb[Al(BH_4)_4]$ and traces of $RbBH_4$ (Figure 3.19). $Rb[Al(BH_4)_4]$ decomposes at about 160 °C followed by a remarkable intensity increase for the peaks from $RbBH_4$, similar to the behavior of $K[Al(BH_4)_4]$.

$CsBH_4$:$Al(BH_4)_3$ system. Upon heating two polymorphs of $Cs[Al(BH_4)_4]$ can be recognized (Figure 3.20). The first-order phase transition of $Cs[Al(BH_4)_4]$ starts at about 85 °C, where the low temperature (LT) polymorph transforms into the high temperature (HT) phase. The decomposition of HT-$Cs[Al(BH_4)_4]$ starts at ~150 °C. Intensities of the peaks of the starting $CsBH_4$ changed insignificantly compared to the changes observed for $M[Al(BH_4)_4]$ ($M = Li^+$, Na^+, K^+). However, the increased background indicates the formation of amorphous product(s). Cubic $CsBH_4$ appears from the amorphous product(s) above 165 °C.

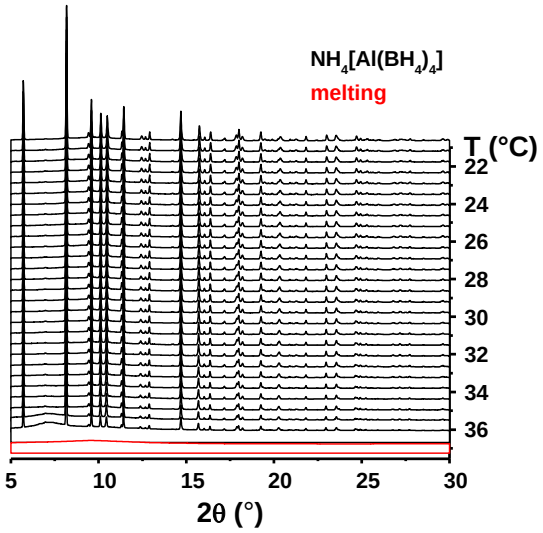

Figure 3.18 – The variable temperature *in situ* plot of XRPD patterns of $NH_4[Al(BH_4)_4]$ (SNBL/ESRF in Grenoble, France; PILATUS 2M pixel detector, λ = 0.68884 Å).

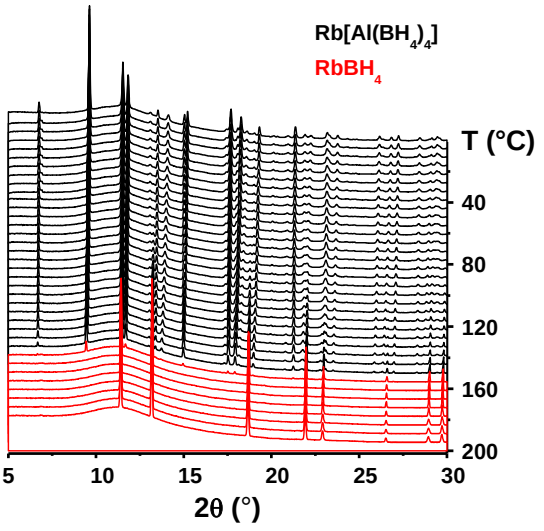

Figure 3.19 – The variable temperature *in situ* plot of XRPD patterns of $Rb[Al(BH_4)_4]$ (SNBL/ESRF in Grenoble, France; PILATUS 2M pixel detector, λ = 0.81712 Å). The formation of $RbBH_4$ is shown by red color.

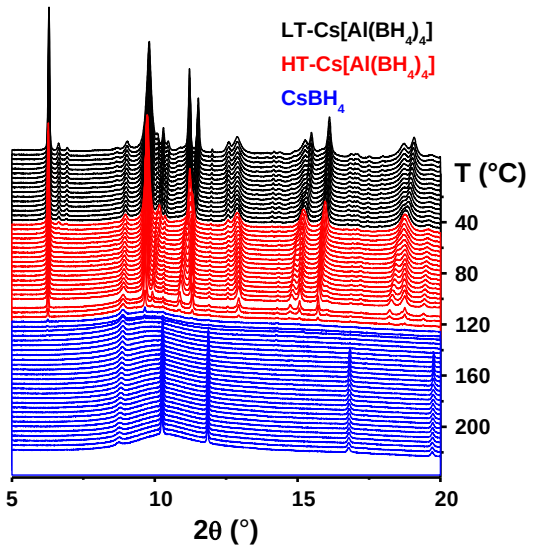

Figure 3.20 – The variable temperature *in situ* plot of XRPD patterns of $Cs[Al(BH_4)_4]$ (Materials Science Beamline at the PSI in Villigen, Switzerland; Mythen II detector, λ = 0.775045 Å).

4.2. Crystal Structures of $M[Al(BH_4)_4]$ ($M = Li^+, Na^+, K^+, NH_4^+, Rb^+, Cs^+$)

The interatomic distances and angles were obtained from the XRPD Rietveld refinement for all $M[Al(BH_4)_4]$ except for $Li[Al(BH_4)_4]$, which will be discussed using the DFT-optimizated values.

Crystal structure of $Li[Al(BH_4)_4]$. $Li[Al(BH_4)_4]$ crystallizes in the monoclinic $P2_1/c$ space group, in which each Al^{3+} and Li^+ cations are surrounded by four BH_4^- anions, coordinated *via* edges (Figure 3.21). As a result of these interactions, a 3D framework constructed from distorted tetrahedra is formed, resembling the structure of $LiBH_4$.[46] The underlying net, as analyzed by the program

TOPOS,[208] is a 4-connected net of a new type containing four nods (two Li^+ and two Al^{3+}) with the point symbol $\{4.6^2.8^3\}\{4.6^4.8\}$. The point symbol summarizes the rings which you can made around nods (in this case four nodes: 2 identical nodes around 2 Li^+ and 2 ones around identical Al^{3+}). In particular, the point symbol $\{4.6^2.8^3\}$ for Li^+ means that starting from Li^+ it is possible to make one ring containing 4 nods, 2 rings containing 6 nods and 3 rings containing 8 nods. The framework character of the compound is underlined by a similar separation of Li^+ and Al^{3+} from the bridging BH_4^- when normalized to the sum of ionic radii (cation + anion). The optimized by DFT calculations Al–H bonds are 1.83–1.92 Å, while the Al···B separations are 2.22–2.26 Å. These values are in good agreement with those found experimentally for $K[Al(BH_4)_4]$ (1.79–1.96 and 2.26 Å, respectively, shown in Table 3.1) and have not been refined due to the complexity of the data (large unit cell and weak Li and H scatterers). The Li···B separations, obtained from the experimental (Rietveld) data and DFT calculations, are 2.35–2.92 and 2.38-2.72 Å, respectively, and are similar to those found in $Li_4Al_3(BH_4)_{12.74}Cl_{0.26}$.[76] The B···Li···B and B···Al···B bond angles, obtained from DFT calculation, are 87.2–139.4 and 95.1–136.4°, respectively, and are similar to those found in $K[Al(BH_4)_4]$ (see Table 3.1).

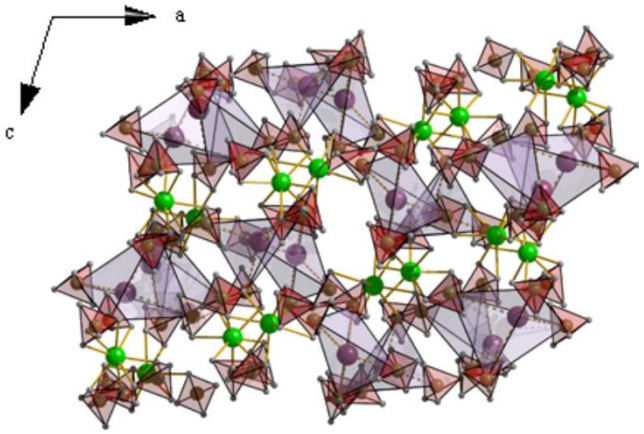

Figure 3.21 – Crystal packing of $Li[Al(BH_4)_4]$ along the *b* axis. Color code: Al = green, B = olive, H = grey, Li = purple.

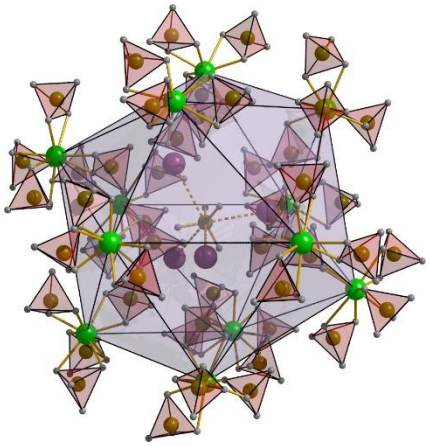

Figure 3.22 – Icosahedron, formed by one $[Li_4(BH_4)]^{3+}$ cation and twelve $[Al(BH_4)_4]^-$ anions, in the structure of $Li_4Al_3(BH_4)_{13}$. Color code: Al = green, B = olive, H = grey, Li = purple.

Some remarks on the $Li_4Al_3(BH_4)_{13}$ crystal structure. $Li_4Al_3(BH_4)_{13}$ crystallizes in the cubic *P*–43*n* space group, identical to the previously published complex $Li_4Al_3(BH_4)_{12.74}Cl_{0.26}$.[76] Corresponding bond lengths and angles, taken form the Rietveld refinements, are almost identical for both structures, each exhibiting a

total 12% porosity. The composition of the compound can be rationalized on the basis of a complex cation $[Li_4(BH_4)]^{3+}$ and a complex anion $[Al(BH_4)_4]^-$, packed similarly to the Cr_3Si (Frank-Kasper phase) type. The former ion is formed by linking four Li^+ cations to each face of the tetrahedral BH_4^- anion (Figure 3.22). The coordination sphere of each Li^+ cation is further completed by three, coordinated *via* edges, BH_4^- anions, arising from different $[Al(BH_4)_4]^-$ anions. The topology analysis indicates that $[(BH_4)Li_4][Al(BH_4)_4]_3$ is an antitype of Ag_3PO_4.[209,210]

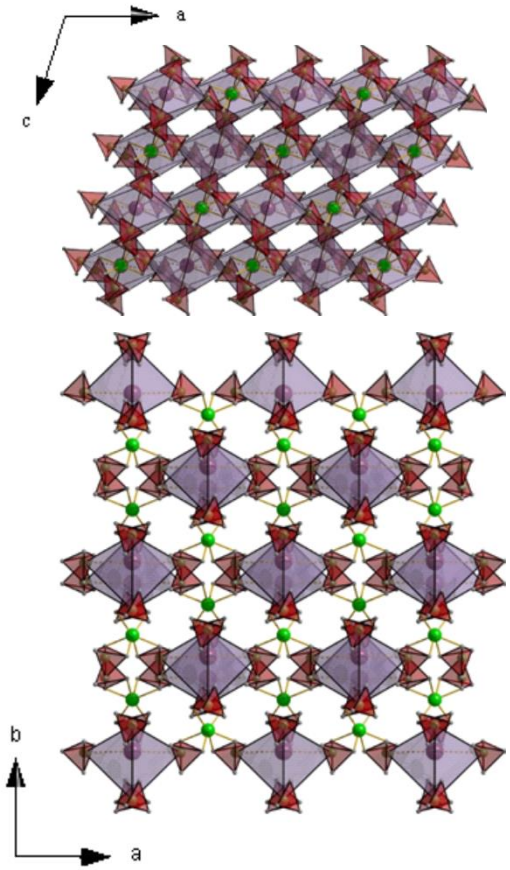

Figure 3.23 – Crystal packing of $Na[Al(BH_4)_4]$ along the *b* (top) and *c* axis. Color code: Al = green, B = olive, H = grey, Na = purple.

Crystal structure of Na[Al(BH$_4$)$_4$]. Na[Al(BH$_4$)$_4$] crystallizes in the monoclinic space group *C*2/*c*. The Na^+ atoms are in a distorted octahedral coordination environment formed by six BH_4^- groups, which are coordinated *via* edges (Figure 3.23). This coordination is similar to other Na-containing borohydrides, *e.g.* Na[Al(BH$_4$)$_{4-x}$Cl$_x$][77] and NaBH$_4$.[40] It is a monoclinic deformation of Na[Sc(BH$_4$)$_4$],[80] which itself is of the $CrVO_4$-type. The $[Al(BH_4)_4]^-$ anion is rotated by 90° in Na[Al(BH$_4$)$_{4-x}$Cl$_x$] compared to Na[Al(BH$_4$)$_4$] and Na[Sc(BH$_4$)$_4$]. Each $[Na(BH_4)_6]^{5-}$ octahedron in the structure of Na[Al(BH$_4$)$_4$] is linked *via* edges to neighboring octahedra, producing layers, which, in turn, are linked by vertices to the tetrahedral $[Al(BH_4)_4]^-$ anions (Figure 3.23). The refined and optimized Al–H and Al···B distances, being 1.77–1.95 and 2.24–2.26 Å, respectively, are in good agreement with the corresponding values in the $[Al(BH_4)_4]^-$ anions, found for K[Al(BH$_4$)$_4$]. The Na···B separations (2.91–3.33 Å) are significantly elongated compared to those in Na[Al(BH$_4$)$_{4-x}$Cl$_x$] (2.46–2.59 Å).[77] The calculated and refined B···Al···B angles are 95.9(3)–131.0(4)°, very similar to those found in the structure of K[Al(BH$_4$)$_4$].

The crystal structures of M[Al(BH$_4$)$_4$] (M = K^+, NH_4^+, Rb^+). The crystal structure of K[Al(BH$_4$)$_4$] was found earlier, than other two members of the isostructural series. The normal mode analysis performed for the *Fdd*2 space group, suggested recently in an independent work,[78] showed that this structure is stable with respect to atomic displacements. However, the simulated annealing procedure resulted in the stable *Fddd* symmetry (Table 3.1). The ground state electronic energy and the zero point energy of the structure with *Fddd* symmetry equals within 1 meV/formula unit with those of the *Fdd2*

one. Thus, our structure in the higher *Fddd* symmetry has the advantage over the one in *Fdd*2.

Table 3.1 – Selected bond lengths (Å) and bond angles (°) in $M[Al(BH_4)_4]$.

	$K[Al(BH_4)_4]$		**$Rb[Al(BH_4)_4]$**		**$NH_4[Al(BH_4)_4]$**	
	Exp.	DFT	Exp.	DFT	Exp.	DFT
M···B	3.285(4) 3.809(4)	3.249 3.833	3.443(7) 3.902(6)	3.471 3.969	3.390(3) 3.908(3)	3.363 4.136
M–H	2.55(1) 2.91(1) 3.20(1)	2.706 2.874 3.051	2.52(2) 2.90(1) 3.53(4)	2.915 2.996 3.259	2.807(3) 2.967(3) 3.193(3)	2.771 3.127 3.169
Al···B	2.262(4)	2.242	2.190(7)	2.252	2.231(3)	2.245
Al–H	1.79(1) 1.96(1)	1.854 1.871	1.767(7) 1.93(2)	1.877 1.859	1.883(3) 1.890(3)	1.861 1.870
H···H	–	–	–	–	1.816(3)	1.758
B···Al···B	97.6(1) 98.9(1) 135.4(1)	95.81 100.37 135.95	97.8(4) 99.3(5) 134.6(5)	96.32 100.72 134.74	95.9(1) 100.2(1) 136.0(1)	97.28 100.11 134.24
N–H···H	–	–	–	–	157.9(1)	164.10

$K[Al(BH_4)_4]$ is the first reported halide-free bimetallic borohydride containing $[Al(BH_4)_4]^-$. The other known bimetallic Al-based complexes, such as $Li_4Al_3(BH_4)_{12.74}Cl_{0.26}$[76] and $Na[Al(BH_4)_{4-x}Cl_x]$,[77] were stabilized by Cl-substitution on the borohydride sites, as determined by structural refinements. The only Cl-free aluminum borohydride complex, $[Ph_3MeP][Al(BH_4)_4]$, contains a bulky organic cation,[189] making it inappropriate for hydrogen storage applications. Interestingly, a synthesis involving $AlCl_3$ results in the $K[Al(BH_4)_4]$ phase with cell parameters very similar to those of the chlorine-free compound, indicating low or no substitution of Cl on the BH_4^- sites.

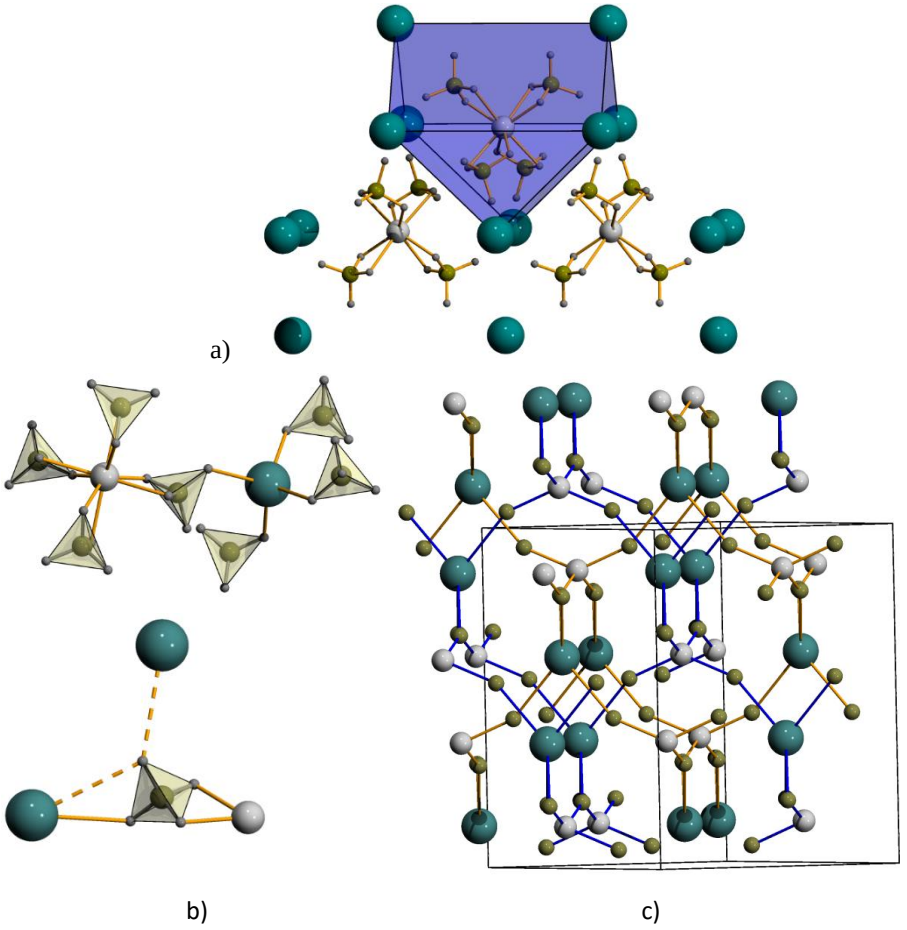

Figure 3.24 *a* – Complex anion $[Al(BH_4)_4]^-$ located in the bi-capped trigonal prismatic cage K_8; *b* – coordination environment of K, Al atoms and the BH_4 group in $K[Al(BH_4)_4]$; the dashed lines depict elongated K–H distances completing the coordination for K to 4H + 8H; *c* – two interpenetrated *dia*-type nets in $K[Al(BH_4)_4]$, hydrogen atoms are omitted for clarity.

$K[Al(BH_4)_4]$ crystallizes in the orthorhombic space group *Fddd*, similar to the LT-$TbAsO_4$ prototype[211], with BH_4^- anions in place of the oxygen atoms, see Figures 3.24. The LT-phase of $TbAsO_4$ (stable below 27.7 K) is an orthorhombic deformation of the tetragonal HT-phase ($I4_1/amd$, $ZrSiO_4$-type). The orthorhombic structure of $K[Al(BH_4)_4]$, stable up to its decomposition, is far from the tetragonal

prototype. This is certainly due to a much stronger deformation of $[Al(BH_4)_4]^-$ from an ideal tetrahedron (see below) as compared to $[AsO_4]^{3-}$. Metal cations have well distorted tetrahedral environments formed by the BH_4^- groups. Aluminum atoms are coordinated to four anions via the BH_2 edges: Al–H1 1.79(1) Å and Al–H3 1.96(1) Å, forming the distorted tetrahedral $[Al(BH_4)_4]^-$ complexes with B···Al···B angles ranging from 97.6(1)° to 135.4(1)°, very close to 100.0(1)–130.8(2)° in the chlorine-containing $Li_4Al_3(BH_4)_{12.74}Cl_{0.26}$.[76] K^+ coordinates the anion asymmetrically via an edge: K–H2 2.55(1) Å, K–H4 3.20(1) Å. The BH_4^- group is coordinated through the vertex of another potassium cation (K-H4 2.92(9) Å), forming a T-shaped coordination for the anion and 4 + 4 coordination polyhedron for K^+ with respect to the BH_4^- groups, see Figure 3.24b. Disregarding the more distant potassium atom, the borohydride group acts like a nearly linear bridging ligand with an Al···B···K angle of 152.7(2)°, similar to the Mg···B···Mg angles in the $Mg(BH_4)_2$ framework structures.[58,60]

The Al···B distance of 2.262(4) Å is slightly longer than 2.10−2.15 Å in *α,β*-$Al(BH_4)_3$ where Al coordinates three borohydrides[66,212] and falls in the 2.22–2.35 Å range for the tetracoordinated Al in $Li_4Al_3(BH_4)_{12.74}Cl_{0.26}$, $[Ph_3MeP][Al(BH_4)_4]$ and $Na[Al(BH_4)_{4-x}Cl_x]$.[76,77,189] Due to the smaller size of Al^{3+}, the Al···B distances are slightly shorter than 2.27–2.38 Å Sc···B and Y···B bond distances in $K[Sc(BH_4)_4]$ and $K[Y(BH_4)_4]$.[81,88] Remarkably, Y^{3+} and Sc^{3+} coordinate the BH_4^- groups via the tetrahedral faces, showing higher coordination numbers and longer metal-hydrogen distances. The short K···B distance of 3.285(4) Å in $K[Al(BH_4)_4]$ (CN = 4 + 4) is similar to 3.26(1) Å distance in $K[Y(BH_4)_4]$ (CN = 6)[88] and slightly

shorter than 3.364 Å in the cubic KBH_4 (CN = 6)[40] and shorter than the distance of 3.51(4) Å for CN = 8 in $K[Sc(BH_4)_4]$.[81] The longer K···B distance of 3.809(4) Å is comparable to the longest K···B distance of 3.95(2) Å[81] for CN = 8 in $K[Sc(BH_4)_4]$. On the other hand, K^+ with CN = 7 in $LiK(BH_4)_2$ shows more regular K···B distances, falling within 3.40–3.47 Å.[72]

$K[Al(BH_4)_4]$ is not isomorphic to $KAlCl_4$ and $NaAlCl_4$, where much more regular tetrahedral $AlCl_4^-$ anions are present, as well as different coordination polyhedra for alkali metal atoms are observed.[213] The title structure can be seen as an iono-covalent compound containing the complex anion $[Al(BH_4)_4]^-$ located in the bi-capped trigonal prismatic cage K_8 (Figure 3.24a). In the related compound, $Na[Al(BH_4)_{4-x}Cl_x]$[77], the complex anion is also located in a deformed square prismatic Na_8 cage. The ratio of the average K···B to Al···B distances of 1.57 is quite large (for comparison with other members see Table 3 in Ref. [214]) indicating an important degree of isolation of the complex anion $[Al(BH_4)_4]^-$ in the K_8 cage.

Neglecting four longer K···B distances, the structure of $K[Al(BH_4)_4]$ can also be viewed as a framework formed by two diamond nets (or cubic ZnS nets, considering the K and Al ordering), shown in Figure 3.24c. The two interpenetrated *dia*-nets are touching each other via one of the two elongated H–K 3.20(1) Å (B···K 3.809(4) Å), shown by the dashed line in Figure 3.24b. The same topology was found for another complex hydride, $Li[Zn_2(BH_4)_5]$.[85] Double interpenetrated frameworks are more clearly distinguishable in the absence of complex anions, i.e. in the high-pressure δ-$Mg(BH_4)_2$[58] and two closely related $Cd(BH_4)_2$ polymorphs.[91] The topologies typical for

coordination frameworks highlight the role of the borohydride anion acting as the bridging directional ligand.[92]

It should be noted, that the structure of $NH_4[Al(BH_4)_4]$ is stabilized by the $N–H^{\delta+}\cdots H^{\delta-}–B$ (1.816(3) Å) dihydrogen bonds (Figure 3.25). This value is supported by the DFT calculations (Table 3.1), and found to be significantly shorter than those in NH_3BH_3 (1.91(5) Å)[215] and NH_4BH_4 (2.28 Å).[216]

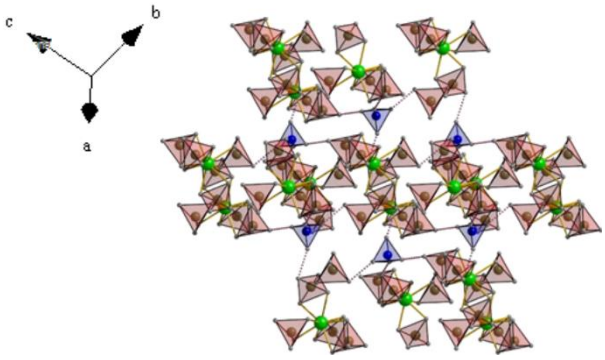

Figure 3.25 – Crystal packing of $NH_4[Al(BH_4)_4]$. Color code: Al = green, B = olive, H = grey, N = blue.

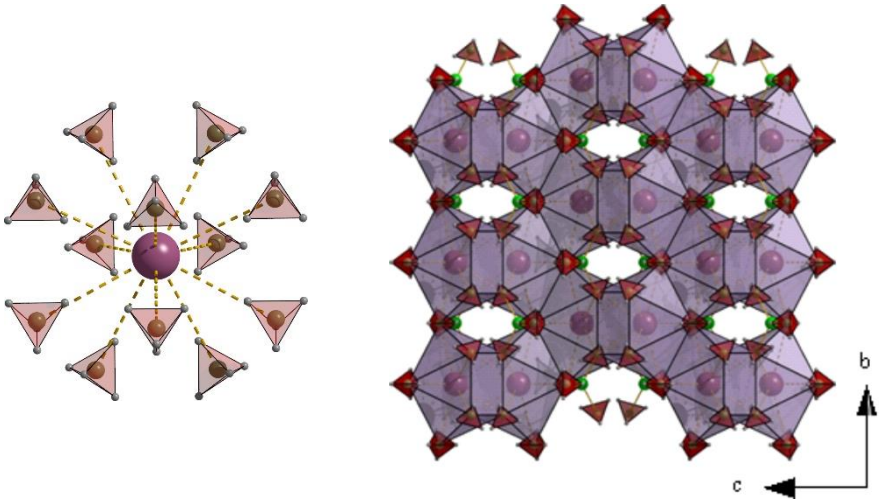

Figure 3.26 – The coordination environment around the Cs^+ atom (left) and crystal packing of $Cs[Al(BH_4)_4]$ along the *a* axis (right). Color code: Al = green, B = olive, H = grey, Cs = purple.

The crystal structure of the high-temperature polymorph of Cs[Al(BH$_4$)$_4$]. It crystallizes in the tetragonal space group *I*4$_1$/*amd*, the crystal structure is derived from the scheelite-type,[217] which is also the prototype of another mixed-cation borohydride Cs[Y(BH$_4$)$_4$].[89] The powder pattern of the RT polymorph was indexed as a monoclinic unit cell which point towards a similar structural relation like scheelite-monazite.[218] In spite of a significant effort made, no reliable structural model was obtained for the RT-phase.

In the high temperature polymorph, the Cs^+ atom coordinates (4 + 8) BH_4^- groups with the Cs···B separations of 3.66(7) and 4.53(3) Å, respectively. The coordination polyhedron comprises two trigonal prisms, rotated by 90 °C (Figure 3.26). They are stacked to adjacent polyhedra *via* pseudo square faces (4.01 × 4.43 Å^2), resulting to the formation of an infinite 3D framework. The refined (Rietveld) Al−H and Al···B distances of 1.541(6) and 2.023(8)−2.174(6) Å, respectively, differ from the previously described $[Al(BH_4)_4]^-$ anions. This can be explained by difficulties with the structure refinement due to the presence of heavy Cs atom. However, the calculated and refined B···Al···B angles of 102.6(4) and 124.3(4)°, respectively, are very similar to those found for other M[Al(BH$_4$)$_4$] complexes.

Formation energies. The enthalpy of formation for M[Al(BH$_4$)$_4$] from Al(BH$_4$)$_3$ and MBH$_4$ (M = Li^+, Na^+, K^+, NH_4^+, Rb^+, Cs^+) was calculated from the ground state energies, as described in the experimental section above. As reference, the *Pna*2 structure was used for Al(BH$_4$)$_3$,[66] while for the alkali metal borohydrides the low temperature structures were used, as described in Ref. [219]. *P*4$_2$/*nmc* symmetry was used for Rb and Cs borohydrides; for the nonspherical

NH_4^+ cation the lowest energy structure of ammonium borohydride has the *P*-42$_1$*c* symmetry. This structure is however unstable with respect to the orientation of NH_4^+ (imaginary modes related to the NH_4^+ rotation), as well as with respect to the decomposition into NH_3BH_3 and H_2.[220] Within these assumptions the formation enthalpy is presented in Figure 3.27 for all compounds.

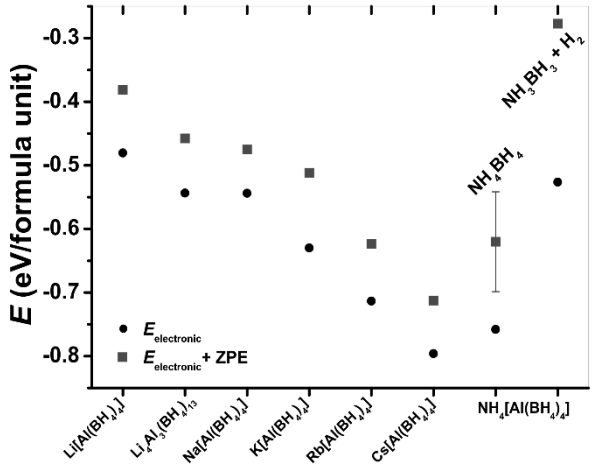

Figure 3.27 – Calculated enthalpy of M[Al(BH$_4$)$_4$]) formation from Al(BH$_4$)$_3$ and MBH$_4$ (M = Li^+, Na^+, K^+, NH_4^+, Rb^+, Cs^+). Black circles are for the ground state electronic energy, black squares account for the zero point vibrations. Data are given per f.u. of M[Al(BH$_4$)$_4$].

For NH$_4$[Al(BH$_4$)$_4$] the two sets of data corresponding to the decomposition into disordered/unstable NH$_4$BH$_4$, and AB with H_2 are shown. The error bar accounts for four imaginary modes related to the NH_4^+ librations.

The calculated enthalpy indicates that each of the new compounds is stable with respect to the decomposition into binary borohydrides, and this stability increases with the mass of alkali metal cation. On the other hand, the energy gain is rather small compared to the stability of the binary borohydrides. For lithium aluminum

borohydride there is an additional decomposition path in line with the experimentally observed formation of $Li_4Al_3(BH_4)_{13}$:

$$Li_4Al_3(BH_4)_{13} + Al(BH_4)_3 \rightarrow 4Li[Al(BH_4)_4] \quad (3.13)$$

The calculated electronic contribution to the enthalpy of this reaction equals –0.29 eV/formula unit. The zero point vibrations lower this enthalpy to –0.15 eV/formula unit. Due to different stoichiometries, the enthalpy is given per formula unit of $Al(BH_4)_3$ that allows comparison with data in Figure 3.27. Indeed, the decomposition into $Li_4Al_3(BH_4)_{13}$ is the most facile among all the reactions.

4.3. Vibrational Spectroscopy study of M[Al(BH4)4] (M = Li+, Na+, K+, NH4+, Rb+, Cs+)

Infrared and Raman spectroscopy study of K[Al(BH4)4]. The vibrational spectroscopy characterization of $K[Al(BH_4)_4]$ was made before the other mixed-cation aluminum borohydrides, thus the analysis of $M[Al(BH_4)_4]$ ($M = Li^+, Na^+, NH_4^+, Rb^+, Cs^+$) is based on it. The strongest bands in the 2100–2600 cm^{-1} range (Figure 3.28) correspond to the B–H stretching and less intense peaks from 990 to 1300 cm^{-1} can be attributed to the B–H bending modes. Only one known strongest peak of KBH_4[54] at 2308 cm^{-1} can be recognized in the stretching mode region in Raman spectrum, the remaining peaks overlap with B–H stretching modes from $K[Al(BH_4)_4]$: the difference of intensities in spectra for different $KBH_4/K[Al(BH_4)_4]$ ratios are shown in Figure 3.29. The other two peaks at 2436 and 2476 cm^{-1} from Raman and 2419 and 2472 cm^{-1} from IR are related to the outward B–H stretching modes from $[Al(BH_4)_4]^-$ with respect to the observed in

crystal structure bidentate coordination. The mentioned doublet in the 2400–2600 cm^{-1} range with 50–80 cm^{-1} splitting is typical for bidentately coordinated borohydrides through one edge only.[221,222] Similar peaks were seen at 2440 and 2480 cm^{-1} for $Li_4Al_3(BH_4)_{12.74}Cl_{0.26}$ in Raman and at 2420 with 2480 cm^{-1} in the infrared spectra, as well as at 2444 and 2503 cm^{-1} for $Na[Al(BH_4)_{4-x}Cl_x]$ in Raman spectra.[76,77]

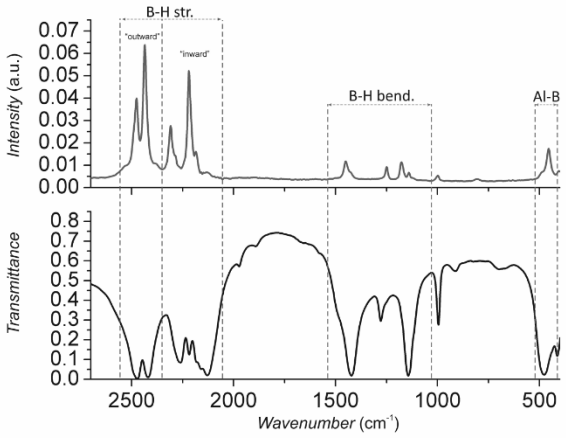

Figure 3.28 – Raman and infrared spectra of $K[Al(BH_4)_4]/KBH_4$ mixture (90.1/9.9 weight %) at room temperature.

In the region of B–H bending modes, a band at 1249 cm^{-1} corresponds to KBH_4. The other peaks at 999, 1140, 1177 and 1450 cm^{-1} in Raman spectrum and 996, 1144, 1278, 1422 cm^{-1} in the IR can be assigned to the BH_2 bending modes in $[Al(BH_4)_4]^-$, similar to $Li_4Al_3(BH_4)_{12.74}Cl_{0.26}$ complex (near 1000, 1020, 1170 and 1450 cm^{-1} in Raman spectrum).[76] The sharp bands at 455 and 477 cm^{-1} in both spectra likely correspond to the Al···H–B stretching mode, also previously seen at 490 cm^{-1} for Li–Al and Na–Al complex borohydrides, as well as for the pure $Al(BH_4)_3$.[76,77,223]

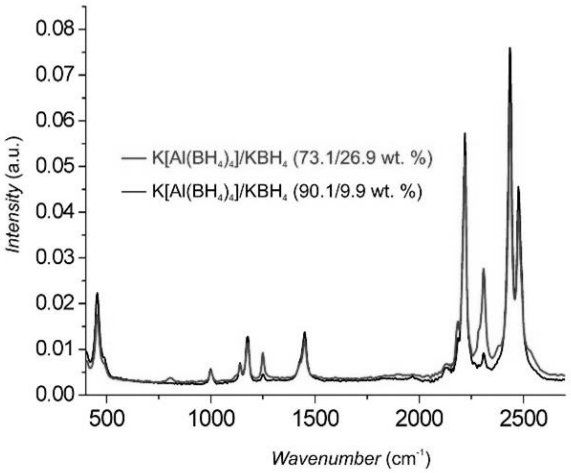

Figure 3.29 – Comparison of Raman spectra on two samples with different $K[Al(BH_4)_4]/KBH_4$ ratios: 73.1/26.9 and 90.1/9.9 wt. %, as determined from XRPD.

The Raman spectra of $M[Al(BH_4)_4]$ ($M = Li^+$, Na^+, NH_4^+, Rb^+, Cs^+). Every Raman spectrum of $M[Al(BH_4)_4]$ ($M = Li^+$, Na^+, NH_4^+, Rb^+, Cs^+) contains bands for the B–H bending and stretching modes of the BH_4^- ligands in the $[Al(BH_4)_4]^-$ anion at 1000–1500 and 2100-2600 cm^{-1}, respectively (Figure 3.30). The stretching mode bands are characteristic for the bidentately coordinated borohydride anions.[221,222] The same was observed in the Raman spectrum of $K[Al(BH_4)_4]$. The complex anion $[Al(BH_4)_4]^-$ anion is also visible in the Raman spectra due to the presence of the characteristic band at about 460 cm^{-1}, arising from the Al···H–B stretching mode. Besides these, the Raman spectrum of $Na[Al(BH_4)_4]$ also contains a characteristic band for $NaBH_4$, centered at about 2330 cm^{-1} (Figure 3.30). The spectrum of $Li[Al(BH_4)_4]$ is further complicated by the presence of bands for $LiBH_4$ and $Li_4Al_3(BH_4)_{13}$ (Figure 3.30).

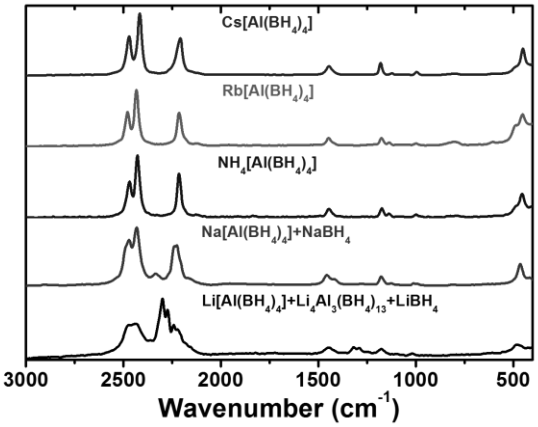

Figure 3.30 – Raman spectra of the studied compounds.

4.4. Thermal Analysis of $M[Al(BH_4)_4]$ ($M = Li^+, Na^+, K^+, NH_4^+, Rb^+, Cs^+$)

Thermal analysis of $Li[Al(BH_4)_4]$ and $Na[Al(BH_4)_4]$. According to XRPD, the examined sample of the product after the reaction of $Al(BH_4)_3$ with $LiBH_4$ contained ~40 wt% of $Li[Al(BH_4)_4]$, ~19 wt% of $Li_4Al_3(BH_4)_{13}$ and ~41 wt% of $LiBH_4$. This ratio can vary due to the instability of the Al-containing borohydrides and uncertainties of the quantitative XRPD analysis. The TGA plot exhibits one decomposition step at 50–90 °C with a 25 wt% weight loss, which was found to be endothermic with the maximum situated at 89 °C (Figure 3.31). Two endothermic minima at 111 and 277 °C correspond, respectively, to the phase transition and melting point of $LiBH_4$. The observed weight loss is significantly smaller compared to the calculated one according to equations (3.9) and (3.10). Discontinuities between the XRPD and TGA data can be explained by the partial degradation of

the sample during transportation/storing for the TGA analysis. In this case the sample contains less $Li[Al(BH_4)_4]$ and $Li_4Al_3(BH_4)_{13}$.

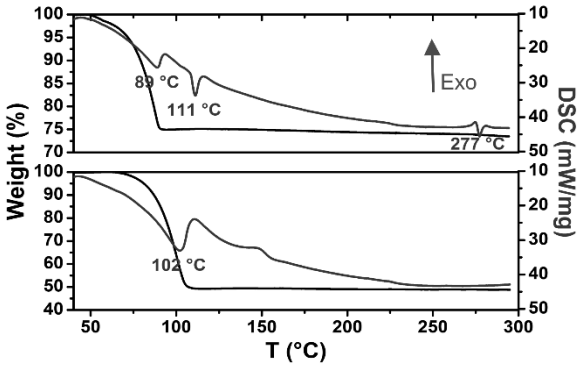

Figure 3.31 – TGA and DSC plots of the samples, obtained after the reaction of $Al(BH_4)_3$ with $LiBH_4$ (top) and $NaBH_4$ (bottom).

According to XRPD, the product after reaction of $Al(BH_4)_3$ with $NaBH_4$ contained ~90 wt% of $Na[Al(BH_4)_4]$ ~10 wt% of $NaBH_4$. This sample decomposed in one endothermic step at 70–110 °C with a total weight loss of 51% (Figure 3.31). This is in agreement with the calculated weight loss of 58 wt% according to equation (3.10).

Thermal and mass spectrometry analysis of $K[Al(BH_4)_4]$. The TGA and DSC curves of the $K[Al(BH_4)_4]/KBH_4$ (73.1/26.9 wt% from XRPD) mixture are shown in Figure 3.32. Only one sharp endothermic peak with the maximum at 160 °C was detected by DSC analysis in the 25−500 °C temperature range. According to the TGA and *in situ* XRPD, the decomposition of the $K[Al(BH_4)_4]$ complex starts at 135 °C and finishes at 175 °C (near 180 °C from XRPD). This decomposition profile is significantly different from the previously reported decomposition of presumably pure $K[Al(BH_4)_4]$ by Semenenko et al.,[155] where two endothermic peaks were detected at

132 and 240 °C. According to their data, the evolution of diborane and hydrogen was also accompanied by considerable amounts of $Al(BH_4)_3$ desorbing at 130 °C. The total mass loses of 20.8 wt% on our sample is equivalent to 28.5 wt% with respect to the pure $K[Al(BH_4)_4]$. Desorption of $Al(BH_4)_3$ would lead to a much larger weight loss of 56.9 wt% for the pure $K[Al(BH_4)_4]$ or 41.8 wt% for our $K[Al(BH_4)_4]/KBH_4$ (73.1/26.9 wt%) sample. According to our diffraction data, the intensity of KBH_4 peaks increases upon the decomposition of $K[Al(BH_4)_4]$ (Figure 3.17), providing ~0.6 mole of KBH_4 upon decomposition of one mole of $K[Al(BH_4)_4]$. Combining this with the TGA data, all the observations can be described by the following hypothetic decomposition reaction:

$$2K[Al(BH_4)_4] \rightarrow KBH_4 + \text{amorphous } \text{“}KAl_2B_3\text{”} + 2B_2H_6 + 8H_2 \quad (3.12)$$

This reaction gives 28.5 wt% loss of mass, as observed by the TGA. The absence of diffraction peaks in the decomposed products rules out the formation of the anticipated crystalline phases, such as AlB_2, K–B borides and KH. It is worth noting that in other independent investigations of $K[Al(BH_4)_4]$, Knight et al.[78] suggested the formation of $Al(BH_4)_3$ and KBH_4 from the sample with a somewhat lower content of $K[Al(BH_4)_4]$ (56 wt%). The authors also observed the formation of diborane and hydrogen during the thermal decomposition of $K[Al(BH_4)_4]$. The evolution of diborane was explained by a possible thermal decomposition of $Al(BH_4)_3$, and the hydrogen release at around 300 °C was attributed to $(BH)_n$ solid deposited on the TGA furnace surface during the experiment.[78]

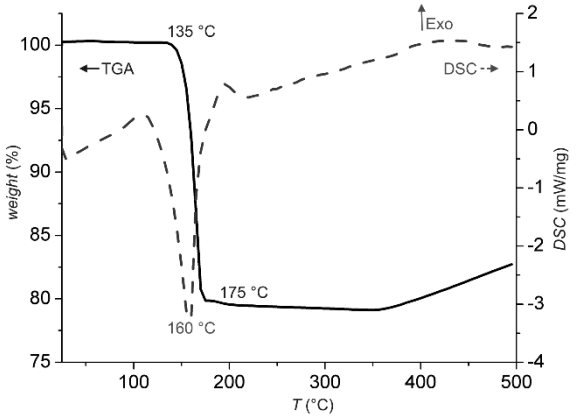

Figure 3.32 – Thermal analysis of $K[Al(BH_4)_4]/KBH_4$ mixture.

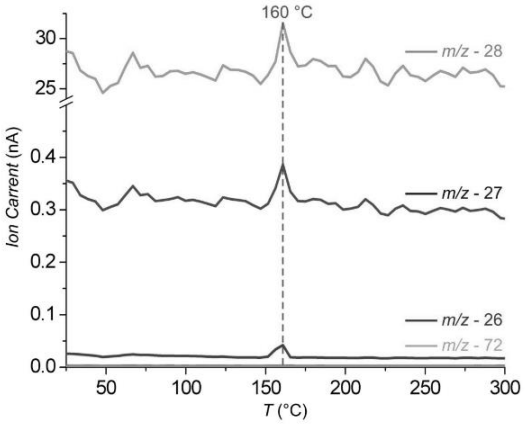

Figure 3.33 – MS curve of evolving gases measured in 25–300 °C temperature range. The lines close to the zero level show the absence of $Al(BH_4)_3$ fragments.

We additionally performed two independent mass spectrometry measurements on the evolving gas products, combined with the simultaneous TGA. Atomic mass units 26 and 27 corresponding to B_2H_6 and 42, 43, 56, 57 and 70–73 a.m.u. corresponding to $Al(BH_4)_3$, as observed in decomposition of $Li_4Al_3(BH_4)_{12.74}Cl_{0.26}$,[185] were chosen as characteristic fragments. From our data shown in Figure 3.33, diborane release is clearly observed at 160 °C, fully consistent with the

maximum of the endothermic peak seen in DSC, and weight losses in TGA and TGA-MS data in Figure 3.34. Due to the fact, that the 28 *m/z* signal in diborane reference data amounts only to ~0.5 %,[224,225] the likely origin of this peak at the decomposition is the release of the molecular nitrogen, which was trapped during the synthesis. The evolution of AlH^+ with 28 *m/z* as byproduct is also not feasible, because this peak has much smaller abundance (~22 %) compared to 27 *m/z* for Al, as seen for aluminum hydride (alane) decomposition from hydrogen-covered aluminum single crystal surfaces.[226] At the same time, diborane was also previously observed by IR data from decomposition of $Li_4Al_3(BH_4)_{12.74}Cl_{0.26}$[185] and $LiZn_2(BH_4)_5$,[227] the former also showed $Al(BH_4)_3$ desorption and no trace of alane formation. In the case of $K[Al(BH_4)_4]$, we did not observe the fragments of $Al(BH_4)_3$ in the TGA-MS curve (Figure. 3.34), however the presence of 42 and 43, 56 and 57 a.m.u. likely belonging to $Al(BH_4)^+$ and $Al(BH_4)_2^+$ can be recognized in the logarithmic plot of the second TGA-MS experiment (Figure S1.1 in the supporting information). Therefore, the decomposition by the reaction 3.12 can be affirmed with the maximum intensity of H_2^+ ion current at 160 °C.

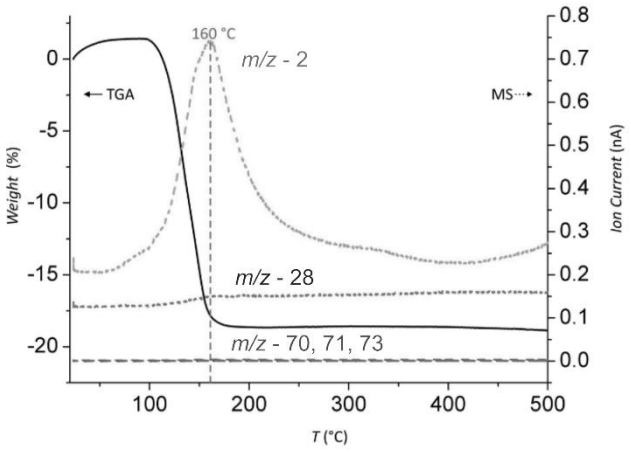

Figure 3.34 – TGA-MS curves in 20–500 °C temperature range. The current for diborane is considerably lower than for hydrogen. The beam current is practically zero for aluminum borohydride.

This decomposition pathway is different from the ones for Li–Al and Na–Al borohydrides of $Li[Al(BH_4)_4]$, $Li_4Al_3(BH_4)_{13}$ and $Na[Al(BH_4)_4]$, desorbing $Al(BH_4)_3$ under vacuum,[185] and shows similarities with alkali metal-yttrium borohydrides, $M[Y(BH_4)_4]$, decomposing to hydrogen and nonvolatile amorphous MYB_4H_n (M = Li, Na, Rb, Cs and n = 4, 3, 3, 2 respectively) products.[89] Our manipulations with $K[Al(BH_4)_4]$ on air show its relatively good stability and its non-explosive character, which is typical even for the smallest amounts of $Al(BH_4)_3$ vapors. No visible segregation of $Al(BH_4)_3$ from $K[Al(BH_4)_4]$ upon heating does not exclude its equilibrium with the starting compounds at temperatures close to ambient, forming a small partial pressure of aluminum borohydride. However, for potential applications in hydrogen storage it is important that this plausible reaction is not observed at elevated temperatures. This prompts for further studies on reactive hydride composites capable

of suppressing diborane release, making $K[Al(BH_4)_4]$ a good candidate for the conversion of aluminum borohydride into a more stable form, to be used for example in reactive hydride composites.[228]

Thermal and mass spectrometry analysis of $NH_4[Al(BH_4)_4]$. The sample, containing ~97 wt% of $NH_4[Al(BH_4)_4]$, decomposed in two clearly defined steps (Figure 3.35). The decomposition of the complex starts at about 35 °C with a weight loss of ~13.6%, while the second decomposition step is observed at 58 °C and reveals a ~20.5% weight loss. A similar two step weight loss was also observed upon the thermal decomposition of $Al(BH_4)_3{\cdot}NH_3BH_3$, which will be discussed in the next chapter (Chapter IV).

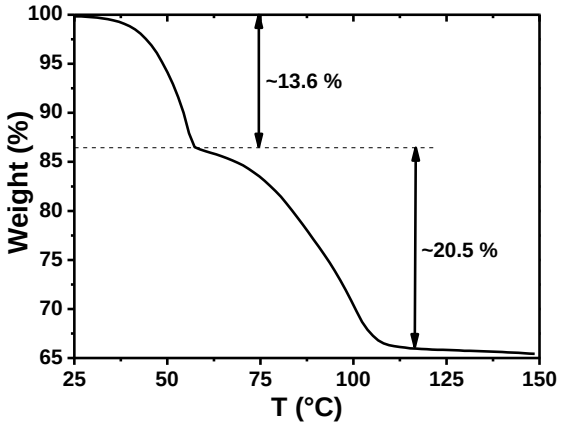

Figure 3.35 – TGA and DSC plots of the sample, obtained after the reaction of $Al(BH_4)_3$ with NH_4BH_4.

According to the TGA−MS data of $NH_4[Al(BH_4)_4]$ it was found, that both decomposition steps are accompanied by the release of hydrogen, diborane and ammonia (Figure 3.36).

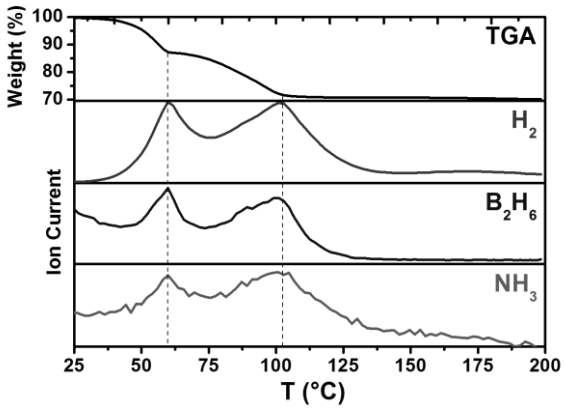

Figure 3.36 – TGA-MS analysis of the sample, obtained after the reaction of $Al(BH_4)_3$ with NH_4BH_4.

Thermal analysis of $Rb[Al(BH_4)_4]$ and $Cs[Al(BH_4)_4]$. The TGA plots of both $Rb[Al(BH_4)_4]$ and $Cs[Al(BH_4)_4]$ each contain two poorly defined decomposition steps with a total weight loss of 13.2 and 4.5%, respectively (Figure 3.37). These values are significantly lower than 41.6 and 32.6 wt%, respectively, expected for the release of volatile $Al(BH_4)_3$.

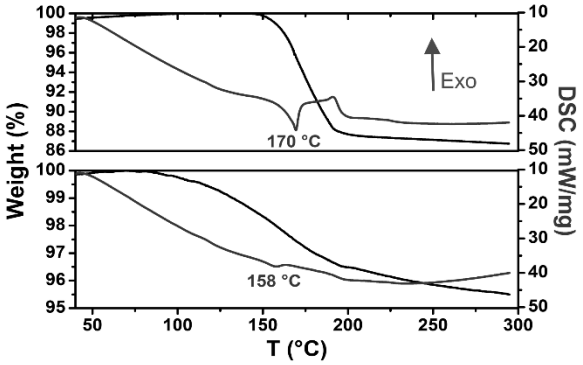

Figure 3.37 – TGA and DSC plots of the samples, obtained after the reaction of $Al(BH_4)_3$ with $RbBH_4$ (top) and $CsBH_4$ (bottom).

Furthermore, the weight loss for $Rb[Al(BH_4)_4]$ is higher than the calculated hydrogen content of 9.4 wt%, indicating release of other gases. Indeed, according to the TGA−MS data it was found that the first decomposition step of $Rb[Al(BH_4)_4]$ is accompanied by the release of hydrogen and diborane, while the former gas is exclusively observed during the second decomposition step (Figure 3.38).

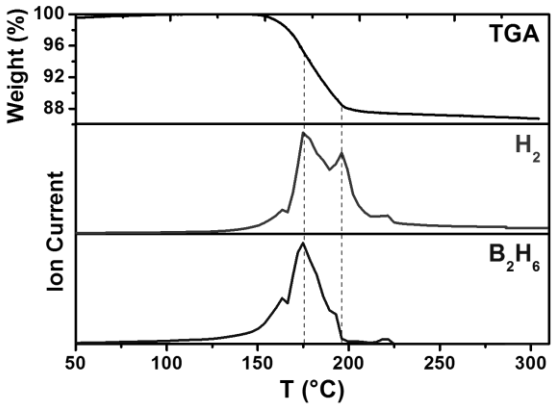

Figure 3.38 – TGA-MS analysis of the sample, obtained after the reaction of $Al(BH_4)_3$ with $RbBH_4$.

The total weight loss for $Cs[Al(BH_4)_4]$ (4.5%) is smaller than the calculated hydrogen content of ~7.4 wt%. This might be an evidence for the release of pure hydrogen upon thermal decomposition, which was also confirmed by the volumetric measurements (see below). However, the TGA-MS data testify to the simultaneous release of hydrogen and diborane during the first decomposition step (Figure 3.39), while only hydrogen was released during the second step similar to the Rb-containing analogue.

The release of side products from $M[Al(BH_4)_4]$, like diborane and ammonia ($NH_4[Al(BH_4)_4]$) diminishes the potential applications for hydrogen storage for the determined compounds.

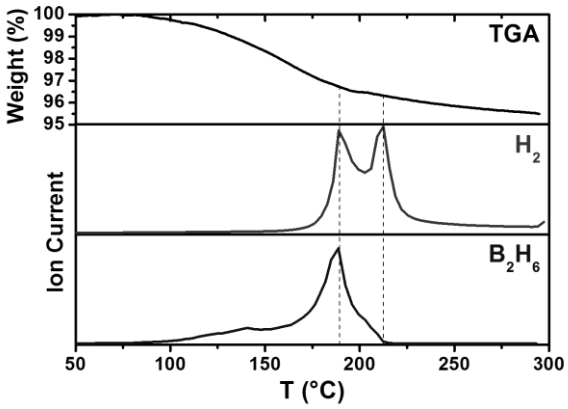

Figure 3.39 – TGA-MS analysis of the sample, obtained after the reaction of $Al(BH_4)_3$ with $CsBH_4$.

The comparison of the decomposition temperatures from *in-situ* XRPD and TGA/DSC methods. We could not collect the DSC data for $Li[Al(BH_4)_4]$ (its decomposition peak was not defined) and $NH_4[Al(BH_4)_4]$ (very unstable), that is why for comparison of stability we will use the data form XRPD, where the experimental conditions (5°C/min heating rate) are similar for all the samples. The decomposition temperatures from the XRPD data are taken when the diffraction peaks of $M[Al(BH_4)_4]$ ($M = Li^+$, Na^+, K^+, NH_4^+, Rb^+, Cs^+) and $Li_4Al_3(BH_4)_{13}$ vanish completely (offset temperature), see Table 3.2. In general, the difference in temperatures between the two methods does not exceed 10 °C, which is reliable for the general conclusion on the stability of the series.

Table 3.2 – Decomposition temperatures of Al-based borohydrides.

Compound	T_{dec} (°C)	
	XRPD	TGA/DSC
$Li[Al(BH_4)_4]$	60	N/A
$Li_4Al_3(BH_4)_{13}$	95	89
$Na[Al(BH_4)_4]$	90	102
$K[Al(BH_4)_4]$	170	160
$Rb[Al(BH_4)_4]$	160	170
$Cs[Al(BH_4)_4]$	150	158
$NH_4[Al(BH_4)_4]$	35	35

N/A – not available.

4.5. Volumetric Studies of $M[Al(BH_4)_4]$ ($M = NH_4^+, Rb^+, Cs^+$)

Volumetric studies of $NH_4[Al(BH_4)_4]$, performed at the fixed temperature of 40 °C, which corresponds to the first decomposition step of the compound (Figure 3.36), revealed the release of about 3 mol of gas (Figure 3.40). The same experiments on $Rb[Al(BH_4)_4]$ and $Cs[Al(BH_4)_4]$ exhibit the release of about 4 and 4.5 mole of gas at 160 °C, respectively (Figure 3.40). Applying 150 bar of hydrogen to the most "pure" regarding hydrogen release, $Cs[Al(BH_4)_4]$, we did not succeed in any hydrogen uptake.

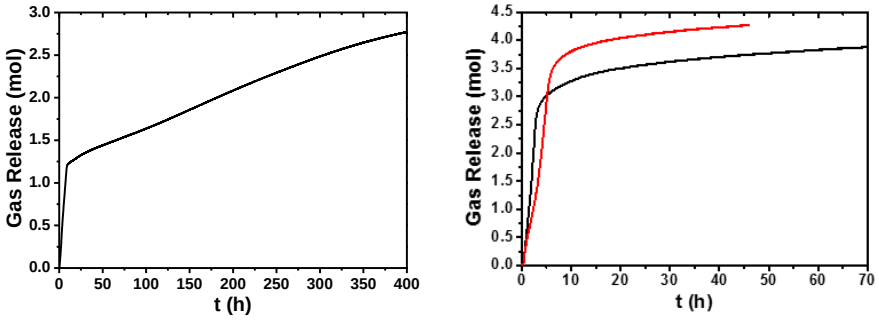

Figure 3.40 – Volumetric desorption curve for $NH_4[Al(BH_4)_4]$ (left), and $Rb[Al(BH_4)_4]$ (black) and $Cs[Al(BH_4)_4]$ (red) (right).

4.6. NMR Spectroscopy Studies of $NH_4[Al(BH_4)_4]$

To shed light on the decomposition process of $NH_4[Al(BH_4)_4]$, ^{11}B, $^{11}B\{^1H\}$, ^{27}Al, $^{27}Al\{^1H\}$ and ^1H NMR spectroscopy experiments were performed in toluene-d_8. The ^{11}B spectrum of the freshly dissolved sample contained three peaks, shown as two overlapped quintuplets, centered at –36.2 and –34.4 ppm, and a triplet of triplets at 17.6 ppm (Figure 3.41). The low-field signal, with coupling constants $^2J_{B,H(bridging)}$ = 135 Hz and $^2J_{B,H(terminal)}$ = 47 Hz, corresponds to diborane, while the high-filed signals, with characteristic coupling constants $^2J_{B,H}$ = 89 Hz, correspond to the BH_4^- anions of $Al(BH_4)_3$ and $Al(BH_4)_3$·NHBH (will be discussed in Chapter IV, 4.6), respectively. The formation of the latter two complexes is also reflected in the ^{27}Al NMR spectrum, which exhibits a broad singlet peak at 99.0 ppm for $Al(BH_4)_3$ and a characteristic doublet of septets, degenerated to a nonuplet, centered at 63.0 ppm (Figure 3.41). However, the $^{11}B\{^1H\}$ spectrum of the same sample allowed to observe an additional singlet peak at -35.0 ppm, accompanied with a peak at 77.8 ppm in the $^{27}Al\{^1H\}$ NMR spectrum and a low intense peak, significantly overlapped with the peaks from diborane protons, at 3.97 ppm in the ^1H NMR spectrum (Figure 3.42). The peak in the ^{27}Al NMR spectrum was shown as a broad septuplet, testifying to coupling from hydrogens.

The ^{11}B and ^{27}Al NMR spectra of the same sample recorded 2 days later each reveal an increase of the corresponding signals for $Al(BH_4)_3$·NHBH and diborane (Figure 3.41). Furthermore, the peak at 3.97 ppm in the ^1H NMR spectrum is significantly increased and is now shown as a broad quintuplet with the coupling constant assigned to

$^{2}J_{HAlH}$ = 6.1 Hz (Figure 3.42). The latter quintuplet, together with the corresponding peaks at –35.0 and 77.8 ppm in the ^{11}B and ^{27}Al NMR spectra, respectively, were tentatively assigned to the formation of [HAl(BH$_4$)$_2$].

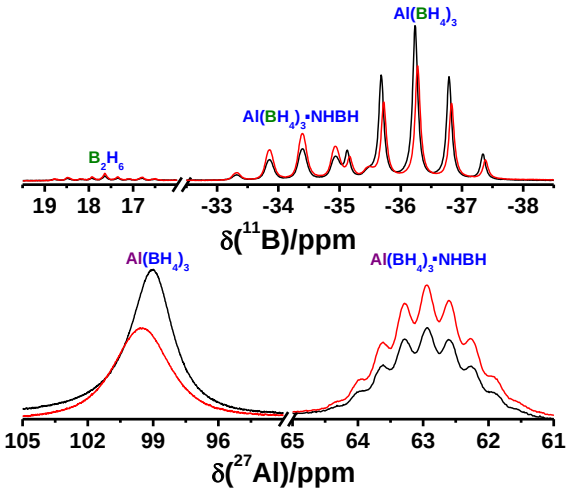

Figure 3.41 – ^{11}B (top) and ^{27}Al (bottom) NMR spectra of the freshly dissolved (black) and after 2 days (red) of NH$_4$[Al(BH$_4$)$_4$] in toluene-d_8 at room temperature.

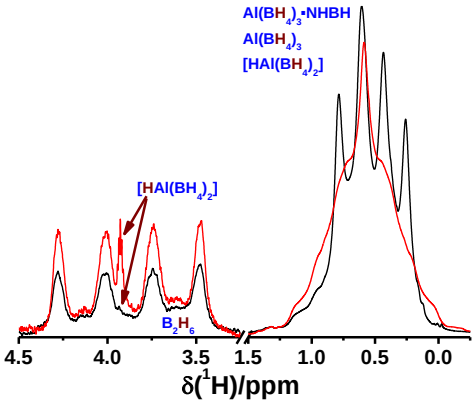

Figure 3.42 – ^{1}H NMR spectra of the freshly dissolved (black) and after 2 days (red) of NH$_4$[Al(BH$_4$)$_4$] in toluene-d_8 at room temperature.

The $^{11}B\{^1H\}$ and $^{27}Al\{^1H\}$ NMR spectra of the same sample recorded after 10 days revealed complete disappearance of $Al(BH_4)_3$. However, new peaks at 69.9 and 75.2 ppm appeared in the ^{27}Al NMR spectrum accompanied with two new peaks at –34.9 and –34.8 ppm in the corresponding $^{11}B\{^1H\}$ NMR spectrum. These peaks can be assigned to the oligo- and/or polymeric structures $[HAl(BH_4)_2]_n$, formed due to the polymerization of $[HAl(BH_4)_2]$ through the bridging μ-H atoms. The $^{11}B\{^1H\}$ NMR spectrum additionally contained peaks at –41.4 and –15.6 ppm, corresponding to the diammoniate of diborane, $[H_2B(NH_3)_2]BH_4$.[229] Furthermore, the $^{11}B\{^1H\}$ NMR spectrum also exhibited peaks at –20.6 ppm, assigned to NH_3BH_3, and at –26.1 and −13.0 ppm, both corresponding to ammonia diborane, $NH_3BH_2(\mu\text{-}H)BH_3$.[229] The BH_3 group, with the bridging μ-H-proton, of the latter compound was found as a triplet of doublets ($^1J_{BH(terminal)}$ = 130 Hz, $^1J_{BH(bridging)}$ = 33 Hz) in the ^{11}B NMR spectrum.

4.7. The Relative Stability of Mixed-Cation M[Al(BH4)4] (M = Li+, Na+, K+, NH4+, Rb+, Cs+) from DFT Calculations and Crystal Structure Considerations

The first attempt to explain the stability of the Al-based series of borohydrides was based on the first Pauling's rule:[230] *For typical ionic solids, the cations are smaller than the anions, and each cation is surrounded by coordinated anions which form a polyhedron. The sum of the ionic radii determines the cation-anion distance, while the cation-anion radius ratio (r_C/r_A) determines the coordination number of the cation, as well as the shape of the coordinated polyhedron of anions.*

The corresponding r_C/r_A ratios, coordination numbers and thermal stability of (M = Li^+, Na^+, K^+, NH_4^+, Rb^+, Cs^+) are shown in Figure 3.43. The comparison of the thermochemical radii (e.g. NH_4^+ and BH_4^-)[231] gives similar r_C/r_A ratios. The Li^+ cation in $Li[Al(BH_4)_4]$ adopts a tetrahedral coordination environment by the BH_4^- groups, matching the stability window defined by the r_C/r_A ratio (Figure 3.43). Nevertheless, this compound exhibits relatively low thermal stability. The Na^+ cation in $Na[Al(BH_4)_4]$ has an octahedral environment by the BH_4^- groups, as expected for the given r_C/r_A ratio (Figure 3.43), and is more stable than its Li-based analogue. The K^+-, Rb^+- and Cs^+-containing derivatives have similar and relatively high stability (Figure 3.43). Their coordination numbers range from 4 + 4 to 4 + 8, being higher than the typical value of 6 in this r_C/r_A window. The $[(BH_4)Li_4]^{3+}$ is significantly larger than the other cations and falls into the stability region of the icosahedral coordination, considering the much larger $[Al(BH_4)_4]^-$ anion. Indeed, this cation has the expected icosahedral coordination by the complex anions (Figure 3.22), but the stability of $[(BH_4)Li_4][Al(BH_4)_4]_3$ is much lower than for M = K^+, Rb^+ and Cs^+ (Figure 3.43). The radius of the $[Al(BH_4)_4]^-$ anion was found, based on the crystal structure data of the described borohydrides, to be equal to ~3 Å. $NH_4[Al(BH_4)_4]$ is in a special position, as it has the same structure and the r_C/r_A ratio as for M = K^+, Rb^+, but it is much less stable, likely due to the formation of the $(N)H^{\delta+}\cdots^{\delta-}H(B)$ dihydrogen bonds (Figure. 3.25), which easily recombine into H_2.

We can thus conclude that the observed coordination numbers do not fully match the stability regions deduced from the geometrical principles of the first Pauling's rule. Moreover, the observed

mismatches do not explain the variation of the decomposition temperatures. The approximation of complex $[BH_4]^-$ and $[NH_4]^+$ and $[Al(BH_4)_4]^-$ as ideal spheres, which is used by Pauling's rule, is rough for the shown series. Therefore, in the second attempt to address the structure-property relation, we had to take into account the electronic factors.

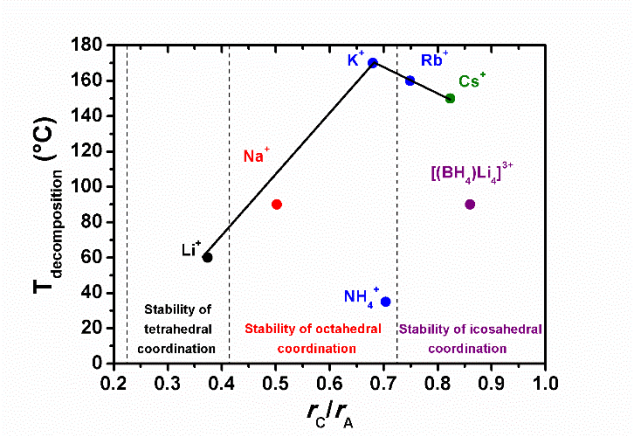

Figure 3.43 – Thermal stability of $M[Al(BH_4)_4]$ ($M = Li^+$, Na^+, K^+, NH_4^+, Rb^+, Cs^+) and of $[(BH_4)Li_4][Al(BH_4)_4]_3$ as a function of the cation-anion ratio. The dashed lines define the stability regions of the coordination polyhedra according to the first Pauling's rule. The observed coordination environments (colored circles: black – tetrahedral, red – octahedral, blue – 4+4, olive – 4+8, purple – icosahedral, the latter is based on the size ratio for the complex cation and the complex anion) do not fully match the stability regions. The observed mismatch does not explain the variation of the decomposition temperatures.

The relation between the formation enthalpy of metal borohydrides (Figure 3.44) and the Pauling electronegativity, pointed out by Nakamori et al.,[183] has driven the idea of mixed cation borohydrides synthesis in order to tune the decomposition temperature. This semi-empirical rule holds well for alkali metals, however deviation

is observed for compounds containing transition metals or metals with a higher valency. Recently, it was shown that the ionic potential ($\varphi = Z^*/r$, *r is the ionic radius of cation*) provides a simple measure of the stability of mixed-cation borohydrides[219] as long as the Born effective charges are taken as the charge of cations. The Born effective charges measure polarization induced by the displacement of ions thus they are sensitive to the nature of interatomic bonding within the crystal and the site symmetry of the ions. The decomposition temperatures of the new compounds reported in this work are depicted in red, and those for the common metal borohydrides are in black (Figure 3.44). The data follow the linear dependence of the decomposition temperature versus the square root of the ionic potential; moreover all $Al(BH_4)_3$-based mixed-cation borohydrides are located in the region of $\varphi^{0.5}$ larger than 2.

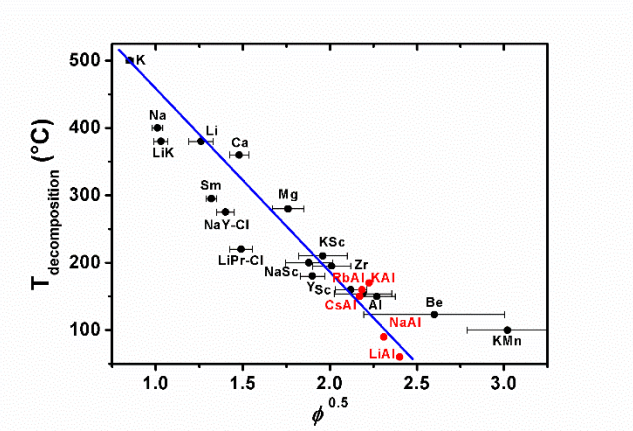

Figure 3.44 – The experimental decomposition temperatures of metal borohydrides as a function of ionic potential obtained using dynamical charges on cations. The results of the present work are shown as red circles, while the data shown in black circles were taken from Ref. [219]

A strong positive correletaion for the numerical values for $\varphi^{0.5}$, presented by Cartledge[232], versus the corresponding Pauling electronegativities for the main-block elements is well known. The series of $M[Al(BH_4)_4]$ ($M = Li^+, Na^+, K^+, Rb^+, Cs^+$) are also in line with this tendency. The calculations for $NH_4[Al(BH_4)_4]$ did not succeed due to the calculated phonons with negative frequencies. However, it seems that the correlation is violated in this case due to the influence of the dihydrogen $H^{\delta-}\cdots H^{\delta+}$ interactions, not present in other borohydrides.

The Al-based bimetallic compounds combining even stronger polarizing Mg^{2+} or Ca^{2+} cations, would lead to the decomposition at room temperature, and thus are most likely unstable under ambient conditions. Indeed, our attempts to isolate bimetallic borohydrides of the $Mg(BH_4)_2$–$Al(BH_4)_3$ and $Ca(BH_4)_2$–$Al(BH_4)_3$ systems were unsuccessful. Consequently, the title family of Al-based borohydrides is likely complete. With its diversity, and convenient and versatile decomposition properties, the aluminum borohydride chemistry will, hopefully, be put into the mainstream research in hydrogen storage, e.g. for the development of reactive hydride composites with an increased hydrogen content.

5. High Pressure Experiments on Isostructural Mixed-Cation $M[Al(BH_4)_4]$ ($M = K^+, NH_4^+, Rb^+$)

A necessary step towards understanding the stability and rational design of light hydrides is a study of their structural response not only to temperature changes but also to the influence of pressure. There are numerous experimental mappings of polymorphism for the

light hydrides which were determined by X-ray and Neutron diffraction.[*e.g.* 233] These investigations are not a trivial task due to the complexity with experiments and data treatment. Nevertheless, the high pressure determinations of most of the alkali-metal and alkali-earth metal borohydrides were performed to this date. Interestingly, the high pressure behavior of the molecular borohydride $Al(BH_4)_3$,[66] was not determined so far. It was curious to know, if this molecular compound can be transformed to inorganic polymers under high pressure. Our attempts of $Al(BH_4)_3$ high pressure investigations did not show the formation of any crystalline phase up to an applied pressure of 20 GPa. This phenomena may occur due to the polymerization of the starting $Al(BH_4)_3$ liquid.

We turned our attention to the samples of $M[Al(BH_4)_4]$ ($M = K^+$, NH_4^+, Rb^+) with high purity of the starting phases (≥90 wt%), which might be investigated at high pressure. Moreover, there is not a single example of the mixed-cation borohydride system investigated at high pressures to date. The isomorphism of $M[Al(BH_4)_4]$ ($M = K^+$, NH_4^+, Rb^+) can give better chances to understand the sequence of phase transitions under high pressure. Furthermore, the presence of N–$H^{\delta+}\cdots H^{\delta-}$–B dihydrogen bonds in $NH_4[Al(BH_4)_4]$ makes it of a great interest for high pressure determination. The dihydrogen bonds $H^{\delta+}\cdots H^{\delta-}$ are known to have relatively high energy and the directionality. It would be interesting to compare these interactions in mixed-cation borohydride of $NH_4[Al(BH_4)_4]$ and other derived complex hydrides, like NH_3BH_3 and NH_4BH_4.

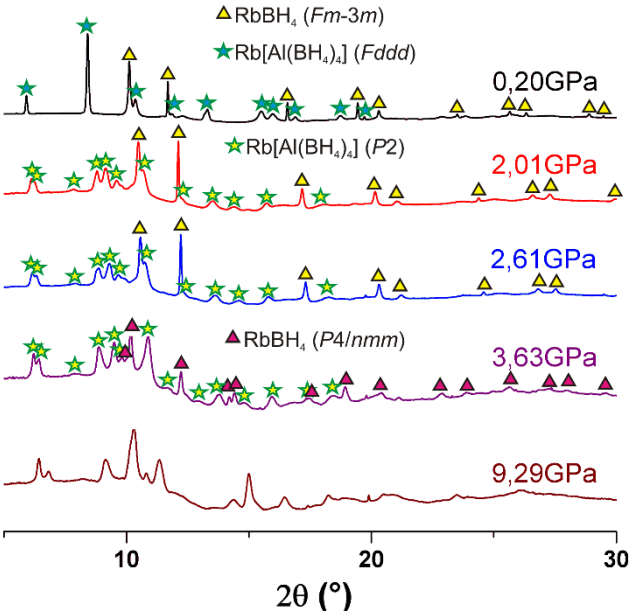

Figure 3.45 – The X-ray powder patterns of the mixture of $Rb[Al(BH_4)_4]$ and $RbBH_4$ as a function of pressure. The phase analysis also demonstrated the known *Fm*-3*m* → *P*4/*nmm* transition of $RbBH_4$ at 3.63 GPa.[234]

According to preliminary results, $K[Al(BH_4)_4]$, $Rb[Al(BH_4)_4]$ and $NH_4[Al(BH_4)_4]$ exhibit phase transitions at 1-2 GPa, see figure 3.45 for the Rb-containing sample. At the moment, we partially treated data for the samples of $Rb[Al(BH_4)_4]$ and $NH_4[Al(BH_4)_4]$. Presumably, they undergo a first order *Fddd* → *P*2 phase transition. The unit cell in the space group of *P*2 (a = 9.12795, b = 6.60655, c = 13.9327 Å; β = 113.50) for $Rb[Al(BH_4)_4]$ at 3.63 GPa was found using FOX.[170] An identical unit cell with similar parameters (a = 9.13796, b = 6.92399, c = 14.29934 Å; β = 113.31°) was observed for $NH_4[Al(BH_4)_4]$ at 1.80 GPa. Remarkably, the sample of $K[Al(BH_4)_4]$ exhibits a different phase transition. However, its crystal structure is not indexed nor solved due to the complexity of the high pressure data.

Despite the fact that these investigations were not a major goal in this work, we are still trying to solve the crystal structures of the $M[Al(BH_4)_4]$ ($M = K^+$, NH_4^+, Rb^+) high pressure polymorphs.

6. Conclusions

In summary, a new family of mixed-cation hydrogen-rich borohydrides $M[Al(BH_4)_4]$ ($M = Li^+$, Na^+, K^+, NH_4^+, Rb^+, Cs^+) was obtained with good to excellent yields by the addition reaction of the corresponding MBH_4 with $Al(BH_4)_3$. Furthermore, the formation of $Li[Al(BH_4)_4]$ was found to be accompanied by the byproduct $Li_4Al_3(BH_4)_{13}$, which becomes a major product at higher temperatures.

The crystal structures of all compounds were elucidated by XRPD and optimized by DFT. It was established that complexes comprise a distorted tetrahedral $[Al(BH_4)_4]^-$ anion.

The experimental decomposition temperatures of metal borohydrides linearly correlate with the ionic potential of metal atoms calculated from dynamical charges on cations, and the $M[Al(BH_4)_4]$ series falls on the least stable and thus the most practical side. The putative bimetallic Mg–Al and Ca–Al borohydrides are most likely unstable under ambient conditions. Consequently, the title family of Al-based borohydrides is likely complete.

The release of $Al(BH_4)_3$ upon thermal decomposition of $M[Al(BH_4)_4]$ ($M = Li^+$, Na^+) can be of interest as the solid-state storage of this highly unstable and explosive compound. Thermal decomposition of the heavier $M[Al(BH_4)_4]$ ($M = K^+$, Rb^+, Cs^+) is accompanied by the release of hydrogen and diborane. Remarkably, the

TGA and volumetric studies of $Cs[Al(BH_4)_4]$ revealed the release of high purity hydrogen at 160 °C. According to the TGA and volumetric studies, the thermal decomposition of $NH_4[Al(BH_4)_4]$ releases a mixture of hydrogen, diborane and ammonia. Contrary to the perovskite-type $NH_4Ca(BH_4)_3$, which decomposes to $Ca(BH_4)_2{\cdot}NH_3BH_3$ by release of one H_2 molecule, the multinuclei NMR experiments have shown the formation of $Al(BH_4)_3$, $Al(BH_4)_3{\cdot}NHBH$, $[HAl(BH_4)_2]$ and diborane upon dissolving of $NH_4[Al(BH_4)_4]$ in toluene-d_8. The NMR data have further revealed a decrease of the $Al(BH_4)_3$ amount with an increase of $Al(BH_4)_3{\cdot}NHBH$, $[HAl(BH_4)_2]$ and diborane quantities over time. It should be noted that the formation of $Al(BH_4)_3{\cdot}NHBH$ has recently been observed upon the thermal decomposition of $Al(BH_4)_3{\cdot}NH_3BH_3$ (which will be discussed in the next Chapter IV).

$M[Al(BH_4)_4]$ can be seen as a convenient store of the highly unstable aluminium borohydride, as well as extremely H-rich substances suitable for the design of new hydrogen storage materials, hopefully, putting alumunium-based borohydrides into the mainstream research.

Chapter IV – Ammonia Borane Complexed with Aluminium Borohydride [2]

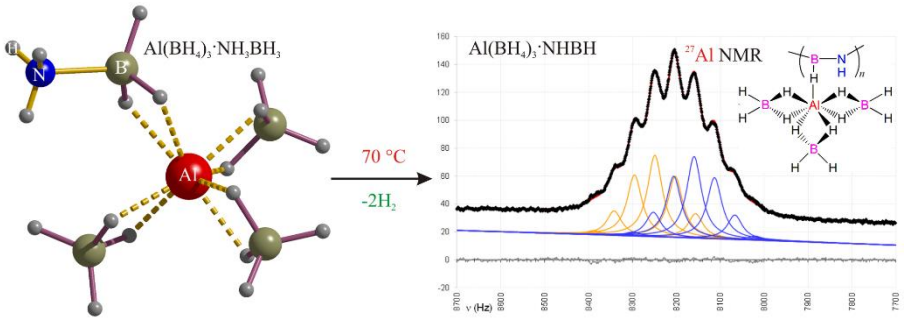

[2] This chapter is based on the following publication:

Dovgaliuk, I.; Le Duff, C.; Robeyns, K.; Devillers, M.; Filinchuk Y. Mild dehydrogenation of ammonia borane complexed with aluminum borohydride, *Chem. Mater.* **2015**, *27*, 768–777.

1. Introduction

In recent years metal borohydrides $M(BH_4)_n$[21,36] and M-B-N-H systems[37,235] of metal amidoboranes (MABs), amine metal borohydrides (AMBs), and complexes with ammonia borane NH_3BH_3 (AB) have been among the most attractive materials for potential solid-state hydrogen storage as they exceed by far the year 2017 system targets of 5.5 wt% of hydrogen and gravimetric density of 40 g/L set by the U.S. Department of Energy.[11] Several metal borohydrides $M(BH_4)_n$ (n = 1, M = Li^+, Na^+;[236,237] n = 2, M = Be^{2+}, Mg^{2+}, Ca^{2+} [181,238,239] and n = 3, M = Al^{3+}, Ti^{3+} [186,240]) have been studied as potential hydrogen storage media. However, the hydrogen desorption temperatures for alkali and most alkaline earth metal borohydrides are far from the range of 60–120 °C useful for hydrogen-fuel cells:[184] indeed, desorption temperatures of about 470°C for $LiBH_4$, and 290–500 °C for $Mg(BH_4)_2$), the instability of $Al(BH_4)_3$ and the toxicity of $Be(BH_4)_2$ make them unpractical. The high stability of borohydrides can be decreased by formation of bimetallic borohydrides. Their stability drops with increasing Pauling electronegativity (χ_p) of the complex-forming cation.[92,183] The most unstable metal borohydride complexes contain highly electronegative Al^{3+}, Zn^{2+}, Cd^{2+} (χ_p = 1.61, 1.65, 1.69, respectively) which create weaker B−H bonds, together with alkali metal cations ($0.79 \leq \chi_p \leq 0.98$). In particular, the series of bimetallic borohydrides of $Al_3Li_4(BH_4)_{13}$, $Na[Al(BH_4)_{4-x}Cl_x]$, $K[Al(BH_4)_4]$ (in the Chapter III),[76,77] $LiZn_2(BH_4)_5$, $NaZn_2(BH_4)_5$, $NaZn(BH_4)_3$ and $KZn(BH_4)_3$[85,86] as well as $KCd(BH_4)_3$, $K_2Cd(BH_4)_4$[91] decompose at rather low temperatures. However, they

evolve toxic diborane B_2H_6 during decomposition, which contaminates fuels cells and decreases the reversibility of these materials.

Another group of materials with competitive hydrogen storage properties are metal borohydride complexes with ammonia and ammonia borane, NH_3BH_3. The presence of $N–H^{\delta+}\cdots H^{\delta-}–B$ dihydrogen bonds in these compounds considerably decreases the dehydrogenation temperatures, to the range of 60–250 °C. Several amine metal borohydrides (AMBs) are considered promising hydrogen storage materials, such as: $LiBH_4{\cdot}NH_3$,[102,103] $M(BH_4)_2{\cdot}2NH_3$ ($M = Mg^{2+}$, Ca^{2+}, Zn^{2+}),[104–106] $Ti(BH_4)_3{\cdot}3NH_3$,[107] $Al(BH_4)_3{\cdot}nNH_3$,[108,109] $LiMg(BH_4)_3{\cdot}2NH_3$,[110,111] $Li_2Ti(BH_4)_5{\cdot}5NH_3$ and $Li_2Al(BH_4)_5{\cdot}6NH_3$.[107,112] AMBs hydrogen decomposition properties are affected both by the nature of the metal cation and the number of coordinated ammonia molecules per cation. It was reported that $LiBH_4{\cdot}NH_3$ and $Ca(BH_4)_2{\cdot}2NH_3$ mainly release ammonia rather than hydrogen under dynamic flow,[104,115] however cobalt-catalyzed thermolysis of $LiBH_4{\cdot}NH_3$ releases 17.8 wt% of H_2.[116] The other representatives $Mg(BH_4)_2{\cdot}2NH_3$, $Al(BH_4)_3{\cdot}6NH_3$ produce only traces of ammonia,[104,109] while $Zn(BH_4)_2{\cdot}2NH_3$, $Ti(BH_4)_3{\cdot}3NH_3$ as well as $Al(BH_4)_3{\cdot}4NH_3$–$LiBH_4$ composite, bimetallic $LiMg(BH_4)_3{\cdot}2NH_3$, $Li_2Ti(BH_4)_5{\cdot}5NH_3$ and $Li_2Al(BH_4)_5{\cdot}6NH_3$ release high purity hydrogen.[104,107,108] The detailed electronic structure of $M(BH_4)_2{\cdot}2NH_3$ ($M = Mg^{2+}$, Ca^{2+}, Zn^{2+}) reveals the highly ionic character of Ca^{2+} in $Ca(BH_4)_2{\cdot}2NH_3$ and partial covalence of Mg–NH_3 and Zn–NH_3 bonds which prevent the release of NH_3 from the latter complexes.[114]

Despite high hydrogen content in ammonia borane (about 19.6 wt%) and acceptable stability upon transportation and storage,

NH_3BH_3 undergoes stepwise decomposition with 6.5 wt% hydrogen released below 112°C and 14.5 wt% near 200 °C, all accompanied by undesirable borazine and aminoborane NH_2BH_2.[117,118] A considerable improvement is achieved by forming metal salts of ammonia borane. This improves the decomposition temperature to ~90 °C for (Li, Na)NH_2BH_3,[120] giving way to a large family of materials. Ammonia borane metal-containing derivatives (MABs) $M(NH_2BH_3)_n$ (n = 1, M = Li^+, Na^+; n = 2, M = Ca^{2+}, Mg^{2+}),[120–123] including bimetallic $Na[Li(NH_2BH_3)_2]$, $Na_2[Mg(NH_2BH_3)_4]$ and mixed-anion $Li_2(NH_2BH_3)(BH_4)$/$LiNH_2BH_3$ systems were obtained in recent years.[124–126] All listed MABs release hydrogen as well as toxic ammonia and NH_2BH_2 traces. For the mixed MAB-AB complex $LiNH_2BH_3{\cdot}NH_3BH_3$, the hydrogen release was reported up to 14.0 wt% in a stepwise manner at 80 and 140 °C and neither borazine nor aminoborane were detected.[127] Metal borohydride-ammonia borane complexes $M(BH_4)_n(NH_3BH_3)_m$ (n = 1, m = 1 or 2 for M = Li^+; n = m = 2 for M = Ca^{2+}, Mg^{2+}) showed more facile hydrogen desorption with less ammonia evolution compared to pure ammonia borane and MABs.[128–131] Further improvements in the properties of these complexes were achieved by combining some AMBs with ammonia borane, such as $Li_2Al(BH_4)_5(NH_3BH_3)_3{\cdot}6NH_3$ and $Mg(BH_4)_2{\cdot}2NH_3$–NH_3BH_3, where high purity hydrogen was released.[130,132]

Compounds in Al−B−N−H systems are among the best in terms of hydrogen storage properties. However, the number of components involved in the mentioned systems goes increasingly high, leaving little (if any) chance for their reversibility. Here we report a new $Al(BH_4)_3{\cdot}NH_3BH_3$ complex with 17.7 wt% of hydrogen, combining

only two hydrogen rich-molecules: $Al(BH_4)_3$ and NH_3BH_3. Remarkably, the complexation transforms aluminium borohydride into a stable solid, which undergoes a two-step thermal decomposition at temperatures below 100 °C. We report on the synthesis, crystal structures, Raman spectroscopic studies of the complex, as well as thermal analysis, ^{11}B, ^{27}Al NMR spectroscopy and volumetric studies of its decomposition and reversibility.

2. Synthesis of $Al(BH_4)_3 \cdot NH_3BH_3$

Caution! $Al(BH_4)_3$ is a highly pyrophoric liquid which explodes on contact with air. All manipulations were carried out in a nitrogen-filled dry box. The reactions were performed using commercially available reagents: $AlCl_3$, NH_3BH_3 (both, from Sigma Aldrich with ≥95% purity) and $LiBH_4$ (≥96% purity, Boss chemical industry CO, China). The $Al(BH_4)_3 \cdot NH_3BH_3$ complex was obtained by a two-step synthesis. The first step involves formation of $Al(BH_4)_3$ by a metathesis reaction:

$$AlCl_3 + 3LiBH_4 \rightarrow Al(BH_4)_3 + 3LiCl \qquad (4.1)$$

We used the same procedure described in details in Chapter III, which is a modification of an earlier one.[191] The final product is obtained by the following addition reaction:

$$Al(BH_4)_3 + NH_3BH_3 \rightarrow Al(BH_4)_3 \cdot NH_3BH_3 \qquad (4.2)$$

For that purpose 1 ml of freshly obtained liquid $Al(BH_4)_3$ is syringe-injected into a bottle with 70 mg of NH_3BH_3 powder. The bottle is kept sealed during 72 hours until formation of big white crystals (Figure 4.1). Ball milling is expected to dramatically speed up the

reaction on a large scale, however this method is difficult to apply for safety reasons. The excess of liquid $Al(BH_4)_3$ was pumped off during 30 seconds. One should avoid extended vacuum pumping of the excess $Al(BH_4)_3$, as it decreases the yield of the product. The obtained crystals self-ignite in contact with moisture and air.

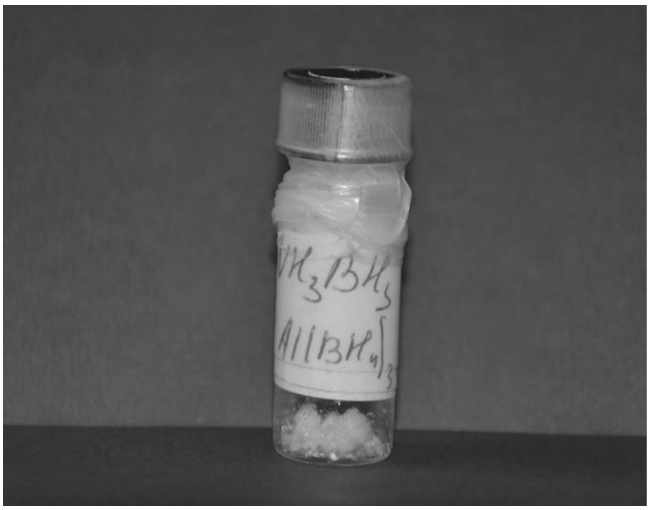

Figure 4.1 – White crystals of $Al(BH_4)_3 \cdot NH_3BH_3$.

3. Experimental Details

The detailed characterization of the complex is presented below. Firstly it is aimed for an identification of its different crystal forms, co-existing at ambient conditions, secondly for the understanding of its complex dehydrogenation and thirdly for determining the nature of the Al-based intermediate species in the dehydrogenation process.

X-ray single crystal analysis. The complex reveals two polymorphs. The crystals of α-$Al(BH_4)_3 \cdot NH_3BH_3$ were selected in the argon filled glove box and then measured at 100 K under nitrogen flow (Oxford cryosystems). For better completeness two crystals were

measured independently using a PILATUS 2M pixel detector and λ = 0.82103 Å synchrotron X-ray radiation at the SNBL beamline, ESRF (Grenoble, France). The recorded data was indexed in the monoclinic space group $P2_1/c$ with a = 7.8585(2), b = 6.8647(1), c = 15.7136(8) Å, β = 96.429(4)° and integrated by CrysAlisPro,[241] the implemented absorption correction was applied**.** The data from the two crystals were integrated separately, scaled (not merged) in XPREP (Bruker) prior to structure solution and refinement.

Data for β-$Al(BH_4)_3 \cdot NH_3BH_3$ were collected on a MAR345 image plate detector (Mo Kα radiation, Zr filter). The crystals of β-$Al(BH_4)_3 \cdot NH_3BH_3$ were loaded into inert grease in an argon-filled glove box and then measured at 295 K under nitrogen flow (Oxford cryosystems). The recorded data was indexed in a monoclinic cell and integrated with CrysAlisPro, and the implemented absorption correction was applied.[241] The structure was solved in the space group Cc with a = 10.8196(8), b = 7.2809(4), c = 11.3260(9) Å, β = 107.69(1)°, with a pseudo-inversion symmetry for 83% of the structure, as determined by ADDSYM in Platon program.

All single crystal data were solved by direct methods and refined by full matrix least-squares on F^2 using SHELXL2014.[164]

X-ray powder diffraction. For variable-temperature *in situ* X-ray powder diffraction the crystals of α- and β-$Al(BH_4)_3 \cdot NH_3BH_3$ were ground in an agate mortar inside the argon-filled glove box and the powder was introduced into 0.7 mm glass capillaries which were sealed with vacuum grease. The capillaries were steadily heated from 20 to 100 °C by a nitrogen blower (Oxford Cryosystems) with 1 and 0.2 °C/min heating rates. The 2D data images obtained at SNBL were

azimuthally integrated by the program Fit2D using LaB_6 as calibrant.[179] The Rietveld method was used for the phase analysis and refinement with Fullprof Suite software.[169]

NMR spectroscopy. NMR spectra were acquired in toluene-d_8 on a Bruker Avance DRX500 spectrometer operating at 500.1 MHz for ^{1}H (160.5 MHz for ^{11}B and 130.3 MHz, for ^{27}Al). Chemical shifts are reported with reference to $SiMe_4$ (TMS) for ^{1}H, $BF_3{\cdot}OEt_2$ for ^{11}B and 1.1M of $Al(NO_3)_3$ in D_2O for ^{27}Al. Spectra were measured on solutions of α-$Al(BH_4)_3{\cdot}NH_3BH_3$ crystals, as well as on the starting products $Al(BH_4)_3$ and NH_3BH_3 dissolved in toluene-d_8 for reference. After dissolving the crystals of α-$Al(BH_4)_3{\cdot}NH_3BH_3$, the evolution of spectra with time was measured: fresh, after 2 and after 18 hours. Other samples studied by NMR were aged at room temperature for 2 months; heated under argon up to 70 °C and up to 100–110 °C in the sealed glass bottles using a mineral oil bath during 40 and 60 minutes, respectively. The residues were dissolved in toluene-d_8 and measured at room temperature.

The deconvolution processing for ^{27}Al NMR spectra has been kindly performed by Prof. Michel Luhmer (ULB), including one level of zero-filling, exponential multiplication of the free induction decay with a line broadening (lb) factor of 1 Hz, Fourier transform and zero-order phase correction; no correction of the initial decay, no first-order phase correction and no baseline correction were applied. The region between 8700 Hz (66.76 ppm) and 7700 Hz (59.09 ppm) was submitted to deconvolution analyses using a home-made program developed in Excel. The ^{27}Al NMR signal was described as a first-order multiplet, constraining intensity ratios according to the Pascal's triangle and

imposing Lorenztian lineshape and identical linewidth for all of the components. The local baseline was accounted for by a second order polynomial (three adjustable parameters).

NMR data of the compounds recognized in the presented spectra. (B_2H_6) ^{1}H NMR, δ: 3.89 (q, $^{1}J_{B,H}$ = 132 Hz, terminal hydrogens), −0.8 ($^{1}J_{B,H}$ = 44 Hz, bridging hydrogens). ^{11}B NMR, δ: 17.6−17.8 (tt, $^{1}J_{B,H}$ = 132). ^{11}B {^{1}H} NMR, δ: 17.6 (s). (Presumably **$Al(BH_4)_3 \cdot NH_3BH_3$**) ^{11}B NMR, δ: −21.8 (quadruplet, $^{1}J_{B,H}$ = 92 Hz, BH_3), −33.8 (quint, $^{1}J_{B,H}$ = 88 Hz, BH_4^-).^{11}B {^{1}H} NMR, δ: −21.9 (s, BH_3), −34.1 (s, BH_4^-). ^{27}Al NMR, δ: 60.3 (s, broad). ^{27}Al {^{1}H} NMR, δ: 60.3 (s). (Decomposition product, presumably **$Al(BH_4)_3 \cdot NHBH$** or its oligomer) ^{11}B NMR, δ: −34.4 (quint, $^{1}J_{B,H}$ = 86 Hz, BH_4^-).^{11}B {^{1}H} NMR, δ: −34.4 (s, BH_4^-). ^{27}Al NMR, δ: 63.0 [nonuplet (doublet of heptuplets], $J_{doublet}$ = 89.4 and $J_{heptuplet}$ = 46.4 Hz, BH_4^- and $^{1}J_{Al,H}$). ^{27}Al {^{1}H} NMR, δ: 63.0 (s).

Raman spectroscopy. Raman spectra with 1064 nm excitation were recorded from 4000 to 100 cm^{-1} with a Bruker RFS 100/s FT-Raman spectrometer (I = 200 mW) at room temperature using a diode-pumped, air-cooled Nd: YAG laser as the excitation. The powder sample was placed in a 0.7 mm glass capillary under argon and sealed with vacuum grease. Variable-temperature Raman spectroscopy was performed using the same spectrometer and temperature control chamber under an argon flow. The spectra were collected in a stepwise manner every 5 °C from 30 to 125 °C.

TGA, DSC and MS analyses. TGA and DSC analyses were performed on powder samples after preliminary X-ray powder diffraction analysis. The data were collected with a TGA/SDTA 851

Mettler and a DSC 821 Mettler devices with heating rates of 1 and 5 °C/min from 25 to 200 °C. The samples for the TGA and DSC analyses were loaded in the argon-filled glove box into crucibles with caps and sealed into aluminium pans, respectively. The experiments were done under 10 ml/min nitrogen flow to prevent hydrolysis or oxidation.

Mass spectrometry (MS) analysis of the residual gas was performed using a Hiden Analytical HPR-20 QMS sampling system. The samples (approximately 2 mg) were loaded into an Al_2O_3 crucible and heated from RT to 70 °C, fixing this temperature during 2 hours (1 °C/min for both) in an argon flow of 20 mL/min. The decomposition up to 200 °C was measured by a ThermoStar^{TM} GSD 301T spectrometer coupled with simultaneous TGA/DTA 851 Mettler. The released gases were analyzed for hydrogen, ammonia, diborane, and borazine in both experiments.

Volumetric study. Volumetric analysis was performed using a Hiden Isochema IMI-SHP analyzer. Four decomposition experiments of the $Al(BH_4)_3 \cdot NH_3BH_3$ complex were made with 50–60 mg of sample, into 5 bar back-pressure of hydrogen/helium, from 30 to 70 °C and from 30 to 100 °C at 1 °C/min heating rate. The gas release was calculated from the calibrated volumes of the system, excluding the volume of the glass wool (2.06 g/cm^3). The re-hydrogenation of the samples decomposed at 70 and 100 °C was made at ~150 bar of hydrogen, by heating them to 70 and 100 °C and cooling down to 30 °C at 0.1 °C/min rate.

4. Results and Discussion

4.1. Crystal Structure of $Al(BH_4)_3 \cdot NH_3BH_3$

We have characterized two polymorphs of $Al(BH_4)_3 \cdot NH_3BH_3$: the low-temperature *α*- and the high-temperature *ß*-phase. The *α*-$Al(BH_4)_3 \cdot NH_3BH_3$ is observed only in freshly synthesized samples, while it slowly transforms at room temperature into the *ß*-phase. The structural details are given in the supporting information (Tables S2.1−2.5 in the supporting information). In both structures, aluminium atoms coordinate three BH_4^- anions and one NH_3BH_3 molecule, forming a mononuclear $Al(BH_4)_3 \cdot NH_3BH_3$ heteroleptic complex, like the one shown in Figure 4.2.

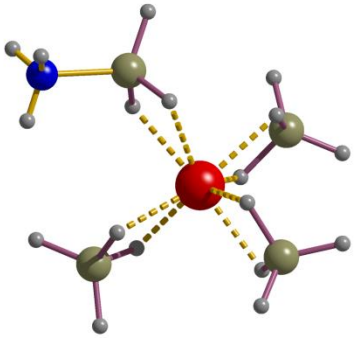

Figure 4.2 – The isolated $Al(BH_4)_3 \cdot NH_3BH_3$ complex, where Al^{3+} cation coordinates three BH_4^- anions and one NH_3BH_3 molecule.

Weak dihydrogen bonds between BH_4^- and $–NH_3$ groups associate the complexes into a 3D structure. $N–H^{\delta+}\cdots H^{\delta-}–B$ bonds are often bifurcated on the N–H side, thus the H···H distances are rather long, exceeding 2.6 Å while $N–H^{\delta+}\cdots H^{\delta-}$ angles are not very close to 180° (see Figure 4.3 and Table 4.1).

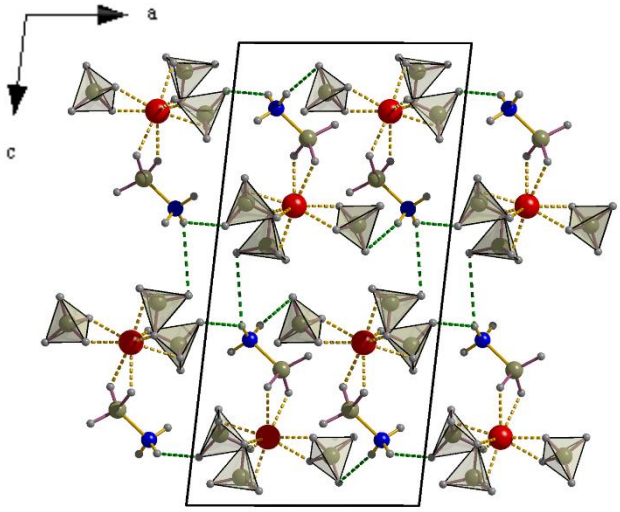

a)

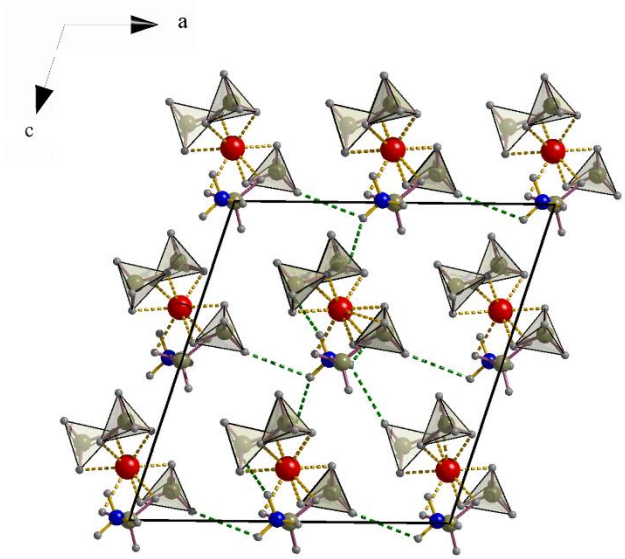

b)

Figure 4.3 – Association of molecular $Al(BH_4)_3 \cdot NH_3BH_3$ complexes by dihydrogen bonds in a) the α-phase; b) the β-phase.

Table 4.1. Interatomic distances and angles between hydrogen atoms in *α,β*-$Al(BH_4)_3{\cdot}NH_3BH_3$

H···H bond	H···H distance, (Å)	N···H···H angle, (°)
	α-$Al(BH_4)_3{\cdot}NH_3BH_3$	
H3C···H4C	2.27(1)	146.1(6)
H3C···H6C	2.53(1)	135.8(6)
H3A···H6C	2.59(1)	102.5(5)
H3B···H6D	2.56(2)	113.1(5)
H3B···H5C	2.28(1)	168.5(6)
H3B···H5B	2.48(1)	125.8(4)
H3B···H5D	2.60(2)	128.3(5)
	β-$Al(BH_4)_3{\cdot}NH_3BH_3$	
H3C···H5C	2.33(7)	129.7
H3C···H6C	2.47(5)	136.8
H3A···H6D	2.46(6)	142.0
H3B···H5D	2.45(5)	111.9
H3B···H4C	2.23(8)	143.8

The Al^{3+} cation is linked via BH_2 edges to three BH_4^- anions and to one ammonia borane molecule. With respect to B-atoms, Al adopts a distorted tetrahedral coordination, and the AlH_8 polyhedron has a shape of a snub disphenoid, as Mg in $Mg(BH_4)_2$ structures.[58,60] This contrasts with planar trigonal AlB_3/trigonal prismatic AlH_6 coordination in both known polymorphs of $Al(BH_4)_3$.[66,212] The Al···B distances with BH_4^- ions are in the narrow range of 2.21–2.23 Å and are slightly longer than 2.10–2.15 Å as determined by gas electron diffraction and in the solid *α,β*-$Al(BH_4)_3$.[66,212] It is nearly identical to the 2.22–2.26 Å Al···B distances in $M[Al(BH_4)_4]$ and $[Ph_3MeP][Al(BH_4)_4]$ where the Al^{3+} cation is also coordinated to 8 hydrogen atoms.[189] The interatomic Al···B distances involving ammonia borane's BH_3 group are slightly longer (2.31 Å), than the distances to the BH_4^- anions. They are still much shorter than metal-

boron distances in other borohydride-NH_3BH_3 complexes, namely 2.63–2.92 Å in $(LiBH_4)_2 \cdot NH_3BH_3$, $LiBH_4 \cdot NH_3BH_3$ and $Ca(BH_4)_2 \cdot 2NH_3BH_3$.[128,129] The Al–H bond distances vary accordingly: they range from 1.65(8) to 1.81(1) Å where BH_4^- is involved, similar to those in Al-based complex hydrides,[189] to 1.86(1)–1.96(8) Å where the BH_3 group is involved. The latter are much shorter than the 2.44 and 2.50 Å M–H bond distances in $Ca(BH_4)_2 \cdot (NH_3BH_3)_2$ and the 2.08-2.32 Å distances in $(LiBH_4)_2 \cdot NH_3BH_3$.

4.2. Relative Stability of $Al(BH_4)_3 \cdot NH_3BH_3$ polymorphs

The phase analysis by X-ray powder diffraction was performed prior to further characterization of the complex by other techniques. Both α- and β-$Al(BH_4)_3 \cdot NH_3BH_3$ can be obtained as single phases using the synthesis procedures described above. Figure 4.4 shows the Rietveld refinement profiles for single phase samples of α- and β-polymorphs. α-$Al(BH_4)_3 \cdot NH_3BH_3$ was found as a single phase only in freshly prepared samples. Within a few days at room temperature we found a mixture of the two phases. The crystals of the β-phase cooled to 100 K did not turn into the α-phase, thus the α to β transition is irreversible or at least slow.

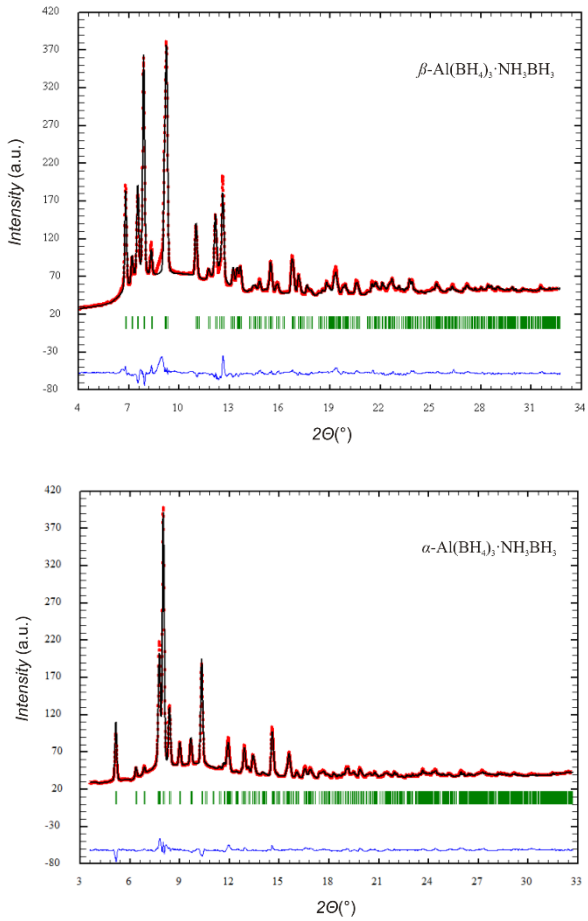

Figure 4.4 – The experimental, calculated and difference diffractograms of α- and β-$Al(BH_4)_3{\cdot}NH_3BH_3$ single phases from X-ray powder diffraction (Mo Kα radiation).

Variable-temperature *in situ* X-ray powder diffraction done on both polymorphs at 1 °C/min heating rate (Figure 4.5) reveals that the α-$Al(BH_4)_3{\cdot}NH_3BH_3$ undergoes a first order phase transition to β-$Al(BH_4)_3{\cdot}NH_3BH_3$ at ~62 °C, the latter is melting and presumably decomposing at ~71 °C. Heating the single phase sample of the β-phase with a 5-fold smaller rate of 0.2 °C/min reveals melting at the lower temperature of 52 °C (see Fig. S2.1 in the supporting information), thus confirming the simultaneous decomposition.

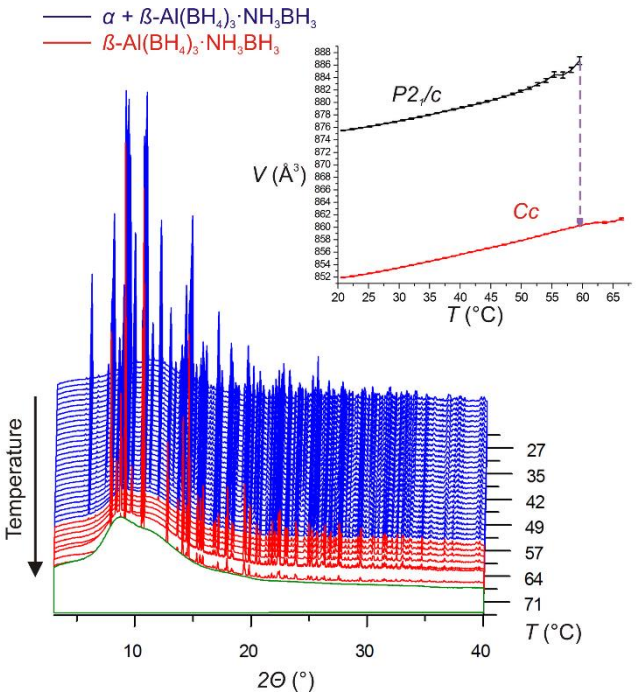

Figure 4.5 – Variable-temperature *in situ* synchrotron X-ray powder diffraction of *α*- and *ß*-$Al(BH_4)_3{\cdot}NH_3BH_3$ (λ = 0.821693 Å from SNBL). The unit cell volume as a function of temperature is shown in the inset.

4.3. Raman Spectroscopy

The Raman spectrum of *ß*-$Al(BH_4)_3{\cdot}NH_3BH_3$ is shown in Figure 4.6. Several stretching B–H modes can be recognized in the 2080–2600 cm^{-1} range, similar to the vibrational modes of $[Al(BH_4)_4]^-$ and of $Al(BH_4)_3$, where BH_4^- is coordinated to Al^{3+} in a bidentate manner.[223] Three intense peaks at 2441, 2496 and 2530 cm^{-1} probably belong to the outward B–H (terminal) stretching modes from different BH_4 and BH_3 groups; the peaks from 2040 to 2300 cm^{-1} correspond to inward B–H (bridging with Al) stretching modes. The vibrations between 950–1650 cm^{-1} can be attributed to B–H bending, and the

peaks near 490 cm^{-1} likely correspond to an Al···H–B stretching band, as observed for $[Al(BH_4)_4]^-$ anion and for $Al(BH_4)_3$.[223,242] The N–H stretching region is represented by two intense peaks at 3240 and 3299 cm^{-1} which are slightly shifted to lower frequencies with respect to the symmetric (3250 cm^{-1}) and antisymmetric (3316 cm^{-1}) stretches in NH_3BH_3.[243] Literature reports the B–N vibrations at around 800 cm^{-1} and we can surmise that the vibration at 858 cm^{-1} belongs to the B–N stretch in the coordinated NH_3BH_3.[243]

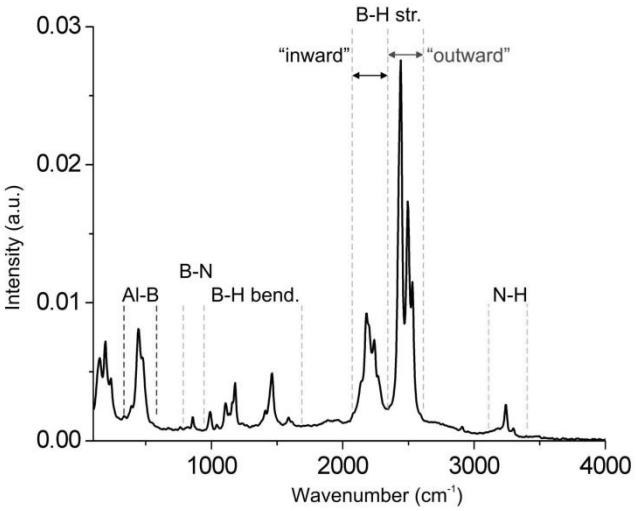

Figure 4.6 – Raman spectrum of *ß*-$Al(BH_4)_3 \cdot NH_3BH_3$.

4.4. Thermal Analysis: Two Decomposition Steps

Several thermal effects are observed on heating the samples from 25 to 200 °C (Figure 4.7a). The first endothermic (~39 kJ/mol) peak near 46–52 °C (DSC) corresponds to the melting/decomposition of *ß*-$Al(BH_4)_3 \cdot NH_3BH_3$. The next endothermic (~65 kJ/mol) peak near 93 °C is assigned to the second decomposition step. TGA also displays

two decomposition steps: the first starts at ~60 °C and finishes at ~80 °C, the second is centered around 90 °C. The bottom part of the Figure 4.7b shows that the higher heating rate increases the decomposition temperature from ~60 °C for 1 °C/min to ~77 °C for 5 °C/min due to the kinetic effect. This behavior is also similar to ammonia borane, which showed different decomposition reaction pathways depending on the heating rate.[117,118]

We performed additional experiments aiming to separate the two decomposition steps, holding samples at the fixed temperature of 70 °C and 80 °C. Remarkably, the mass loss asymptotically reached very different values of 5 and 25 wt%, respectively, see Figure 4.7b. The decomposition step at 70 °C with a ~5 wt% loss looks very interesting, as it suggests that potentially pure hydrogen is released from the sample (see the volumetric studies for more details). The decomposition of the other borohydride–ammonia borane complexes, $M(BH_4)_n(NH_3BH_3)_m$ (n = 1, m = 1, 2 for M = Li^+; n = m = 2 for M = Ca^{2+}, Mg^{2+}), yields significant amounts of ammonia, diborane and borazine, besides hydrogen, on the first decomposition step.[128–131] While these compounds undergo complete decomposition involving both borohydride and ammonia borane moieties, the thermal analysis of the title complex suggests hydrogen release from ammonia borane in the first step, followed by a diborane release (theoretical 27 wt% loss) in the second step. The volumetric and mass spectrometry studies help to verify this hypothesis.

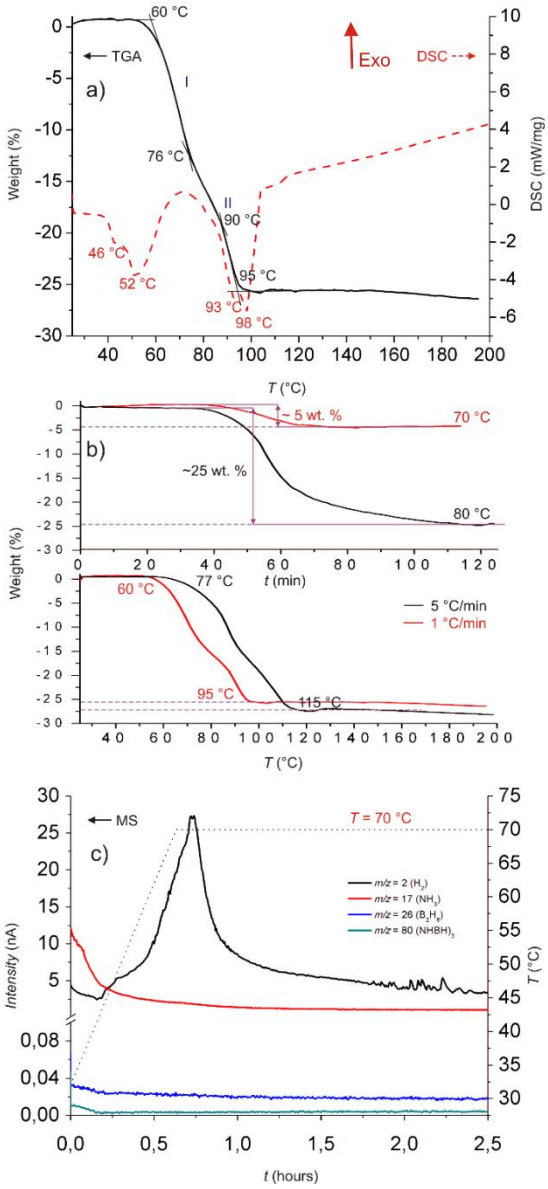

Figure 4.7 – Thermal analysis of $Al(BH_4)_3 \cdot NH_3BH_3$ complex: a) overlap of the TGA and DSC data collected at 1 °C/min rate; b) weight loss as a function of time, at constant temperatures of 70 and 80 °C (top graph), and as a function of the heating rate (bottom); c) MS curves of evolving gases measured in 30–70 °C temperature range. The signals of ammonia, diborane and borazine are close to zero level, which confirms the high purity of hydrogen release at 70 °C.

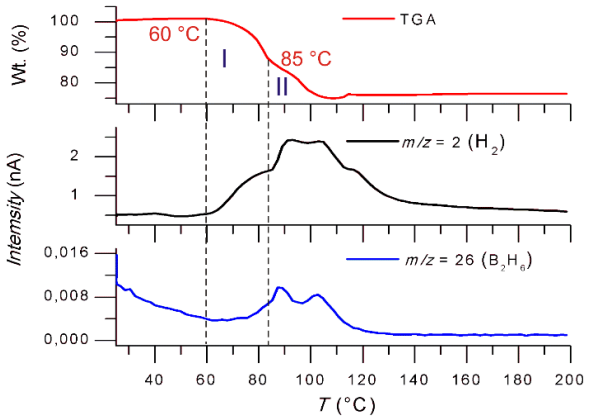

Figure 4.8 – The TGA and MS measurements of $Al(BH_4)_3 \cdot NH_3BH_3$ upon heating to 200 °C (1 °C/min heating). The hydrogen desorption starts around 60 °C, which corresponds to the first decomposition step, and diborane evolution is observed only after the start of the second decomposition step. It is possible that there is also the third step around 105 °C which was not easily visible by TGA, but two maximums in MS suggest its presence.

The MS determination of the released gases was made in the same manner as the TGA: the first decomposition step is characterized isothermally at 70 °C and the complete decomposition at temperatures above 100 °C. Remarkably, desorption at 70 °C showed exclusively the release of hydrogen, while the possible impurities of ammonia, diborane and borazine were not detected, see Figure 4.7c. Further heating provokes release of diborane, which was detected around the start of the second decomposition step at 85 °C, see Figure 4.8. Variable-temperature *in situ* Raman spectroscopy also confirmed decomposition of the complex around 75 °C, see Figure S2.2. Unfortunately, the detailed characterization of the decomposition products of the first and second steps was not possible from Raman

spectra. Visually, the residue of the fully decomposed (at 150 °C) samples resembles foamed polymer-like products.

4.5. Volumetric Study of the Decomposition and a Reversibility Test

Taking into account the information from TGA and DSC analysis, we performed two volumetric measurements at different temperatures: 70 °C, which corresponds to the first decomposition step, and 100 °C, which relates to the second decomposition step.

Samples were steadily heated at 1 °C/min rate, as in the TGA experiment. Decomposition at 70 °C produces ~1.15 mmol of gas from 0.54 mmol of the starting complex (Figure 4.9), i.e. 2.15 mol of gas per formula unit (f. u.). To verify this result, two additional volumetric experiments were done for the first step of the decomposition in He and H_2 backpressure at 70 °C, yielding 1.93 and 2.10 mol of gas per f. u. The second decomposition step at 100 °C shows the release of ~2.81 mmol of gas per f. u. Combined with the TGA data we infer that the first decomposition step gives ~2 moles of hydrogen per $Al(BH_4)_3 \cdot NH_3BH_3$ unit (~5 wt% mass loss), and the second step gives almost 1 mole of diborane (close to ~25 wt% mass loss).

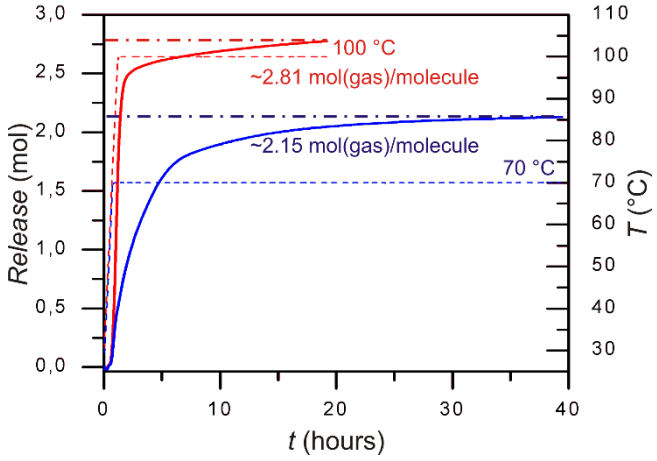

Figure 4.9 – Volumetric analysis of $Al(BH_4)_3 \cdot NH_3BH_3$ decomposition at 70 °C, 0.54 mmol of the complex and at 100 °C, 0.58 mmol of the complex, at 1 °C/min heating rate.

Our attempts to rehydrogenate at 150 bar the samples decomposed at 70 and 100 °C were not successful: the H_2 pressure returns exactly to the same value after very slow cooling (see Figures S2.3).

4.6. NMR Spectroscopy Study of $Al(BH_4)_3 \cdot NH_3BH_3$ and Its Decomposition

Multinuclei ^{1}H, ^{11}B and ^{27}Al NMR spectra were measured on $Al(BH_4)_3$ prior to being used in the synthesis of $Al(BH_4)_3 \cdot NH_3BH_3$ and were found to be in good agreement with the literature.[244] Interpretation of the ^{1}H NMR spectra being difficult due to the presence of very broad signals around 0.5 ppm (Figure S2.4), that is why herein we focused our attention on the interpretation of the ^{11}B and ^{27}Al NMR spectra and all the ^{1}H NMR spectra will be shown in the supporting

information (Figures S2.4–S2.6). The main ^{11}B peak for $Al(BH_4)_3$ is found at –36.3 ppm with negligible amount of diborane, due to slow $Al(BH_4)_3$ degradation, present at 17.8 ppm (not even visible in Figure 4.10b). The main ^{27}Al peak for $Al(BH_4)_3$ is at 99.7 ppm, and an unknown impurity observed at 78.2 ppm (Figures 4.10a and 4.10b). Broad signals in the spectra originate from the solid Al-containing material in the probe, and from the ^{11}B in the borosilicate NMR tubes, as proved by blank measurements, and can be removed by using a backward linear prediction during data processing.

Samples of $Al(BH_4)_3 \cdot NH_3BH_3$ stored in a glovebox at 25–30 °C over two weeks turned into a viscous mass, prompting us to study by NMR spectroscopy the decomposition products obtained at different temperatures. In order to observe the changes of $Al(BH_4)_3 \cdot NH_3BH_3$ we performed experiments on: 1) freshly dissolved sample in toluene-d_8; 2) the same sample in solution kept at room temperature for 2 (Figure S2.7 in supporting information) and 18 hours; 3) samples heated to 70 and 100 °C, as in the volumetric study, and then dissolved in toluene-d_8.

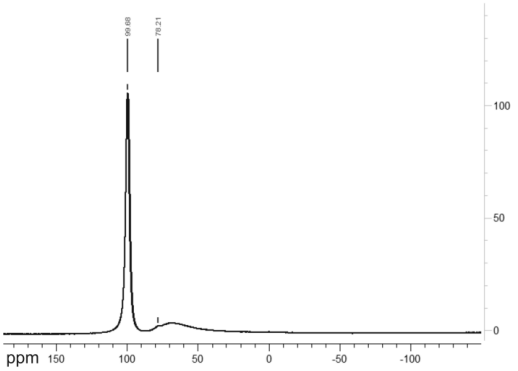

a)

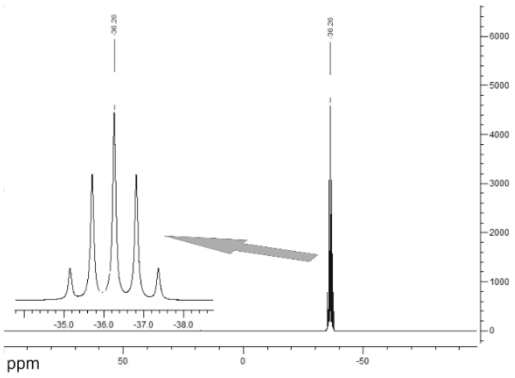

b)

Figure 4.10 – a) ^{27}Al NMR and b) ^{11}B NMR spectra of $Al(BH_4)_3$ in toluene-d_8.

$Al(BH_4)_3{\cdot}NH_3BH_3$ does not decompose into $Al(BH_4)_3$, as no signal at 99.7 ppm in the ^{27}Al NMR spectrum appears, instead, we observe a signal at 60.3 ppm which is not present anymore after 18h. In the ^{11}B NMR spectrum (Figure 4.11b) we observe a sextuplet, consisting of two overlapped quintets at –33.8 and –34.4 ppm, and a quadruplet at −21.9 ppm (Figure 4.11c). The presence of a small amount of diborane B_2H_6 was observed as a triplet of triplets at 17.5 ppm in the ^{11}B NMR spectrum.[245] It is likely the result of partial decomposition of $Al(BH_4)_3{\cdot}NH_3BH_3$ into B_2H_6, for instance *via* the following reaction:

$$n\mathrm{Al(BH_4)_3{\cdot}NH_3BH_3} \rightarrow [\mathrm{Al(BH_4)_2(NH_2)}]_n + n/2\mathrm{H_2} + n/2\mathrm{B_2H_6} \quad (4.3)$$

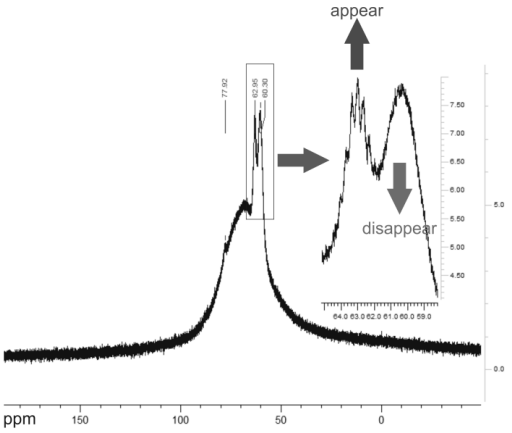

a)

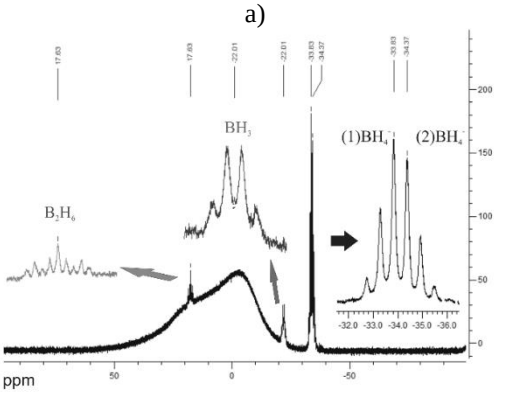

b)

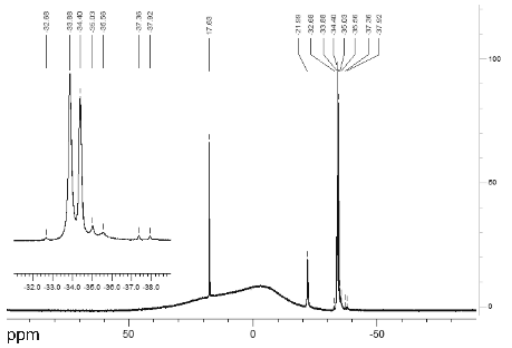

c)

Figure 4.11 – a) ^{27}Al NMR, b) ^{11}B and c) ^{11}B{H} NMR spectra of freshly dissolved $Al(BH_4)_3{\cdot}NH_3BH_3$ in toluene-d_8.

There is no diborane forming up to 70 °C in the absence of the solvent, see the MS data in Figure 4.7. However, the intensity of the diborane peak increases with time in the toluene solution.

In contrast to the broad signal of the starting compound at 60.3 ppm which disappears with time, the intensity of a nonuplet at 63.0 ppm increases in the ^{27}Al NMR spectrum (Figures 4.11a and 4.12a). In the ^{11}B NMR spectrum a quintet at –34.4 ppm, corresponding to the BH_4^- anion, increasingly dominates the spectrum over the disappearing signal at –33.8 ppm present at 2 and 18 hours (Figures 4.11b and 4.12b).

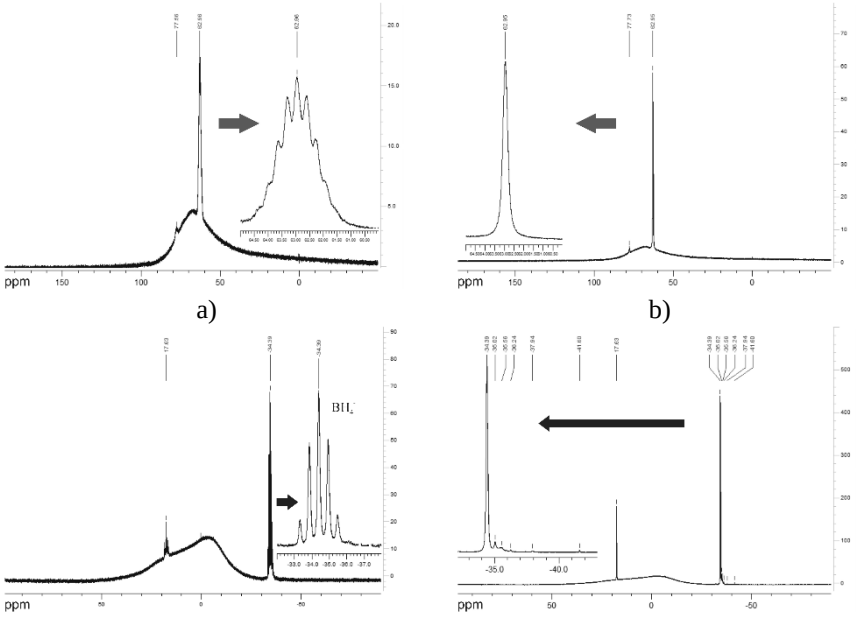

Figure 4.12 – a) ^{27}Al and b) ^{27}Al{H} NMR spectra of $Al(BH_4)_3{\cdot}NH_3BH_3$ in toluene-d_8 after 18 hours; c) ^{11}B and d) ^{11}B{H} NMR spectra of $Al(BH_4)_3{\cdot}NH_3BH_3$ in toluene-d_8 after 18 hours.

In the sample decomposed at ~70 °C, the same main NMR signals, as in the 18h-aged sample spectrum, were observed at 63 and −34.5 ppm in the ^{27}Al and ^{11}B NMR spectra, respectively (compare

Figures 4.12 and 4.13). The intensities of the several other minor signals at 82.0, 77.6 and 74.4 ppm changed in the ^{27}Al spectrum. After 100 °C we observe (Figure 4.14) only a single ^{27}Al NMR signal at 81.9 ppm, which probably has the same nature as the one at 82.0 ppm heated to 70 °C (Fig. 4.13a).

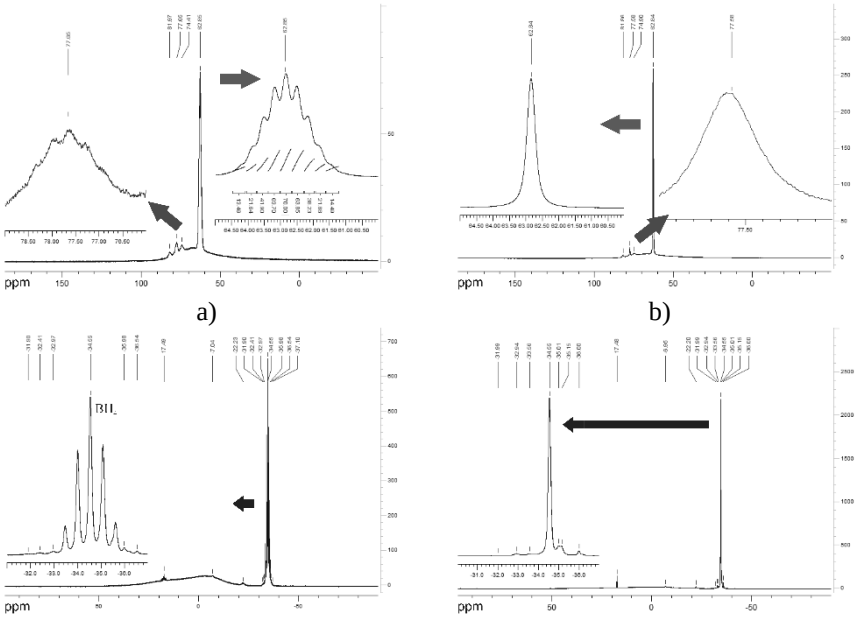

Figure 4.13 – a) ^{27}Al and b) ^{27}Al{H} NMR spectra of $Al(BH_4)_3{\cdot}NH_3BH_3$ in toluene non-deuterated after heating to 70 °C; c) ^{11}B and d) ^{11}B{H} NMR spectra of $Al(BH_4)_3{\cdot}NH_3BH_3$ in toluene non-deuterated after heating to 70 °C.

^{11}B NMR signals at –35.0 ppm are present in all the samples as well as an unknown signal in the ^{27}Al spectrum and are suspected to belong to AlB_xH_y products, as well as the ^{11}B signals at –36.0 ppm with ^{27}Al 81.9 and 82.0 ppm. They can be the result of B_2H_6 reaction with the starting compound or/and forming products previously described for $Al(BH_4)_3$ with B_2H_6, giving the AlB_4H_{11} at 100 °C.[245] The assignment of the remaining weak ^{11}B signals is not certain, but they likely belong to polyhydroboranes. The presence of compounds such as

DADB $[BH_2(NH_3)_2]BH_4$ is excluded because no characteristic BH_2 signal at around –15 ppm ^{11}B spectrum was detected in our experiment.[246]

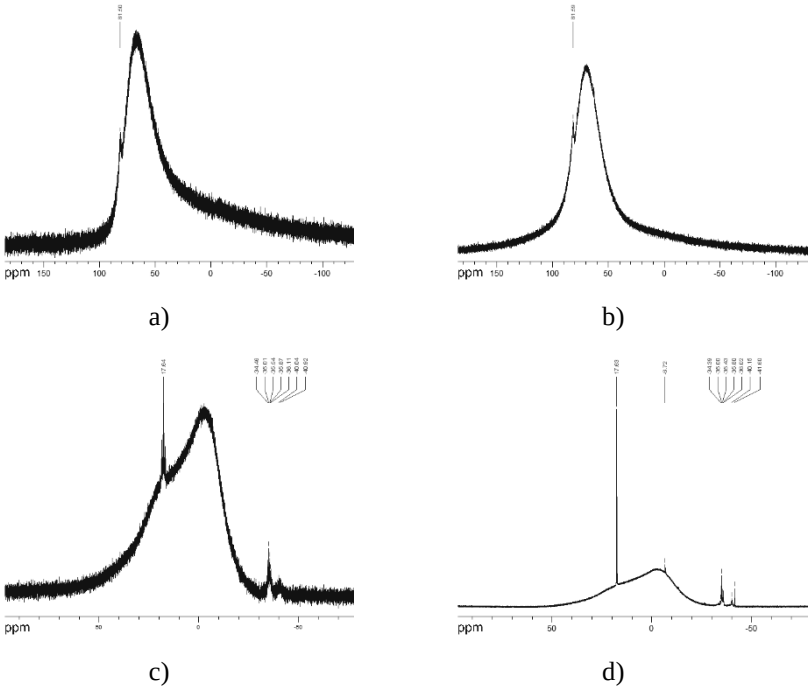

Figure 4.14 – a) ^{27}Al and b) $^{27}Al\{H\}$ NMR spectra of $Al(BH_4)_3{\cdot}NH_3BH_3$ in toluene-d_8 after heating to 100 °C; c) ^{11}B and d) $^{11}B\{H\}$ NMR spectra of $Al(BH_4)_3{\cdot}NH_3BH_3$ in toluene toluene-d_8 after heating to 100 °C.

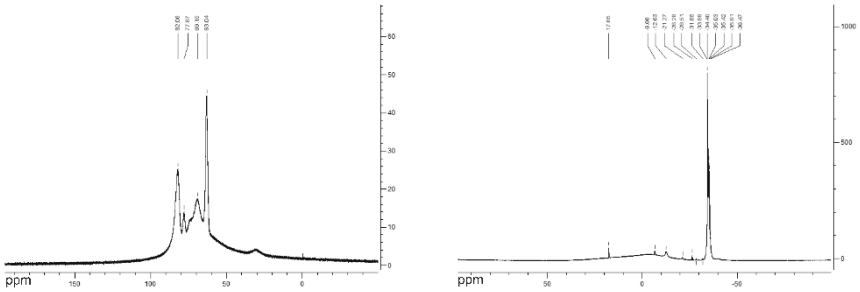

Figure 4.15 – a) ^{27}Al and b) $^{11}B\{H\}$ NMR spectra of $Al(BH_4)_3{\cdot}NH_3BH_3$ in toluene-d_8 after degradation at room temperature during 2 months.

Notably, the fresh $Al(BH_4)_3 \cdot NH_3BH_3$ sample kept in toluene-d_8 solution at room temperature; the sample aged in the inert atmosphere at ambient temperature and then dissolved in toluene-d_8 (Figure 4.15); and the sample heated to 70 °C and then dissolved in toluene-d_8 all give the same spectral features. No insoluble products were formed upon the dissolution in toluene. Therefore, it is likely the same decomposition pathway is taking place in toluene solutions and in the absence of any solvent. This means we can interpret by NMR the decomposition intermediate obtained in TGA/DSC and volumetric experiments, responsible for the release of 2 moles of H_2. Its fingerprint is the nonuplet at 63.0 ppm in the ^{27}Al NMR spectrum, with an intensity distribution of 14:22:40:64:70:64:40:22:14. With proton decoupling, this nonuplet at 63.0 ppm becomes a singlet (Figures 4.12a and 4.12b, 4.13a and 4.13b), implying the splitting of this peak into nine lines is indeed due to protons coupled to aluminium. The experimental signal exhibits nine maxima or shoulders but, as can be seen in Figure 4.16a, it is not properly described by a first-order nonuplet (relative intensity ratios of 1:8:28:56:70:56:28:8:1; four adjustable parameters: chemical shift, linewidth, overall intensity, and one scalar coupling constant). In contrast, considering a doublet of heptuplets as model yields excellent agreement (Figure 4.16b; relative intensity ratios of {1:6:15:20:15:6:1}:{1:6:15:20:15:6:1}; five adjustable parameters including the overall intensity). The relevant best-fit parameters are δ = 62.954 ppm, $\Delta\nu_{½}$ = 40.0 Hz (full linewidth at half-height corrected for lb), scalar coupling constant: $J_{doublet}$ = 89.4 Hz, $J_{heptuplet}$ = 46.4 Hz. Our observed *J* value of 46.4 Hz is similar to that reported for $^1J_{Al,H}$ of 44 Hz in $Al(BH_4)_3$.[247]

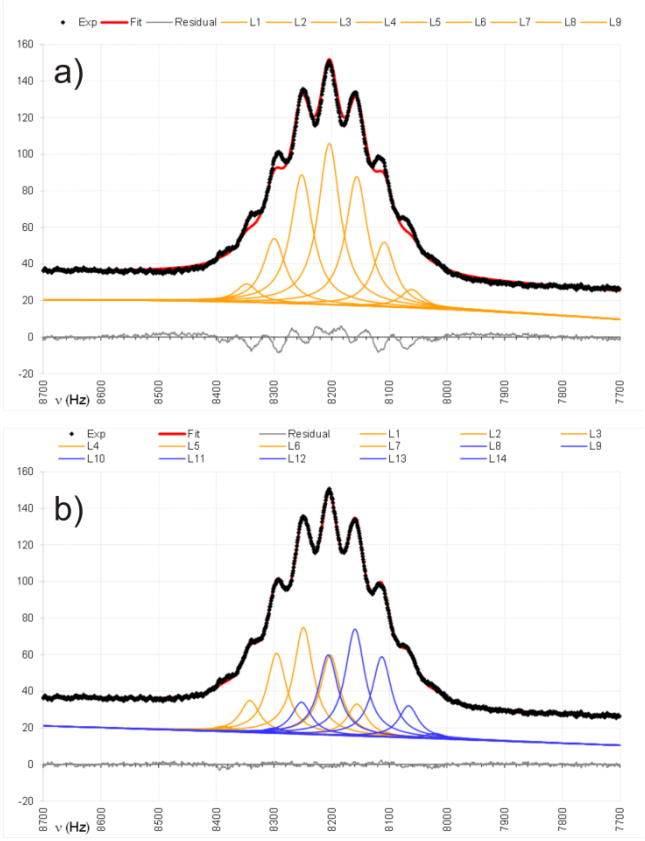

Figure 4.16 – Best-fit of a) a first-order nonuplet and b) a first-order doublet of heptuplets to the ^{27}Al NMR signal observed at 63.0 ppm.

4.7. Decomposition Intermediate

The NMR study shows that the first step of the decomposition of $Al(BH_4)_3 \cdot NH_3BH_3$ yields a product where an Al ion is bound to three borohydride anions with edges and further bound to one hydrogen, most likely a part of an "HN–HB" molecule or its oligomers, as shown in the scheme below:

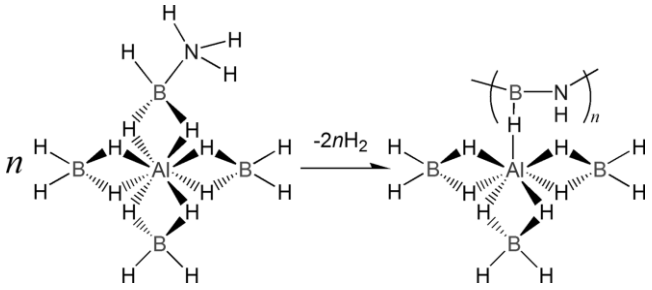

This evidence ties in very well with the results of our volumetric/TGA data suggesting the loss of 2 H_2 molecules. The 6H + 1H coordination of Al in the decomposition intermediate of $Al(BH_4)_3 \cdot NH_3BH_3$ is the first evidenced by the deconvolution analysis of the ^{27}Al NMR spectrum. The molecular structure of the other aluminium borohydride complexes had been previously assigned on the basis of the supposed reaction equilibria in solutions and the known solid state structures.[189,248] In all cases the BH_4^- anions are coordinated via the BH_2 edges. Broad singlets at 49.5 ppm in the spectra of $[(Ph_3P)_2N][Al(BH_4)_4]$ in CD_2Cl_2 correspond to 8 equivalent H around Al,[189] and at 99.7 ppm in the spectrum of $Al(BH_4)_3$ correspond to 6 equivalent H around Al; both are significantly different from the 63.0 ppm shift we observed. The complex with the closest chemical shift is $[AlH(BH_4)_2]_n$ with a signal at 64.7 ppm: it contains 4H from the BH_4^- groups and 2H bridging Al atoms.[244]

5. Perspectives of Tuning Properties of $AlX_3 \cdot L$ Complexes, $X = Cl^-, BH_4^-$ and $L = CH_3NH_2BH_3, (CH_2NH_2BH_3)_2$

5.1. Motivation

The improvement of hydrogen storage properties of AB complexed with $Al(BH_4)_3$ moved our attention to new possible combinations of other Al salts with different BH_3-containing ligands, like methylamine borane $CH_3NH_2BH_3$ (MeAB) and ethylenediamine-bisborane $(CH_2NH_2BH_3)_2$ (EDBB). The determination of the influence of both the anion and the ligand on the thermal decomposition properties of these starting materials is very important for the control of the hydrogen purity and thermodynamics of the decomposition processes.

The AB derivatives of MeAB and EDBB have also been previously investigated as potential hydrogen storage compounds. However, on their own they have several disadvantages for potential hydrogen storage. In particular, MeAB exhibits a high degree of volatility upon thermal treatment,[249] and EDBB exhibits thermal stability higher than that of its parent counterparts, AB and MeAB.[250] That is why we tried to obtain and characterize their complexes with AlX_3 ($X = Cl^-, BH_4^-$) salts, expecting the analogy with the $Al(BH_4)_3$ complex with AB. The substitution of one hydrogen in NH_3 group by alkyl group may also prevent the second decomposition step of $Al(BH_4)_3 \cdot NH_3BH_3$.

We obtained three new compounds. The first is $Al(BH_4)_3 \cdot CH_3NH_2BH_3$, which is indeed a close analogy of $Al(BH_4)_3 \cdot NH_3BH_3$ adopting a molecular structure. The second

compound, $[Al(CH_3NH_2BH_3)_2Cl_2][AlCl_4]$, is an autoionised isomer of the expected $AlCl_3{\cdot}CH_3NH_2BH_3$. The last as yet compound, $[Al(NH_2CH_2CH_2NH_2)(BH_4)_2][Al(BH_4)_4]$, is a result of unwanted borane splitting from the EDBB compex. The obtained compounds, especially the first two, are of interest not only in terms of hydrogen storage, but might be potentially studied for catalytic activity of Al atoms in the cationic form. These results were obtained quite recently, and only their crystal structures from X-ray single crystal diffraction were characterized. Further analysis of thermal decomposition will be done soon in collaboration with Aarhus University.

5.2. Synthesis of *L* (*L* = $CH_3NH_2BH_3$, $(CH_2NH_2BH_3)_2$) and of $AlX_3{\cdot}L$ Complexes (X = Cl^-, BH_4^-)

The syntheses of MeAB and EDBB. Powders of $CH_3NH_2BH_3$ and $(CH_2NH_2BH_3)_2$ were obtained according to the simplified procedures described in the literature.[250,251] These syntheses were performed using commercially available methylamine hydrochloride, ethylene diamine dihydrochloride (Sigma-Aldrich, 98 %) and $NaBH_4$ (Alfa Aesar, 97 %). The 37 mmol of $NaBH_4$ and stoichiometric amounts of methylamine hydrochloride or ethylene diamine dihydrochloride have been dissolved in 125 ml of THF and were stirred during ~24 h at room temperature, according to the reactions:

$$CH_3NH_2{\cdot}HCl + NaBH_4 \rightarrow CH_3NH_2BH_3 + NaCl + H_2 \quad (4.3)$$

$$(CH_2NH_2)_2{\cdot}2HCl + 2NaBH_4 \rightarrow (CH_2NH_2BH_3)_2 + 2NaCl + 2H_2 \quad (4.4)$$

The obtained mixtures were filtrated on air to flasks and the filtrate was pumped using rotary evaporator. The remaining viscous liquid was washed with hexane to precipitate crystals of methylamine borane and ethylenediamine bis-borane. The obtained white powders were dried on air and dissolved in D_2O for multinuclei ^{1}H, ^{13}C and ^{11}B NMR spectroscopy measurements, which confirmed the desired compounds.

The syntheses of $[Al(CH_3NH_2BH_3)_2Cl_2][AlCl_4]$. The obtained crystals of $CH_3NH_2BH_3$ were mixed with powder of $AlCl_3$ (Sigma-Aldrich, 95 %) in an inert glove box. The mixture readily melts/reacts at room temperature giving a slurry, which can be crystallized at room temperature or in the fridge (–35 °C). Single crystal X-ray analysis reveals formation of $[Al(CH_3NH_2BH_3)_2Cl_2][AlCl_4]$, according to the possible autoionized reaction:

$$2AlCl_3 + 2CH_3NH_2BH_3 \rightarrow [Al(CH_3NH_2BH_3)_2Cl_2][AlCl_4] \quad (4.5)$$

However, this is not the only crystalline phase, which was observed from the X-ray powder diffraction. Further analysis is required to determine the possible byproduct(s) or polymorph(s) of reaction (4.5).

The interaction of $AlCl_3$ with $(CH_2NH_2BH_3)_2$. In contrast to the spontaneous reaction of $AlCl_3$ with MeAB, the same interaction with $(CH_2NH_2BH_3)_2$ in 1 : 1 or 2 : 1 molar ratio does not yield new products neither at room temperature, nor upon heating to 70 and 85 °C.

The syntheses of $Al(BH_4)_3 \cdot CH_3NH_2BH_3$. Reaction conditions to obtain $Al(BH_4)_3 \cdot CH_3NH_2BH_3$ are similar to the preparation of $Al(BH_4)_3 \cdot NH_3BH_3$. The amount of the reagents can be scaled up to 100–200 mg of $CH_3NH_2BH_3$ and 2–3 ml of $Al(BH_4)_3$, here the X-ray

powder diffraction analysis confirms only a single phase of $Al(BH_4)_3 \cdot NH_3BH_3$.

The interaction of $Al(BH_4)_3$ with $(CH_2NH_2BH_3)_2$ and the formation of $[Al(NH_2CH_2CH_2NH_2)(BH_4)_2][Al(BH_4)_4]$. In order to observe the interaction of $Al(BH_4)_3$ with EDBB, we used the same reaction procedure, as for the $Al(BH_4)_3 \cdot NH_3BH_3$ and $Al(BH_4)_3 \cdot CH_3NH_2BH_3$ syntheses. During the search for a single crystal, the presence of two types of crystal shapes was observed: flakes (major) and needles (minor). The determination of the needle-like single crystals confirmed the formation of $[Al(NH_2CH_2CH_2NH_2)(BH_4)_2][Al(BH_4)_4]$ complex, probably by the following reaction:

$$2Al(BH_4)_3 + (CH_2NH_2BH_3)_2 \rightarrow [Al(NH_2CH_2CH_2NH_2)(BH_4)_2][Al(BH_4)_4] + B_2H_6 \quad (4.6)$$

Unfortunately, the X-ray powder diffraction analysis of the sample reveals the major presence of the starting EDBB, thus the fraction of $[Al(NH_2CH_2CH_2NH_2)(BH_4)_2][Al(BH_4)_4]$ is negligible. On the other hand, splitting of diborane puts the chemistry of this system far away from that of $Al(BH_4)_3 \cdot NH_3BH_3$. This side reaction will likely prevent us from obtaining a complex with EDBB.

5.3. Crystal Structures of $AlX_3 \cdot L_n$ Complexes ($X = Cl^-, BH_4^-$) and of L ($L = CH_3NH_2BH_3, (CH_2NH_2BH_3)_2$)

The complex $[Al(CH_3NH_2BH_3)_2Cl_2][AlCl_4]$ crystallizes in the *Pbca* space group (a = 12.5826(5), b = 12.6510(5), c = 20.4039(8) Å), see the details in Tables S2.5–S2.7. The $[AlCl_2(CH_3NH_2BH_3)_2]^+$ cation

adopts a distorted tetrahedral coordination with ∠B···Al···B of 104.1(2)° and ∠Cl···Al···Cl of 108.5(6)°, compared to the $[AlCl_4]^-$ anion with angles close to the ideal tetrahedral, ∠Cl···Al···Cl 107.9(7)–112.1(7)°. The distribution from 96.7(1), 99.4(1) to 124.3(1), 125.3(1)° for the ∠Cl···Al···B angles is more similar to ∠B···Al···B in homoleptic $M[Al(BH_4)_4]$ (M = Li^+, Na^+, K^+, NH_4^+, Rb^+, Cs^+) and $[Ph_3MeP][Al(BH_4)_4]$,[189] than to the nearly ideal tetrahedral shape of the heleroleptic complex anion in $Na[Al(BH_4)_2Cl_2]$.[77]

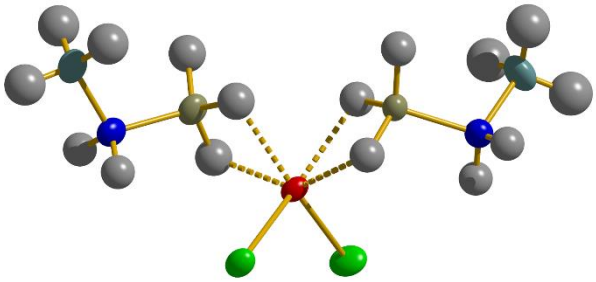

Figure 4.17 – The representation of $[Al(CH_3NH_2BH_3)_2Cl_2]^+$ cation with anisotropic displacement ellipsoids and isotropic spheres (hydrogen). Color code: Al–red, B–olive, Cl–green, N-blue, C–teal, H–grey.

The Al···Cl separations in the $[Al(CH_3NH_2BH_3)_2Cl_2]^+$ cation of 2.11(1) and 2.14(1) Å are in a good agreement with the 2.1–2.3 Å from other known cationic complexes of Al, see Figure 4.17.[252] $CH_3NH_2BH_3$ ligand coordinates to Al *via* bridging hydrogens of the BH_3 groups with Al···B and Al−H distances of 2.24(5)–2.26(4) and 1.8(2)–1.9(2) Å, respectively. The same coordination was found in the molecular $Al(BH_4)_3 \cdot NH_3BH_3$ complex, where corresponding distances of 2.31 and 1.65(8)-1.81(1) Å are quite similar, see the section 4.1. The C···N, B···N distances of 1.48(5) and 1.57(5) Å are almost identical to the non-complexed $CH_3NH_2BH_3$.[249,253] The C−H, N−H and B−H

apparent bond distances of 0.98, 0.91 and 1.16 Å in $[AlCl_2(CH_3NH_2BH_3)_2]^+$ cation are also quite similar to those of 0.96, 0.88 and 1.13 Å, reported for the neutral molecule of $CH_3NH_2BH_3$.[249,253]

$Al(BH_4)_3{\cdot}CH_3NH_2BH_3$ crystallizes in the triclinic space group *P*-1 (a = 6.2764(3), b = 7.9566(5), c = 10.3058(8) Å; α = 70.28(1), β = 74.74(1), γ = 86.04(1)°), see the details in Tables S2.9 and S2.10. In contrast to $[AlCl_2(CH_3NH_2BH_3)_2][AlCl_4]$, it adopts a molecular structure and resembles the heteroleptic complex of $Al(BH_4)_3{\cdot}NH_3BH_3$. Aluminum atoms coordinate three BH_4^- anions and one $CH_3NH_2BH_3$ molecule, forming a mononuclear $Al(BH_4)_3{\cdot}CH_3NH_2BH_3$ complex, like the one shown in Figure 4.18.

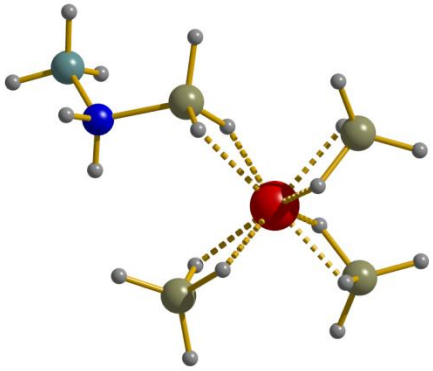

Figure 4.18 – The isolated $Al(BH_4)_3{\cdot}CH_3NH_2BH_3$ complex, where Al^{3+} cation coordinates three BH_4^- anions and one $CH_3NH_2BH_3$ molecule. Color code: Al–red, B–olive, N-blue, C–teal, H–grey.

Al^{3+} cation is linked via BH_2 edges to three BH_4^- anions and to one methylamine borane molecule. It adopts a distorted tetrahedral coordination, and the AlH_8 polyhedron has the shape of a snub disphenoid, similar to Al in $Al(BH_4)_3{\cdot}NH_3BH_3$ or Mg in $Mg(BH_4)_2$ structures.[58,60] The Al···B distances with the BH_4^- ions are in the

narrow range of 2.22–2.24 Å and are similar to 2.21−2.23 Å as determined in *α,β*-$Al(BH_4)_3{\cdot}NH_3BH_3$ polymorphs. It is nearly identical to the Al···B distances of 2.22–2.26 Å in $K[Al(BH_4)_4]$ and $[Ph_3MeP][Al(BH_4)_4]$, where the Al^{3+} cation is also coordinated to 8 hydrogen atoms.[189] The interatomic Al···B contact involving the methylamine borane's BH_3 group is slightly longer (2.34 Å), than the distances to the BH_4^- anions, fully consistent with the same elongation in $Al(BH_4)_3{\cdot}NH_3BH_3$ (2.31 Å). However, they remain much shorter than the metal-boron distances in the known metal borohydride-NH_3BH_3 complexes, namely 2.63−2.92 Å in $(LiBH_4)_2{\cdot}NH_3BH_3$, $LiBH_4{\cdot}NH_3BH_3$ and $Ca(BH_4)_2{\cdot}2NH_3BH_3$.[128,129] The Al−H bond distances vary accordingly: they range from 1.76(2) to 1.80(2) Å for the BH_4^- groups, similar to those in Al-based complex hydrides, to 1.89(1) and 1.96(1) Å where the $-BH_3$ group is involved. The latter are much shorter than the 2.44 and 2.50 Å M−H bond distances in $Ca(BH_4)_2{\cdot}(NH_3BH_3)_2$ and the 2.08−2.32 Å distances in $(LiBH_4)_2{\cdot}NH_3BH_3$.

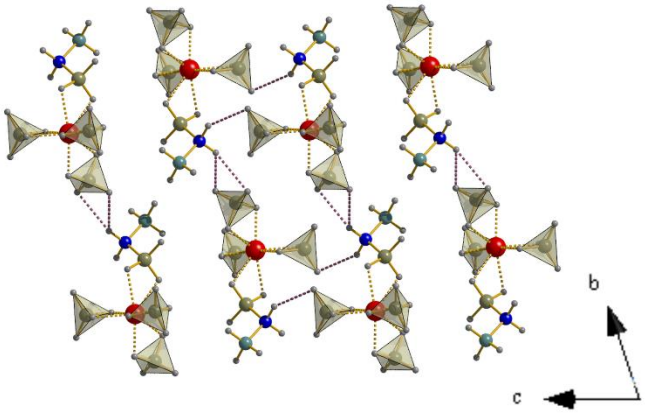

Figure 4.19 – The $Al(BH_4)_3{\cdot}CH_3NH_2BH_3$ molecules linked *via* dihydrogen bonds, depicted by violet dashed lines.

The molecules of $Al(BH_4)_3{\cdot}CH_3NH_2BH_3$ are linked *via* simple and bifurcated $N–H^{\delta+}\cdots H^{\delta-}–B$ dihydrogen bonds with H···H distances of 2.10–2.42 Å and ∠H···H–N angles of 130–160°, see Figure 4.19. These values are slightly below the sum of the van der Waals distance of 2.4 Å, and are in an agreement with directionality criterion accepted for dihydrogen bonds.[254]

$[Al(NH_2CH_2CH_2NH_2)(BH_4)_2][Al(BH_4)_4]$ crystalizes in the monoclinic space group $P2_1/c$ (a = 8.4168(5), b = 12.0021(7), c = 16.2933(12) Å; β=101.89(1)°), see the details in Tables S2.11 and S2.12. It is the first autoionized Al-borohydride complex known so far. Both ions adopt a distorted tetrahedral coordination for Al atoms. The ∠N···Al···N of 86.5(2)° is similar the other known bidentate chelates of Al.[252] The ∠B···Al···B of 118.1(3)° in the cation is close to tetrahedral, while the the angles around Al in the $[Al(BH_4)_4]^-$ anion range from 98.9(3) to 135.4(3)°, typical for a slightly flattened tetrahedron. This geometry is similar in aluminum borohydrides of alkali-metals $M[Al(BH_4)_4]$ ($M = Li^+$, Na^+, K^+, NH_4^+, Rb^+, Cs^+) and in $[Ph_3MeP][Al(BH_4)_4]$.[189]

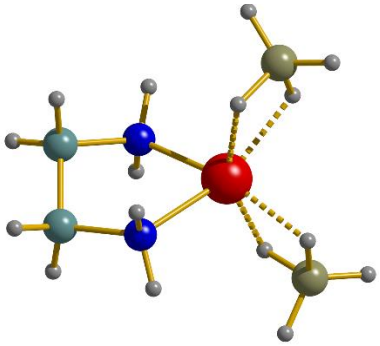

Figure 4.20 – Geometry of $[Al(NH_2CH_2CH_2NH_2)(BH_4)_2]^+$ cation in the solid state. Color code: Al–red, B–olive, N-blue, C–teal, H–grey.

$[Al(NH_2CH_2CH_2NH_2)(BH_4)_2]^+$ is a chelate cation, where the Al atom is linked *via* N atoms to the same ethylene diamine molecule, and *via* BH_2 edges to two BH_4^- groups, see Figure 4.20. Remarkably, the Al···B distances of 2.16(7) and 2.17(8) Å in the cation are slightly shorter, compared to the separations of 2.23(8)−2.27(8) Å in $[Al(BH_4)_4]^-$. The Al···N distances of 1.95(4) and 1.96(4) Å are typical (1.9−2.0 Å) for other Al-containing cations.[252] The Al−H distances of 1.72(4)-1.77(5) Å in the cation and 1.79(4)−1.89(4) Å in the anion are correlated with the Al···B distances. The structure also has both bifurcated and simple dihydrogen $N–H^{\delta+}\cdots H^{\delta-}–B$ bonds with H···H distances of 2.0–2.4 Å and ∠H···H–N angles of 136–160°.

6. Conclusions

The thermal decomposition of the new complex, $Al(BH_4)_3{\cdot}NH_3BH_3$, showed several striking features as compared with the previously investigated systems involving ammonia borane. We found that the decomposition of the complex in toluene solutions and upon heating the solid gives the same intermediate, releasing 2 equivalents of hydrogen at 70 °C and then diborane at 100 °C. The first decomposition step occurs at considerably lower temperature than for the pure NH_3BH_3, desorbing the first equivalent at 120 °C and the second at 150 °C.[255] To our knowledge, this is the first metal borohydride - ammonia borane complex, resulting in pure hydrogen release. The other systems produce significant amounts of ammonia, diborane and borazine already on the first decomposition step.[128−131] Also, we do not observe polyaminoboranes (PAB) and polyborazylene,

which form during liquid state pyrolysis of NH_3BH_3 in ionic liquids and in the presence of strong Lewis and Brønsted acids. They would result in ^{11}B signals in the –10 to for –13 ppm for BH_2^+, near –5 ppm for N–BH_2–N and near –22 ppm from BH_3 polymer terminating groups for PAB and 26 ppm for polyborazylene.[256,257]

The system of $Al(BH_4)_3 \cdot NH_3BH_3$ is also encouraging in terms of a possible direct rehydrogenation of ammonia borane, which is currently regenerated successfully only via multistep chemical cycles.[133,134] The striking property of the title system is the endothermic dehydrogenation on the first decomposition step (39 kJ/mol, including melting), compared to the exothermic one for ammonia borane (-22 kJ/mol on the first decomposition step, including melting).[117] Despite our unsuccessful attempts to directly rehydrogenate the intermediate, a catalyzed reaction may be possible. The absence of complicated mixtures on the dehydrogenation may also allow for a viable chemical recycling of ammonia borane.

The favorable decomposition pathway producing pure hydrogen and the decomposition temperature make this system an attractive model for efficient hydrogen elimination from ammonia borane. Taking into account all our data, we conclude that the decomposition of the starting complex into the Al-based intermediate can be assigned to $Al(BH_4)_3$ as a unique mild Lewis acid which coordinates both the starting and the dehydrogenated BH_n groups (n = 1, 3). This urges to use other Al-based Lewis acids, less challenging with respect to stability and safety than aluminum borohydride.

Our recent investigations proved the possibility to obtain the other derived complexes, such as $Al(BH_4)_3 \cdot CH_3NH_2BH_3$, which adopts

a molecular structure, similar to the $Al(BH_4)_3{\cdot}NH_3BH_3$, and the unique autoionized complex $[Al(CH_3NH_2BH_3)_2Cl_2][AlCl_4]$, being an isomer of $AlCl_3{\cdot}CH_3NH_2BH_3$. Further analysis of these compounds will help to understand the possibility to improve the hydrogen storage properties of AB, MeAB and EDBB by complexation with AlX_3 salts.

Chapter V – A Composite of $NaAlH_4$ and Ammonia Borane[3]

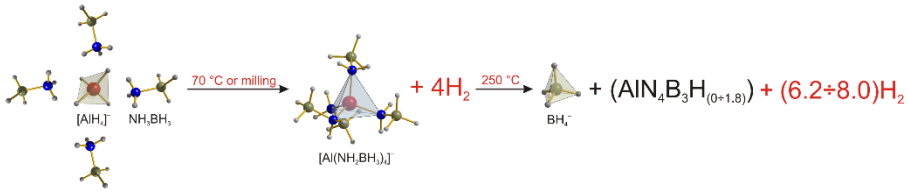

[3] This chapter is based on the following publication:

Dovgaliuk, I.; Jepsen, L. H.; Safin, D. A.; Łodziana, Z.; Dyadkin, V.; Jensen, T. R.; Devillers, M.; Filinchuk, Y. A composite of complex and chemical hydrides yields the first Al-based amidoborane with improved hydrogen storage properties, *Chem. Eur. J.* **2015**, *21*, 14562–14570.

1. Introduction

Alkali metal alanates, $M(AlH_4)_n$, have shown remarkable hydrogen storage properties. For example, $NaAlH_4$, the most intensively studied member of this class of compounds, has a reversible hydrogen capacity of 5.6 wt%.[27] However, high de- and rehydrogenation temperatures for alanates (e.g. 210–220 °C for $NaAlH_4$) as well as moderate hydrogen content have directed attention to lighter complex hydrides such as borohydrides, $M(BH_4)_n$.[21,36] At the same time, reversible systems based on borohydrides were developed only in the form of reactive hydride composites (RHCs), containing complex and binary metal hydrides. In particular, the reversible system, comprising $LiBH_4$ and MgH_2, doped with $TiCl_3$ to catalyze rehydrogenation, yields 8–10 wt% of hydrogen according to the following reaction:[99,258]

$$MgH_2 + 2LiBH_4 \rightleftharpoons MgB_2 + 2LiH + 4H_2 \quad (5.1)$$

In the middle of the last decade, an intensive research has been focused on the so-called chemical hydrides, in particular ammonia borane, NH_3BH_3 (AB).[37,235] The high hydrogen content in AB (about 19.6 wt%, 152 g/L) and its stability under ambient conditions have attracted significant attention to this compound.[259] AB undergoes stepwise decomposition with 6.5 wt% of hydrogen released below 112 °C and the total amount of 14.5 wt% at about 200 °C. However, this release is accompanied by the evolution of undesirable borazine $(BHNH)_3$, aminoborane BH_2NH_2 and diborane B_2H_6.[117,118] Another disadvantage of practical application of AB as a hydrogen storage

material arises from its spectacular foaming leading to dramatic volume expansion during its thermolysis.

A significant improvement in hydrogen release temperature was achieved by forming metal amidoboranes (MABs), $M(NH_2BH_3)_n$, from AB and metal hydrides, decreasing the decomposition temperature to about 90 °C for M = Li^+ and Na^+.[120] Recently, numerous MABs (M = Li^+, Na^+, K^+, Mg^{2+}, Ca^{2+}, Sr^{2+}, Y^{3+}),[120–123, 260–262], including mixed-metal $Na[Li(NH_2BH_3)_2]$,[124] $Na_2[Mg(NH_2BH_3)_4]$[125] and $K_2[Mg(NH_2BH_3)_4]$,[263] have been obtained and characterized. Although all the listed MABs release NH_3 and NH_2BH_2 in addition to hydrogen, $LiNH_2BH_3{\cdot}NH_3BH_3$ produces up to 14.0 wt% of pure hydrogen upon heating to 230 °C.[127] A system that can reversibly release pure hydrogen at lower temperatures is seen as the ultimate goal for practical hydrogen storage.

The formation of metal amidoboranes starting from binary hydrides and AB can be considered by itself as a method to produce hydrogen. In this case, the MH_n–AB (M = Li^+, Na^+, K^+, Ca^{2+}, Mg^{2+}, Al^{3+}, Y^{3+})[262,158,264] mixtures can be considered as RHCs according to the following reaction:

$$MH_n + nNH_3BH_3 \rightarrow M(NH_2BH_3)_n + nH_2 \qquad (5.2)$$

Although this reaction releases hydrogen at mild conditions (*e.g.*, ~70 °C for M = Mg^{2+}),[123] it is of low purity, ranging from 90 % for M = Li^+, Mg^{2+} and Al^{3+}, and can be also contaminated by a large amount of NH_3 as observed for M = Na^+ and Ca^{2+}.[158]

On the contrast, the lithium- or sodium-containing composites of alanates with AB release relatively pure hydrogen.[158–160] The alanates are not binary, like in reaction (5.2), but complex hydrides; and

the reaction pathways for these Al-based systems are not yet determined. Thus, understanding the behaviour of Al-based composites can help to develop a new family of materials with improved hydrogen storage properties. This goal prompted current studies of the composition, structure and reaction mechanisms of the hydrogen release in the alanate-AB systems. By combining the beneficial properties of the hydrogen storage systems based on aluminium, boron and nitrogen, new possibilities to create a reversible high hydrogen density storage material are generated.

This work is focused on the $NaAlH_4$–4AB system, where the first Al-based amidoborane, $Na[Al(NH_2BH_3)_4]$, is obtained. Crystallographic studies allowed to determine its composition and structure, thus, defining the previously unexplored, but favourable 1:4 stoichiometry of the starting composite. $Na[Al(NH_2BH_3)_4]$ is formed *via* either mechanochemical treatment at room temperature or by heating the mixture up to ~70 °C according to the following equation:

$$NaAlH_4 + 4NH_3BH_3 \rightarrow Na[Al(NH_2BH_3)_4] + 4H_2 \qquad (5.3)$$

It was found that reaction (5.3) is slightly exothermic and non-reversible. However, $Na[Al(NH_2BH_3)_4]$ also releases, in two steps, additionally up to 8 equivalents of H_2. Remarkably, this desorption is partially reversible. Thus, the decomposition properties of $Na[Al(NH_2BH_3)_4]$ were systematically investigated by *in situ* synchrotron radiation X-ray powder diffraction (SRXRPD), thermal analysis coupled with mass spectrometry, temperature-programmed photographic analysis (TPPA) and volumetric methods. It was established that the hydrogen re-absorption does not regenerate $NaAlH_4$

or $Na[Al(NH_2BH_3)_4]$, but rather occurs between amorphous product(s) and intermediate(s) of the dehydrogenation process.

$Na[Al(NH_2BH_3)_4]$ is the first compound coming from the combination of complex and chemical hydrides going beyond the addition reaction, its formation is favoured by the lower stability of the Al–H bonds compared to the B−H ones, and due to the Lewis acidity of the complex-forming aluminium cation. On the other hand, the $NaAlH_4$–4AB system opens a route to design a series of aluminium tetraamidoboranes, using, e.g., other alkali and alkali-earth metal alanates instead of $NaAlH_4$, with improved hydrogen storage properties.

2. Materials and Synthesis

All samples were obtained from commercially available $LiAlH_4$, $NaAlH_4$, $TiCl_3$ and NH_3BH_3 (95, 93, 99.99 and 98 % purity, respectively) purchased from Alfa Aesar, Sigma Aldrich Co and Katchem. All operations were done in gloveboxes with high purity argon atmosphere. The starting materials were placed into stainless steel vials and milled in a planetary ball mill Fritsch Pulverisette 7, using the Easy GTM gas pressure and temperature detection system to monitor the reaction. The gas release measured during ball milling for the $NaAlH_4$−4AB composite is shown in Figure 5.1. The rotation speed was set to 600 rpm and the ball to powder mass ratio to 30:1. Synthetic approaches for different samples are listed in Table 5.1.

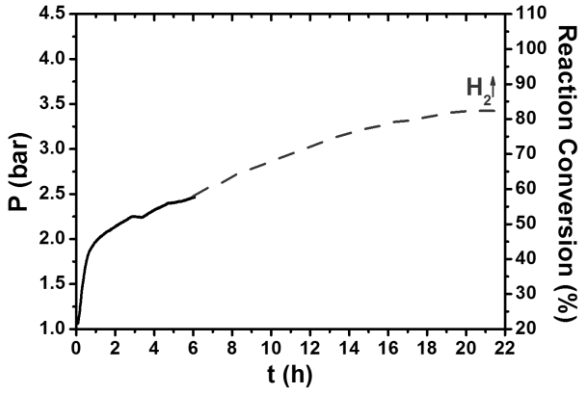

Figure 5.1 – The *in situ* monitoring of the hydrogen release during ball milling of $NaAlH_4$–4AB. The dashed line is an interpolation between the measured solid line and the final observed pressure of 3.5 bar (4.3 bar expected for the complete reaction).

Table 5.1 – Samples studied in this work.

Sample	Synthetic approach	Phase composition from XRPD (RT)
s1	$NaAlH_4$–4AB 160 milling/break cycles of 3/5 minutes	~55 wt% of $Na[Al(NH_2BH_3)_4]$ ~26 wt% of NH_3BH_3 ~19 wt% of $NaAlH_4$
s2	$NaAlH_4$–4AB 20 milling/break cycles of 3/3 minutes	~83 wt% of NH_3BH_3 ~17 wt% of $NaAlH_4$
s3	$NaAlH_4$–4AB 240 milling/break cycles of 3/5 minutes	~90 wt% of $Na[Al(NH_2BH_3)_4]$ ~4 wt% of NH_3BH_3 ~6 wt% of $NaAlH_4$
s4	$NaAlH_4$–4AB doped by 2 mol % of $TiCl_3$ 240 milling/break cycles of 3/5 minutes	~88 wt% of $Na[Al(NH_2BH_3)_4]$ ~11 wt% of NH_3BH_3 ~1 wt% of $NaAlH_4$

3. Experimental Details

X-ray powder diffraction analysis (XRPD). Samples were filled into 0.5 mm thin-walled glass capillaries and sealed under argon atmosphere. Laboratory diffraction data were recorded on a MAR345

diffractometer, rotating anode MoKα radiation equipped with a XENOCS focusing mirror. Sample **s3** was tested for rehydrogenation using a sapphire-based cell for *in situ* XRPD.[173] The starting powder was kept in a single-crystal sapphire capillary with 1.09 mm outer diameter. Decomposition of $Na[Al(NH_2BH_3)_4]$ under 5 bar of hydrogen was performed by heating the capillary from room temperature to 250 °C with a heating rate of 1 °C/min. The decomposed sample was heated to 250 °C under 150 bar of hydrogen, while powder diffraction data was continuously collected for ~26 h.

Variable temperature *in situ* synchrotron X-ray powder diffraction (SRXRPD). SRXRPD data were collected on a PILATUS@SNBL diffractometer (SNBL, ESRF, Grenoble, France) equipped with a Dectris PILATUS 2M single photon counting pixel area detector (λ = 0.823065 Å). Temperature was increased linearly in time using Oxford Cryostream 700+ at a 5 °C/min rate from room temperature to 150 °C. Powder patterns were obtained using raw and integrated data preprocessed by the SNBL Toolbox software against data of the LaB_6 standard.[265]

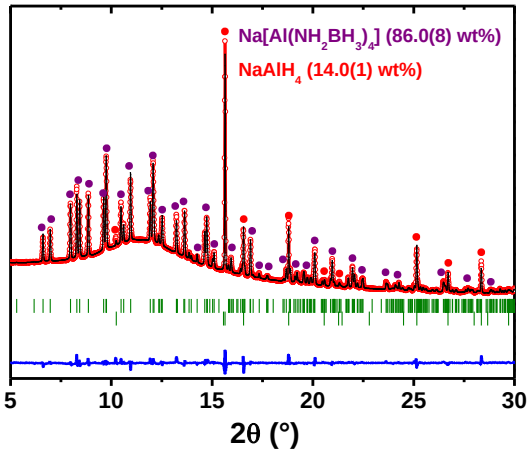

Figure 5.2 – Rietveld refinement profile (R_{wp} = 12.7 %) for **s1** at 100 °C (SNBL/ESRF synchrotron, λ = 0.823065 Å). $Na[Al(NH_2BH_3)_4]$: SG. *P*–1, *a* = 9.4352(2), *b* = 7.7198(1), *c* = 7.6252(1) Å; *α* = 97.211(1), *β* = 109.223(2), *γ* = 89.728(2)°; R_F = 5.7 %. $NaAlH_4$: SG. $I4_1/a$, *a* = 5.0398(1), *b* = 11.4319(1) Å; R_F = 6.7 %.

Crystal structure determination. The SRPXRD data for **s1** at 100 °C was indexed in a triclinic crystal lattice and the structure of $Na[Al(NH_2BH_3)_4]$ was solved in the *P*–1 space group using the program FOX.[167] ADDSYM procedure did not reveal any higher symmetry. The obtained crystal structure was further optimized by DFT calculations (see below) in order to obtain accurate hydrogen positions. The final structure, obtained from DFT calculations, was refined using bond distance restraints for H-atoms by the Rietveld method implemented in Fullprof (Figure 5.2).[169]

DFT optimization. Theoretical calculations were performed in order to prove the structural model and the thermodynamic properties of the determined system. We owe thanks to Professor Zbigniew Łodziana from the Department of Structural Research INP Polish

Academy of Sciences for these calculations. The structure of $Na[Al(NH_2BH_3)_4]$ was optimized by simulated annealing within plane wave formulation of the DFT method.[199] Electronic configurations of $1s^1$ for H, $2s^22p^1$ for B, $2s^22p^3$ for N, $2p^63s^1$ for Na and $3s^23p^1$ for Al were represented by projected augmented wave potentials.[200] The gradient corrected (GGA) functional[201] and correction for weak dispersive interaction were applied.[266] The initial structure from the Rietveld refinement was optimized with respect to the internal atomic positions and unit cell shape. This optimized structure was heated to T = 400 K at a rate of 100 K/ps and cooled down to T = 0 K at a rate of 20 K/ps. No constraints were imposed on the internal atomic positions and the unit cell parameters were kept fixed. Nose-Hoover thermostat[202,267] was applied for this procedure, and the time step for integration of equations of motion was 0.6 fs. Six independent structures with the lowest energy from the temperature range below 50 K were optimized with respect to internal atomic positions with the conjugated gradient method; then the symmetry was determined to be P–1 for five structures with the lowest ground state energy. For these structures the symmetry was imposed and the unit cell shape, together with atomic positions, was re-optimized. Within the accuracy of GGA calculations all five structures were identical with the following lattice parameters at the ground state: a = 9.435, b = 7.719, c = 7.625 Å; α = 97.213, β = 109.219, γ = 89.725°. The total energy of the optimized structure was 0.03 eV/formula unit lower than that for the initial guess, proposed by FOX. Normal mode analysis was performed with the finite displacement method for the Γ point; atoms were displaced by ±0.25 Å along each Cartesian direction. All modes are real positive.

In order to assess the enthalpy of the reaction (5.3), the ground state and vibrational properties were calculated for AB and $NaAlH_4$, based on their crystal structures.[31,268] For all systems two independent calculations were done with and without corrections for weak dispersive interactions. The enthalpy was calculated within harmonic approximation.[204] Thus, it consists of the electronic ground state energy and contribution from the vibrational degrees of freedom.

For the phonon calculations the dynamical matrix was constructed from the forces exerted on atoms upon displacements. The dynamical matrix was diagonalized and the normal mode frequencies and polarization vectors were extracted. The enthalpy of the reaction (5.3), $H(T) = E_0 + H_{vibra}(T)$, was calculated within harmonic approximation as a sum of vibrational $H_{vibra}(T) = \sum_i \frac{1}{2}\hbar\omega_i + \sum_i \hbar\omega_i \left(\exp\left(\frac{\hbar\omega_i}{kT}\right) - 1\right)^{-1}$ and electronic contributions at the ground state E_0 for each reactant and products (ω_i is the normal mode frequency at T = 0 K, k is the Boltzmann constant). For the hydrogen in the gas phase, terms related to rotational, translational and pV are added as (7/2)kT. The ground state energy normal modes were calculated for two independent cases: with and without weak van der Waals forces. For AB the later interactions are important. The lattice parameters calculated for the ground state are given in Table S3.2 in the Supporting Information.

Fourier Transform Infrared Spectroscopy (FTIR). Infrared spectra were recorded with a NICOLET 380 FTIR spectrometer from Thermo Electron Corporation in collaboration with Aarhus University. Samples were exposed to air for about 15 s when transferring from the sample vial to the instrument. In order to determine decomposition

products of **s3**, the same measurements were performed after heating in a Schlenk tube under argon atmosphere at 250 °C for 3 h.

Thermal analysis and mass spectrometry. Thermogravimetric analysis (TGA) and differential scanning calorimetry (DSC) measurements were done using a PerkinElmer STA 6000 apparatus simultaneously with mass spectrometry (MS) analysis of the residual gas with the use of a Hiden Analytical HPR-20 QMS sampling system, in collaboration with Aarhus University. Samples (~2 mg) were loaded into an Al_2O_3 crucible and heated from room temperature to 400 °C (5 °C/min) in an argon flow of 20 mL/min. Released gases were analyzed for hydrogen, ammonia, diborane, and borazine.

Temperature programmed photographic analysis (TPPA). Approximately 10 mg of **s2** and **s3** were sealed under argon in a glass tube placed in a home-built aluminium heating block as described recently.[73] Samples were heated from room temperature to 300 °C ($\Delta T/\Delta t$ = 5 °C/min), while **s2** was also heated from room temperature to 76 °C ($\Delta T/\Delta t$ = 3 °C/min) and kept at this temperature for 1 h pictures of the samples were collected every five seconds. The data were obtained in collaboration with Aarhus University.

Volumetric analysis and reversibility tests. Volumetric analysis was performed using a Hiden Isochema IMI-SHP analyzer. 40–50 mg of **s2–s4** was heated from 30 to 85 °C and to 250 °C, respectively, (1 °C/min, $p(H_2)$ = 5 bar). Subsequently, rehydrogenation was performed at $p(H_2)$ = 150 bar by heating **s2** to 85°C, and **s3** and **s4** to 250 °C, respectively (0.1 °C/min). Gas release was calculated from the calibrated volumes of the system, excluding the volume of the glass

wool (2.06 g/cm^3). The final uptake was calculated from the difference between the average start uptake at 30 °C (equal to the temperature of the manifold) and the decomposition uptake after cooling to the same temperature, in order to decrease uncertainties of calibrations. Usually, the uptake calculated by the manifold's IMI software at 250 °C is about 3% lower (~0.2 mol) than at 30 °C.

4. Results and Discussion

4.1 Phase Analysis and *in situ* SRXRPD data

The *in situ* SRXRPD patterns have been collected from room temperature to 150 °C (5 °C/min) (Figure 5.3) for the $NaAlH_4$–4AB mixture **s1**, obtained after 160 milling/break cycles (Table 5.1). The temperature-dependent composition of **s1**, extracted from the sequential Rietveld refinement, are given in Figure 5.3.

At room temperature **s1** contains Bragg reflections from AB[215] (26.3 wt%), $NaAlH_4$[22] (18.5 wt%) and from the previously unknown $Na[Al(NH_2BH_3)_4]$ (55 wt%). Peaks from AB disappear at around 90 °C without appearance of new peaks. At the same time, intensities of the peaks of $Na[Al(NH_2BH_3)_4]$ are continuously increasing and the peaks become narrower. According to the sequential refinement, the weight fraction of $Na[Al(NH_2BH_3)_4]$ increases after ~80 °C due to the reaction of AB with $NaAlH_4$ (Figure 5.3). $NaAlH_4$ peaks vanish at ~120 °C with an appearance of peaks for $NaBH_4$ implying the formation of amorphous product(s).

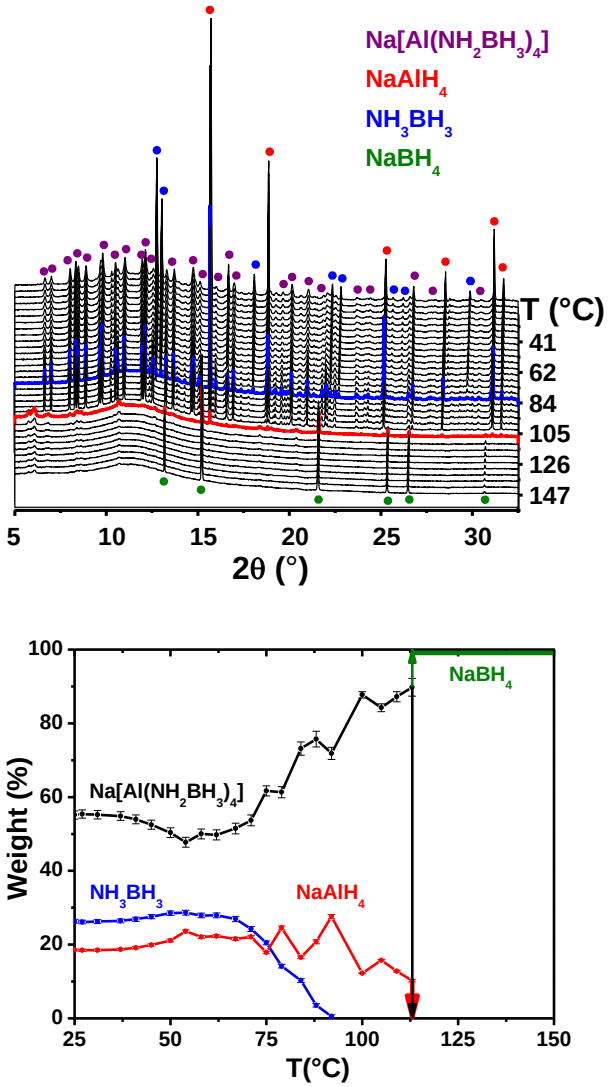

Figure 5.3 – The variable temperature plot of SRXRPD patterns of **s1** (SNBL/ESRF synchrotron, λ = 0.823065 Å) (top), and fractional content of compounds extracted from the Rietveld refinement of powder patterns (bottom).

Complementary measurements on the $NaAlH_4$–4AB mixture **s2** (Table 5.1), obtained after 20 milling/break cycles, exhibited the formation of a negligible amount of $Na[Al(NH_2BH_3)_4]$ (Figure 5.4). Thus, **s2**, being a homogenous physical mixture of AB and $NaAlH_4$,

was used to examine the temperature as a stimulus of the formation of $Na[Al(NH_2BH_3)_4]$ in the reaction (5.3). Variable temperature XRPD studies made on **s2** from room temperature to 76 °C at 1 °C/min rate have revealed the formation of $Na[Al(NH_2BH_3)_4]$, accompanied by the disappearance of the crystalline precursors (Figure 5.5). XRPD patterns collected on **s2** at 76 °C show that $Na[Al(NH_2BH_3)_4]$ gradually decomposes during 1 h with the formation of $NaBH_4$ and an amorphous product(s) (Figure 5.4). The same behavior was described by Ohnuki et al.[160] However, in their work numerous peaks were not well resolved, probably, due to a negligible amount of the then-unknown $Na[Al(NH_2BH_3)_4]$ and the limitations of the laboratory XRPD. Indeed, the formation of $Na[Al(NH_2BH_3)_4]$ with high yields requires a long-time milling that was not done earlier. Moreover, the stoichiometry of the starting mixture studied previously was 1:1[160] but not 1:4, hence, significantly decreasing the yield. $Na[Al(NH_2BH_3)_4]$ can be readily obtained by gentle heating of the $NaAlH_4$–4AB composite at about 80 °C. However, the resulting $Na[Al(NH_2BH_3)_4]$ starts to decompose extensively when kept for extended times at this temperature. Therefore this synthetic approach seems to be less attractive and more reliable alternative synthesis should be suggested. With this in mind we have directed our attention to the prolonged ball-milling of the $NaAlH_4$–4AB composite at room temperature. Indeed, as a result we have obtained the mixture **s3**, containing about 90 wt% of $Na[Al(NH_2BH_3)_4]$ (Table 5.1, Figure 5.6).

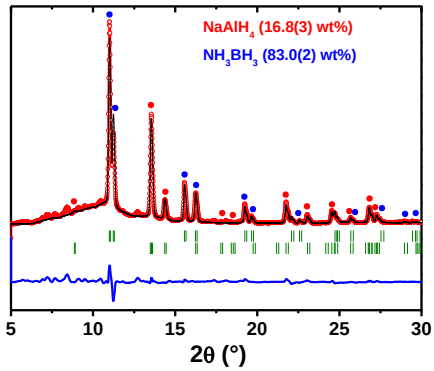

Figure 5.4 – Rietveld refinement profile for **s2** (MAR345 diffractometer, rotating anode with Mo-Kα radiation, XENOCS focusing mirror).

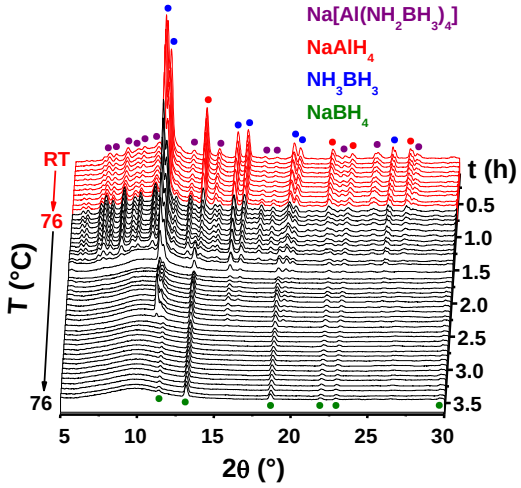

Figure 5.5 – The variable temperature plot of XRPD patterns of **s2** (MAR345 diffractometer, rotating anode with Mo-Kα radiation, XENOCS focusing mirror). The temperature was increased from room temperature up to 76 °C during about 1 h, and kept at the same temperature for another 1 h, leading to the gradual increasing of the concentration of $Na[Al(NH_2BH_3)_4]$, which peaks gradually disappeared during the next 1 h due to the decomposition of $Na[Al(NH_2BH_3)_4]$ with the formation of $NaBH_4$.

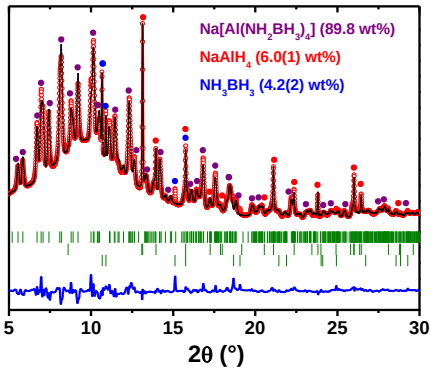

Figure 5.6 – Rietveld refinement profile for **s3** (SNBL/SRF synchrotron, λ = 0.68884 Å).

We have also attempted to characterize the corresponding Li-containing system,[158–160] by milling the $LiAlH_4$–4AB composite using the same experimental conditions as for the Na-containing mixture. However, the reaction appeared to be extremely violent. In particular, after a few seconds of milling the pressure exceeded twice the calculated value, coming close to the limit of the reaction vial, and as a result the milling was automatically stopped. Characterization of the resulting sample by XPRD revealed metallic Al and $LiBH_4$ along with other unidentified phases present as weak peaks (Figure S3.1 in the Supporting Information). This indicates that the $LiAlH_4$–4AB mixture reacts highly exothermically, and the ball milling is not an appropriate synthesis route.

The formation of borohydrides upon decomposition of $Na[Al(NH_2BH_3)_4]$ of the $LiAlH_4$–4AB composite, also recently found in the reaction products from MH_n–AB[158] and $MAlH_4$–AB (M = Li, Na)[160] composites, is remarkable. The origin of BH_4^- in the systems with AB was explained[160] by the exchange reaction between its ionic

dimer, diammoniate of diborane (DADB) $[(NH_3)_2BH_2]BH_4$,[269] and alkali metal alanate salts. This mechanism is not suitable in our case, since $NaBH_4$ is one of the decomposition products of $Na[Al(NH_2BH_3)_4]$. Characteristic peaks of $NaBH_4$ appear immediately after the decomposition of $Na[Al(NH_2BH_3)_4]$. It should be noted, that the unreacted AB does not participate in this process, since it still remains in the mixture during some time after the decomposition of $Na[Al(NH_2BH_3)_4]$ and the appearance of the $NaBH_4$ peaks (Figure 5.5). Thus, our work shows that the formation of borohydrides is not an intrinsic property of AB but of the amidoboranes decomposition.

4.2 Crystal Structure of $Na[Al(NH_2BH_3)_4]$

The crystal structure of $Na[Al(NH_2BH_3)_4]$ was solved in the triclinic space group *P*–1. Experimental coordinates and those optimized by DFT methods are listed in Tables S3.1 in the Supporting Information. Indexing / solution of triclinic structures from powder diffraction data is generally difficult, and this is the second amidoborane with a triclinic crystal system, after the mixed-metal complex $Na[Li(NH_2BH_3)_2]$.[124] The central Al^{3+} atom has a tetrahedral environment formed by four nitrogen atoms from four $NH_2BH_3^-$ anions (Figure 5.4). Thus, the tetrahedrally configured $[Al(NH_2BH_3)_4]^-$ anion is a new member of Al^{3+} complex hydrides with a tetrahedral coordination, after alanates $[AlH_4]^-$, complex amides $[Al(NH_2)_4]^-$ and complex borohydrides $[Al(BH_4)_4]^-$. The Na^+ atoms are octahedrally coordinated by six BH_3 groups arising from six $NH_2BH_3^-$ anions (Figure 5.7), similar to Na^+ in $Na_2[Mg(NH_2BH_3)_4]$.[125] Thus, all

$NH_2BH_3^-$ anions exhibit a bridging coordination mode linking Al^{3+} and Na^+ cations with the formation of a 3D polymer structure (Figure 5.8).

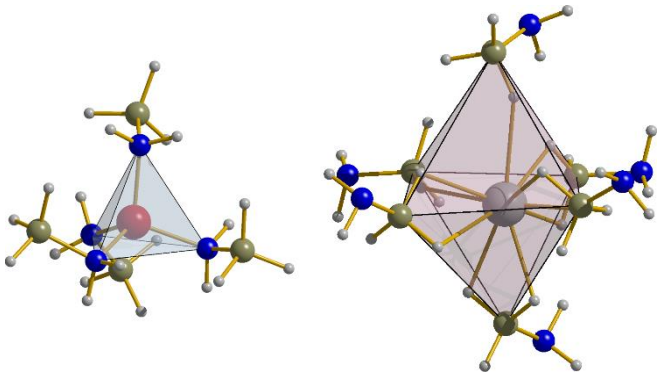

Figure 5.7 – Ball and stick plots of the tetrahedral $[Al(NH_2BH_3)_4]^-$ (left) and the octahedral $[Na(NH_2BH_3)_6]^{5-}$ (right) fragments. Color code: N = blue, B = olive, H = grey, Al = red, Na = dark grey.

The Al···N bond lengths range from 1.840(9) to 1.929(8) Å and are close to 1.90 Å found in the DFT-optimized experimental model of $Na[Al(NH_2BH_3)_4]$, which, in turn, is slightly longer than 1.85 Å observed in $Na[Al(NH_2)_4]$.[270] The Na···B distances are 2.92(1)-3.55(2) Å and 2.90–3.64 Å, as evidenced from the XRPD experiments and DFT calculations, respectively. These values are in line with 2.90–3.63 Å Na···B distances found in $Na_2[Mg(NH_2BH_3)_4]$.[125] Remarkably, the dihydrogen $N–H^{\delta+}\cdots H^{\delta-}–B$ bonds in $Na[Al(NH_2BH_3)_4]$ (1.96(1)–2.28(1) Å from XRPD and 1.92–2.34 Å from DFT) are close to the shortest dihydrogen bonds (1.91(5) Å) in pristine AB,[215] and significantly shorter compared to all known MABs (Table S3.3 in the Supporting Information).[118, 120-124, 260-262]

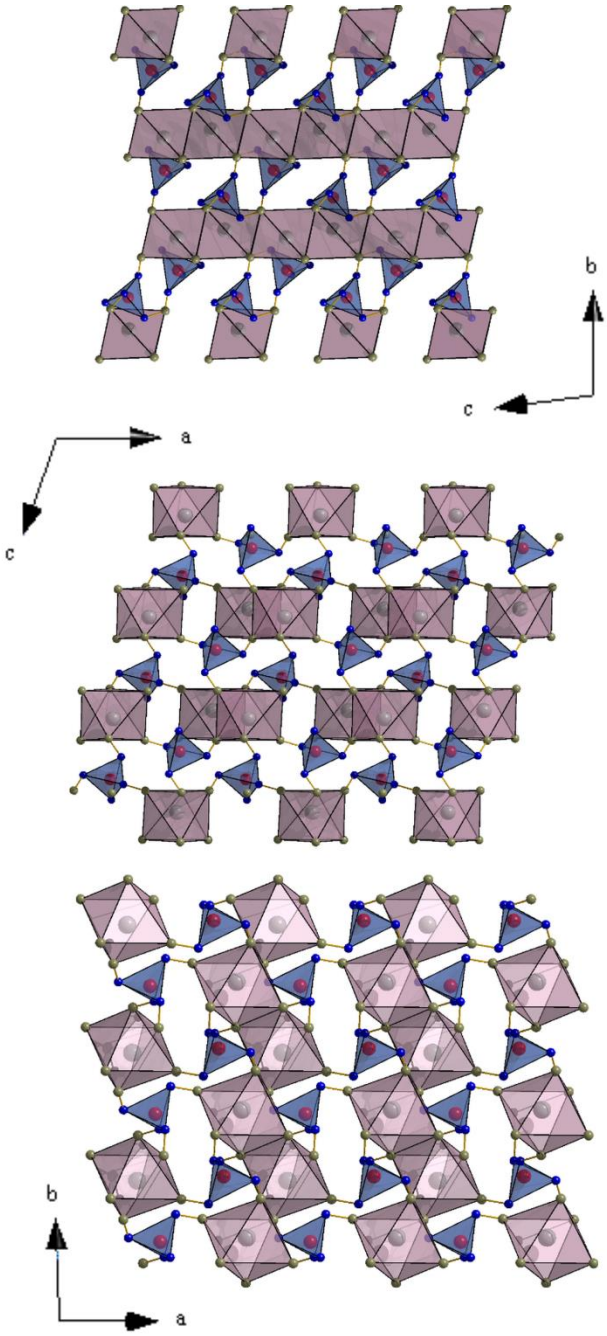

Figure 5.8 – Crystal packing of Al and Na coordination polyhedra in the structure of $Na[Al(NH_2BH_3)_4]$ along the *a* (top), *b* (middle) and *c* (bottom) axis. Color code: N = blue, B = olive, Al = red, Na = dark grey. Hydrogen atoms are omitted for clarity.

4.3 Fourier Transformed Infrared (FTIR) Spectroscopy

In order to characterize changes induced by ball-milling, FTIR measurements on **s2**, **s3** as well as on AB were conducted. The IR spectra of **s2** and **s3** exhibit characteristic bands for the B–H (1100-1150 and 2340–2420 cm^{-1}), N–H (1500–1650 and 3200–3430 cm^{-1}) and B-N (780 cm^{-1}) vibration modes similar to those for AB (Figure 5.9).[271] While the IR spectrum of **s2** shows no significant changes compared to those of the pristine AB and $NaAlH_4$, the spectrum of **s3** contains new bands at 630–673 cm^{-1} assigned to the Al–N vibrational modes (similar to $Na[Al(NH_2)_4]$ and aluminium nitride AlN).[270,272] Calculated values for the selected vibrational modes in $Na[Al(NH_2BH_3)_4]$ are given in Figure 5.10.

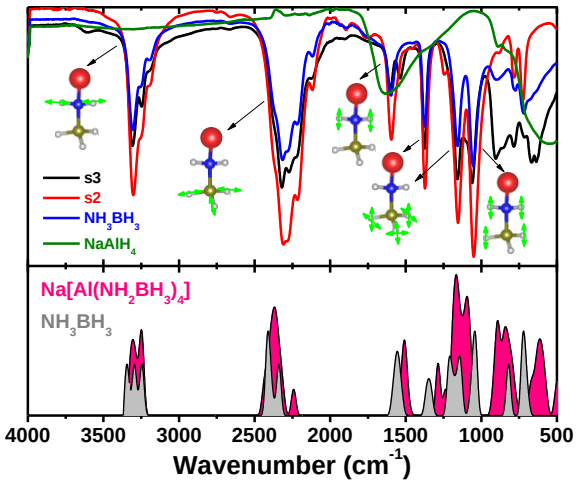

Figure 5.9 – FTIR spectra of **s2** and **s3** (top panel). Spectra of NH_3BH_3 and $NaAlH_4$ are given for comparison. The bottom panel shows phonon spectra of $Na[Al(NH_2BH_3)_4]$ and NH_3BH_3.

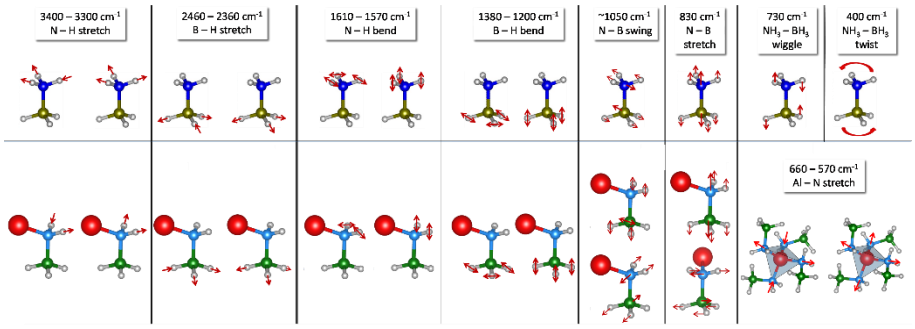

Figure 5.10 – Calculated vibrational normal modes for NH_3BH_3 (top) and $Na[Al(NH_2BH_3)_4]$ (bottom). The modes related to the N–B distortions are accompanied by rotations of the rigid AlN_4 tetrahedron. Color coding for atoms is the same as in Figure 5.7 in the main text.

4.4 Temperature-Programmed Photographic Analysis

As mentioned in the Introduction, one of the disadvantages to the practical application of AB for hydrogen storage arises from its spectacular foaming leading to a dramatic volume expansion during its thermolysis. With this in mind, we have applied a temperature-programmed photographic analysis to visually observe the volume expansion of **s2** and **s3** during thermal decomposition from room temperature to 275 °C. The **s2** mixture showed a drastic volume expansion upon heating starting from about 70 °C, increasing up to ~110 °C (Figure 5.11). In the applied experimental conditions with 5 °C/min heating rate, this observation can be explained by the decomposition of the unreacted AB, as its decomposition temperature is at about 107 °C.[118,273] Indeed, at ~110 °C the foaming reaches its maximum.

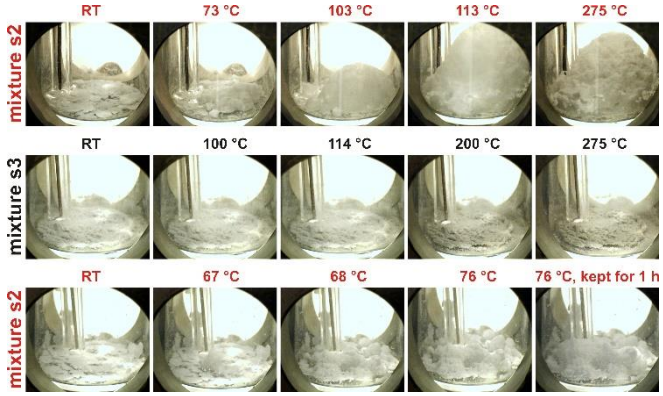

Figure 5.11 – Temperature-programmed photographic analysis of **s2** and **s3** at 5 °C/min heating rate. The foaming during the AB decomposition (top) is not observed for $Na[Al(NH_2BH_3)_4]$ (middle), and is suppressed for the **s2** reaction mixture by annealing at 76 °C (bottom).

The volume of **s3** remained constant under the same experimental conditions (Figure 5.11), showing a remarkable difference between the starting composite $NaAlH_4$–4AB and the reaction product $Na[Al(NH_2BH_3)_4]$. On the other hand, the foaming of the unreacted AB can be decreased by keeping the temperature below the decomposition of AB, *viz.* at 76 °C, where $Na[Al(NH_2BH_3)_4]$ is forming from **s2** over about one hour. This is yet another evidence of the formation of $Na[Al(NH_2BH_3)_4]$ at temperatures below the decomposition of AB.

4.5 Thermal Analysis and Mass Spectrometry

Simultaneous TGA–DSC–MS analysis has been conducted on **s2** aiming to characterize the hydrogen release through the formation of $Na[Al(NH_2BH_3)_4]$; and on **s3** aiming to observe the decomposition properties of $Na[Al(NH_2BH_3)_4]$. Thermal decomposition of both

samples is described mainly by two resolved steps of weight loss centered at about 120 and 160 °C (Figure 5.12). The first step in the TGA plot for **s2** is seen as a sharp weight deviation due to the so-called "jet" effect, which is explained by a drastic volume expansion upon heating. This finding is in line with spectacular foaming, which, in turn, is the result of the decomposition of unreacted AB, as it was observed by the TPPA (Figure 5.11 and the description above).

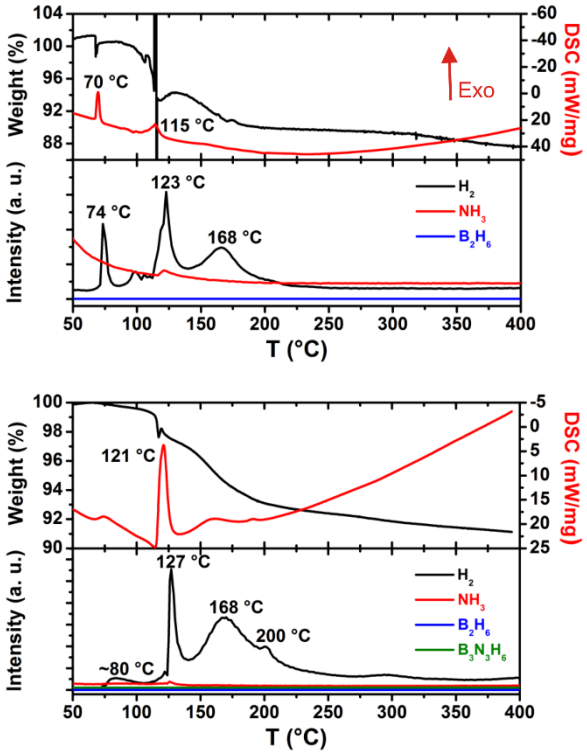

Figure 5.12 – TGA-DSC-MS analyses for **s2** (top) and **s3** (bottom) performed in a dynamic argon atmosphere.

Both decomposition steps were found to be exothermic and correspond to hydrogen evolution. An additional exothermic peak was found at about 75 °C for both samples (much less pronounced in the

DSC plot of **s3**), and can be explained by the reaction between $NaAlH_4$ and AB according to equation (5.3). The exothermic peak at 115 °C in the DSC plot of **s2** is the result of the decomposition of the unreacted AB that is in agreement with our XRPD data (Figure 5.5) and thermal decomposition pathway of pristine AB.[10]

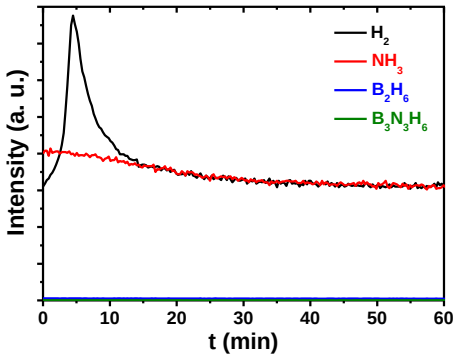

Figure 5.13 – The MS signal from **s2** during the annealing at 71 °C for 1 h, showing hydrogen release.

According to the TGA–MS data, neither borazine nor diborane and only traces of ammonia were observed during the decomposition of **s2** and **s3** (Figure 5.12). The total mass loss of ~9 wt% for **s3** indicates a partial hydrogen release out of the theoretical 11.9 wt% in $Na[Al(NH_2BH_3)_4]$. Notably, the formation of $Na[Al(NH_2BH_3)_4]$ from **s2** at the constant temperature of 71 °C results in hydrogen release without detectable impurities of ammonia, diborane and borazine (Figure 5.13). The calculated enthalpy of the reaction (5.3) at room temperature was found to be about –25 and -30 kJ/mol (Figure 5.14), calculated with and without van der Waals interactions, respectively. These results are in agreement with the exothermic events in the DSC data (Figure 5.12).

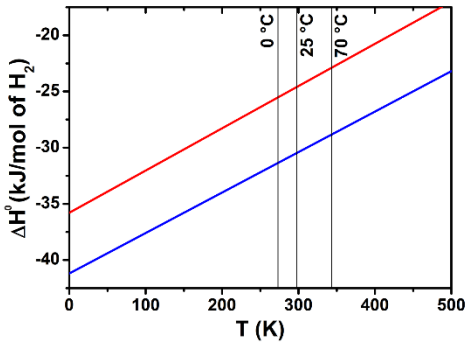

Figure 5.14 – Calculated standart enthalpy values of the hydrogen formation according to the reaction (5.3) in the main text. Red and blue lines correspond to the calculations with and without van der Waals interactions, respectively.

4.6 Reaction Pathways, Volumetric Analysis and Reversibility Tests

The **s2** mixture heated to 85 °C releases about 3.5 mol of hydrogen per one mole of aluminium (Figure 5.15). This value is close to the calculated 4 moles of hydrogen according to the reaction (5.3), and, together with diffraction, thermal and mass spectrometry analyses, proves the formation of $Na[Al(NH_2BH_3)_4]$ during the heating of the $NaAlH_4$–4AB composite.

Volumetric studies of the decomposition of **s3** and of the $TiCl_3$-dopped but otherwise identical sample **s4** (Table 5.1) were performed from room temperature up to 250 °C. The decomposition profiles of **s3** and **s4** differ slightly, showing a total hydrogen release of about 6.2 and 6.6 mol per one mole of $Na[Al(NH_2BH_3)_4]$ for **s3** and **s4**, respectively (Figure 5.15).

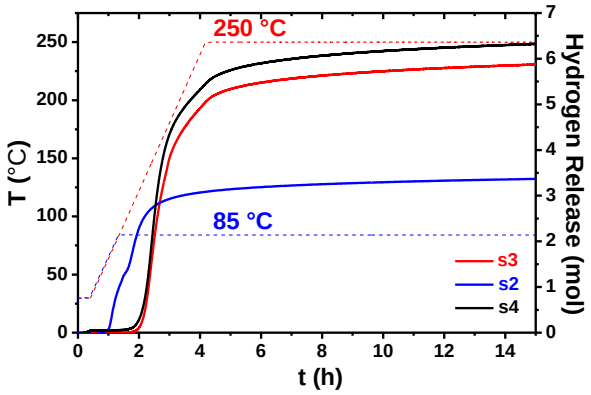

Figure 5.15 – Volumetric desorption curves for **s2–s4**.

We have also applied the volumetric technique to study the two decomposition steps centered at about 120 and 160 °C (Figure 5.15), by fast heating of **s3** to 120 °C, after which the temperature was kept constant for 60 h, followed by the complete decomposition at 250 °C (constant tempearture for 30 h). Complete separation of these two steps seems impossible due to their partial overlap as evidenced from the TGA–DSC–MS experiments (Figure 5.12). However, the two decomposition steps are clearly visible on the volumetric curve (Figure 5.16). The first decomposition step at 120 °C yields ~5.3 mol of hydrogen, while the total amount of about 8.0 mol is desorbed at 250 °C. These data confirm the prevalent formation of hydrogen: the weight loss of ~9 wt% in the TGA is in agreement with 8 mol of hydrogen gas found volumetrically.

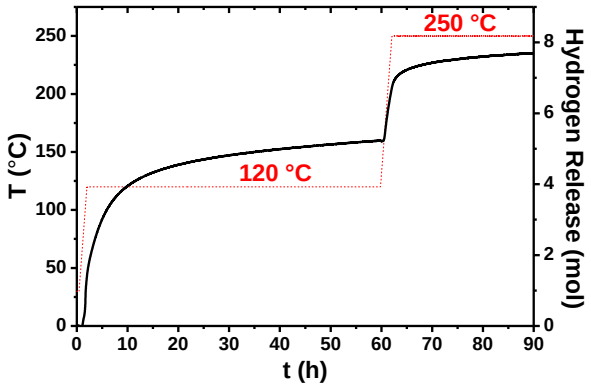

Figure 5.16 – Volumetric data on the hydrogen desorption of **s3**.

The absence of the crystalline Al and Na_3AlH_6 (the decomposition products of $NaAlH_4$),[27] of the boron nitride (BN), which can be formed during the decomposition of AB;[117,118] as well as of AlN, which hypothetically can form via the decomposition of $Na[Al(NH_2BH_3)_4]$ at 250 °C has been shown by XRPD (Figure 5.17). The only crystalline phase present there is $NaBH_4$. However, the FTIR spectrum of the final residue reveals all characteristic bands of $NaBH_4$ and a number of additional bands suggesting the presence of the Al–N, B–N, B–H and N–H groups. The latter two bands are similar to those observed upon thermal decomposition of the pristine AB with the formation of polymeric $(NH_xBH_x)_n$ ($1 \leq x \leq 2$) species (Figure 5.18).[271,272] Furthermore, in resemblance to binary amidoboranes $M(NH_2BH_3)_n$ (n = 1, M = Li^+, Na^+, K^+; n = 2, M = Ca^{2+}, Mg^{2+})[122,274–276] and to the Li_3AlH_6–4AB[158] system, we observed the formation of amorphous product(s), most likely, of the hydrogen-poor Al–N–B–H composition(s). Interestingly, recent theoretical calculations of the decomposition mechanism of $Al(NH_2BH_3)_3$ propose

the formation of $Al(NBH)_3$.[277] However, to the best of our knowledge, no experimental evidence of the existence of $Al(NH_2BH_3)_3$ was reported so far. Taking into account all the data on the decomposition pathway of $Na[Al(NH_2BH_3)_4]$ obtained in this work, the following simplified total decomposition reaction can be suggested:

$$Na[Al(NH_2BH_3)_4] \rightarrow NaBH_4 + AlN_4B_3H_{(0\div1.8)} + (6.2\div8.0)H_2 \quad (5.4)$$

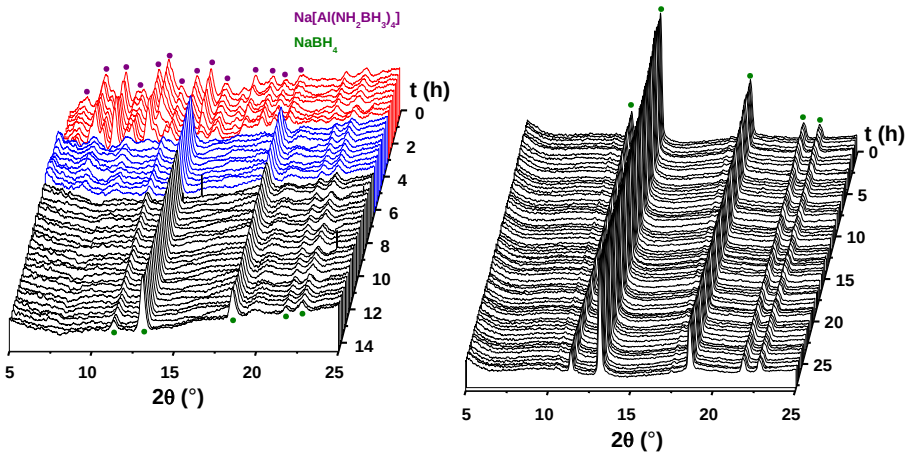

Figure 5.17 – The variable temperature plot of *in-situ* XRPD patterns of **s3**, collected from room temperature to 250 °C at $p(H_2)$ = 5 bar (left), followed by the rehydrogenation at 250 °C and $p(H_2)$ = 150 bar (right) (MAR345 diffractometer, rotating anode with Mo-Kα radiation, XENOCS focusing mirror).

Two regeneration tests were performed for **s3** and **s4** by applying 150 bar of hydrogen: one at 85 °C, to check for a hypothetical transformation back to the starting $NaAlH_4$–4AB composite; and another at 250 °C, to attempt a rehydrogenation of $AlN_4B_3H_{(0\div1.8)}$. It was found that $Na[Al(NH_2BH_3)_4]$ does not take hydrogen at temperatures up to 85 °C but instead decomposes slowly (Figures 5.19a,e). Thus, the final uptake was negative both for **s3** and **s4**. This behavior is expected, since the reaction (5.3) is slightly

exothermic according to the DSC data (Figure 5.12) and the DFT calculations (Figure 5.16).

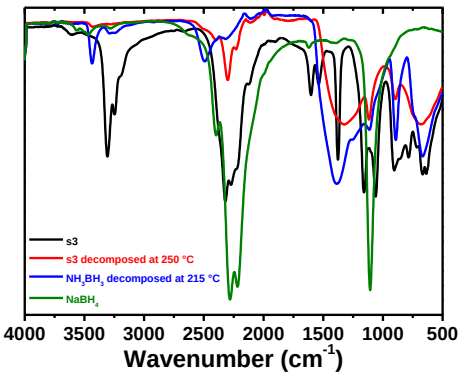

Figure 5.18 – FTIR spectra of **s3** and the product of its decomposition at 250 °C and cooled down to room temperature. Spectra of NH_3BH_3, decomposed at 250 °C and cooled down to room temperature, and $NaBH_4$ are given for comparison.

Slow hydrogen absorption was observed at 250 °C for the completely decomposed samples **s3** and **s4** (Figures 5.19b,f). Surprisingly, about 1.7 out of 6.2 mol (~27%) of the released hydrogen has been adsorbed by the amorphous residue during ~225 h (Figures 5.19c,g). The absorbed amount can be readily released (Figures 5.19d,h). This reversible absorption can be due to the hydrogen uptake with the formation of the amorphous intermediate(s) observed between the two decomposition steps at 120 and 160 °C (Figure 5.3). This scenario is likely, since *in situ* XRPD done at 250 °C and 150 bar of hydrogen did not show any crystalline phases forming upon the rehydrogenation during 26 h of the decomposed **s3** (Figure 5.17). This rehydrogenation can be a result of a continuous hydrogen absorption in the amorphous compound $AlN_4B_3H_{(0\div1.8)}$ to phases with a higher hydrogen content.

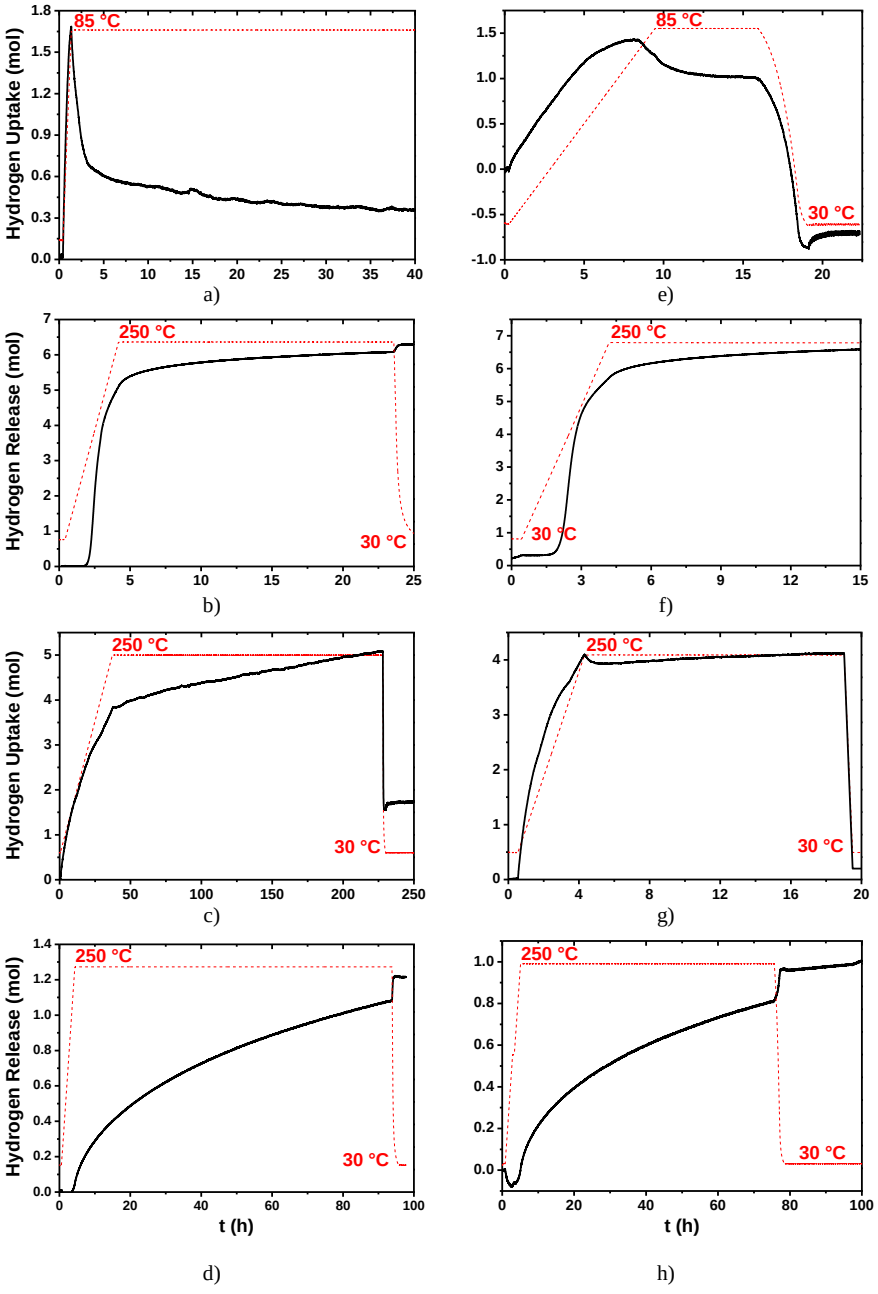

Figure S3.6 – The volumetric rehydrogenation (first and third rows) and desorption (second and fourth rows) data for **s3** (left column) and **s4** (right column).

5. Conclusions

The new $NaAlH_4$–4AB composite, combining complex and chemical hydrides, releases pure hydrogen and produces the first Al-based amidoborane, $Na[Al(NH_2BH_3)_4]$. The reaction proceeds already at 70 °C or under mechanochemical treatment at room temperature. This is the first example of a reaction where a complex hydride anion is deprotonating AB. Until now only binary metal hydrides were reacted with AB, forming amidoboranes, see equation (5.2). Breaking of the Al–H bonds in the $[AlH_4]^-$ anion is, apparently, easier than of the B–H bonds in the $[BH_4]^-$ anion since the latter one does not deprotonate AB. Therefore, alkali and alkali earth metal borohydrides (M = Li^+, Mg^{2+} and Ca^{2+}) merely form adducts with AB:[128–131, 278]

$$M(BH_4)_n + mNH_3BH_3 \rightarrow M(BH_4)_n \cdot (NH_3BH_3)_m \qquad (5.5)$$

The formation of $Na[Al(NH_2BH_3)_4]$ by the reaction (5.3) is not reversible at 150 bar of hydrogen, which is in line with the observed exothermic dehydrogenation. Therefore, an RHC based on the reaction (5.3) cannot be used as a reversible hydrogen store.

$Na[Al(NH_2BH_3)_4]$ decomposes in two steps with the formation of $NaBH_4$, up to 8 equivalents of pure hydrogen and an amorphous product $AlN_4B_3H_{(0\div1.8)}$. The latter reversibly reabsorbs about 27% of hydrogen. This reabsorption regenerates neither $NaAlH_4$ nor $Na[Al(NH_2BH_3)_4]$ but occurs between the amorphous product and intermediate(s) of the dehydrogenation. Further in-depth studies of $AlN_4B_3H_{(0\div1.8)}$, *viz.* its chemical structure and an optimization of the rehydrogenation process, are required.

During the recent years, Al-based complex hydrides attracted an ever-growing attention as potential hydrogen storage media. Indeed, the reaction (5.3) is possible not only because the Al–H bonds are less stable than the B–H ones but also due to the strong Lewis acidity of the Al^{3+} cation forming the tetraamidoborane complex. The title system opens an avenue to a series of aluminium tetraamidoboranes, $M[Al(NH_2BH_3)_4]$, with improved hydrogen storage properties, such as hydrogen storage density, hydrogen purity and reversibility. Our preliminary experiments, not presented in this work, show that the reaction (5.3) easily takes place in a THF solution at room temperature, and these conditions are successfully applied to the reaction in the $LiAlH_4$-4AB system, uncontrollable in the solid state.

Future works can also exploit the combination of amidoborane and borohydride ligands in the same Al-based compound, tuning their stability via different electron donor-acceptor properties of the ligands. Our recent discovery of the $M[Al(BH_4)_4]$ series (see, Chapter III) allows this goal to be achieved in a one-step reaction with $M[Al(NH_2BH_3)_4]$.

Chapter VI – CO_2-promoted Hydrolysis of KBH_4[4]

[4] This chapter is based on the following publication:

Dovgaliuk, I.; Hagemann, H.; Leyssens, T.; Devillers, M.; Filinchuk, Y. CO_2-promoted hydrolysis of KBH_4 for efficient hydrogen co-generation, *Int. J. Hydr. Energy* **2014**, *39*, 19603–19608.

1. Introduction

Hydrogen can be released from borohydrides either by thermolysis or via hydrolysis. Alkali metal borohydrides, MBH_4, were also intensively studied with respect to hydrogen release by hydrolysis, where hydrogen can be generated in accordance with the following simplified reaction:[137]

$$MBH_4 + (2+n)H_2O \rightarrow MBO_2 \cdot nH_2O + 4H_2 \qquad (6.1)$$

Depending on hydrolysis conditions, such as temperature, $LiBH_4$ gives different products:[138,139] $LiBO_2$, $LiBO_2 \cdot H_2O$, $LiBO_2 \cdot 2H_2O$, the latter also known as $Li[B(OH)_4]$.[140] $NaBH_4$ attracted the biggest attention due to its higher stability and ease to handle as compared with $LiBH_4$ (the latter reacts vigorously with water at room temperature), and high hydrogen content of 10.6 wt%, contrary to 7.4 wt% in KBH_4.[141] Aqueous solutions of $NaBH_4$ are usually chemically stabilized by rendering solutions basic and do not generate significant amounts of H_2 under ambient conditions.[142] However, $NaBH_4$ hydrolysis rate can be dramatically accelerated upon the addition of certain heterogeneous catalysts.[143,144] Among the conventional catalysts studied for the reaction, ruthenium-based catalysts were proposed to be most effective for promoting H_2 generation.[145,146] The hydrolysis of KBH_4 was also reported,[147] showing the lowest hydrolysis rate without the use of catalysts.

Acid is known to accelerate hydrolysis of borohydrides.[279] However, the hydrolysis of metal borohydrides in the presence of CO_2 has not been studied so far, even though its influence on the hydrogen release rate from aqueous solution of $NaBH_4$ has been noticed already in 1962:[279] the influence of CO_2 on $NaBH_4$ hydrolysis in open air was

assigned to the lowering of the pH of the solution. Our work is dedicated to the hydrolysis of KBH_4 in open air, attempting to clarify the role of CO_2, as well as to the hydrolysis reaction promoted by CO_2 gas put through the reaction mixture. Such process is interesting due to its potential of producing hydrogen on-board, making use of the exhaust gases (CO_2 and H_2O) from hydrocarbon fuels. The co-generation of hydrogen may thus improve the energy density of the system, as well as allow for CO_2 sequestration.

We found that CO_2 boosts up the hydrolysis reaction rates, transforming in solution the borohydride ions, BH_4^-, into tetraborates, $B_4O_5(OH)_4^{2-}$. Analysis of solid residues reveals a new complex intermediate, $K_9[B_4O_5(OH)_4]_3(CO_3)(BH_4)\cdot 7H_2O$. This substance was studied by single-crystal and X-ray powder diffraction, DSC, TGA, Raman, IR spectroscopy and elemental analysis, all the results are consistent with the presence of three different anions and of the crystallized water molecules.

2. Experimental Details

Hydrolysis reaction on open air. A ~190 g/L water solution of potassium borohydride (95 % purity, Sigma Aldrich) was left at 4º C in an open flask for approximately one year. The solution was found completely dried and transparent needle-like hexagonal crystals were observed, see Figure 6.1. Microscopy analysis revealed that the sample was almost single-phase, with only a small fraction of cubic crystals corresponding to the original KBH_4. The needle-like crystals, which formed the largest part of the solid phase, were hand-picked from the

mixture for further characterization. They were found to be well soluble in water.

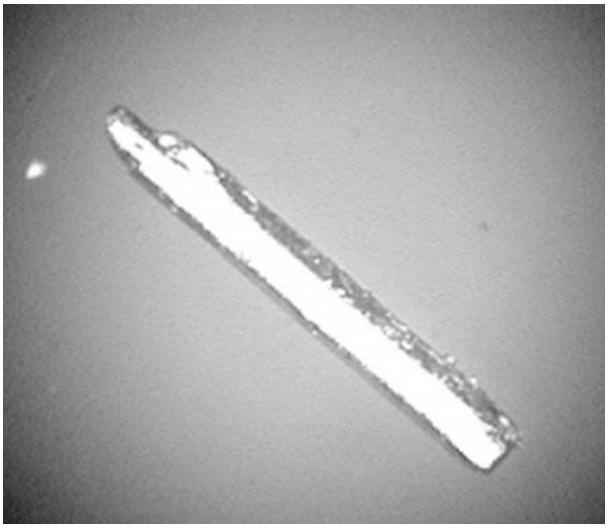

Figure 6.1 – The optical microscopy image of a hexagonal crystal of $K_9[B_4O_5(OH)_4]_3(CO_3)(BH_4)\cdot 7H_2O$.

Single-crystal synchrotron X-ray diffraction. Synchrotron radiation with $\lambda = 0.69790$ Å and a MAR345 detector were used for the data collection (SNBL/ESRF) at room temperature. The structure was solved by direct methods and refined by a full matrix least-squares technique on F^2 using SHELXL97 program.[164] The experimental details for the two alternative compositions from structure analysis are presented in a Table 6.1. Further characterization by other methods (see below) suggested a $K_9[B_4O_5(OH)_4]_3(CO_3)(BH_4)\cdot 7H_2O$ composition of the complex with disordered BH_4^-, which gives slightly better *R*–values compared to the initially assumed $K_9[B_4O_5(OH)_4]_3BO_3\cdot 8.2H_2O$ composition (see the comparison in the Table 6.1).

Hydrolysis reaction promoted by CO_2. As both elementary and IR analyses indicate the crystals to contain the carbonate anion (see

below), we attempted to repeat this synthesis under the CO_2 atmosphere. The same phase was obtained albeit by a much faster hydrolysis of KBH_4 under partial CO_2 pressure. 5 ml portions of 190 g/L aqueous solution of KBH_4 were exposed to CO_2 gas at room temperature. Hydrogen was readily desorbed from the solution on contact with CO_2, and the reaction was completed within minutes. Different portions of incompletely and completely hydrolyzed (saturated with CO_2) solutions were dried and the resulting powder was analyzed by X-ray powder diffraction. The completely hydrolyzed sample did not contain the $K_9[B_4O_5(OH)_4]_3(CO_3)(BH_4)\cdot 7H_2O$ phase, while it was the major crystalline phase in the incompletely hydrolyzed samples.

Table 6.1 – Experimental details of crystal structure analysis.

Formula	Hypothetical composition $K_9[B_4O_5(OH)_4]_3BO_3\cdot 8.2H_2O$	True composition $K_9[B_4O_5(OH)_4]_3(CO_3)(BH_4)\cdot 7H_2O$
Formula mass	1122.62	1124.26
T [K]	296(2)	
λ [Å]	0.69790 (synchrotron)	
Space group	*P*-62*c*	
Z	2	
Cell parameters [Å]	a = 7.8585(2) c = 15.7136(8)	
V [Å^3]	1881.54(13)	
ρ_{calc} [g·cm^{-3}]	1.982	1.984
μ [mm^{-1}]	1.146	1.144
F(000)	1126	1132
θ range max [°]	29.87	
Reflections collected	11935	
Independent reflections	1949 [R_{int} = 0.0982]	
Data / restraints / parameters	1949 / 0 / 106	1949 / 0 / 107

Goodness-of-fit	1.131	1.134
R indices [$I \geq 2\sigma(I)$]	$R_1 = 0.0411$, $wR_2 = 0.1165$	$R_1 = 0.0381$, $wR_2 = 0.1084$
R indices (all data)	$R_1 = 0.0419$, $wR_2 = 0.1169$	$R_1 = 0.0390$, $wR_2 = 0.1088$

Addition of aqueous solutions of sodium hydrogen carbonate ($NaHCO_3$) to potassium borohydride leads to a vigorous hydrogen evolution, indicating that the hydrogen carbonate is a strong enough acid to promote BH_4^- hydrolysis, yielding the carbonate anion and hydroxyborates.

X-ray powder diffraction. In line with the crystal structure model, the X-ray powder diffraction analysis of the separated and ground hexagonal crystals and of the mixture with cubic KBH_4 were made. The diffraction experiments were done on 0.5 mm glass capillaries, MAR345 image plate diffractometer with Mo Kα radiation. The received data images were azimuthally integrated by the program Fit2D,[179] using LaB_6 callibrant, followed by a calculation of intensity uncertainties. Phase analysis was done using Rietveld method with Fullprof Suite software.[169]

Infrared and Raman spectroscopy was performed to verify the crystal structure model. The infrared spectra were recorded on Shimadzu Benelux FTIR-84005 spectrometer between 400 and 4000 cm^{-1} using pressed pellets of the sample powder with dried KBr. Raman spectroscopy analysis was done using a Raman Thermo Scientific with a 532 nm DXR laser between 200 and 3500 cm^{-1}.

Time-resolved online ATR-FTIR spectra were recorded on a ReactIR 15 spectrometer (Mettler-Toledo) equipped with a diamond probe with a resolution of 4 cm^{-1}. Spectra were collected continuously at 1 min intervals. CO_2 gas was put through a 190 g/L water solution of

KBH_4 during the 4 hours of the measurements. Changes of the spectra were recorded during the first 90 minutes.

Thermal analyses were done using TGA/SDTA 851 Mettler and DSC 821 Mettler in the temperature range 25–500 °C with a heating rate of 10°C/min and under a 0.5 ml/min nitrogen flow to avoid oxidizing reactions.

Elemental analysis. The determination of carbon, hydrogen and nitrogen quantity was made using microanalysis at MEDAC Ltd (England).

3. Results and Discussion

3.1 Crystal Structure and Phase Analysis

The X-ray single crystal analysis of the hexagonal crystals allowed to establish a new crystal structure with a *P*−62*c* space group shown on Figure 6.2a. Although structure solution first suggested a composition of $K_9[B_4O_5(OH)_4]_3BO_3{\cdot}8.2H_2O$, containing two types of anions: tetraborate and orthoborate, with four independent co-crystallized water molecules, a slightly different picture was obtained by a combination of techniques. In particular, Raman analysis suggested the presence of carbonate anions, and IR as well as Raman analysis clearly revealed the presence of a borohydride group. This forced us to revise the structural assignment of the molecular entities, changing the orthoborate to a carbonate, and one of the poorly resolved water molecules to a borohydride group orientationally disordered around the –6 axis. The resulting formula is charge-neutral, $K_9[B_4O_5(OH)_4]_3(CO_3)(BH_4){\cdot}7H_2O$, and the calculated content of

carbon is 1.08 wt%, close to the measured value of 1.11 wt%. The fit to the single-crystal diffraction data is furthermore slightly better than for the original model (compare the two columns in Table 6.1). The compound is thus stabilized by a very small amount of the atmospheric CO_2 that slowly reacted with the borohydride solution yielding CO_3^{2-} anions.

The X-ray powder diffraction pattern of the manually separated and ground crystals is shown in the bottom of Figure 6.2b. It fits very well with that of the crystal structure model described above. According to the Rietveld refinement, the sample hydrolyzed on open air contains a $K_9[B_4O_5(OH)_4]_3(CO_3)(BH_4)\cdot 7H_2O$ intermediate as a major phase (bottom Fig. 2b) and traces of potassium tetraborate dihydrate $K_2[B_4O_5(OH)_4]\cdot 2H_2O$.[280] The same intermediate was also observed after incomplete hydrolysis of KBH_4 under CO_2 (middle pattern in the Figure 6.2b). Structure determination is difficult to perform due to the low resolution; however K_2CO_3, $KHCO_3$, as well as other known K-B-O-H compounds listed in the Pearson's crystal database are not present in the mixture. It likely involves tetraborate and (hydrogeno)carbonate anions, since all the borohydride is hydrolyzed.

The new compound $K_9[B_4O_5(OH)_4]_3(CO_3)(BH_4)\cdot 7H_2O$ is a complex salt, containing isolated tetraborate $[B_4O_5(OH)_4]^{2-}$, tetrahydroborate BH_4^- and carbonate CO_3^{2-} anions, Figure 6.2a. The tetraborate ion is common in alkali metal–B–O–H chemistry, present in borax [281] and in its potassium-based analogue $K_2[B_4O_5(OH)_4]\cdot 2H_2O$.[282] The geometry of the tetraborate anion is not affected by the presence of carbonate and borohydride, as it is practically identical to the one in $K_2[B_4O_5(OH)_4]\cdot 2H_2O$. More complex

polymeric anions contain fragments identical to tetraborate, as in the infinite 1D anion found in $K_4[B_{10}O_{15}(OH)_4]$.[283]

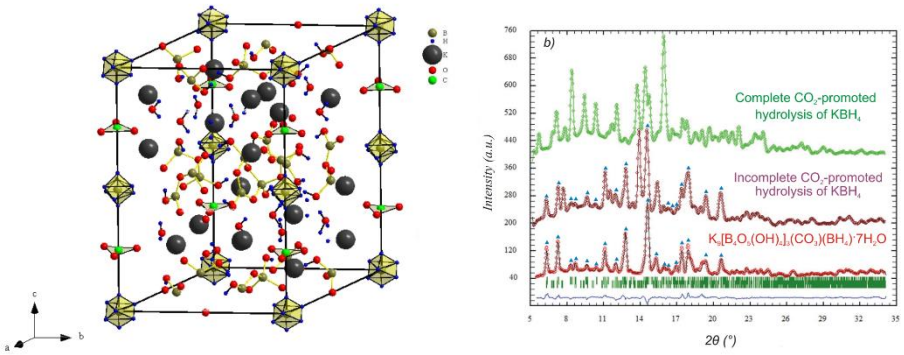

Figure 6.2 – a) The crystal structure of $K_9[B_4O_5(OH)_4]_3(CO_3)(BH_4)\cdot 7H_2O$, space group $P\bar{6}2c$, cell parameters: a = 11.2551(4), c = 17.1508(8) Å; b) Powder diffraction patterns from the samples in KBH_4–H_2O–CO_2 system. The bottom pattern shows the Rietveld fit for the sample hydrolyzed on open air, the peaks of $K_9[B_4O_5(OH)_4]_3(CO_3)(BH_4)\cdot 7H_2O$ are highlighted by the blue triangles. The peak positions of the minor phase, $K_2[B_4O_5(OH)_4]\cdot 2H_2O$, are marked by the second row of green bars. The middle pattern from a partly reacted KBH_4–H_2O–CO_2 contains $K_9[B_4O_5(OH)_4]_3(CO_3)(BH_4)\cdot 7H_2O$ as the major phase, and the top pattern shows no title phase in the fully hydrolyzed product.

In the title structure, the CO_3^{2-} anion has a trigonal prismatic coordination by K atoms, capped on the square sides, increasing the coordination number to 9. These three extra contacts correspond to the shortest K···O distances of 2.725(3) Å and to the linear B–O···K arrangement. The structure contains two independent K cations, coordinated to 9 and 10 oxygen atoms from both anions and from four independent water molecules, designated Ow1–Ow3. The K···Ow distances range from 2.706(4) to 3.468(1) Å; the latter contact corresponds to the weakly bound Ow3 site, populated by 49(1)%. The

hydrogen atoms of the hydroxyl groups and the localized H-atoms of water molecules Ow1 and Ow2 form short and well directed hydrogen bonds. Unlike in the hydrated $NaBH_4$,[51,284] there are no dihydrogen bonds formed between $O–H^{\delta+}$ and $H^{\delta-}–B$.

3.2 Infrared and Raman Spectroscopy

The infrared and Raman spectra of the complex include the typical anions' characteristic peaks (Figure 6.3). Most of the Raman and IR shifts correspond to the tetraborate anion $[B_4O_5(OH)_4]^{2-}$ known from borax $Na_2[B_4O_5(OH)_4]\cdot 6H_2O$ and potassium tetraborate dyhydrate $K_2[B_4O_5(OH)_4]\cdot 2H_2O$: ($B_{tetr}$–O) 573, 826, 944, 1006; (B_{trig}–O) 1337 cm^{-1}.[285–287] The characteristic shifts of tetrahydroborate BH_4^- anion are close to those of KBH_4: 1226, 2188, 2267, 2290 and 2346 cm^{-1}.[54,288] The strong Raman shift at 1050 cm^{-1} is typical for the carbonate anion (1040–1100 cm^{-1}).[286]

The evolution of the time-resolved ATR–FTIR spectra is shown in Figure 6.4. During the bubbling of CO_2 through the water solution of KBH_4 the intensity of the BH_4^- band near 1100 cm^{-1} is going down to practically zero in 30–40 min, while the intensity of HCO_3^- (~1630 cm^{-1}) does not change significantly. The new peaks appear at 930-1000 and 1320–1420 cm^{-1}, and are identified as $[B_4O_5(OH)_4]^{2-}$ anion or similar derivatives forming during the hydrolysis.[287,289] In contrast to CO_2-promoted hydrolysis, the KBH_4 solution kept at room temperature without access of CO_2 (closed even from air) retains BH_4^- bands after 24 and even 96 hours, see Figure 6.5.

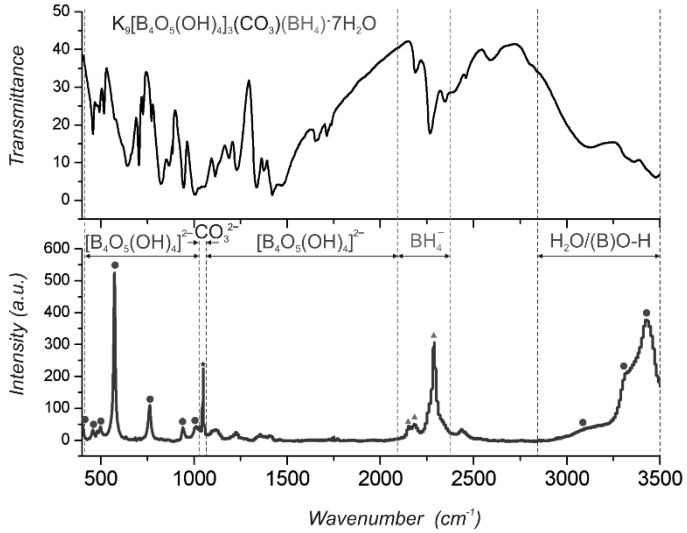

Figure 6.3 – The infrared (top) and Raman (bottom) spectra of $K_9[B_4O_5(OH)_4]_3(CO_3)(BH_4)\cdot 7H_2O$ at RT.

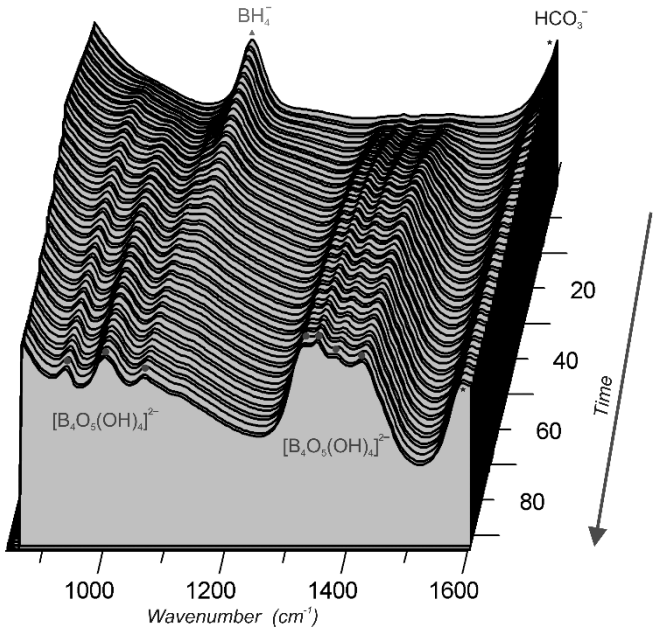

Figure 6.4 – The time-resolved online ATR-FTIR (adsorption) plot.

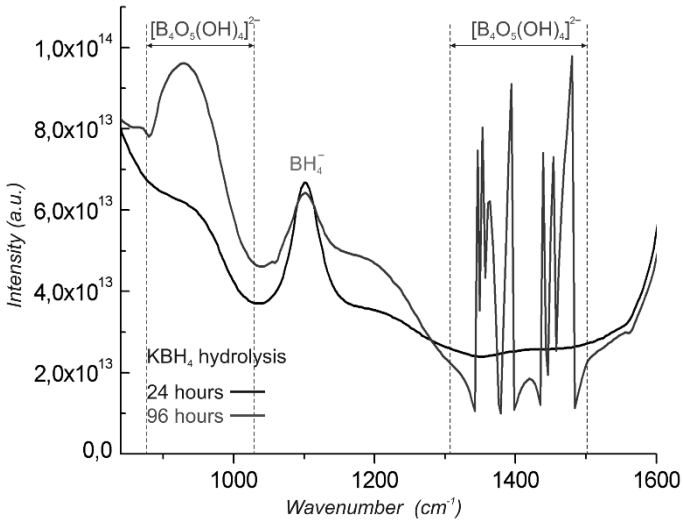

Figure 6.5 – The ATR-FTIR spectra from hydrolyzed of KBH_4 under inert atmosphere after 24 and 96 hours, the signals from in 1300–1500 cm^{-1} are affected by the oversaturation.

3.3 Thermal Analysis

The title compound steadily gives mass loss starting from room temperature up to 350 °C. From TGA and DSC curves in Figure 6.6, we can discern only one big decomposition step, of about 19.3 wt. % of mass loss. The latter is higher than the expected loss of 7 water molecules (11.2 wt%) and rather corresponds to the loss of 12 H_2O (19.2 wt%). The phenomena of releasing water both from crystalline and coordinated water (dehydration) as well as from complex anions containing OH (dehydroxylation) was known so far only for hydrated borates.[290]

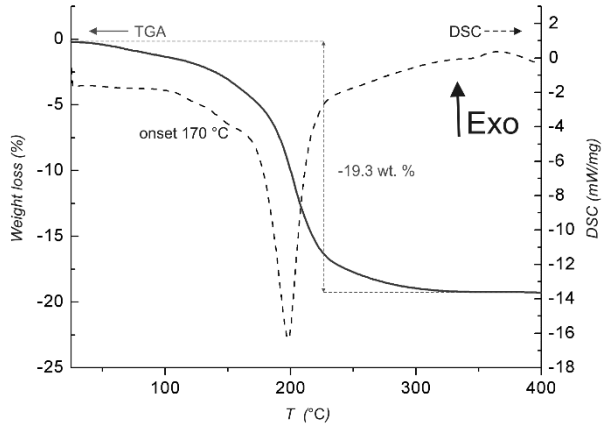

Figure 6.6 – Thermal analysis of $K_9[B_4O_5(OH)_4]_3(CO_3)(BH_4)\cdot 7H_2O$ crystals.

4. Conclusions

Hydrolysis of potassium borohydride in the presence of CO_2 yields an intermediate, containing three anions: the borohydride is almost fully hydrolyzed into tetraborate, with 1/13 of unreacted BH_4^- co-crystallized in the solid, along with a minor amount of the carbonate. The same $K_9[B_4O_5(OH)_4]_3(CO_3)(BH_4)\cdot 7H_2O$ solid is obtained by slow reaction of atmospheric CO_2 with a water solution of KBH_4, as well as upon bubbling the gas through the solution. The latter drastically increases the rate of hydrogen production, and thus enables to hydrolyze KBH_4 on demand, by controlling the CO_2 gas flow. This prompts us to suggest borohydride hydrolysis promoted by CO_2 as a convenient system for the co-generation of hydrogen using spent fossil fuel gases (CO_2 + H_2O). The structural data and the studies in solution, in particular by time-resolved FTIR measurements allow us to suggest the following reaction for the formation of the intermediate:

$$13KBH_4 + 37H_2O + 3CO_2 \rightarrow$$

$$\rightarrow K_9[B_4O_5(OH)_4]_3(CO_3)(BH_4)\cdot 7H_2O + 2K_2CO_3 + 48H_2 \quad (6.2)$$

It produces 16 moles of H_2 per mole of the adsorbed CO_2 and thus is gravimetrically very efficient. This reaction shows gravimetric hydrogen release of 8.4 wt%, higher than the total hydrogen content in KBH_4 (7.5 wt%). Thus it allows converting efficiently carbon dioxide into fuel, H_2. Regarding the yield of H_2 per KBH_4, it reaches 92.3% compared to the complete hydrolysis of all the BH_4^- groups. Carbon dioxide in water solution is a cheap and mild acid which drastically accelerates the hydrolysis of borohydrides. In particular, the hybrid system with CO_2/H_2O exhaust gases used for hydrolysis of borohydrides can achieve two targets: the generation of hydrogen for PEMFCs as an additional source of energy and the capture of carbon dioxide.

Chapter VII – General Conclusions

This work presents several approaches to design new materials with better hydrogen storage properties in the field of complex hydrides. The biggest efforts have been devoted to the family of mixed-cation $M[Al(BH_4)_4]$ ($M = Li^+$, Na^+, K^+, NH_4^+ Rb^+, Cs^+) compounds. They were obtained by the reaction of solid MBH_4 with liquid $Al(BH_4)_3$, the latter is highly unstable and explosive on air. Our synthetic approach excludes the formation of so-called "dead weight" MCl, as well as of the borohydride/chloride solid-state solutions and substitutions previously obtained by milling $AlCl_3 + 3MBH_4$ mixtures. The chloride-free compounds also show different crystal structures, determined by synchrotron X-ray powder diffraction and completed by DFT calculations.

The thermal decomposition properties of $M[Al(BH_4)_4]$ are diverse: $Al(BH_4)_3$ is released below 100 °C for $M = Li^+$ and Na^+, while heavier derivatives evolve hydrogen and diborane at 150 °C. $Li[Al(BH_4)_4]$ firstly decomposes into $Li_4Al_3(BH_4)_{13}$ at 60 °C, desorbing $Al(BH_4)_3$, and the latter decomposes at 90 °C, releasing the rest of the starting borohydrides. Among this family, $NH_4[Al(BH_4)_4]$ occupies a special place, as it contains protic and hydridic hydrogens, recombining into hydrogen already at 35 °C. The major decomposition product was found to be $Al(BH_4)_3{\cdot}NHBH$, which we observed for the first time upon the thermal decomposition of $Al(BH_4)_3{\cdot}NH_3BH_3$.

The experimental decomposition temperatures of metal borohydrides linearly correlate with the square root of the ionic

potential of metal atoms, and the $M[Al(BH_4)_4]$ series falls on the least stable and thus the most practical side. The putative bimetallic Mg–Al and Ca–Al borohydrides are most likely unstable under ambient conditions. Consequently, the title family of Al-based borohydrides is likely complete. The new family of solids with convenient and versatile properties puts aluminum borohydride chemistry in the mainstream research in hydrogen storage, e.g. for the development of reactive hydride composites with an increased hydrogen content.

The alternative way to stabilize $Al(BH_4)_3$ is the reaction with NH_3BH_3, which results in the new molecular compound $Al(BH_4)_3 \cdot NH_3BH_3$. Remarkably, this complex decomposes at ~70 °C, releasing 2 equivalents of pure hydrogen both in toluene solution and upon heating the solid. It shows considerably lower decomposition temperature, compared to the pure NH_3BH_3, desorbing the first equivalent at 120 °C and the second at 150 °C. To our knowledge, this is the first metal borohydride - ammonia borane complex, resulting in pure hydrogen release. This decomposition reaction yields an amorphous intermediate $Al(BH_4)_3 \cdot NHBH$, characterized by NMR methods, which decomposes above 100 °C.

The striking property of the title system is the endothermic dehydrogenation on the first decomposition step (39 kJ/mol, including melting), compared to the exothermic one for the pure ammonia borane (-22 kJ/mol on the first decomposition step, including melting). This feature gives a theoretical possibility for the direct rehydrogenation of $Al(BH_4)_3 \cdot NHBH$, despite our trials were unsuccessful. The absence of complicated mixtures on the dehydrogenation may allow also for a viable chemical recycling of ammonia borane.

The alternative way to obtain hydrogen using new Al-based RHC was also explored in this work. In particular, the chosen RHC system $NaAlH_4$–$4NH_3BH_3$ shows fascinating properties: the reaction proceeds already at 70 °C or under mechanochemical treatment at room temperature. This is the first example of a reaction where a complex hydride anion deprotonates AB. Until now only binary metal hydrides were reacted with AB, forming amidoboranes. The reaction was found to be exothermic, making this RHC nonapplicable as a reversible hydrogen store.

Nevertheless, the properties of the first Al-based amidoborane, $Na[Al(NH_2BH_3)_4]$, look more promising. This compound decomposes in two steps with the formation of $NaBH_4$, 8 equivalents of pure hydrogen and an amorphous product with the presumable composition of $AlN_4B_3H_{(0\div1.8)}$. The latter reversibly reabsorbs about 27% of the released hydrogen. This reabsorption regenerates neither $NaAlH_4$ nor $Na[Al(NH_2BH_3)_4]$ but occurs between the amorphous product and intermediate(s) of the dehydrogenation. The example of $Na[Al(NH_2BH_3)_4]$ decomposition to $AlN_4B_3H_{(0\div1.8)}$ requires further in-depth studies, *viz.* its chemical structure and an optimization of the rehydrogenation.

Perspectives

Our investigations open several potential applications for Al-based coplex hydrides. Firstly, the solid state storage of the unstable $Al(BH_4)_3$ was implemented. The future green rocket bipropellants might be based on $M[Al(BH_4)_4]$ ($M = Li^+$, Na^+) in combination with H_2O_2 or other oxidizing agents. The new series of Al-based complex

borohydrides can also be used in the development of the reactive hydride composites with high hydrogen storage capacity.

The second important result of this work shows the possibility of the endothermic dehydrogenation of ammonia borane in $Al(BH_4)_3 \cdot NH_3BH_3$, giving rise to a possible direct rehydrogenation. A significant drop of the decomposition temperature and the suppression of the undesirable decomposition products are the strong points of this system. Moreover, this model can be developed towards substituted ammonia boranes and other Al salts. We conclude that the decomposition of the staring complex into the Al-based intermediate can be assigned to $Al(BH_4)_3$ as a unique mild Lewis acid which coordinates both the starting and the dehydrogenated BH_n groups (n = 1, 3). This urges to use other Al-based Lewis acids e. g. $AlCl_3$, less challenging with respect to stability and safety than aluminum borohydride. Our work proved the possibility to obtain the other derived complexes, such as $Al(BH_4)_3 \cdot CH_3NH_2BH_3$, which adopts molecular structure similar to $Al(BH_4)_3 \cdot NH_3BH_3$, and the unique autoionized complex $[Al(CH_3NH_2BH_3)_2Cl_2][AlCl_4]$, being an isomer of $AlCl_3 \cdot CH_3NH_2BH_3$. Further analysis of these compounds will help to understand the possibility to improve the hydrogen storage properties of ammonia boranes complexed with Al salts.

Thirdly, the Al-based amidoborane was obtained for the first time and it was shown that it can be partially reversible in terms of hydrogen storage, making it one of the most attractive systems today. Our preliminary experiments show that the reaction of $Na[Al(NH_2BH_3)_4]$ formation easily takes place in a THF solution at room temperature, and these conditions are successfully applied to the

reaction in the $LiAlH_4$-4AB system, uncontrollable in the solid state. Future works can also exploit the combination of amidoborane and borohydride ligands in the same Al-based compound, tuning their stability via different electron donor-acceptor properties of the ligands, e.g. by combining $M[Al(BH_4)_4]$ and $M[Al(NH_2BH_3)_4]$ series. Further investigations on their decomposition products and the conditions of reversibility will shed a light to the possibility to obtain materials for solid-state hydrogen storage.

Appendices

1. Supporting information for Chapter III

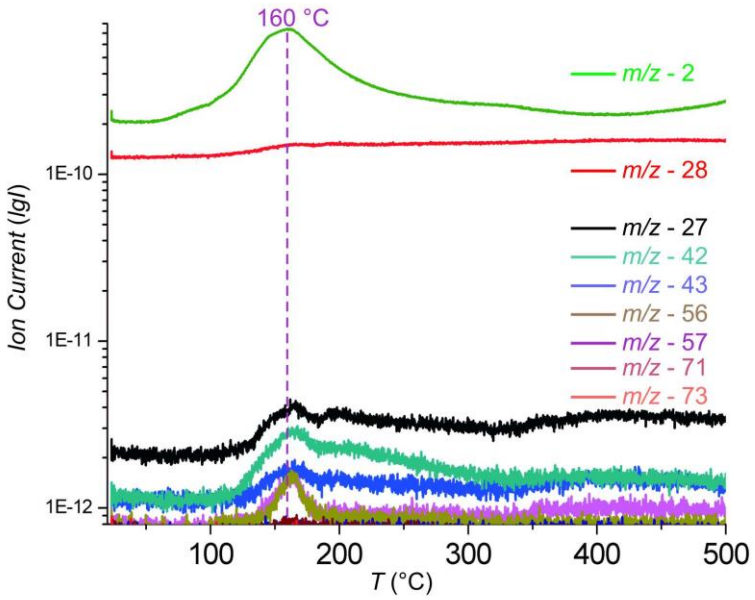

Figure S1.1 – The logarithmic plot of ion current with temperature change. The highest change is observed for H_2^+ at *m/z* = 2. The peak with *m/z* = 27 corresponds to diborane $B_2H_5^+$. The *m/z* = 42, 43, 56 and 57 can indicate an evolution of $Al(BH_4)_3$, however on the linear scale this change is not visible.

2. Supporting information for Chapter IV

Table S2.1 – Crystal structure and refinement data for α,β-$Al(BH_4)_3{\cdot}NH_3BH_3$

Polymorph	α-$Al(BH_4)_3{\cdot}NH_3BH_3$	β-$Al(BH_4)_3{\cdot}NH_3BH_3$
Formula mass	102.37	102.37
T [K]	150(2)	293(2)
λ [Å]	0.82103 (synchrotron)	0.71073 (Mo Kα)
Space group	$P2_1/c$	Cc
Z	4	4
Cell parameters	a = 7.8585(2), b = 6.86473(14), c = 15.7136(8) Å; β = 96.429(4) °.	a = 10.8196(8), b = 7.2809(4), c = 11.3260(9) Å; β = 107.695(8) °.
V [Å^3]	842.36(5)	850.0(1)
ρ_{calc} [g·cm^{-3}]	0.807	0.800
μ [mm^{-1}]	0.198	0.135
F (000)	232	232
θ range max [°]	31.773	25.677
Reflections collected	7815	2629
Independent reflections	1661 [$R_{(int)}$ = 0.0299]	1442 [$R_{(int)}$ = 0.0577]
Completeness	95.0 % (theta: 29.513°)	99.2 % (theta = 25.242°)
Data / restraints / parameters	1661 / 49 / 102	1442 / 120 / 101
Goodness-of-fit	1.082	1.060
R indices [$I \geq 2\sigma(I)$]	R_1 = 0.0280, wR_2 = 0.0768	R_1 = 0.0645, wR_2 = 0.1618
R indices (all data)	R_1 = 0.0301, wR_2 = 0.0780	R_1 = 0.0895, wR_2 = 0.1801
Largest difference peak/hole [eÅ^{-3}]	0.158 and -0.214	0.400 and -0.265

Table S2.2 – Atomic coordinates (x 10^4) and equivalent isotropic displacement parameters (Å^{2}x 10^3) for α-$Al(BH_4)_3{\cdot}NH_3BH_3$. U(eq) is defined as one third of the trace of the orthogonalized U^{ij} tensor.

	x	y	z	U(eq)
Al(1)	6828(1)	1001(1)	6479(1)	16(1)
B(2)	6573(1)	944(1)	7933(1)	19(1)
N(3)	8079(1)	169(1)	8583(1)	22(1)
B(4)	8903(2)	-1246(2)	6544(1)	24(1)
B(5)	4020(1)	1170(2)	6074(1)	19(1)
B(6)	7788(2)	3213(2)	5609(1)	26(1)

Table S2.3 – Hydrogen coordinates (x 10^4) and isotropic displacement parameters ($Å^2$x 10^3) for α-$Al(BH_4)_3 \cdot NH_3BH_3$.

	x	*y*	*z*	U(eq)
H(2A)	6158(14)	-246(16)	7440(7)	29
H(2B)	7083(14)	2209(15)	7559(7)	29
H(2C)	5487(14)	1389(17)	8232(8)	29
H(3A)	8818(8)	-316(11)	8319(2)	33
H(3B)	7713(4)	-659(10)	8893(4)	33
H(3C)	8493(7)	1077(8)	8878(4)	33
H(4A)	9025(17)	311(16)	6814(8)	37
H(4B)	7518(14)	-1402(19)	6224(8)	37
H(4C)	9696(16)	-1350(18)	6043(8)	37
H(4D)	9087(15)	-2257(18)	7077(7)	37
H(5A)	4898(14)	-105(15)	5960(8)	28
H(5B)	4878(14)	2313(16)	6469(7)	28
H(5C)	3554(15)	1783(17)	5498(7)	28
H(5D)	3141(14)	760(16)	6482(7)	28
H(6A)	7267(16)	1663(16)	5431(9)	38
H(6B)	7805(16)	3360(20)	6331(7)	38
H(6C)	9069(14)	3220(20)	5464(9)	38
H(6D)	6938(16)	4275(17)	5312(9)	38

Table S2.4 – Atomic coordinates (x 10^4) and equivalent isotropic displacement parameters ($Å^2$x 10^3) for β-$Al(BH_4)_3 \cdot NH_3BH_3$ U(eq) is defined as one third of the trace of the orthogonalized U^{ij} tensor.

	x	*y*	*z*	U(eq)
Al(1)	4407(5)	-257(2)	3344(4)	44(1)
B(2)	5000(11)	-2272(17)	5000(10)	55(3)
N(3)	4585(9)	-4288(10)	4925(8)	78(2)
B(4)	3894(11)	-2462(18)	1919(9)	65(4)
B(5)	6031(9)	1694(17)	4068(9)	52(3)
B(6)	2760(13)	1670(20)	2603(11)	66(4)

Table S2.5 – Hydrogen coordinates (x 10^4) and isotropic displacement parameters ($Å^2$x 10^3) for β-$Al(BH_4)_3 \cdot NH_3BH_3$.

	x	*y*	*z*	U(eq)
H(2A)	4090(50)	-1350(100)	4760(80)	82
H(2B)	5600(80)	-2110(130)	4320(70)	82
H(2C)	5500(80)	-1880(120)	5870(50)	82
H(3A)	4051	-4525	4171	117
H(3B)	4178	-4508	5486	117
H(3C)	5282	-5004	5074	117
H(4A)	4780(60)	-1490(90)	2210(70)	98
H(4B)	3300(80)	-2050(120)	2570(60)	98
H(4C)	4220(60)	-3780(60)	2130(80)	98
H(4D)	3370(60)	-2140(110)	1030(40)	98
H(5A)	5760(80)	700(90)	3250(50)	79
H(5B)	5180(50)	1330(110)	4450(70)	79
H(5C)	5910(70)	3000(60)	3750(60)	79
H(5D)	6870(50)	1280(90)	4710(50)	79
H(6A)	2950(90)	710(100)	3450(60)	99
H(6B)	3650(50)	1470(130)	2260(80)	99
H(6C)	1970(50)	1180(110)	1920(50)	99
H(6D)	2760(80)	2990(60)	2910(70)	99

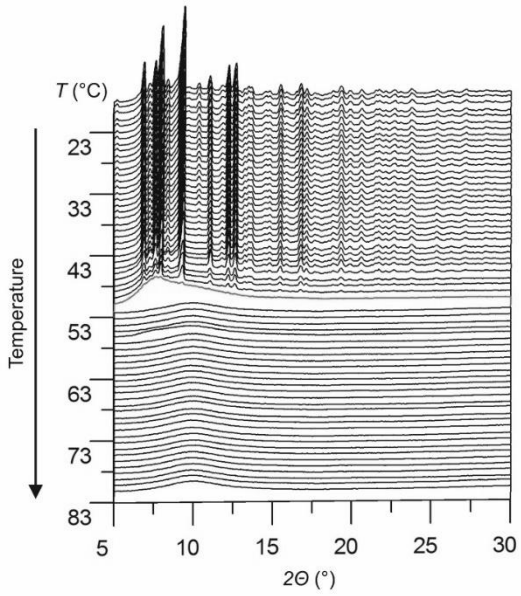

Figure S2.1 – *In-situ* temperature variable X-ray powder diffraction analysis of β-$Al(BH_4)_3 \cdot NH_3BH_3$, with 0.2 °C/min heating rate. The melting temperature is around 52 °C.

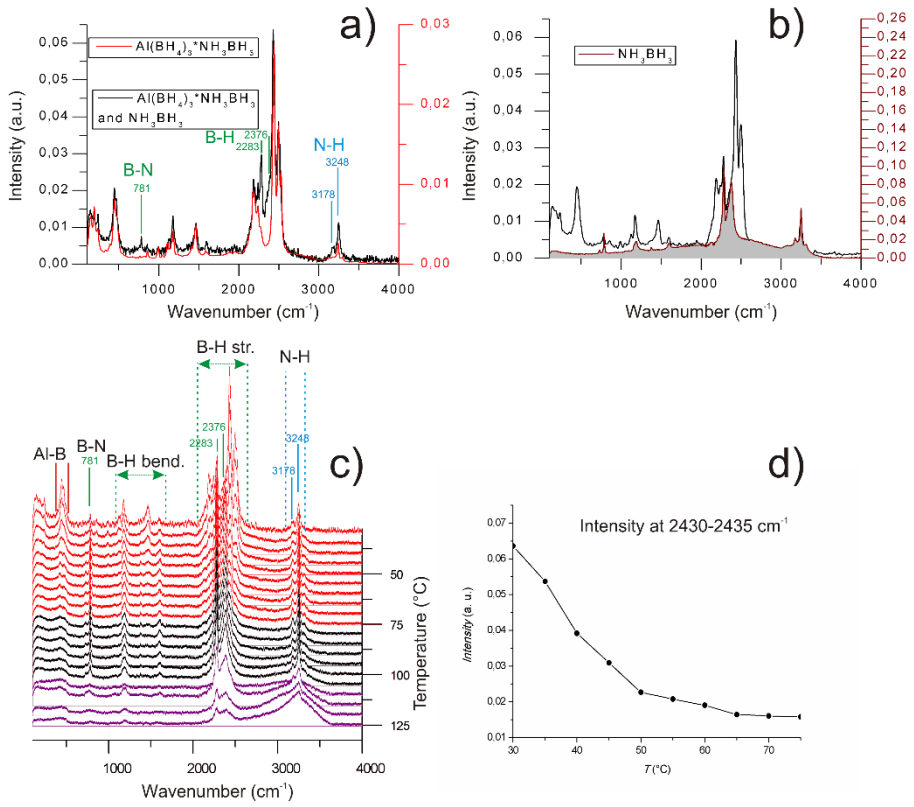

Figure S2.2 – a) and b) The sample, used for variable-temperature Raman measurements, contained some impurity of NH_3BH_3, possibly form the unreacted NH_3BH_3, or due to the slow decomposition of the complex at low temperature (the sample was kept in argon during ~6 months at –35 °C). The comparison between the diffraction-pure $Al(BH_4)_3 \cdot NH_3BH_3$ and the "aged" sample is given in the Fig. S2.3a. The significantly different intensities between samples are highlighted and are characteristic for NH_3BH_3.

c) and d) According to variable-temperature Raman spectroscopy, $Al(BH_4)_3 \cdot NH_3BH_3$ decomposes near 75 °C, depicted by red color in the Fig. S2.3c. The highest drop of its intensities is observed for B–H (corresponding to B–H, coordinated with Al) and Al–B vibration regions. The temperature dependence of the most intense peak at 2430–2435 cm^{-1} is shown in Fig. 2.3d. The peaks of NH_3BH_3 are becoming sharper at higher temperature, however their intensities do not changes significantly until 105 °C, where NH_3BH_3 decomposes. Unfortunately, it is difficult to follow the two-step decomposition of $Al(BH_4)_3 \cdot NH_3BH_3$ in this experiment.

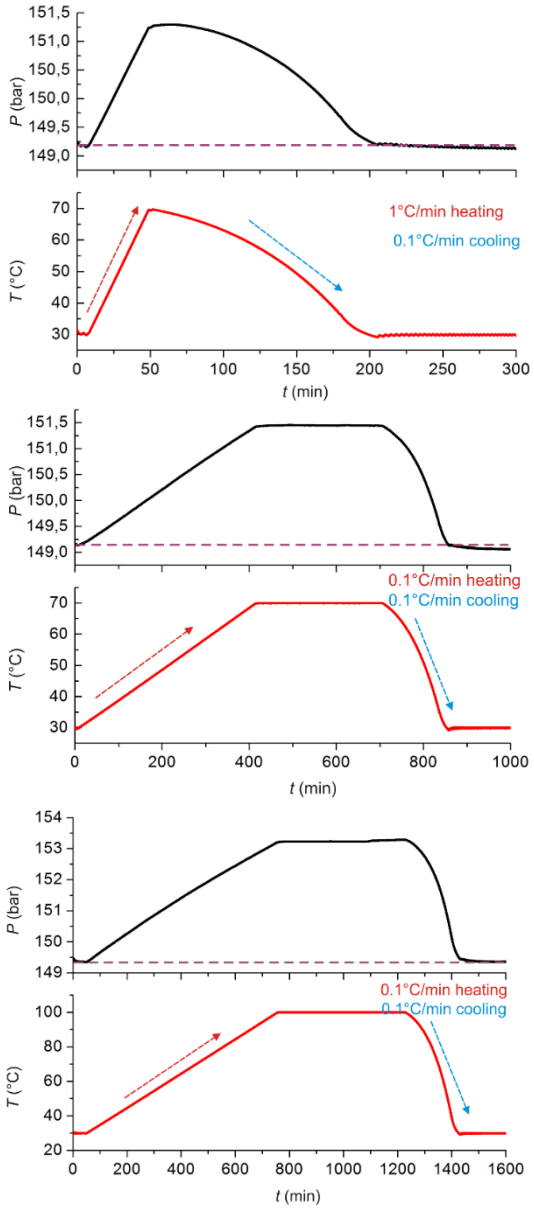

Figure S2.3 – The two cycles of $Al(BH_4)_3 \cdot NH_3BH_3$ regeneration (top and middle) decomposed at 70 °C and 1 cycle at 100 °C (boom). The pressure before applying ~150 bar of hydrogen at 30 °C and after heating it to 70°C (top and middle) with 100 °C (bottom) with cooling back to 30 °C doesn't significantly differ after cycles. The pressure changes are correlated to temperature variation rather than to chemical adsorption.

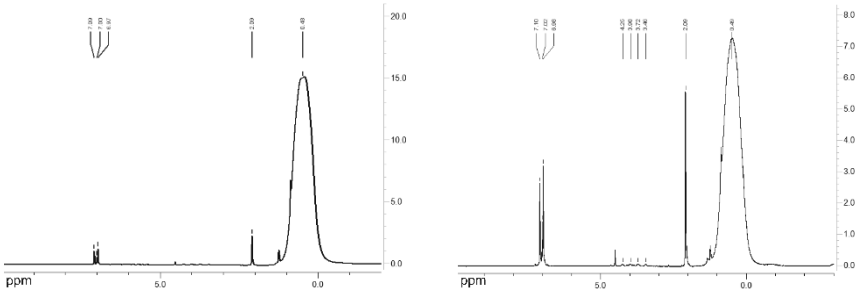

a) b)

Figure S2.4 – a) and b) ^{1}H NMR spectra of freshly obtained $Al(BH_4)_3$ in toluene-d_8, where concentration of $Al(BH_4)_3$ in spectrum a) is higher than in spectrum b).

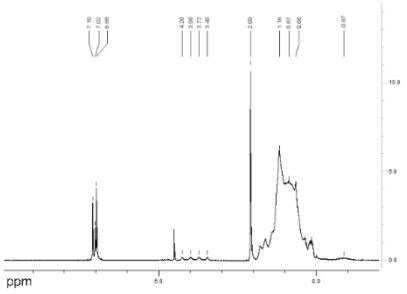

Figure S2.5 – ^{1}H NMR spectra of freshly dissolved $Al(BH_4)_3 \cdot NH_3BH_3$ in toluene-d_8.

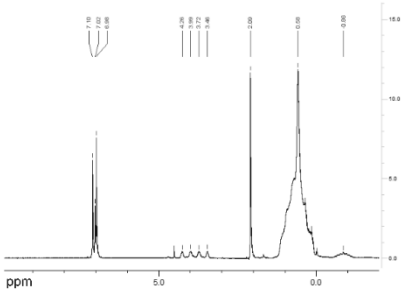

Figure S2.6 – ^{1}H NMR spectra $Al(BH_4)_3 \cdot NH_3BH_3$ in d_8 toluene after 18 hours.

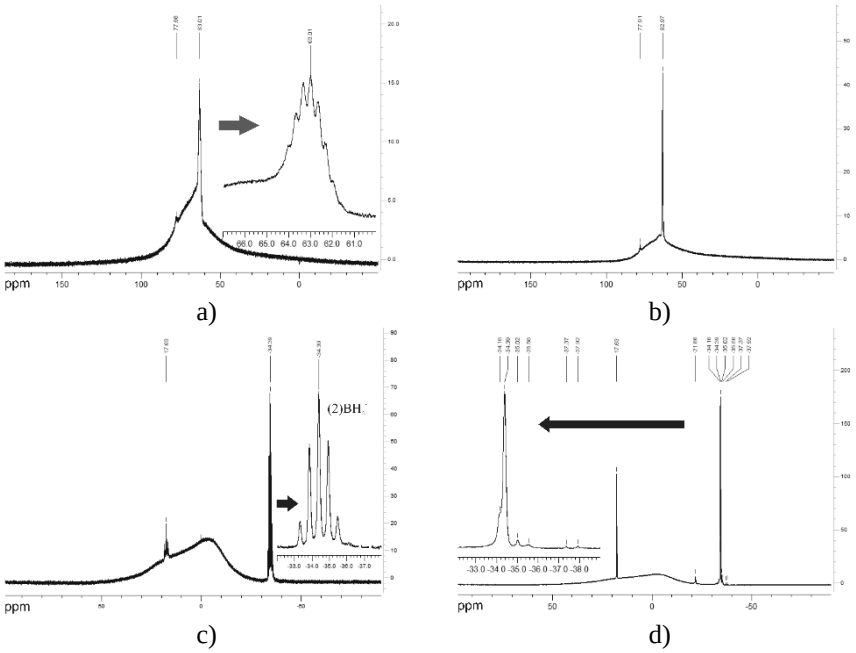

Figure S2.7 – a) ^{27}Al and b) ^{27}Al{H} NMR spectra of $Al(BH_4)_3{\cdot}NH_3BH_3$ in toluene-d_8 after 2 hours; c) ^{11}B and d) ^{11}B{H} NMR spectra of $Al(BH_4)_3{\cdot}NH_3BH_3$ in toluene-d_8 after 2 hours.

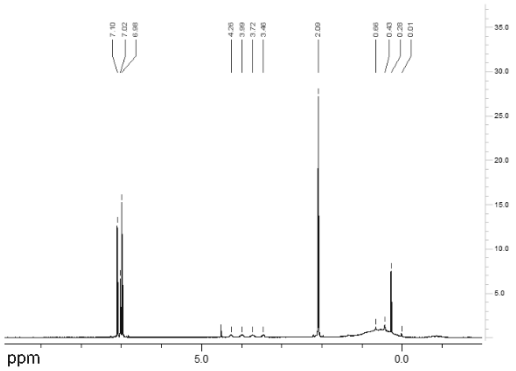

Figure S2.8 – ^{1}H NMR spectra $Al(BH_4)_3{\cdot}NH_3BH_3$ in toluene-d_8 after heating to 100 °C.

Table S2.6 – Crystal structure and refinement data for $AlX_3 \cdot L$

Compound	$[Al(CH_3NH_2BH_3)_2Cl_2][AlCl_4]$	$Al(BH_4)_3 \cdot CH_3NH_2BH_3$	$[Al(en)(BH_4)_2][Al(BH_4)_4]$
Formula mass	356.45	116.40	203.11
T [K]	150(2)	150(2)	150(2)
λ [Å]	0.71073 (Mo Kα)	0.71073 (Mo Kα)	0.71073 (Mo Kα)
Space group	*Pbca*	*P*–1	$P2_1/c$
Z	8	2	4
Cell parameters a, b, c [Å]	a = 12.5826(5) b = 12.6510(5) c = 20.4039(8)	a = 6.2764 (3) b = 7.9566 (5) c = 10.3058 (8)	a = 8.4168(5), b = 12.0021(7) c = 16.2933(12)
α, β, γ [°]		α = 70.277(7) β = 74.744 (5) γ = 86.041 (4)	β = 101.886(7)
V [Å^3]	3247.9(2)	467.28(6)	1610.66(18)
ρ_{calc} [g·cm^{-3}]	1.458	0.827	0.838
μ [mm^{-1}]	1.14	0.13	0.14
F (000)	1440	132	456
θ range max [°]	25.187	25.348	25.027
Reflections collected	11779	5863	9112
Independent reflections	2927 [$R_{(int)}$ = 0.088]	5863	2807 [$R_{(int)}$ = 0.119]
Completeness	99.5 % (theta = 25.242°)	99.8 % (theta = 25.242°)	98.6 % (theta = 25.242°)
Data / restraints / parameters	2927 / 0 / 133	5863 / 30 / 106	2807 / 32 / 181
Goodness-of-fit	1.02	1.02	1.16
R indices [$I \geq 2\sigma(I)$]	R_1 = 0.042, wR_2 = 0.086	R_1 = 0.040, wR_2 = 0.124	R_1 = 0.102, wR_2 = 0.174
R indices (all data)	R_1 = 0.077, wR_2 = 0.075	R_1 = 0.060, wR_2 = 0.118	R_1 = 0.15, wR_2 = 0.16
Largest difference peak/hole [eÅ^{-3}]	0.39 and –0.33	0.29 and –0.23	0.36 and –0.25

Table S2.7 – Atomic coordinates (x 10^4) and equivalent isotropic displacement parameters ($Å^2$x 10^3) for $[Al(CH_3NH_2BH_3)_2Cl_2][AlCl_4]$, U(eq) is defined as one third of the trace of the orthogonalized U^{ij} tensor.

	x	*y*	*z*	U(eq)
Al(1)	36163(10)	62198(8)	57885(5)	21.8(3)
Cl(2)	42864(9)	70958(7)	65643(4)	35.3(3)
Cl(3)	41216(8)	69067(7)	48806(4)	28.2(2)
B(4)	1875(4)	6119(3)	5558(2)	28.8(10)
N(5)	1450(3)	6695(2)	49317(14)	29.8(8)
C(6)	741(4)	6021(3)	45297(18)	35.4(10)
B(7)	4046(4)	4573(3)	61209(19)	25.2(10)
N(8)	4945(3)	4448(2)	66407(13)	29.7(8)
C(9)	4612(4)	3787(3)	72088(17)	39.8(12)
Al(11)	26534(10)	65031(8)	83288(5)	22.5(3)
Cl(12)	18382(9)	58793(7)	75025(4)	33.0(3)
Cl(13)	18734(9)	59285(7)	92014(4)	27.9(2)
Cl(14)	42738(9)	60516(8)	83434(5)	40.8(3)
Cl(15)	25682(9)	81945(7)	83369(5)	32.3(3)

Table S2.8 – Hydrogen coordinates (x 10^4) and isotropic displacement parameters ($Å^2$x 10^3) for $[Al(CH_3NH_2BH_3)_2Cl_2][AlCl_4]$.

	x	*y*	*z*	U(eq)
H(4A)	1194(12)	5732(16)	5822(8)	43
H(4B)	2265(17)	6710(11)	5892(8)	43
H(4C)	2471(16)	5501(16)	5411(3)	43
H(5A)	10890	72850	50560	36
H(5B)	20120	69030	46830	36
H(6A)	11010	53530	44290	53
H(6B)	05670	63870	41210	53
H(6C)	860	58750	47740	53
H(7A)	3774(12)	3743(13)	5945(8)	38
H(7B)	4364(8)	5053(16)	5677(8)	38
H(7C)	3331(13)	5015(16)	6353(5)	38
H(8A)	55230	41490	64480	36
H(8B)	51380	51000	67880	36
H(9A)	39680	40860	74050	60
H(9B)	51820	37760	75360	60
H(9C)	44680	30650	70590	60

Table S2.9 – Atomic coordinates (x 10^4) and equivalent isotropic displacement parameters ($Å^2$x 10^3) for $Al(BH_4)_3 \cdot CH_3NH_2BH_3$, U(eq) is defined as one third of the trace of the orthogonalized U^{ij} tensor.

	x	*y*	*z*	U(eq)
Al(1)	49960(8)	67166(7)	20222(5)	20.1(2)
B(2)	5562(3)	3728(3)	3236(2)	24.7(5)
N(3)	7721(2)	27647(19)	26978(16)	24.1(4)
C(4)	8693(3)	1588(3)	03846(2)	32.6(5)
B(5)	1345(4)	6589(3)	2903(3)	29.9(5)
B(6)	5806(4)	9341(3)	2111(3)	28.9(5)
B(7)	7433(4)	6739(3)	-0013(2)	26.3(5)

Table S2.10 – Hydrogen coordinates (x 10^4) and isotropic displacement parameters ($Å^2$x 10^3) for $Al(BH_4)_3 \cdot CH_3NH_2BH_3$.

	x	*y*	*z*	U(eq)
H(2A)	6158(14)	-246(16)	7440(7)	37
H(2B)	4689(14)	4238(15)	2382(10)	37
H(2C)	6008(6)	4853(16)	3521(13)	37
H(3A)	74270	21190	21950	29
H(3B)	87480	36020	21050	29
H(4A)	90730	22940	43730	49
H(4B)	300	10490	34250	49
H(4C)	76200	06440	44980	49
H(5A)	271(3)	641(3)	352(2)	45
H(5B)	234(3)	682(3)	1722(16)	45
H(5C)	042(3)	536(2)	325(2)	45
H(5D)	054(3)	779(2)	301(2)	45
H(6A)	488(3)	906(3)	135(2)	43
H(6B)	620(4)	792(2)	284(2)	43
H(6C)	738(3)	996(3)	147(2)	43
H(6D)	473(3)	000(3)	279(2)	43
H(7A)	551(2)	686(3)	20(2)	39
H(7B)	783(3)	662(3)	1064(16)	39
H(7C)	789(3)	549(2)	-21(2)	39
H(7D)	821(3)	797(2)	-77(2)	39

Table S2.11 – Atomic coordinates (x 10^4) and equivalent isotropic displacement parameters ($Å^2$x 10^3) for $[Al(NH_2CH_2CH_2NH_2)(BH_4)_2][Al(BH_4)_4]$, U(eq) is defined as one third of the trace of the orthogonalized U^{ij} tensor.

	x	*y*	*z*	U(eq)
Al(1)	67800(17)	42122(12)	17204(9)	29.1(4)
B(2)	8644(8)	5312(6)	1432(5)	42.3(16)
B(3)	4273(8)	4737(6)	1359(5)	49.8(18)
N(4)	7608(4)	2766(3)	1457(2)	30.9(10)
C(5)	8414(6)	2237(4)	2262(3)	37.7(13)
C(6)	7319(6)	2422(4)	2877(3)	36.1(12)
N(7)	6876(5)	3624(3)	2850(2)	34.1(10)
Al(11)	25537(17)	34359(11)	49655(9)	27.6(4)
B(12)	4083(6)	3982(4)	6213(3)	19.5(11)
B(13)	4606(8)	2939(6)	4357(4)	39.7(15)
B(14)	627(8)	2534(6)	5451(5)	46.6(17)
B(15)	976(9)	4330(6)	3883(5)	49.8(18)

Table S2.12 – Hydrogen coordinates (x 10^4) and isotropic displacement parameters ($Å^2$x 10^3) for $[Al(NH_2CH_2CH_2NH_2)(BH_4)_2][Al(BH_4)_4]$.

	x	*y*	*z*	U(eq)
H(2A)	847(6)	504(4)	2057(17)	63
H(2B)	760(4)	496(4)	098(2)	63
H(2C)	848(6)	6143(16)	143(3)	63
H(2D)	965(4)	495(4)	131(3)	63
H(3A)	531(4)	521(4)	173(3)	75
H(3B)	479(6)	396(3)	115(3)	75
H(3C)	357(6)	444(4)	174(3)	75
H(3D)	376(6)	522(4)	087(2)	75
H(4A)	67790	23300	11880	37
H(4B)	83320	28540	11170	37
H(5A)	94900	25800	24730	45
H(5B)	85680	14300	21800	45
H(6A)	63290	19590	27220	43
H(6B)	78890	22130	34500	43
H(7A)	76280	40080	32250	41
H(7B)	58940	37090	29930	41
H(12A)	395(5)	3109(17)	600(3)	29
H(12B)	336(4)	453(3)	574(2)	29
H(12C)	353(5)	400(3)	6700(19)	29
H(12D)	525(2)	420(3)	633(3)	29
H(13A)	377(5)	239(3)	461(3)	60
H(13B)	431(6)	3802(19)	451(3)	60
H(13C)	578(3)	282(4)	463(3)	60
H(13D)	430(6)	286(4)	3729(11)	60
H(14A)	82(6)	3446(16)	547(3)	70
H(14B)	154(5)	217(4)	513(3)	70
H(14C)	81(6)	228(4)	6054(15)	70
H(14D)	-47(3)	236(4)	509(3)	70
H(15A)	119(6)	3421(16)	392(4)	75
H(15B)	172(5)	475(4)	443(2)	75
H(15C)	147(6)	460(4)	340(3)	75
H(15D)	-19(3)	443(5)	393(4)	75

3. Supporting information for Chapter V

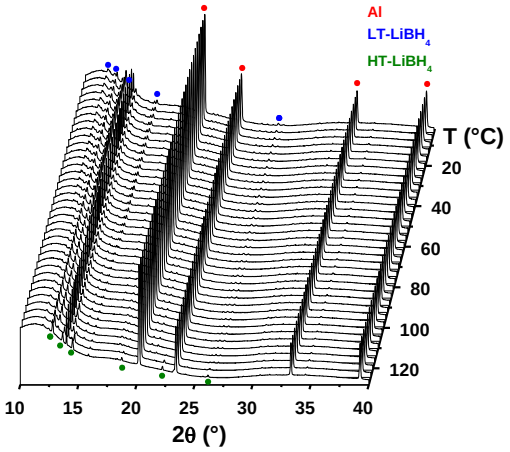

Figure S3.1 – The variable temperature plot of XRPD patterns of the $LiAlH_4$–4AB composite after ball milling (SNBL/SRF synchrotron, λ = 0.823065 Å). Transformation of the low temperature (LT) orthorhombic polymorph, present alongside with metallic aluminium, to high temperature (HT) hexagonal form of $LiBH_4$ was found.

Table S3.1 – Atomic coordinates and isotropic atomic displacements for $Na[Al(NH_2BH_3)_4]$.

		Experimental data				DFT data		
Atom	Wyck.	*x*	*y*	*z*	U [Å^2]	*x*	*y*	*z*
Na1	2i	0.1429(6)	0.7228(7)	0.0397(6)	0.059(2)	0.14514	0.71106	0.05273
Al1	2i	0.2803(4)	0.2439(5)	0.6364(6)	0.0256(15)	0.28000	0.24528	0.63692
N1	2i	0.6581(9)	0.8779(9)	0.1606(10)	0.0113(15)	0.65158	0.87372	0.14871
N2	2i	0.3017(8)	0.1254(9)	0.4168(10)	0.0113(15)	0.30791	0.11082	0.42315
N3	2i	0.6104(7)	0.5401(11)	0.3135(10)	0.0113(15)	0.61196	0.53865	0.32940
N4	2i	0.0694(8)	0.2757(9)	0.5947(11)	0.0113(15)	0.07273	0.28206	0.59668
B1	2i	0.6745(14)	0.0820(15)	0.2292(16)	0.0113(15)	0.67187	0.07873	0.22372
B2	2i	0.1600(12)	0.0768(14)	0.2338(15)	0.0113(15)	0.16229	0.06401	0.24040
B3	2i	0.4316(14)	0.5769(17)	0.2511(16)	0.0113(15)	0.43403	0.56381	0.25547
B4	2i	0.0400(13)	0.4176(14)	0.7461(15)	0.0113(15)	0.03852	0.42232	0.74857
H11	2i	0.5492(9)	0.8461(9)	0.0759(10)	0.0113(15)	0.54267	0.84192	0.06405
H12	2i	0.7217(9)	0.8486(9)	0.0749(10)	0.0113(15)	0.71518	0.84437	0.06305
H13	2i	0.5736(14)	0.1235(15)	0.2926(16)	0.0113(15)	0.57088	0.12017	0.28711
H14	2i	0.7968(14)	0.1085(15)	0.3532(16)	0.0113(15)	0.79412	0.10525	0.34767
H15	2i	0.6691(14)	0.1682(15)	0.1022(16)	0.0113(15)	0.66646	0.16491	0.09674
H21	2i	0.3474(8)	1.0100(9)	0.4582(10)	0.0113(15)	0.35354	0.99539	0.46458
H22	2i	0.3814(8)	0.1869(9)	0.3787(10)	0.0113(15)	0.38761	0.17236	0.38507
H23	2i	0.0810(12)	1.9684(14)	0.2672(15)	0.0113(15)	0.08332	1.95558	0.27376
H24	2i	0.0921(12)	0.1973(14)	0.2024(15)	0.0113(15)	0.90745	0.80433	0.79709
H25	2i	0.2030(12)	0.0065(14)	0.1080(15)	0.0113(15)	0.79656	0.99508	0.89143
H31	2i	0.6370(7)	0.4907(11)	0.4395(10)	0.0113(15)	0.63858	0.48928	0.45533
H32	2i	0.6375(7)	0.4441(11)	0.2252(10)	0.0113(15)	0.63902	0.44268	0.24106
H33	2i	0.4026(14)	0.7053(17)	0.3457(16)	0.0113(15)	0.40506	0.69218	0.35008
H34	2i	0.6018(14)	0.4240(17)	0.9047(16)	0.0113(15)	0.60423	0.41090	0.90910
H35	2i	0.6308(14)	0.5796(17)	0.7274(16)	0.0113(15)	0.63331	0.56648	0.73172
H41	2i	0.0137(8)	0.1604(9)	0.5918(11)	0.0113(15)	0.01702	0.16681	0.59381
H42	2i	0.0188(8)	0.3111(9)	0.4632(11)	0.0113(15)	0.02217	0.31748	0.46516
H43	2i	0.9041(13)	0.4331(14)	0.7070(15)	0.0113(15)	0.90263	0.43780	0.70941
H44	2i	0.0951(13)	0.3714(14)	0.9023(15)	0.0113(15)	0.09364	0.37612	0.90474
H45	2i	0.0989(13)	0.5590(14)	0.7446(15)	0.0113(15)	0.09738	0.56368	0.74708

Table S3.2 – Calculated lattice parameters for $NaAlH_4$, NH_3BH_3 and $Na[Al(NH_2BH_3)_4]$.

	$NaAlH_4$ (Å)	**NH_3BH_3 (Å)**	**$Na[Al(NH_2BH_3)_4]$ (Å, °)**
Present without van der Waals interactions	a = 4.999, c = 11.122	a = 5.209, b = 4.988, c = 5.447	a = 9.435, b = 7.719, c = 7.625; α = 97.21, β = 109.22, γ = 89.73
Present with van der Waals interactions	a = 4.746, c = 10.572	a = 5.576, b = 4.269, c = 4.768	a = 9.056, b = 7.290, c = 7.241; α = 97.89, β = 110.28, γ = 88.53
Experimental data	a = 5.0265, c = 11.3706[1] a = 5.0398, c = 11.4319[a]	a = 5.395, b = 4.887, c = 4.986[2]	a = 9.4352, b = 7.7198, c = 7.6252; α = 97.211; β = 109.223, γ = 89.728[a]
Calculated data	a = 5.0004, c = 11.1141[3]	a = 5.172, b = 4.968, c = 5.612[4]	

[a] Obtained in this work at 100 °C.

[1] Gross, K. J.; Guthrie, S.; Takara S. et al. *J. Alloys Compd.* **2000**, *297*, 270–281.

[2] Klooster, W. T.; Koetzle, T. F.; Siegbahn, P. E. M. et al. *J. Am. Chem. Soc.* **1999**, *121*, 6337–6343.

[3] Frankcombe, T. J.; Løvvik, O. M. *J. Phys. Chem. B* **2006**, *110*, 622–630.

[4] Bheema Lingam, C.; Ramesh Babu, K.; Tewari S. P.; *J. Comput. Chem*. **2011**, *32*, 1734–1742.

Table S3.3 – Dihydrogen bond lengths (Å) and angles (°) for in $Na[Al(NH_2BH_3)_4]$.

	Experimental data		**DFT data**	
$N–H^{\delta+}\cdots H^{\delta-}–B$	d(H···H)	∠(N–H···H)	d(H···H)	∠(N–H···H)
N(1)–H(11)···H(15)–B(1)	2.06(2)	169.0(8)	1.95	167.8
N(1)–H(12)···H(25)–B(2)	2.18(1)	134.4(7)	2.17	133.5
N(2)–H(22)···H(13)–B(1)	2.16(2)	139.3(8)	2.12	141.7
N(3)–H(31)···H(35)–B(3)	2.24(1)	137.2(8)	2.13	138.8
N(3)–H(32)···H(15)–B(1)	2.28(1)	157.6(8)	2.34	160.2
N(4)–H(41)···H(23)–B(2)	1.96(1)	143.9(8)	1.92	144.0
N(4)–H(42)···H(45)–B(4)	2.00(1)	162.1(8)	1.97	163.9

4. Supporting information for Chapter VI

Table S4.1 - Elemental analysis of carbon and hydrogen.

Element	C	H	N
% Theory	1.08	2.56	
% Found	1.11	2.80	<0.10

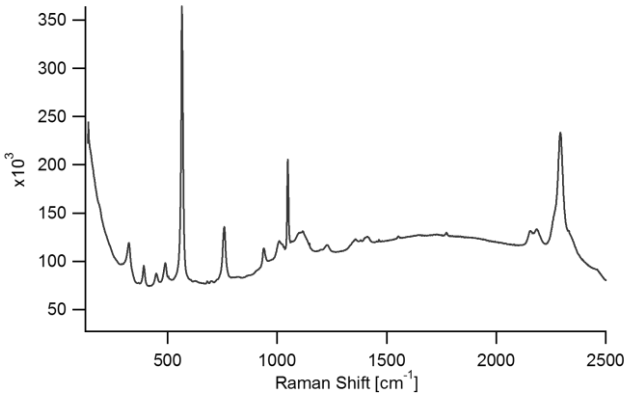

Figure S4.1 – Raman spectrum of the title compound excited at 488nm. It corresponds well to the spectrum excited at 532 nm (Figure 6.3)

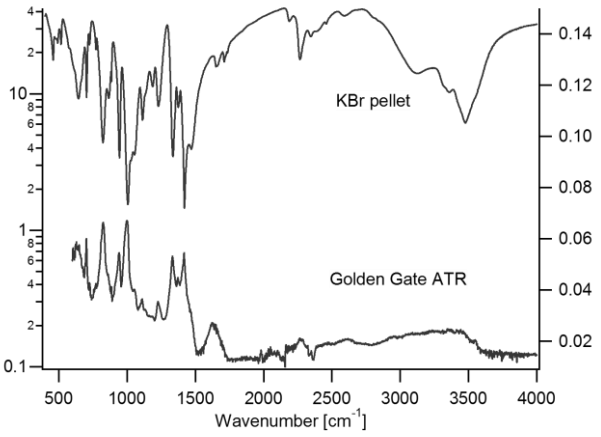

Figure S4.2 – Comparison of the transmission IR spectrum of a KBr pellet with the title compound upper trace) with the ATR FT-IR of a neat sample. The B–H stretches at 2300 cm^{-1} do not appear well for this ATR spectrum, as this region is equally subject to the diamond absorption by the ATR cell.

5. In Pursuit of the Crystal Structure of $Ti(BH_4)_3$

5.1 Motivation

As it was mentioned in the Chapter V, the presence of Ti in alanates allows for their rehydrogenation.[27] The mechanism of the reactions between complex hydrides and these additives is still not fully knonw,[291] that is why any information on Ti-containing hydrides is of interest for hydrogen storage community. In particular, $Ti(BH_4)_3$ is among the least investigated borohydrides due to its extreme reactivity and instability. The investigations of gaseous $Ti(BH_4)_3$ reveals autocatalytic decomposition at 25 °C.[292] Serious difficulties of the characterization of $Ti(BH_4)_3$ in the solid state allowed only for the gas-phase studies. Hence, the structure of gaseous $Ti(BH_4)_3$ has been characterized using electron diffraction[293] and photoelectron spectroscopic methods.[294] Due to the recent development of X-ray powder diffraction methods, which allow to determine compounds at low temperatures and inert conditions, we tried to determine the crystal structure of $Ti(BH_4)_3$.

5.2 Experiments and Preliminary Results

Synthesis. The synthesis of $Ti(BH_4)_3$ has been performed, using the commercially available $TiCl_4$ (Sigma-Aldrich, ≥99 %) and $LiBH_4$ (Boss chemical industry Co., 96 %). The reaction (7.1) between the reagents was performed in the inert glove box according to the simplified procedure, described by Refs.[292,293]:

$$2TiCl_4 + 8LiBH_4 \rightarrow 2Ti(BH_4)_3 + 8LiCl + B_2H_6 + H_2 \qquad (7.1)$$

Presumably $Ti(BH_4)_3$ was prepared by passing a stream of $TiCl_4$ vapor thought a layer of powdered $LiBH_4$ (situated under the dry glass filter) at room temperature. The volatile products were removed under continuous vacuum and trapping at 77 K. During the reaction, the products were condensing on the glass under dynamic vacuum, with formation of greenish (at room temperature) and down the vacuum line of purple (77 K) colour, in accordance to the phase transitions of $Ti(BH_4)_3$ described in the literature. For the transportation, the trapped products were kept in the dry ice before the synchrotron X-ray powder diffraction measurements.

Variable-temperature synchrotron X-ray powder diffraction determination. The synchrotron measurements were performed at SNBL (Grenoble, France). The trapped purple powder was placed under nitrogen atmosphere on the copper plate partly submerged in the liquid nitrogen. The sample was loaded on the cold surface and manipulated under the microscope. It was mouned on the MicroMeshes pin, frozen in LN2 and put rapidly under the nitrogen stream at 100 K. The gas flow was gradually heated (6 °C/min) from 100 K to 400 K, see the diffraction data in Figure 7.1.

According to the variable-temperature powder diffraction, three different regions can be recognized: at 100−245 K, at 245−317 K and above 317 K, they are depicted by black, red and blue colors, respectively in the Figure 7.1. In the first region we saw two different crystalline phases, their diffraction peaks vanishing at 245 and 317 K. The more stable of the two phases was identified as $TiCl_3 \cdot 6H_2O$.[295]

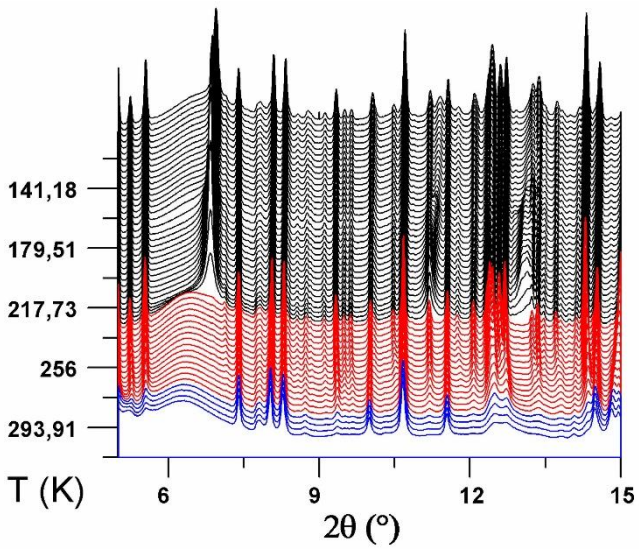

Figure 7.1 – Temperature evolution of X-ray powder diffraction patterns from $TiCl_4$ reacted with $LiBH_4$ (SNBL, λ = 0.823065 Å).

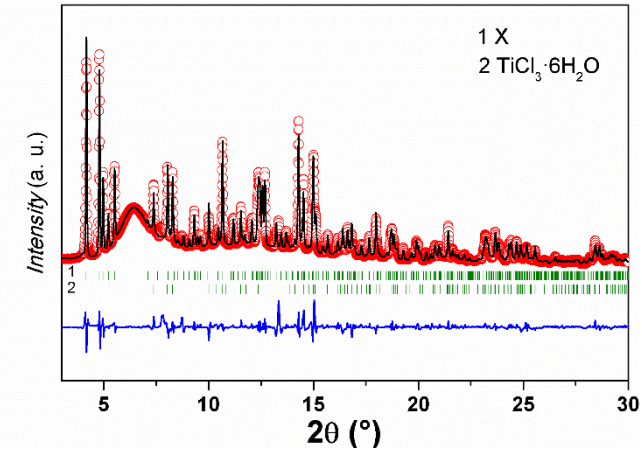

Figure 7.2 – The phase analysis of $TiCl_4$ reacted with $LiBH_4$ (SNBL, λ = 0.823065 Å) collected at 245 K. The phase of "X" was refined in Le Bail mode (SG. *I*2/*m* *a* = 18.3733(9); *b* = 11.7120(6); *c* = 12.6878(6) Å; *β* = 100.632(4)°).

The data below 245 K are difficult to analyze, due to the broadening of the diffraction peaks with a simple unknown phase. That is why we focused our attention on the second phase, "X" at the point when the broad peaks disappear. The indexing in DICVOL[166] of the

resolved diffraction peaks of “X”, suggested the monoclinic unit cell. Le Bail fit with the space group *I*2/*m* fits well the diffraction pattern, see Figure 7.2. The obtained unit cell volume of 2683.4(2) $Å^3$ of the phase “X” is very close to one of 2652 $Å^3$ for α-$Al(BH_4)_3$ (space group *C*2/*c*),[66] supporting the likely composition $Ti(BH_4)_3$. However, neither crystal structure of α-$Al(BH_4)_3$, nor direct space method of crystal structure solution in FOX[167] succeed with possible $Z = 16$ of $Ti(BH_4)_3$ in this lattice.

In conclusion, this volume of the unit cell, as well as the decomposition temperature near 40 °C are suggesting the presence of $Ti(BH_4)_3$ (decomposing at 25 °C) or its chlorine-containing derivative, e.g. $TiCl(BH_4)_2$.[292] Moreover, the complex of $TiCl_3 \cdot 6H_2O$ confirms the reduction of Ti^{4+} to Ti^{3+}. Unfortunately, the presence of H_2O is undesirable for the further investigations, as numerous unwanted products can form. That is likely why our efforts to solve the crystal structure of “X” did not succeed. For the further analysis of the products of the reaction 7.1, it is necessary to improve the synthesis procedure, both for the synthetic and for X-ray powder diffraction procedures.

Publications

1. Articles published/submitted to peer-review journals:

1.1 **Dovgaliuk**, **I.**; Ban, V.; Sadikin, Y.; Ĉerny, R.; Aranda, L.; Casati, N.; Devillers, M.; Filinchuk, Y. The first halide-free bimetallic aluminum borohydride: synthesis, structure, stability, and decomposition pathway, *J. Phys. Chem. C* **2014**, *118*, 145−153.

1.2 **Dovgaliuk**, **I.**; Hagemann, H.; Leyssens, T.; Devillers, M.; Filinchuk, Y. CO_2-promoted hydrolysis of KBH_4 for efficient hydrogen co-generation, *Int. J. Hydr. Energy* **2014**, *39*, 19603−19608.

1.3 **Dovgaliuk**, **I.**; Le Duff, C. S.; Robeyns, K.; Devillers, M.; Filinchuk, Y. Mild dehydrogenation of ammonia borane complexed with aluminum borohydride, *Chem. Mater.* **2015**, 27, 768−777.

1.4 **Dovgaliuk, I.**; Safin, D. A.; Jepsen, L. H.; Lodziana, Z.; Dyadkin, V.; Jensen, T. R.; Devillers, M.; Filinchuk, Y. A composite of complex and chemical hydrides yields the first Al-based amidoborane with improved hydrogen storage properties, *Chem. Eur. J.* **2015**, DOI: 10.1002/chem.201501302

1.5 **Dovgaliuk, I.**; Safin, D. A.; Tumanov, N. A.; Morelle, F.; Ĉerny, R.; Łodziana, Z.; Devillers, M.; Filinchuk, Y. Stabilizing explosive aluminum borohydride in a $M[Al(BH_4)_4]$ series with versatile properties beneficial for hydrogen storage, *Adv. Funct. Mater. submitted*.

2. Abstracts of presentations at the international conferences (the presenting author is underlined)

2.1 **Dovgaliuk, I.**; Hagemann, H.; Devillers, M.; Filinchuk, Y. CO_2–boosted hydrolysis of KBH_4, *International Symposium on Metal-Hydrogen Systems 2012 (MH2012)*, **2012**, Kyoto, Japan / poster.

2.2 Filinchuk, Y.; **Dovgaliuk, I.**; Ban, V.; Tumanov, N.; Morelle, F. Hybrid hydride materials, *E-MRS Fall Meeting – Symposium C – "Nanostructured Materials for solid State Hydrogen Storage"*, **2013**, Warsaw, Poland / oral.

2.3 **Dovgaliuk, I.**; Černý R.; Devillers, M.; Filinchuk Y. Novel Alkali-Metal-Aluminum Borohydrides, *Gordon Research Conference (GRC) on Hydrogen-Metal Systems*, **2013**, Lucca, Italy / poster.

2.4 **Dovgaliuk, I.**; le Duff, C.; Robeyns, K.; Devillers, M.; Filinchuk Y. Crystal Structures and Decomposition Properties of Hydrogen-Rich $Al(BH_4)_3 \cdot NH_3BH_3$ Complex, *International Symposium on Metal-Hydrogen Systems 2014 (MH2014)*, **2014**, Manchester, UK. / oral.

2.5 Filinchuk, Y.; Ban, V.; Morelle, F.; Tumanov, N.; **Dovgaliuk, I.**; Černy, R.; Sadikin, Y.; Schouwink, P. Mechanochemical synthesis of hydrides followed in situ by X-ray diffraction, *International Symposium on Metal-Hydrogen Systems 2014 (MH2014)*, **2014**, Manchester, UK. / oral.

2.6 **Dovgaliuk, I.**; Safin, D. A.; Jepsen, L. H.; Łodziana, Z.; Dyadkin, V.; Jensen, T. R.; Devillers, M.; Filinchuk, Y. The Crystal Structure and Decomposition Properties of the First Al-based

Amidoborane from in situ X-ray Powder Diffraction, 29th European Crystallographic Meeting (ECM29), **2015**, Rovinj, Croatia / oral.

2.7 Picasso, C.; **Dovgaliuk, I.**; Filinchuk, Y. Reduction of CO_2 by KBH_4 at mild conditions, *E-MRS Fall Meeting – Symposium C – "Hydrogen Storage in Solids: Materials, Systems and Application Trends"*, **2015**, Warsaw, Poland / oral.

3. Presentations at local meetings:

3.1 **Dovgaliuk, I.**; Hagemann, H.; Devillers M.; Filinchuk Y. CO_2–promoted hydrolysis of KBH_4, *Journée de L'école doctorale CHIM*, 16 November **2012**, Louvain-la-Neuve, Belgium / poster.

3.2 **Dovgaliuk, I.**; Devillers M. and Y. Filinchuk Novel Al-based complex hydrides, *PhD-student's Day*, May **2013**, Louvain-la-Neuve, Belgium / poster.

3.3 **Dovgaliuk, I.**; Ban, V.; Tumanov, N.; Morelle, F.; Robeyns, K.; Picasso, C.; Tinant, B.; Filinchuk Y. Materials chemistry by diffraction methods, *IMCN Scientific Advisory Committee Meeting*, 13th of March **2014**, Louvain-la-Neuve, Belgium / poster.

3.4 **Dovgaliuk, I.**; Devillers, M.; Filinchuk, Y. Synthesis, structure and properties of novel borohydrides for hydrogen storage, *PhD-student's Day*, May **2014**, Louvain-la-Neuve, Belgium / oral.

3.5 **Dovgaliuk, I.**; le Duff, C.; Robeyns, K.; Devillers, M.; Filinchuk Y. Crystal Structures and Decomposition Properties of Hydrogen-Rich $Al(BH_4)_3 \cdot NH_3BH_3$ Complex, *8th Belgian Crystallography Symposium BCS-8,* **2014**, Brussels, Belgium / poster **(Best poster award)**.

3.6 Picasso Fernandez-Marcote, C. V.; Tumanov, N.; **Dovgaliuk, I.**; Filinchuk Y. Conversion of CO_2 into organics compounds via reaction with metal borohydrides, *8th Belgian Crystallography Symposium BCS-8*, **2014**, Brussels, Belgium / poster.

3.7 **Dovgaliuk, I.;** Devillers M.; Filinchuk Y. $M[Al(BH_4)_4]$ ($M = Li^+, Na^+, K^+, NH_4^+, Rb^+, Cs^+$) a New Family of Hydrogen-Rich Borohydrides, *PhD-student's Day*, May **2015**, Louvain-la-Neuve, Belgium / poster.

3.8 Møller, K. T.; **Dovgaliuk, I.**; Safin, D. A.; Robeyns, K.; Jensen, T. R.; Filinchuk Y. Tuning the AlL_3–BH_3NH_2R System, *PhD-student's Day*, May **2015**, Louvain-la-Neuve, Belgium / poster.

References

[1] Basic Research Needs for Electrical Energy Storage – a report of the Basic Energy Sciences Workshop on Electrical Energy Storage, April 2–4, 2007. U.S. Department of Energy Report, July 2007.

[2] L. Klebanoff, editor, *Hydrogen Storage Technology Materials and applications* (New York: CRC Press, **2013**).

[3] Jena, P. *J. Phys. Chem. Lett.* **2011**, *2*, 206–211.

[4] Eberle, U.; Felderhoff, M.; Schüth, F. *Angew. Chem. Int. Ed.* **2009**, *48*, 6608–6630.

[5] Graetz, J. *Chem. Soc. Rev.* **2009**, *38*, 73–82.

[6] Van den Berg, A. W. C.; Areán, C.O. *Chem. Commun.* **2008**, *6*, 668–681.

[7] Schlapbach, L.; Züttel, A. *Nature* **2001**, *414*, 353–358.

[8] Steele, B. C. H.; Heinzel, A. *Nature* **2001**, *414*, 345–352.

[9] Taken from http://www.hygen.com/how-a-hydrogen-fuel-cell-vehicle-works/

[10] DOE Hydrogen, Fuel Cells & Infrastructure Technologies Program Multi-Year Research, Development, and Demonstration Plan, Hydrogen Storage Technical Plan, 2007 http://www1.eere.energy.gov/hydrogenandfuelcells/mypp/.

[11] Klebanoff, L.E.; Keller, J.O. *Int. J. Hydrogen Energy* **2013**, *38*, 4533–4576.

[12] Chandra, D.; Reilly, J. J.; Chelappa, R. *JOM* **2006**, *2*, 26–32.

[13] Thomas, K. M. *Catal. Today* **2007**, *120*, 389–398.

[14] Corma, A.; Díaz-Cabañas, M. J.; Jordá, J. L. et al. *Nature* **443**, 842–845.

[15] Furukama, H.; Milller, M. A.; Yaghi, O. M. *J. Mater. Chem.* **2007**, *17*, 3197–3204.

[16] Budd, P. M.; Butler, A.; Selbie, J. et al. *Phys. Chem. Chem. Phys.* 2007, 9, 4992–1802.

[17] Lee, J. Y.; Wood, C. D.; Bradshaw D. et al. *Chem. Commun.* **2006**, 2670–2672.

[18] Y. Fukai, *The Metal-Hydrogen System – Basic bulk Properties* (Berlin: Springer-Verlang, **1993**).

[19] L. Schlapbach, editor, *Topics in App. Phys. Vol. 63*: *Hydrogen in intermetallic compounds I* (Berlin: Springer, **1988**).

[20] Schüth, F.; Bogdanovic, B.; Felderhoff, M. *Chem. Commun.* **2004**, 2249–2258.

[21] Orimo, S.; Nakamori, Y.; Eliseo, J. R.; Züttel, A.; Jensen, C. M. *Chem. Rev.* **2007**, *107*, 4111–4132.

[22] Hauback, B. C.; Brinks, H. W.; Jensen, C. M. et al. *J. Alloys Compd.* **2003**, *358*, 142–145.

[23] Hauback, B. C.; Brinks, H. W.; Fjellvåg, H. *J. Alloys Compd.* **2002**, *346*, 184–189.

[24] Hauback, B. C.; Brinks, H. W.; Heyn, R. H. et al. *J. Alloys Compd.* **2005**, *394*, 35–38.

[25] Fossdal, A.; Brinks, H. W.; Fichtner, M. et al. *J. Alloys Compd.* **2005**, *387*, 47–51.

[26] Løvvik, O. M. *Phys. Rev. B* **2005**, *71*, 144111, 1–5.

[27] Bogdanović, B.; Schwikardi, M. *J. Alloys Compd.* **1997**, *253–354*, 1–9.

[28] Srinivasan, S. S.; Brinks, H. W.; Hauback, B. C. et al. *J. Alloys Compd.* **2004**, *377*, 283– 289.

[29] Block, J.; Gray, A. P. *Inorg. Chem.* **1965**, *4 (3)*, 304–305.

[30] Brinks, H.W.; Hauback, B.C. *J. Alloys Compd.* **2003**, *354*, 143–147.

[31] Gross, K. J.; Guthrie, S.; Takara, S. et al. *J. Alloys Compd.* **2000**, *297*, 270–281.

[32] Rönnebo, E.; Noréus, D.; Kadir, K. et al. *J. Alloys Compd.* **2000**, *299*, 101–106.

[33] Morioka, H.; Kakizaki, K.; Chung, S. et al. *J. Alloys Compd.* **2003**, *353*, 310–314.

[34] Mamatha, M.; Bogdanovic, B.; Felderhoff, M. et al. *J. Alloys Compd.* **2006**, *407*, 78–86.

[35] Fichtner, M.; Fuhr, O.; Kircher, O. *J. Alloys Compd.* **2003**, *356–357*, 418–422.

[36] Ley, M. B.; Jepsen, L. H.; Lee, Y.-S. et al. *Mater. Today* **2014**, *17*, 122–128.

[37] Jepsen, L. H.; Ley, M. B.; Lee, Y.-S. et al. *Mater. Today* **2014**, *17*, 129–135.

[38] Züttel, A.; Borgschulte, A.; Oriomo, S-I. *Scr. Mater.* **2007**, *56*, 823–828.

[39] George, L.; Saxena, S. K. *Int. J. Hydrogen Energy* **2010**, *35*, 5454–5470.

[40] Filinchuk, Y.; Chernyshov, D.; Dmitriev, V. *Z. Kristallogr.* **2008**, *223*, 649–659.

[41] Ohba, N.; Miwa, K.; Aoki, M. et al. *Phys. Rev. B* **2006**, 075110.

[42] Hwang, S-J.; Bowman, R.; Reiter, J. W. et al. *J. Phys. Chem. C* **2008**, *112*, 3164–3169.

[43] Soloveichik, G. L.; Andrus, M.; Gao, Y. et al. *Int. J. Hydrogen Energy* **2009**, *34*, 2144–2152.

[44] Soulie, J-Ph.; Renaudin, G.; Černý, R. et al. *J. Alloys Compd.* **2002**, *346*, 200–205.

[45] Orimo, S. I.; Nakamori, Y.; Ohba, N. et al. *Appl. Phys. Lett.* **2006**, *89*, 021920.

[46] Hwang, S. J.; Robert, C.; Bowman, J. et al. *J. Phys. Chem. C* **2008,** *112*, 3164–3169.

[47] Züttel, A.; Rentsch, S.; Fischer, P. *J. Alloys Compd.* **2003**, *356–357*, 515–520.

[48] Fischer, P.; Züttel, A. *Mater. Sci. Forum.* **2004**, *443–444*, 287–290.

[49] Martelli, P.; Caputo, R.; Remhof, A. et al. *J. Phys. Chem. C* **2010**, *114*, 7173–7177.

[50] Urgnani, J.; Torres, F. J.; Palumbo, M. et al. *Int. J. Hydrogen Energy* **2008**, *33*, 3111–3115.

[51] Filinchuk, Y.; Hagemann, H. *Eur. J. Inorg. Chem.* **2008**, *20*, 3127–3133.

[52] Luck, R. L.; Schelter, E. J. *Acta Cryst. C* **1999**, *55*.

[53] Stasinevich, D. S.; Egorenko G. A. *Russ. J. Inorg. Chem.* **1968,** *13*, 341–343.

[54] Renaudin, G.; Gomes, S.; Hagemann, H et al. *J. Alloys Compd.* **2004**, *375*, 98–106.

[55] Marynick, D. S.; Lipscomb, W. N. *Inorg. Chem.* **1972**, *11*, 820–823.

[56] Černý, R.; Filinchuk, Y.; Hagemann, H. et al. *Angew. Chem. Int. Ed.* **2007**, *46*, 5765 –5767.

[57] Li, H. W.; Miwa, K.; Ohba, N. et al. *Nanotechnology* **2009**, *20*, 204013.

[58] Filinchuk, Y.; Černý, R.; Hagemann, H. *Chem. Mater.* **2009**, *21*, 925–933.

[59] Her, J.-H.; Stephens, P. W.; Gao, Y. et al. *Acta Cryst. B* **2007**, *63*, 561–568.

[60] Filinchuk, Y.; Richter, B.; Jensen, T. R. et al. *Angew. Chem. Int. Ed.* **2011**, *50*, 11162–11166.

[61] Miwa, K.; Aoki, M.; Noritake, T. et al. *Phys. Rev. B* **2006**, *74*, 155122.

[62] Kim, Y.; Hwang, S-J.; Shim, J-H. et al. *J. Phys. Chem. C* **2012**, *116*, 4330 – 4334.

[63] Ozolins, V.; Majzoub, E. H.; Wolverton, C. et al. *J. Am. Chem. Soc.* **2009**, *131*, 230–237.

[64] Filinchuk, Y.; Rönnebro, E.; Chandra, D. *Acta Mater.* **2009**, *57*, 732–738.

[65] Buchter, F.; Łodziana Z.; Remhof, A. et al. *J. Phys. Chem. B* **2008**, *112*, 8042–8048.

[66] Aldridge, S.; Blake, A. J.; Downs, A. J. et al. *J. Chem. Soc., Dalton Trans*. **1997**, 1007–1012.

[67] Ogg, R. A.; Ray J. D. *Discuss. Faraday Soc.* **1955**, *19*, 239–246.

[68] Himpsl, F. L. and Bond A. C. *J. Am. Chem. Soc.* **1981**, *103*, 1098–1102.

[69] Stavila V.; Her, J.-H.; Zhou W. et al. *J. Sol. St. Chem.* **2010**, *183*, 1133–1140.

[70] Løvvik, O. M.; Swang, O. *Europhys. Lett.* **2004**, *67*, 607–613.

[71] Graetz, J.; Lee, Y.; Reilly, J. J. et al. *Phys. Rev. B* **2005**, *71*, 184115.

[72] Nickels, E. A.; Jones, M. O.; David, W. I .F et al. *Angew. Chem. Int. Ed.* **2008**, *47*, 2817–2819.

[73] Paskevicius, M.; Ley, M. B.; Sheppard, D. A. et al. *Phys. Chem. Chem. Phys.* **2013**, *15*, 19774–19789.

[74] Seballos, L.; Zhang, J.; Roberto E. et al. *J. Alloys Compd.* **2009**, *476*, 446–450.

[75] Schounwink, P.; Ley, B. M.; Tissot, A. et al. *Nature Commun.* **2014**, *5*, 5706.

[76] Lindemann, I.; Ferrer, R. D.; Dunsch et al. *Chem. Eur. J.* **2010**, *16*, 8707–8712.

[77] Lindemann, I.; Ferrer, R. D.; Dunsch, L. et al. *Faraday Discuss.* **2011**, *151*, 231–242.

[78] Knight, D. A.; Zidan, R.; Lascola, R. et al. *J. Phys. Chem. C* **2013**, *117,* 19905–19915.

[79] Kim, K. C.; Hwang, S.-J.; Bowman Jr., R. C. et al. *J. Phys. Chem. C* **2009**, *113*, 9956–9968.

[80] Černý, R.; Severa, G.; Ravnsbæk, D. B. et al. *J. Phys. Chem. C* **2010**, *114*, 1357–1364.

[81] Černý, R.; Severa, G.; Ravnsbæk, D. B. et al. *J. Phys. Chem. C* **2010**, *114*, 19540–19549.

[82] Korablov, D.; Ravnsbæk, D. B.; Ban. V. et al. *Int. J. Hydrogen Energy* **2013**, *38*, 8376–8383.

[83] Llamas-Jansa, I.; Aliouane, N.; Deledda, S. et al. *J. Alloys Compd.* **2011**, *509S*, S684–S687.

[84] Roedern, E.; Jensen, T. R. *J. Phys. Chem. C* **2014,** *118*, 23567–23574.

[85] Ravnsbæk, D. B.; Filinchuk, Y.; Cerenius, Y.et al. *Angew. Chem. Int. Ed.* **2009**, *48*, 6659–6663.

[86] Černý, R.; Ravnsbæk, D. B.; Schounwink, P. et al. *J. Phys. Chem. C* **2012**, *116*, 1563–1571.

[87] Ravnsbæk, D. B.; Ley M. B.; Lee Y.-S. et al. *Int. J. Hydrogen Energy* **2012**, *37*, 8428–8438.

[88] Jaroń, T.; Grochala, W. *Dalton Trans.* **2011**, *40*, 12808–12817.

[89] Jaroń, T.; Wegner, W.; Grochala, W. *Dalton Trans.* **2013**, *42*, 6886–8893.

[90] Li, H.-W.; Oriomo, S.; Nakamori, Y. et al. *J. Alloys Compd.* **2007**, *446-447*, 315–318.

[91] Ravnsbæk, D. B.; Sørensen, L.; Filinchuk, Y. et al. *Angew. Chem. Int. Ed.* **2012**, *51*, 3582–3586.

[92] Rude, L. H.; Nielsen, T. K.; Ravnsbæk, D. B. et al. *Phys. Status Solidi A* **2011**, *208*, 1754–1773.

[93] Černý, R.; Schounwink, P.; Sadikin, Y. et al. *Inorg. Chem.* **2013**, *52*, 9941–9947.

[94] Chen, P.; Xiong, Z.; Luo, J. et al. *Nature* **2002**, *420*, 302–304.

[95] Orimo, S.; Nakamori, Y.; Eliseo, J. R.; Züttel, A.; Jensen, C. M. *Chem. Rev.* **2007**, *107*, 4111–4132.

[96] Luo, W.; Sickafoose S. *J. Alloys Compd.* **2006**, *407*, 274– 281.

[97] Pinkerton, F. E.; Meisner, G. P.; Meyer M. S. et al. *J. Phys. Chem. B*, **2005**, *109*, 6–8.

[98] Filinchuk, Y. E.; Yvon, K.; Meisner G. P. et al. *Inorg. Chem.* **2006**, *45*, 1433-1435.

[99] Vajo, J. J.; Skeith S. L. *J. Phys. Chem. B* **2005**, *109*, 3719–3722.

[100] Bösenberg, U.; Ravnsbæk, D. B.; Hagemann H. et al. *J. Phys. Chem. C* **2010,** *114*, 15212–15217.

[101] Wang, J.; Zhang, J.-G.; Man, T.-T. et al. *Chem. Asian J.* **2013**, *8*, 1076–1089.

[102] Guo, Y. H.; Xia, G.; Zhu, Y. et al. *Chem. Commun.* **2010**, *46*, 2599–2506.

[103] Guo, Y. H.; Sun, W. W.; Guo, Z. P. et al. *J. Phys. Chem. C* **2010**, *114*, 12823–12827.

[104] Soloveichik, G.; Her, J.-H.; Stephens, P. W. et al. *Inorg. Chem.* **2008**, *47*, 4290–4298.

[105] Chu, H.; Wu, G.; Xiong, Z. et al. *Chem. Mater.* **2010**, *22*, 6021–6028;

[106] Gu, Q.; Gao, L.; Guo, Y. et al. *Energy Environ. Sci.* **2012**, *5*, 7590–7600.

[107] Yuan, F.; Gu, Q.; Chen, X. et al. *J. Mater. Chem.* **2012**, *24*, 3370–3379.

[108] Guo, Y. H.; Yu, X.; Sun, W. et al. W. *Angew. Chem. Int. Ed.* **2011**, *50*, 1087–1091.

[109] Guo, Y. H.; Jiang, Y.; Xia, G.; Yu, X. *Chem. Commun.* **2012**, 48, 4408–4410.

[110] Sun, W.; Chen, X.; Gu, Q. et al. *Chem. Eur. J.* **2012**, *18*, 6825–6834.

[111] Yang, Y.; Liu, Y.; Wu, H. et al. *Phys. Chem. Chem. Phys.* **2014**, *16*, 135–143.

[112] Guo, Y.; Wu, H.; Zhou, W. et al. *J. Am. Chem. Soc.* **2011**, *133*, 4690–4693.

[113] Jepsen, L. H.; Ley, M. B.; Lee, Y.-S. et al. *Mater. Today* **2014**, *17*, 129–135.

[114] Chen X.; Yu X. *J. Phys. Chem. C* **2012**, *116*, 11900−11906.

[115] Johnson, S. R.; David, W. I. F.; Royse, D. M. Et al. *Chem. Asian J.* **2009**, *4*, 849–854.

[116] Zheng, X.; Wu, G.; Li, W. Et al. *Energy Environ. Sci.* **2011**, *4*, 3593–3600.

[117] Wolf, G.; Baumann, J.; Baitalow, F. et al. *Thermochim. Acta* **2000**, *343*, 19–25.

[118] Baitalow, F.; Baumann, J.; Wolf, G. et al. *Thermochim. Acta* **2002**, *391*, 159–168.

[119] Neiner, D.; Karkamkar, A.; Linehan, J. C. et al. *J. Phys. Chem. C* **2008**, *113*, 1098–1103.

[120] Xiong, Z.; Yong, C. K.; Wu, G. et al. *Nat. Mater.* **2008**, *7*, 138–141.

[121] Diyabalanage, H. V. K.; Shrestha, R. P.; Semelsberger, T. A. et al. *Angew. Chem. Int. Ed.* **2007**, *46*, 8995–8997.

[122] Wu, H.; Zhou, W.; Yildirim, T. et al. *J. Am. Chem. Soc.* **2008**, *130*, 14834–14839.

[123] Luo, J.; Kang, X.; Wang, P. et al. *Energy Environ. Sci.* **2013**, *6*, 1018–1025.

[124] Fijalkowski, K. J.; Genova, R. V.; Filinchuk, Y. et al. *Dalton Trans.* **2011**, *40*, 4407–4413.

[125] Wu, H.; Zhou, W.; Pinkerton, F. E. et al. *Chem. Commun.* **2011**, *47*, 4102–4204.

[126] Luo, J.; Wu, H.; Zhou, W. et al. *Int. J. Hydrogen Energy* **2013**, *38*, 197–204.

[127] Wu, C.; Wu, G.; Xiong, Z. et al. *Chem. Mater.* **2010**, *22*, 3–5.

[128] Luo, J.; Wu, H.; Zhou, W. et al. *Int. J. Hydrogen Energy* **2012**, *37*, 10750–10757.

[129] Wu, H.; Zhou, W.; Pinkerton, F. E. et al. *J. Mater. Chem.* **2010**, *20*, 6550–6556.

[130] Chen, X.; Yuan, F.; Gu, Q. et al. *Dalton Trans.* **2013**, *42*, 14365–14368.

[131] Jepsen, L.H.; Ban, V.; Møller, K. T. et al. *J. Phys. Chem. C* **2014**, *118*, 12141–12153.

[132] Tan, Y.; Gu, Q.; Kimpton, J. A et al. *J. Mater. Chem. A* **2013**, *1*, 10155–10165.

[133] Summerscales, O. T.; Gordon, J. C. *Dalton Trans.* **2013**, *42*, 10075–10084.

[134] Sutton, A. D.; Burrell, A. K.; Dixon, D. A. et al. *Science* **2011**, *331*, 1426–1429.

[135] Nielsen, T. K.; Karkamkar, A.; Bowden, M. et al. *Dalton Trans.* **2013**, *42*, 680–683.

[136] Schouwink, P.; Morelle, F.; Sadikin, Y. et al. *Energies* **2015**, *8*, 8286–8299.

[137] Laversenne, L.; Goutaudier, C.; Chiriac, R. et al. *J Therm Anal Cal.* **2008**, *94*, 785–790.

[138] Goudon, J. P.; Bernard, F.; Renouard, J. et al. *Int. J. Hydrogen Energy* **2010**, *35*, 11071–11076.

[139] Kojima, Y.; Kawai, Y.; Kimbara, M. et al. *Int. J. Hydrogen Energy* **2004**, *29*, 1213–1217.

[140] Fronczek, F. R.; Aubry, D. A.; Stanley, G. G. *Acta Cryst. E* **2001**, *57*, i62–63.

[141] Santos, D. M. F.; Sequeira, C. A. C. *Renewable Sustainable Energy Rev.* **2011**, *15*, 3980–4001.

[142] Minkina, V. G; Shabunya, S. I.; Kalinin, V. I. Et al. *Int. J. Hydrogen Energy* **2008**, *33*, 5629–5635.

[143] Andrieux, J; Demirci, U. B.; Hannauer, J et al. *Int. J. Hydrogen Energy* **2011**, *36*, 224–233.

[144] Demirci, U. B.; Miele, P. *Phys. Chem. Chem. Phys.* **2010**, *44*, 14651–14665.

[145] Wee, J. H. *J. Power Sources* **2006**, *155*, 329–339.

[146] Demirci, U. B.; Garin, F. *J. Alloys Compd.* **2008**, *463*, 107–111.

[147] Şahin, Ö.; Özdemir, M. *Int. J. Hydrogen Energy* **2006**, *32*, 2330–2336.

[148] Demirci, U. B.; Akdim, O.; Miele, P. *Int. J. Hydrogen Energy* **2009**, *34*, 2638–2645.

[149] Tan, Y.; Yu. X. *RSC Adv.* **2013**, *3*, 23879–23894.

[150] Ager, J. W.; Shaner M. R.; Walczak K. A. Walczak et al. *Energy Environ. Sci.* **2015**, *8*, 2811–2824.

[151] Schneider, S.; Hawkins, T.; Ahmed Y. et al. *Angew. Chem. Int. Ed.* **2011**, *50*, 5866–5888.

[152] Sadikin Y.; Brighi, Matteo; Schouwink, P. DOI 10.1002/aenm.201501016.

[153] Orengo, F. *Chimica* **1955**, *11*, 55.

[154] Proell, W.; Bowman, N. *J. Space Flight* **1950**, *2*, 1.

[155] Semenenko, K. N.; Kravchenko, O. V. *Russ. J. Inorg. Chem.* **1972**, *17*, 1084-1086.

[156] Titov, L. V.; Eremin, E. R. *Izv. Akad. Nauk SSSR, Ser. Khim.* **1975**, *5*, 1188-1189.

[157] Tang, Z.; Tan, Y.; Chen, X. et al. *Angew. Chem. Int. Ed.* **2013**, *52*, 12659–12663.

[158] Nakagava, Y.; Isobe, S.; Ikarashi, Y. et al. *J. Mater. Chem. A* **2014**, *2*, 3926–3931.

[159] Xia, G.; Tan, Y.; Chen, X. et al. *J. Mater Chem. A* **2013**, *1*, 1810–1820.

[160] Nakagawa, Y.; Ikarashi, Y.; Isobe, S. et al. *RSC Adv.* **2014**, *4*, 20626–20631.

[161] Tang, Z.; Tan, Y.; Wu, H. et al. *Acta Materialia* **2013**, *61*, 4787–4796.

[162] V. K. Pecharsky, P. Y. Zavalij editors, *Fundamentals of Powder diffraction and Structural Characterization of Materials* (New York: Springer, **2009**).

[163] C. Giacovazzo *International Tables for Crystallography*. Vol. B, Chapter 2.2, **2006**, 210–234.

[164] Sheldrick, G. M. *Acta Crystallogr.* **2008**, *A64*, 112–122.

[165] W. I. F. David, K. Shankland, L. B. McCusker, Ch. Baerlocher editors, *Structure Determination from Powder Diffraction Data* (Oxford: University Press, **2002**).

[166] Boultif, A.; Louer, D. *J. Appl. Crystallogr.* **2004**, 37, 724–731.

[167] Favre-Nicolin, V.; Ĉerný, R. *J. Appl. Crystallogr.* **2002**, *35*, 734–743.

[168] LMGP-Suite Suite of Programs for the interpretation of X-ray Experiments, by Jean Laugier and Bernard Bochu, ENSP/Laboratoire des Matériaux et du Génie Physique, BP 46. 38042 Saint Martin d'Hères, France. WWW: http://www.inpg.fr/LMGP and http://www.ccp14.ac.uk/tutorial/lmgp/.

[169] Rodriguez-Carvajal, J. *Physica B* **1993**, *192*, 55–69.

[170] Ĉerný, R. *Chem. Met. Alloys* **2008**, *1*, 120–127.

[171] R. A. Young editor, *The Rietveld Method* (Oxford: University Press, **1993**).

[172] Paskevicius, M.; Ley, M. B.; Shepard, D. A. et al. *Phys. Chem.Chem. Phys.* **2013**, *15*, 9774–19789.

[173] Jensen, T. R.; Nielsen, T. K.; Filinchuk, Y. Et al. *J. Appl. Crystallogr.* **2010**, *43*, 1456–1463.

[174] Allan, D. R.; Miletich, R.; Angel, R. J. *Rev. Sci. Instrum.* **1996**, *67*, 840.

[175] Forman, R. A.; Piermarini, G. J.; Barnett, J. D.; Block, S. *Science* **1972**, *176*, 284–285.

[176] Piermarini, G. J.; Block, S.; Barnett, J. D.; Forman, R. A. *J. Appl. Phys.* **1975**, *46*, 2774.

[177] Piermarini, G. J. *J. Appl. Phys.* **1973**, *44*, 5377.

[178] Adams, D. M.; Appleby, R.; Sharma, S. K. *J. Phys. E.* **1976**, *9*, 1140–1144.

[179] Hammersley, A. P.; Svensson, S. O.; Hanfland, M. et al. *High Press. Res.* **1996**, *14*, 235–248.

[180] Züttel, A.; Rentsch, S.; Fischerb, P. et al. *J. Alloys Compd.* **2003**, *356–357*, 515–520.

[181] Chłopek, K.; Frommen, C.; Lèon, A. et al. *J. Mater. Chem.* **2007**, *17*, 3496–3503.

[182] Schrauzer, G. N. *Naturwissenschaften* **1955**, *42*, 438.

[183] Nakamori, Y.; Miwa, K.; Ninomiya, A. Et al. *Phys. Rev. B* **2006**, *74*, 45126.

[184] Grochala, W.; Edwards, P. P. *Chem. Rev.* **2004**, *104*, 1283–1315.

[185] Lindemann, I.; Borgschulte, A.; Callini, E. et al. *Int. J. Hydrogen Energy* **2013**, *38*, 2790–2795.

[186] Schlesinger, H. I.; Sanderson, R. T.; Burg, A. B. *J. Am. Chem. Soc.* **1940**, *62*, 3421–3425.

[187] Hagemann, H.; Černý. R. *Dalton Trans.* **2010**, *39*, 6006–6012.

[188] Huot, J.; Ravnsbæk, D. B.; Zhang, J. et al. *Prog. Mater. Sci.* **2013**, *58*, 30–75.

[189] Dou, D.; Liu, J.; Krause Bauer J. A. et al. *Inorg. Chem.* **1994**, 33, 5443–5447.

[190] Jaroń, T.; Orłowski, P. A.; Wegner, W. et al. *Angew. Chem. Int. Ed.* **2015**, *54*, 1236–1239.

[191] Schlesinger, H. I.; Brown, H. C.; Hyde, E. K. *J. Am. Chem. Soc.* **1953**, *75*, 209-213.

[192] Sivasubramanian, P.; Mohtadi, R.; Zidan, R. et al. *Appl. Spectrosc.* **2012**, *66*, 591-594.

[193] Mairesse, G.; Barbier, P.; Wignacourt, J.-P. *Acta Crystallogr.* **1978**, *B34*, 1328–1330.

[194] Mairesse, G.; Barbier, P.; Wignacourt, J.-P. *Acta Crystallogr., Sect. B: Struct. Sci* **1979**, *35*, 1573–1580.

[195] Parry, R. W.; Schults D. R.; Girardot P. R. *J. Am. Chem. Soc.* **1958**, *80*, 1–3.

[196] Kraus, W.; Nolze, G. *J. Appl. Crystallogr.* **1996**, *29*, 301–303.

[197] O'Boyle, N. M.; Banck, M.; James, C. A.; Morley, C.; Vandermeersch, T.; Hutchison, G. R. *J. Cheminformatics*, **2011**, *3*, 33.

[198] Spek, A. L. PLATON. University of Utrecht, The Netherlands, **2006**.

[199] Kresse, G.; Furthmüller, J. *Phys Rev B* **1996**, *54*, 11169–11186.

[200] Blöchl, P. E. *Phys. Rev. B* **1994**, *50*, 17953–17989.

[201] Perdew, J. P.; Burke, K.; Ernzerhof, M. *Phys. Rev. Lett.* **1996**, *77*, 3865–3868.

[202] Nosé, S. *J. Chem. Phys.* **1984**, *81*, 511–519.

[203] Stokes, H. T.; Hatch, D. M. *J. Appl. Cryst.* **2005**, *38*, 237–238.

[204] Born M.; Huang, K. *Dynamical Theory of Crystal Lattices*, Oxford University Press, Oxford, UK, **1954**.

[205] Shannon, R. D. *Acta Crystallogr.* **1976**, *A32*, 751–767.

[206] Kim, K. C.; Sholl, D. S. *J. Phys. Chem. C* **2010**, *114*, 678–686.

[207] Ley, M. B.; Roedern, E.; Jensen, T. R. *Phys. Chem. Chem. Phys.* **2014**, *16*, 24194-24199.

[208] Blatov, V. A. *Struct. Chem.* **2012**, *23*, 955–963.

[209] Newsam, J. M.; Cheetham, A. K.; Tofield, B. C. *Solid State Ionics* **1980**, *1*, 377-393.

[210] Wyckoff, R.W.G. *Z. Kristallogr.* **1925**, *62*, 529–539.

[211] Schäfer, W.; Müller-Vogt *Acta Crystallogr.* **1979**, *B35*, 588-592.

[212] Almenningen, A.; Gundersen, G.; Haaland, A. *Acta Chem. Scand.* **1968**, *22*, 328-334.

[213] Krebs, B.; Greiwing, H.; Brendel, C. J. et al. *Inorg. Chem.* **1991**, *30*, 981–988.

[214] Schouwink, P.; D'Anna V.; Brix Ley M. et al. *J. Phys. Chem. C* **2012**, *116*, 10829-10840.

[215] Bowden, M. E.; Gainsford, G. J.; Robinson, W. T. *Aust. J. Chem.* **2007**, *60*, 149-153.

[216] Flacau, R.; Ratcliffe, C. I.; Desgreniers, S. Et al. *Chem. Commun.* **2010**, *46*, 9164-9166.

[217] Sillén L. G.; Nylander A. L. *Ark. Kemi Mineral. Geol.* **1943**, *17A*, 1–27.

[218] Kokkoros, M. P. *Prakt. Athener Akad.* **1942**,*17*, 163–174.

[219] Błoński, P.; Łodziana, Z. *Phys. Rev. B* **2014**, *90*, 054114.

[220] Gutowski M.; Autrey T. *Prepr. Pap.-Am. Chem. Soc., Div. Fuel Chem.* **2004**, *49*, 275–276.

[221] Marks, T. J.; Kolb, J. R. et al. *Chem. Rev.* **1977**, *77*, 263–293.

[222] Makhaev, V. D. *Russ. Chem. Rev.* **2000**, *69*, 727–746.

[223] Coe, D.A.; Nibler, J. W. *Spectrochim. Acta* **1973**, *29A*, 1789–1804.

[224] Dibeler, V. H.; Mohler, F. L. *J. Am. Chem. Soc.* **1948**, *70*, 987–989.

[225] *NIST Chemistry WebBook, Mass Spectrum and Infrared Spectrum of Diborane, NIST Number 20;* National Institute of Standards and Technology: Gaitherburg MD, 2005.

[226] Winkler, A.; Resch, Ch.; Redulic, K.D. *J. Chem. Phys.* **1991**, *95*, 7682–7688.

[227] Borgshulte, A.; Callini, E.; Probst, B. et al. *J. Phys. Chem. C* **2011**, *115,* 17220–17226.

[228] Shevlin, S. A.; Guo, Z. X. *Chem. Soc. Rev.* **2009**, *38*, 211–225.

[229] Chen, X.; Bao, X.; Zhao, J.-C. et al. *J. Am. Chem. Soc.* **2011**, *133*, 14172–14175.

[230] Pauling, L. *J. Am. Chem. Soc.* **1929**, *51*, 1010–1026.

[231] Jenkins, H. D. B.; Thakur, K. P. *J. Chem. Educ.* **1979**, *56*, 576–577.

[232] Cartledge, G. H. *J. Am. Chem. Soc.* **1928**, *50*, 2855–2863.

[233] Sundqvist, B. *Solid State Phenomena* **2009**, *150*, 175–195.

[234] Filinchuk, Y.; Talyzin, A. V.; Hagemann, H. et al. *Inorg. Chem.* **2010**, *49*, 5285–5292.

[235] Chua, Y. S.; Chen, P.; Wu, G. et al. *Chem. Commun.* **2011**, *47*, 5116–5129.

[236] Li, H.-W.; Yan, Y.; Oriomo, S.-I. et al. *Energies* **2011**, *4*, 185–214.

[237] Mao, J.; Guo, Z.; Nevikovets, I. P. et al. *J. Phys. Chem. C* **2012**, *116*, 1596–1604.

[238] Burg, A. B.; Schlesinger, H. I. *J. Am. Chem.Soc.* **1940**, *62*, 3425–3429.

[239] Kim, Y.; Hwang, S.-J.; Shim, J.-H. Et al. *J. Phys. Chem. C* **2012**, *116*, 4330–4334.

[240] Volkov, V. V.; Myakishev K. G. *Izv. Sib. Otd. Akad. Nauk SSSR, Ser. Khim. Nauk* **1977**, *1*, 77–82.

[241] Agilent Technologies (2012). Agilent Technologies UK Ltd., Oxford, UK, Xcalibur/SuperNova CCD system, CrysAlisPro Software system, Version 1.171.36.24.

[242] Jensen, J. O. *Spectrochim. Acta A* **2003**, *59*, 1575–1578.

[243] Hess, N. J.; Bowden, M. E.; Parvanov, V. M. Et al. *J. Chem. Phys.* **2008**, *128*, 34508.

[244] Downs, A. J.; Jones, L. A. *Polyhedron* **1994**, *13*, 2401–2415.

[245] Chen, X.; Zhang, Y.; Wang, Y. et al. *Chem. Sci.* **2012**, *3*, 3183–3191.

[246] Lingam, H. K.; Chen, X.; Zhao, J.-C. et al. *Chem. Eur. J.* **2012**, *18*, 3490–3492.

[247] Maybury, P. C.; Ahnell, J. E. *Inorg. Chem.* **1967**, *6*, 1286–1291.

[248] Nöth, H.; Rurländer, R. *Inorg. Chem.* **1981**, *20*, 1062–1072.

[249] M. E. Bowden, I. W. M. Brown, G. J. Gainford, H. Wong *Inorg. Chim. Acta* **2008**, *361*, 2147–2153.

[250] Leardini, F.; Valero-Pedraza, M. J.; Perez-Mayoral, E. et al. *J. Phys. Chem. C* **2014**, *118*, 17221−17230.

[251] Kelly, H. C.; Edwards, J. O. *Inorg. Chem.* **1963**, *2*, 226−227.

[252] Atwood, D. A. *Coord. Chem. Rev.* **1998**, *176*, 407–430.

[253] Aldridge, S.; Dows, A. J.; Tang, C. Y. et al. *J. Am. Chem. Soc.* **2009**, *131*, 2231-2243.

[254] V. I. Bakhmutov editor, *Dihydrogen Bonds: Principles, Experiment, and Applications* (New Jersey: Wiley-Interscience, **2008**).

[255] Karkamkar, A.; Aardahl, C.; Autrey, T. *Material Matters*, **2007**, *2*, 6**–**9.

[256] a) Bluhm, M. E.; Bradley, M. G.; Butterick III, R. et al. *J. Am. Chem. Soc.* **2006**, *48*, 7748–7749; b) Himmelberger, D. W.; Alden, L. R.; Bluhm, M. E. et al. *Inorg. Chem.* **2009**, *18*, 9883–9889.

[257] Stephens, F. H.; Baker, R. T.; Matus, M. H. et al. *Angew. Chem. Int. Ed.* **2007**, *46*, 746–749.

[258] Bösenberg, U.; Doppiu, S.; Mosegaard, L. Et al. *Acta Mater.* **2007**, *55*, 3951–3958.

[259] Staubitz, A.; Robertson, A. P. M.; Manners, I. *Chem. Rev.* **2010**, *110*, 4079–4124.

[260] Diyabalanage, H. V. K.; Nakagava, T.; Shrestha, R. P. et al. *J. Am. Chem. Soc.* **2010**, *132*, 11836–11837.

[261] Zhang,Q.; Tang, C.; Fang, C. et al. *J. Phys. Chem. C* **2010**, *114*, 1709–1714.

[262] Genova, R. V.; Fijalkowski, K. J.; Budzianowski, A. et al. *J. Alloys Compd.* **2010**, *499*, 144–148.

[263] Chua, Y. S.; Li, W.; Wu, G. Et al. *Chem. Mater.* **2012**, *24*, 3574–3581.

[264] Zhang, Y.; Shimoda, K.; Miyaoka, H. Et al. *Int. J. Hydrogen Energy* **2010**, *35*, 12405–12409.

[265] V. Dyadkin, SNBL ToolBox. Swiss-Norwegian Beam Lines at ESRF, Grenoble, France, Release 2014-2.

[266] Grimme, S. *J Comp. Chem.* **2006**, *27*, 1787–1899.

[267] Hoover, W. G. *Phys. Rev. A* **1985**, *31*, 1695–1697.

[268] Gross, K. J.; Guthrie, S.; Takara, S. et al. *J. Alloys Compd.* **2000**, *297*, 270–281.

[269] Stowe, A. C.; Shaw, W. J.; Linehan, J. C. et al. *Phys. Chem. Chem. Phys.* **2007**, *9*, 1831–1836.

[270] Lutz, H. D.; Lange, N. *Z. Anorg. Allg. Chem.* **1992**, *613*, 83–87.

[271] Baumann, J.; Baitalow, F.; Wolf G. *Thermochim. Acta* **2005**, *430*, 9–14.

[272] Chen, X.; Gonsalves, K. E. *J. Mater. Res.* **1997**, *12*, 1274–1286.

[273] Hu, M. G.; Geanangel, R. A.; Wendlandt, W. W. *Thermochim. Acta* **1978**, *23*, 249–255.

[274] Shimoda, K.; Doi, K.; Nakagawa, T. Et al. *J. Phys. Chem. C* **2012**, *116*, 5957–5964.

[275] Shimoda, K.; Zhang, Y.; Ishikawa, T. et al. *J. Mater. Chem.* **2011**, *21*, 2609–2615.

[276] Leardini, F.; Ares, J. R.; Bodega, J. Et al. *J. Phys. Chem. C* **2012**, *116*, 24430–24435.

[277] Wang, K.; Arcisauskaite, V.; Jiao, J.-S. et al. *RSC Adv.* **2014**, *4*, 14624–14632.

[278] Jepsen, L. H.; Skibsted, J.; Jensen, T. R. *J. Alloys Compd.* **2013**, *580*, S287–S291.

[279] Davis, R. E.; Bromels, E.; Kibby, C. L. *J. Am. Chem. Soc.* **1962**, *84*, 885–892.

[280] Marezio, M.; Plettinger, H. A.; Zachariasen, W. H. *Acta Crystallogr.* **1963**, *16*, 975–980.

[281] Levy, H. A.; Lisensky, G. C. *Acta Crystallogr. B* **1978**, *34*, 3502–3510.

[282] Luo, X.; Pan, S.; Fan, X. et al. *J. Cryst. Growth* **2009**, *311*, 3517–3521.

[283] Zhang, H.-X.; Zhang, J.; Zheng, S.-T. et al. *Cryst. Growth Des.* **2005**, *5*, 157–161.

[284] Custelcean, R.; Jackson, J. E. *Chem. Rev.* **2001**, *101*, 1963–1980.

[285] Devi, S. A.; Philip, D.; Aruldhas, G. *J. Sol. State Chem.* **1994**, *133*, 157–162.

[286] Kazuo Nakamoto Infrared and Raman spectra of Inorganic and Coordination Compounds, Wiley - Intrescience publications p. 121−125 (485 p).

[287] Jun, L,; Shuping, X.; Shiyang, G. *Spectrohim Acta* **1995**, *51A*, 519–532.

[288] Harvey, K. B.; Mcquak, N. R. *Can. J. Chem.* **1971**, *49*, 3272–3281.

[289] Miller, F. A.; Wilkins, C. H. *Anal. Chem.* **1952**, *24*, 1253–1294.

[290] Waslavska, I. *J. Therm. Anal.* **1998**, *94*, 519–532.

[291] Francombe, T. J. *Chem. Rev.* **2012**, *112*, 2164–2178.

[292] Hoekstra, H. R.; Katz, J. J. *J. Am. Chem. Soc.* **1949**, *71*, 2488–2492.

[293] a) Dain, C. J.; Downs, A. J.; Rankin D. W. H. *Angew. Chem. Int. Ed. Engl.* **1982**, *21*, 534–535. b) Dain, C. J.; Downs, A. J.; Goode, M. J.; Evans, D. G.; Nicholls, K. T.; Rankin D. W. H.; Robertson, H. E. *J. Chem. Soc. Dalton Trans.* **1991**, 967–977.

[294] Egdell, R. G.; Green, J. C. *Inorg. Chim. Acta* **2008**, *361*, 462–466.

[295] Spundflashe, E.; Fink, H.; Seifert, J. I. *Z. Anorg. Chem.* **1989**, *579*, 143–150.